On-chip generation of high-dimensional entangled states of light

Saverio Francesconi

Université de Paris

École Doctorale 564
Physique en Île-de-France

Laboratoire
Matériaux et Phénomènes Quantiques

On-chip generation of high-dimensional entangled states of light

Par
Saverio FRANCESCONI

Thèse de doctorat de Physique

Dirigée par **Sara DUCCI**

Présentée et soutenue publiquement le 14/12/2020,
devant la commission d'examen composée de :

MCF	Florent Baboux	Univ. de Paris	Co-encadrant de thèse
DR	Marco Bellini	INO-CNR	Rapporteur
PR	Sara Ducci	Univ. de Paris	Directrice de thèse
PR	Eric Lantz	Univ. de Franche-Comté	Examinateur
PR	Agnes Maître	Sorbonne Université	Examinatrice
DR	Isabelle Robert-Philip	L2C-CNRS	Rapporteure

On-chip generation of high-dimensional entangled states of light

Nonclassical states of light are key resources for quantum information technologies thanks to their easy transmission, robustness to decoherence and variety of degrees of freedom to encode information. In this context, this PhD thesis is dedicated to the development of novel semiconductor photon pair sources. Exploiting the high flexibility offered by spontaneous parametric down conversion (SPDC) in AlGaAs waveguides, we demonstrate the generation and the engineering of high-dimensional nonclassical states of light encoded in frequency.

First, we employ a source based on a counter-propagating phase-matching scheme and demonstrate that tailoring the spatial profile (intensity and phase) of the pump beam enables the control of the photon pair spectral correlations and wavefunction symmetry directly at the generation stage, without any post-selection. In particular, tuning the pump beam waist allows to produce correlated, anti-correlated and separable frequency states, while modifying the spatial phase profile allows to switch between symmetric and antisymmetric spectral wavefunctions and to modify the exchange statistics of the photons, as evidenced measured via Hong-Ou-Mandel interferometry. We also investigate more complex quantum states: we demonstrate that this source, thanks to its geometry and to an anti-reflection coating, can also emit photon pairs entangled in a hybrid polarization/frequency degree of freedom.

We then start the development of a novel device formed by a lattice of parallel co-propagating nonlinear waveguides, design to emit spatially entangled photon pairs via cascaded quantum walks. We report the optimization of its clean room fabrication processes and first optical characterizations of this novel device.

Keywords: quantum optics, photonics, AlGaAs, spontaneous parametric down conversion, photon pair source, entanglement, Hong-Ou-Mandel, frequency correlations engineering.

Génération sur puce d' états photoniques intriqués à haute dimension

Les états non classiques de lumière sont des ressources clés pour les technologies de l'information quantique, grâce à leur facilité de transmission, leur robustesse à la décohérence et leur variété de degrés de liberté utilisables pour coder l'information. Dans ce contexte, cette thèse de doctorat est consacrée au développement de nouvelles sources semi-conductrices de paires de photons. En exploitant la grande flexibilité offerte par la conversion paramétrique spontanée (SPDC en anglais) dans les guides d'ondes AlGaAs, nous démontrons la génération et l'ingénierie d'états non classiques de lumière à haute dimension codés en fréquence.

Tout d'abord, nous utilisons une source basée sur un accord de phase contra-propageant et démontrons que l'ingénierie du profil spatial (en intensité et phase) du faisceau de pompe permet de contrôler les corrélations spectrales et la symétrie de la fonction d'onde des paires de photons directement à la génération, sans aucune post-sélection. En particulier, la variation de la taille du faisceau de pompe permet de produire des états en fréquence corrélés, anti-corrélés et séparables en fréquence ; tandis que l'ingénierie du profil de phase spatial permet de passer d'une fonction d'onde spectrale symétrique à antisymétrique et ainsi de modifier la statistique d'échange des photons, comme démontré par interférométrie de Hong-Ou-Mandel. Nous avons aussi exploré des états quantiques encore plus complexes: en effet, nous démontrons que cette source, grâce à sa géométrie et à un traitement antireflet, peut émettre des paires de photons intriqués dans un degré de liberté hybride polarisation/fréquence.

Nous développons ensuite un nouveau dispositif formé par un réseau de guides d'ondes non linéaires dessiné pour d'émettre des paires de photons intriqués dans des modes spatiaux grâce à l'effet des marches quantiques en cascade. Nous présentons l'optimisation des procédés de fabrication en salle blanche et des première caractérisation optiques de ce nouveau dispositif.

Mots clés : optique quantique, photonique, conversion paramétrique, AlGaAs, intrication, source de paires de photons, corrélations en fréquence.

Contents

Introduction

Since its introduction in the beginning of 20^{th} century, the theory of quantum mechanics has led to a completely unexpected description of nature at the fundamental level. It depicts a world that is fundamentally probabilistic, where for example a single object can exist, at the same time, in a superposition of states that collapses when observed, or, two objects in remote locations can be instantaneously connected. The latter effect, called entanglement, is one of the most fascinating properties of quantum mechanics: if two objects are entangled they cannot be described as independent but only as a unique system. Even though individual measurements on one object are random, they determine the result of the same kind of measurements carried out on the second object, revealing the presence of non-local correlations [1, 2].

Today, the possibility of explicitly addressing, controlling and detecting individual quantum systems has led to what is called the "second quantum revolution" [3], in which quantum mechanics is employed not only to describe the world but also to harness "quantum" phenomena to develop radically new *quantum technologies*.

In this perspective, quantum technologies are receiving a growing attention: several governments have launched large research programs, such as the Chinese program that has demonstrated satellite-based quantum key distribution QKD distribution protocols [4, 5] or the European Quantum Technologies flagship initiative. At the same time, national and multinational companies and start-ups have begun to take part in the development of quantum technologies, especially for applications in quantum communication (e.g. Toshiba, IDQuantique) and computing (e.g. Google, IBM, Microsoft, IonQ, D-Wave, Intel).

The European Quantum Technologies Flagship [6] has identified four main development directions: *quantum communication*, in which individual or entangled photons are used to transmit data in a secure way; *quantum simulations*, in which well-controlled systems are used to reproduce the behavior of less accessible systems; *quantum computation*, which employs quantum effects to greatly speed up certain calculations; and *quantum sensing and metrology* in which quantum systems are exploited to enhance the performance of measurements.

Yet, the development of quantum technologies for real-world applications is challenging due to the necessity of controlling single quantum systems while protecting them from a noisy environment and decoherence. To address this problem, many physical systems, each one with its strengths and limitations, are under investigation. For instance, for quantum computational tasks, trapped ions [7] and superconductive circuits [8, 9] are very promising candidates. Indeed, the latter platform has been employed in 2019 to experimentally demonstrate the advantage

of a quantum computer over a classical one [9]. On the other hand, ultra-cold atoms and ions in optical lattices [10], photonic systems [11, 12] and superconducting circuits [13] are good candidates for quantum simulation. In quantum metrology and sensing, neutral atoms, trapped ions and solid state spins are the most investigated platforms [14]. Concerning quantum communication, photons are naturally best suited. Indeed, since they travel at the speed of light and interact weakly with the environment, they can convey information over long distances, in particular at wavelengths compatible with telecommunication networks.

Integrated quantum photonics

Regarding the quantum technology field, light has a notable property: it exhibits quantum features at room temperature. Quantum optics indeed has been the testing ground for the ideas of quantum information science. For example, photons have been employed to experimentally demonstrate for the first time entanglement and non-locality [15].

In the last two decades, the technological advances in integrated photonics together with new theoretical proposals of quantum computational schemes, circuit-based [16] or measurement-based [17], have led to demonstrations of chip-based quantum protocols, in quantum simulation [18, 19], quantum information processing [20, 21] and quantum key distribution (QKD) [22, 23].

The integration of several quantum "building" blocks in the same photonic chip is a key step towards the deployment of real-world applications of quantum technologies. A fully integrated quantum photonic device should indeed gather in the same chip three main stages: the generation of quantum states of light, their propagation and manipulation through optical circuits and their detection.

The advantages of integrated quantum photonics are several. First of all, the capability of miniaturizing optical components enables scaling up the device complexity, while still having a limited footprint. Second, since all the components are integrated in the same device, they do not suffer from mechanical instability, as it is the case for bulk systems, resulting in an intrinsic phase stability. Moreover, despite being a more recent quantum technology compared to other platforms, such as trapped ions or superconducting circuits, integrated quantum photonics can leverage the solid know-how and manufacturing processes from the complementary metal–oxide–semiconductor (CMOS) and III-V industry.

The first integrated quantum photonic chip has been demonstrated in 2008 by Politi et al. [24] and from then impressive developments have been made in a variety of material platforms. In particular, single-photon sources and single-photon detectors (either superconductive nanowire single-photon detectors or transition edge sensors) have been successfully integrated in waveguides or more complex circuits [25–28]. However, even if high-quality single elements have been already demonstrated, the complete integration of generation, manipulation and detection stages in a single chip is still a challenging task.

Integrated photon pair sources

The on-chip generation of quantum light is one of the fundamental brick to develop integrated quantum photonic devices. In particular, two regimes are normally employed: the non-classicality can be produced either by engineering the quadratures of a multiphoton field (e.g. squeezing) [29] or directly by the generation of single photons or photon pairs [30]. Since integrated photon pair sources are the main topic of this thesis, we now provide a brief overview of the state of the art.

Photon pair sources can be divided in two main categories: deterministic sources and probabilistic sources.

Deterministic sources are ideally able to emit photon pairs on demand and are mainly obtained by employing quantum dots.

Quantum dots are nanostructures that provide three dimensional confinement for charged carriers with a size comparable to the de Broglie wavelength of the electron. Thanks to confinement, their energy levels are discrete, combining thus the advantages of atom-like emitters and solid-state systems.

The ground state of a quantum dot can be excited into a biexciton state, formed by two electron-hole pairs. When the quantum dot decays, it produces two photons in cascade: after the first photon is emitted, the quantum dot is left in a single-exciton state that rapidly decays by emitting a second photon [31–33]. By exploiting this process, quantum dots are able to emit polarization entangled photon pairs with high fidelity (up to 98%) [33–35].

The main issues for quantum dot integration are the control over the quantum dot shape, which can influence the photon distinguishability, and over its position. Moreover, since quantum dots naturally emit in all directions, the photon collection has to be engineered by embedding quantum dots in photonic nanostructures, such as pillars, waveguides or Bragg gratings [36, 37].

Up to now, the principal drawback of quantum dots as photon pair emitters is their cryogenic operation temperature, which needs to be smaller than the quantum dot binding energy.

Probabilistic sources of photon pairs rely on the interaction of a bright pump laser with a nonlinear medium. In this case the devices work at room temperature but the generation is probabilistic, which means the photons cannot be produced on-demand. Depending on the crystalline symmetry of the employed nonlinear material two processes can take place.

Non centrosymmetric materials, such as gallium arsenide (GaAs) or lithium niobate (LN), have non-zero second-order nonlinear coefficients that enable Spontaneous Parametric Down Conversion (SPDC), in which a pump photon decays in two lower energy photons, called signal and idler.

On the other hand, centrosymmetric materials, such as silicon (Si), enable only third-order nonlinear processes, in particular Spontaneous Four-Wave Mixing (SFWM), in which two pump photons annihilate to produce a photon pair.

Both processes require energy conservation and are efficient only if the total momentum of the interacting photons is conserved. The fulfillment of this condition, called "phase-matching", and that of energy conservation strongly constrains

the properties of the generated photons, which thus exhibit quantum correlations in one or even more degrees of freedom. This peculiarity of nonlinear sources is largely exploited to generate entangled photon pairs [38].

The ability to achieve these processes on a photonic chip is a key issue to develop real-world applications of quantum technologies. Nonlinear processes in waveguides or optical cavities, thanks to the higher confinement of the electric fields and the corresponding increase of the interaction length, feature an enhanced light-matter interaction, considerably improving the conversion efficiency compared to bulk materials. In particular, efficient integrated sources of entangled photons have been demonstrated both in $\chi^{(2)}$ materials, such as gallium aresenide (GaAs) [25, 39], lithium niobate (LN) [40, 41] and potassium titanyl phosphate (KTP) [42], and in $\chi^{(3)}$ materials, such as silicon (Si) [39, 43], silicon nitride (Si_3N_4) [44, 45] and silica (SiO_2) [46].

Integrated quantum photonic platforms

Differently from electronics where silicon is the dominant material, in integrated photonics a variety of material platforms have been studied to implement elementary building blocks [47].

Silicon-based platforms include silica-on-silicon (SoS), silicon-on-insulator (SoI) and silicon nitride-on-silica. These platforms are CMOS-compatible and thus inherit well-developed industrial fabrication processes.

Silica-on-silicon has allowed to realize the first integrated quantum photonic circuit [24] in 2008 and a universal linear optical network able to process up to 6 parallel inputs [48] in 2015. This platform allows to fabricate low-loss waveguides (≈ 0.05 dB/cm [49]), but it is characterized by a low refractive index contrast that limits the integration density (the typical bend radius is in the mm range).

Silicon-on-insulator waveguides feature high refractive index contrast, leading to bend radii of the order of 1 µm allowing for a higher integration density, up to hundreds of optical components per square centimeter [43, 50]. In addition, the strong $\chi^{(3)}$ nonlinearity enables photon pair generation via spontaneous four wave mixing, while the compatibility with the hybrid integration of superconductive nanowire single-photon detectors (SNSPDs) allows to detect photons with high quantum efficiency and a low dark count rate. Recently, this platform has been employed to demonstrate the implementation of a two-qubit programmable quantum processor [51] and of chip-to-chip quantum teleportation [50]. The main drawbacks of silicon-on-insulator devices are two-photon absorption at telecom wavelength, which limits the maximum pump power that can circulate in a waveguide, and the propagation losses that are usually in the range 2-3 dB/cm.

Silicon nitride potentially combines high refractive index contrast and ultra-low propagation losses [52]. Being exempt from two-photon absorption, silicon nitride enables to employ higher pump power to compensate its lower nonlinear $\chi^{(3)}$ coefficient with respect to silicon. This platform has been recently employed to realize a 8 x 8 multimode interferometer that allows any arbitrary unitary transformation [53].

III-V semiconductor based platforms, such as gallium arsenide (GaAs) and indium phosphide (InP), offer new capabilities compared to silicon-based platforms. Thanks to the direct band-gap of their electronic structure, they enable on-chip integration of electrically driven tunable light sources. Many III-V materials do not have inversion symmetry and thus enable second-order nonlinear processes, in particular SPDC, while presenting an electro-optic effect, allowing fast on-chip switching [54]. Finally, the use of III-V ternary (e.g. AlGaAs, InGaAs) or quaternary (e.g. AlInGaP) permits to realize integrated heterostructures and to control the material properties (i.e. refractive index and nonlinear coefficient). The propagation losses are comparable to those of the SoI-based devices (≈ 2 dB/cm). The III-V platform has allowed to demonstrate both optically and electrically injected single-photon sources based on GaAs/InGa quantum dots [36, 55, 56] and parametric entangled photon pair sources based on AlGaAs [57–60]. The integration with superconductive nanowire single-photon detectors (SNSPDs) has also been demonstrated [61], leading to the realization of the first completely on-chip quantum optics experiment [62].

Lithium niobate is a versatile dielectric optical material and has been used to realized the first integrated sources of photon pairs [63]. Its high chemical stability and transparency combined with a strong $\chi^{(2)}$ nonlinearity have allowed an extensive development of passive devices. In addition, periodically poling permits to satisfy and engineer quasi-phase-matching in the centimeter scale, while the guided regime assures a tight confinement of light, enhancing the SPDC efficiency [64] and controlling the properties of the generated photon pairs [65]. Recently, periodically poled lithium niobate (PPLN) waveguides have been employed to demonstrate squeezing on an integrated device [66] and reconfigurable quantum state generation in two-waveguide coupled systems [67, 68]. The main drawbacks of this platform are the difficulty of integrating active optical components (e.g. a pump laser) and the low refractive index that limits the integration density. The latter problem has been recently tackled by the development of lithium niobate-on-insulator [69] which features a higher refractive-index-contrast and has led to realization of compact components, such as micro-disks [70], micro-rings [71] and photonic crystal resonators [72].

Diamond-on-insulator inherits from bulk diamond its exceptional mechanical and thermal stability, a wide band-gap and low concentration of free-electrons. In addition, the presence of hundreds of mid-gap defects (color centers), many of which are outstanding quantum systems, has made this platform a promising candidate to develop single-photon sources at room temperature [73], quantum memories [74] and precision sensing [75]. Recent advances in fabrication techniques have enabled the field of diamond nanophotonics, leading to the realization of diamond photonic crystal cavities [76], while the demonstration of femtosecond laser direct writing on bulk diamond [77] has opened the way to high-density integration.

Femtosecond laser micromachining is a maskless fabrication technique that allows to realize three-dimensional guiding structures following an arbitrary geometry with a high writing speed (of the order of cm/s). It is employed in several

material platforms, for example silicate glass [78], bulk diamond [77] and PPLN crystal [79, 80]. In particular femtosecond laser written circuits on silicate glass share almost all the strong and weak points of silica-on-silicon: low propagation losses but large bend radii. In addition, its very low birefringence makes this platform a very good candidate for the propagation and manipulation of polarization-encoded qubits [78]. Among other achievement, femtosecond laser written optical networks have been employed to generate hyper-entangled states [81] and to study transport phenomena of quantum walkers [82].

We note that, even if high-quality single elements have been already demonstrated in several platforms, their full integration on a single material is a challenging task and the range of available "building" blocks may be inadequate. A possible solution could be an approach based on hybrid integration [83], in which components realized with different platforms are combined on the same chip, leveraging the strengths of different materials.

Encoding information into photons

In quantum photonic devices, information is encoded and manipulated exploiting one or more degrees of freedom of the quantized electromagnetic field. Two main strategies are currently developed. On one hand information can be encoded in the quadrature amplitudes of a multi-photon electromagnetic field (continuous variable approach), employing squeezed light and homodyne detection [84]. On the other hand, information can be encoded in the degrees of freedom of single- or few-photon fields (discrete variable approach) [30].

Since the work presented in this thesis deals with photon pair sources, we now give a brief overview of the main encoding strategies in the few-photons regime, presenting their advantages and drawbacks.

Polarization is probably the most investigated degree of freedom and, thanks to its ease of generation and manipulation, it represents a common and practical way to encode quantum information. However, the ease of polarization encoding comes at the price of a two-dimensional Hilbert space, which thus limits the quantity of information encoded on each photon. Polarization encoding has been employed in the first tests of quantum optics (e.g. Bell's inequality violation [85]) and from then in several quantum information studies, ranging from quantum simulation [86] to computing [87] and communication [88].

Orbital angular momentum (OAM) is related to the photon transverse-mode spatial structure. Information is encoded in the number of phase twistings per wavelength along the propagation direction [89]. Contrary to polarization, OAM is potentially an unbounded degree of freedom, with an infinite Hilbert space, even if this poses some challenges in its characterization. This degree of freedom is particularly suited for free-space propagation [90] and has been employed to demonstrate QKD protocols with high key generation rates per photon [91]. Recently, air-core fibers supporting OAM modes have been demonstrated and exploited to perform QKD over a distance of 1.2 km [92]. Moreover, OAM-encoded photons

have also been used to perform fundamental tests of quantum mechanics, notably the violation of high-dimensional Bell's inequalities [93].

Spatial or **path encoding** is the representation of qubits in terms of occupied spatial modes and can also provide a Hilbert space of higher dimension compared to polarization. In integrated optics, waveguide circuits are a perfect implementation of path encoding, in which both separation and coupling between different modes is obtained with directional couplers [67]. Recent demonstrations have been reported for tunable path-entanglement generation and manipulation [43, 94], simulation of the quantum dynamics of a four-atom molecule [95] and of Anderson localization of quantum walkers [82]. Note that the spatial degree of freedom is a natural candidate to study the nature of topological states of light and it has been employed to demonstrate topological protection [96] and topological interference [97] of photon pairs.

Time-bin encoding is implemented by using an unbalanced Mach-Zender interferometer in which the path difference between the arms is greater than the photon coherence time. Information is then encoded in the photon arrival time at the detectors. Thanks to its resilience to polarization noise and chromatic dispersion, time-bin encoding is a good candidate for applications in state teleportation [98, 99] and quantum key distribution [100, 101], both free-space and fibered. Moreover, the on-chip manipulation and the analysis of time-bin qubit has been recently demonstrated [102].

Time-frequency encoding employs the photon spectrum as degree of freedom, which, in the near infrared, can be manipulated with standard telecom components, such as phase shaper and elecro-optic modulators [103, 104]. This degree of freedom is particularly appealing for quantum communications, thanks to its robustness to propagation in optical fibers and its capability to convey large-scale quantum information in a single spatial mode. Frequency has a potentially infinite Hilbert space which can be exploited to enhance quantum information protocols (e.g. the QKD key rate [105]).

High-dimensional quantum states

In recent years, photonic high-dimensional quantum states have been studied as a means to provide novel capabilities for quantum information. The dimensionality of a quantum state can be increased in two ways: either by extending the number of involved particles (N) or by increasing their respective local dimensionality (d), obtaining a total Hilbert space scaling as d^N.

In case of single photons (N=1), it has been demonstrated that increasing their dimensionality not only leads to higher information capacities, but also enables to enhance the security to eavesdropping [106] and the robustness to noise [107] in QKD schemes.

When considering more locally separated photons, entanglement in high-dimensional degrees of freedom can be exploited to enhance flexibility in quantum computing [108], to perform fundamental tests of quantum mechanics [109, 110]

and to enable a rich variety of quantum simulations [18, 110].

A particular remark has to be done for continuous degrees of freedom of single photons (e.g. energy-time or position-momentum degrees of freeedom). Indeed, they display a perfect analogy with the continuous variables of a multiphoton mode of the electromagnetic field (i.e. its quadratures), thanks to a direct analogy between the operators which act in the single-mode multiphoton Hilbert space of the electromagnetic field and those that act in the single-photon multimode Hilbert space of the electromagnetic field [111]. This would thus enable to perform CV quantum information processing in the few-photon regime [112, 113], provided that non-Gaussian entangled states or non-Gaussian operations are implemented [114]. Moreover, photonic quantum states entangled in continuous degrees of freedom have been demonstrated as a key resource for a large variety of applications, such as clock synchronization [115], quantum optical coherent tomography [116], dispersion cancellation in long-distance fiber-based communication [117] and quantum imaging [118, 119].

The most investigated photonic degrees of freedom to implement high-dimensional protocols are orbital angular momentum [93], transverse-spatial [120] and path modes [43, 121], frequency [41, 104, 122], and time-bin [123]. Among them, frequency and path modes are the most suitable for on-chip integration, since they can be conveyed in waveguides and allow a scaling-up of the device.

Entangled high-dimensional path states can be created on-chip by using multiple indistinguishable photon-pair sources [124] and manipulated with beamsplitters and phase-shifters [110]. This technique has recently enabled the on-chip generation and analysis of a 14-dimensional path entangled state [43], employing a total of 16 identical SFWM sources.

On the other hand, integrated nonlinear cavities, such as micro-rings [104, 125] and waveguides [126], allow for a versatile generation of entangled high-dimensional frequency states, in the form of discrete frequency bins, which can be accessed and manipulated with off-the-shelf telecom components.

In all cases, in order to implement quantum information protocols that take advantage of high dimensionality, it is of paramount importance to gain control over the generated quantum states in a scalable and efficient way, being able to measure and manipulate them at will.

Outline of the thesis

This thesis deals with the generation and the engineering of high-dimensional quantum states of light in semiconductor nonlinear devices made of AlGaAs, focusing on two particular degrees of freedom of photons: frequency and spatial modes.

During this work two different devices have been developed and employed. The first is a photon pair source exploiting a transverse pump geometry to achieve a counter-propagating phase-matching scheme. As we will see, this pump configuration makes the device particularly versatile for frequency entanglement engineering.

The second device, still at the development stage, is an array of nonlinear waveguides emitting photon pairs via a modal phase-matching scheme. The waveguides in the array are evanescently coupled and the generated photons can tunnel in the

neighboring ones, leading to cascaded quantum walks. As a result, the generated photons are entangled in the spatial degree of freedom.

The manuscript is divided into three sections.

In the first part we give a complete description of the processes underpinning the working principle of the sources. In chapter 1 we start by describing the nonlinear processes occurring in $\chi^{(2)}$ materials, focusing in particular on AlGaAs waveguides and on spontaneous parametric down conversion (SPDC). In chapter 2 we give a theoretical analysis of the quantum state produced in the counter-propagating source: the Joint Spectral Amplitude (JSA), a function describing the frequency-time properties of the photon pairs, is derived and deeply analyzed.

The second part of the thesis deals with the measurement and the control of frequency entangled states emitted by the counter-propagating source, obtained via pump beam shaping. In chapter 3 we present the setup used to tailor the pump beam, which is based on a spatial light modulator and a wavefront analyzer. Then, in chapter 4, we detail two experimental techniques that we use to characterize the time-frequency properties of the photon pairs: a single-photon fiber spectrograph and stimulated emission tomography (SET). Chapter 5 and chapter 6 present the experimental results of the frequency engineering: tuning the pump beam waist allows to produce correlated, anti-correlated and separable frequency states, while modifying the spatial phase profile allows to switch between symmetric and antisymmetric spectral wavefunctions and to modify the exchange statistics of the photons, which is measured via Hong-Ou-Mandel interferometry. Finally, in chapter 7 we move a step further towards more complex quantum states by describing the generation of a photon pair state entangled in a hybrid polarization/frequency degree of freedom and its analysis via a Hong-Ou-Mandel interferometer. Since the quality of this quantum state is strongly influenced by the waveguide facet reflectivity, in chapter 8 we report the development of an anti-reflection coating for the counter-propagating source.

In the third part of this thesis we present the waveguide array device for the generation of spatially entangled states, detailing its design and working principle, focusing in particular on the engineering of spatial correlations. Afterwards, the fabrication process is reported, followed by the optical characterization of the first generation of samples.

We conclude this manuscript by summarizing the main results of this work and its main future applications and developments.

Part I

Photon pair generation by Spontaneous Parametric Down-Conversion in a semiconductor ridge waveguide

Chapter 1

Second-order Nonlinear Optics in AlGaAs waveguides

In this first chapter of the manuscript we introduce the necessary concepts and tools to understand the topics covered in this thesis. We first give a classical description of nonlinear optics, focusing on the second order processes, in particular on Spontaneous Parametric Down-Conversion (SPDC) which is exploited in our source to produce entangled biphoton states. The analysis follows the book *Nonlinear Optics* written by R.Boyd [127].

Then we analyze the nonlinear processes in the guided regime, giving an introduction to the optical properties of GaAs and AlGaAs, materials employed to fabricate the nonlinear waveguide sources used in this thesis.

Finally we present the two types of sources, developed by our team, that we

have employed in this PhD work.

The first is a ridge waveguide based on a counter-propagating phase-matching scheme under transverse pumping. It is employed in Part II of this thesis to demonstrate the engineering of frequency biphoton states and of their exchange statistics and to generate entanglement in a hybrid polarization/frequency degree of freedom.

The second source is a Bragg reflection waveguide, based on modal phase matching, that emits co-propagating twin photons. It is employed in Part III of this thesis to develop a device capable of generating and controlling spatially entangled biphoton states.

1.1 Introduction to nonlinear optics

Nonlinear optics is the study of optical effects that occur in matter when intense optical fields are involved. The beginning of this branch of optics is closely related to the invention of the laser in 1960 by Maiman [128], having provided sufficiently intense beams to observe these effects. In 1961 Franken et al. observed, for the first time, second harmonic generation of a ruby laser light in a quartz crystal [129]. Since then, systematic studies of optical nonlinearities have been performed and a full range of new effects and phenomena have been discovered, including sum frequency generation, stimulated Raman scattering, self focusing, Kerr effect and many others.

Nonlinear processes are linked to the nonlinear behavior of the polarization induced by an intense field inside an optical medium. This nonlinearity allows a coupling among electromagnetic fields at different frequencies, thus generating new fields.

1.1.1 Nonlinear polarization

To introduce nonlinear optical effects let us consider an electric field $E(t)$ passing through a nonlinear medium. The latter responds by generating an induced polarization that can be written, considering scalar fields and an isotropic homogeneous medium without losses and dispersion and with an instantaneous response, as follows:

$$\begin{aligned} P(t) &= \epsilon_0\Big[\chi^{(1)}E(t) + \chi^{(2)}E^2(t) + \chi^{(3)}E^3(t) + \cdots\Big] = \\ &= \underbrace{P^{(1)}(t)}_{P^L(t)} + \underbrace{P^{(2)}(t) + P^{(3)}(t) + \cdots}_{P^{NL}(t)} \end{aligned} \tag{1.1}$$

where ϵ_0 is the permittivity of free space, $\chi^{(1)}$ is the linear susceptibility of the medium, $\chi^{(2)}$ and $\chi^{(3)}$ are the second-order and third-order nonlinear optical susceptibility. In the second row of the equation we have separated linear and nonlinear polarization: the first is proportional to $\chi^{(1)}$, which in condensed matter is of the order of unity, while the second depends on the higher orders of the optical susceptibility, whose values decrease rapidly with the order. Consequently, for a field, which is weak compared to the nonlinear orders of the susceptibility

(i.e. $\chi^{(1)}E \gg \chi^{(2)}E^2 + \chi^{(3)}E^3 + ...$), the response is well described by P^L, while otherwise P^{NL} becomes substantial.

When the nonlinear polarization is significant, the medium can generate fields at new frequencies. To better explain this behavior, we now consider a medium presenting only a second-order susceptibility and an optical field impinging on it, composed of two distinct frequencies:

$$E(t) = E_1 e^{-i\omega_1 t} + E_2 e^{-i\omega_2 t} + \text{c.c.} \tag{1.2}$$

By substituting this expression into Equation 1.1 we find that the nonlinear polarization is:

$$\begin{aligned} P^{(2)}(t) = \epsilon_0 \chi^{(2)} \Big[& E_1^2 e^{-2i\omega_1 t} + E_2^2 e^{-2i\omega_2 t} + 2E_1 E_2 e^{-i(\omega_1+\omega_2)t} + \\ & 2E_1 E_2^* e^{-i(\omega_1-\omega_2)t} + \text{c.c.} \Big] + \Big[E_1 E_1^* + E_2 E_2^* \Big] \end{aligned} \tag{1.3}$$

This expression consists of terms oscillating at different frequencies with respect to the input field. The first two terms have double frequency ($2\omega_1$ and $2\omega_2$), then the third and the fourth oscillate at the sum frequency ($\omega_1 + \omega_2$) and at the difference frequency ($\omega_1 - \omega_2$), respectively. The last two are non-oscillating contributions.

In this example we have considered an isotropic medium and thus the susceptibility was a scalar; in the general case the m-th order susceptibility, $\chi^{(m)}$, is a tensor of $m+1$ rank, therefore the nonlinear polarization is no more parallel to the incident optical field. In section 1.3 we will review the optical properties of AlGaAs, focusing in particular on its nonlinear susceptibility tensor.

1.1.2 Propagation in a nonlinear medium

Above we have seen how an intense field can induce a nonlinear polarization in the medium oscillating at frequencies not present in the incident field; this acts as a source of new frequency components of the electromagnetic field. We now use the Maxwell's laws to give an analytic description of the generation and the propagation of the electric field components.

For a non-magnetic and dielectric optical medium with no free charges ($\rho = 0$) or currents ($\mathbf{J} = 0$), Maxwell's laws are:

$$\boldsymbol{\nabla} \times \mathbf{E} = -\frac{\partial \mathbf{B}}{\partial t} \tag{1.4}$$

$$\boldsymbol{\nabla} \times \mathbf{H} = \frac{\partial \mathbf{D}}{\partial t} \tag{1.5}$$

$$\boldsymbol{\nabla} \cdot \mathbf{B} = 0 \tag{1.6}$$

$$\boldsymbol{\nabla} \cdot \mathbf{D} = 0 \tag{1.7}$$

where $\mathbf{B} = \mu_0 \mathbf{H}$ and $\mathbf{D} = \epsilon_0 \mathbf{E} + \mathbf{P}$. Combing them together, we obtain a wave equation describing the coupling between the optical field and the nonlinear polarization:

$$\nabla^2 \mathbf{E} - \frac{1}{c^2}\frac{\partial^2 \mathbf{E}}{\partial t^2} = \frac{1}{\epsilon_0 c^2}\frac{\partial^2 \mathbf{P}}{\partial t^2} \tag{1.8}$$

It is now convenient to split $\mathbf{P}$ into its linear and nonlinear part as:

$$\mathbf{P} = \mathbf{P}^L + \mathbf{P}^{NL} \tag{1.9}$$

Similarly for the displacement field $\mathbf{D}$:

$$\mathbf{D} = \epsilon_0\mathbf{E} + \mathbf{P}^L + \mathbf{P}^{NL} = \mathbf{D}^L + \mathbf{P}^{NL} \tag{1.10}$$

where the linear part of $\mathbf{D}$ is given by $\mathbf{D}^L = \epsilon_0\mathbf{E} + \mathbf{P}^L$. Using these quantities the wave equation Equation 1.8 becomes:

$$\nabla^2\mathbf{E} - \frac{1}{\epsilon_0 c^2}\frac{\partial^2\mathbf{D}^L}{\partial t^2} = \frac{1}{\epsilon_0 c^2}\frac{\partial^2\mathbf{P}^{NL}}{\partial t^2} \tag{1.11}$$

We now consider a lossless and dispersionless medium, the relation between $\mathbf{D}^L$ and the electric field $\mathbf{E}$ is:

$$\mathbf{D}^L = \epsilon_0\, \boldsymbol{\epsilon}^{(1)} \cdot \mathbf{E} \tag{1.12}$$

where $\boldsymbol{\epsilon}^{(1)}$ is a real, frequency-independent, relative dielectric tensor. For the case of an isotropic material, this relation reduces to:

$$\mathbf{D}^L = \epsilon_0\, \epsilon^{(1)}\mathbf{E} \tag{1.13}$$

with $\epsilon^{(1)}$ scalar. The wave equation (Equation 1.11) consequently becomes:

$$\nabla^2\mathbf{E} - \frac{n^2}{c^2}\frac{\partial^2\mathbf{E}}{\partial t^2} = \frac{1}{\epsilon_0 c^2}\frac{\partial^2\mathbf{P}^{NL}}{\partial t^2} \tag{1.14}$$

where n, with $n^2 = \epsilon^{(1)}$, is the refractive index of the medium. This is a driven wave equation: the nonlinear response of the medium acts as a source for the left-side terms. If the source term is absent, the equation describes free waves propagating with velocity c/n.

At this point, in order to continue our calculation, we need to identify the explicit form of the nonlinear polarization of Equation 1.14. This will allow us to directly relate the nonlinear properties of the medium to the generated fields.

1.1.3 Three-Wave mixing

We now focus on second-order processes, usually referred to as "Three-Wave Mixing" because they involve interactions among three waves.

We thus consider three fields at frequency $\omega_1, \omega_2, \omega_3$. If these frequencies are far from the medium resonances, there is no energy transfer between the fields and the medium, but only among the three fields. Therefore, energy conservation defines the possible process:

$$\hbar\omega_3 = \hbar\omega_1 + \hbar\omega_2 \tag{1.15}$$

where $\hbar$ is the reduced Planck constant. Figure 1.1 illustrates the possible three-wave processes:

- **Sum Frequency Generation (SFG)**: two pump fields interact with the medium to generate a third field at frequency $\omega_3 = \omega_1 + \omega_2$;

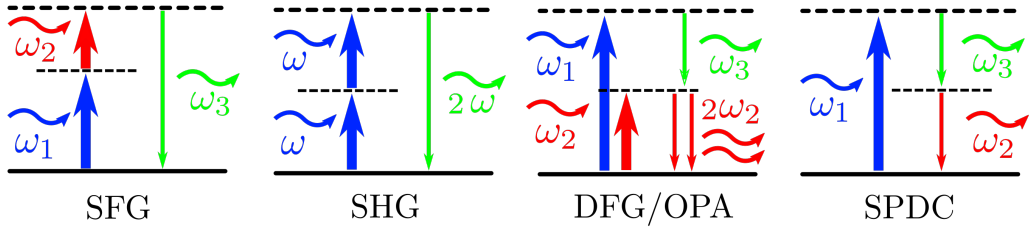

Figure 1.1: Energy schemes of Three-Wave Mixing processes. The solid lines represent real energy levels while the dashed ones represent virtual levels.

- **Second Harmonic Generation (SHG)**: it is a particular case of SFG, the two pump beams have degenerate frequencies $\omega = \omega_1 = \omega_2$ and they generate a field at frequency 2ω;

- **Difference Frequency Generation (DFG)**: two pump fields interact with the medium to produce a third field at frequency $\omega_3 = \omega_1 - \omega_2$. Looking at the energy conservation diagram we can see that for every photon created at the difference frequency (ω_3), a photon of the higher input frequency (ω_1) must be destroyed and one of the lower input frequency (ω_2) is created. This leads to an amplification of the latter field, and thus the process is called "Optical Parametric Amplification" (OPA);

- **Spontaneous Parametric Down Conversion (SPDC)**: the previous process can take place even if only one pump field is present (ω_1). In this case the generated fields at frequency ω_2 and ω_3 arise from its interaction with vacuum fluctuations; they are weaker and the sum of their frequencies is fixed at $\omega_2 + \omega_3 = \omega_1$ by the energy conservation.

In the following chapter we will extensively study the quantum theory of Spontaneous Parametric Down Conversion (SPDC). Here, we continue our classical analysis focusing on Sum Frequency Generation (SFG), but the procedure is roughly the same for the analysis of SHG and DFG.

We start by choosing the z axis as the direction of propagation of the three involved fields, which can be written as:

$$\begin{aligned} \mathbf{E}_1(\mathbf{r},t) &= \mathbf{e}_1 A_1(\mathbf{r}) e^{i(k_1 z - \omega_1 t)} + \text{c.c.} \\ \mathbf{E}_2(\mathbf{r},t) &= \mathbf{e}_2 A_2(\mathbf{r}) e^{i(k_2 z - \omega_2 t)} + \text{c.c.} \\ \mathbf{E}_3(\mathbf{r},t) &= \mathbf{e}_3 A_3(\mathbf{r}) e^{i(k_3 z - \omega_3 t)} + \text{c.c.} \end{aligned} \tag{1.16}$$

where the vector $\mathbf{e}_j$ indicates the polarization direction, $A_j(\mathbf{r})$ is the electric field complex amplitude and k_j is the wavevector modulus.

On the other hand, the nonlinear source term appearing in the wave equation, Equation 1.14, for SFG can be written as [127]:

$$P_3^{NL}(z,t) = 4\epsilon_0 d_{\text{eff}} E_1 E_2 e^{-i\omega_3 t} + \text{c.c.} \tag{1.17}$$

where d_{eff} is the nonlinear effective coefficient for a given set of polarizations and field directions. It is linked to the nonlinear susceptibility tensor $\chi^{(2)}$ through geometrical and symmetry considerations that we will detail for GaAs in section 1.3.

We now plug the interacting fields (Equation 1.16) and the nonlinear polarization (Equation 1.17) into the wave equation (Equation 1.14). Here we make two assumptions. First we consider a nonlinear process having a low conversion efficiency, so we suppose the pump fields E_1 and E_2 to be not depleted during the propagation in the medium:

$$\begin{aligned} A_1(x,y,z) &= A_1(x,y,0) \\ A_2(x,y,z) &= A_2(x,y,0) \end{aligned} \tag{1.18}$$

Secondly, we apply the Slowly Varying Amplitude Approximation, which assumes that the fields amplitude varies slowly on the scale of an optical wavelength:

$$\left|\frac{\partial^2 A}{\partial z^2}\right| \ll \left|k\frac{\partial A}{\partial z}\right| \tag{1.19}$$

Doing so the wave equation transforms in one equation, describing the propagation of the sum-frequency field A_3:

$$\frac{\mathrm{d}A_3}{\mathrm{d}z} = 2i\frac{\omega_3}{n_3 c} d_{\text{eff}} A_1(x,y,0) A_2(x,y,0) e^{i\Delta k z} \tag{1.20}$$

where we have employed the relation for the wavevector $k_3^2 = \dfrac{n_3^2\omega_3^2}{c^2}$ and n_3 is the medium refractive index at frequency ω_3. In addition, we have introduced the quantity:

$$\Delta k = k_3 - k_1 - k_2 \tag{1.21}$$

called *wavevector mismatch*. This last parameter is a key factor for all nonlinear processes, as we will show in the following paragraph. Equation 1.20 is called *coupled-amplitude equation*, because it describes the evolution of the amplitude A_3 as a consequence of its coupling to A_1 and A_2. Here we have supposed that the input fields at ω_1 and ω_2 are not depleted, but, in a more general case, also the variation of A_1 and A_2 along z has to be taken into account, leading to three coupled equations of the form of Equation 1.20, one for each interacting field [127].

1.1.4 Phase-matching

Looking at Equation 1.20 we note that, for the case $\Delta k = 0$, the amplitude A_3 of the generated field increases linearly with z, and consequently the intensity increases quadratically with z. This conditions is called "perfect phase-matching" and when it is satisfied the energy transfer from E_1 and E_2 to E_3 is efficient along the whole medium. This is due to a fixed phase relation between the generated wave and the nonlinear polarization that allows a constructive interference and thus an efficient frequency conversion. On the other hand, if $\Delta k \neq 0$, the amplitude of the generated field along the propagation direction oscillates because of the presence of an imaginary term, and does not build up.

Let us now derive some more analytic results. The amplitude of the sum-frequency field at the output of the nonlinear medium is obtained by integrating Equation 1.20 from $z = 0$ to $z = L$. The intensity of the field is then calculated from the magnitude of the time-averaged Poynting vector:

$$I_3 = 2n_3\epsilon_0 c|A_3|^2 \tag{1.22}$$

We thus obtain:

$$I_3(L) = I_3^{(0)}\mathrm{sinc}^2\left(\frac{\Delta kL}{2}\right) \tag{1.23}$$

where $I_3^{(0)}$ represents the maximum intensity available and reads:

$$I_3^{(0)} = \frac{2\,d_{\mathrm{eff}}^2\,\omega_3^2 I_1 I_2 L^2}{n_1 n_2 n_3 \epsilon_0 c^3} \tag{1.24}$$

In Figure 1.2a we plot $I_3(z)$ as a function of z/L for two different conditions: a perfect phase-matching $\Delta k = 0$ (in red) and a phase-mismatch of $\Delta k = 3/L$ (in blue). In the first case the intensity grows quadratically during propagation, while in the second it oscillates due to the consecutive constructive and destructive interference between the interacting fields. In addition, Figure 1.2b reports I_3 as a function of the wavevector mismatch ($\Delta kL/2$), normalized to the maximum intensity available $I_3^{(0)}$. As we have already commented, the efficiency of the sum-frequency process drastically decreases as the phase mismatch increases. Therefore, the condition of perfect phase-matching $\Delta k = 0$ is of fundamental importance for the efficiency of the nonlinear conversion.

In case of a highly efficient nonlinear process, the intensity of the sum-frequency field is no more given by Equation 1.23, which has been derived for non-depleted input beams. However, even in this case, an efficient generation of the output field requires a perfect phase-matching $\Delta k = 0$.

We can interpret the phase-matching condition from a particle point of view as the conservation of momentum of the photons. Indeed, two photons of momentum respectively $\hbar k_1$ and $\hbar k_2$ can generate only a photon of momentum $\hbar k_3 = \hbar k_1 + \hbar k_2$. The momentum conservation, unlike energy conservation, is not verified automatically and moreover it is not trivial to obtain. For this reason, different techniques have been developed to satisfy phase-matching condition which will be illustrated in the next sections.

Conversion efficiency

As a last point of this paragraph, we define the nonlinear conversion efficiency of the nonlinear process, which is independent from the input field intensities and therefore can be employed to compare different sources or situations. To this end, we introduce the optical power of an electromagnetic field:

$$P = \int_S I dS \tag{1.25}$$

where the integration is performed over the area S of the beam. Therefore the output power $P_3(L)$ generated by the nonlinear process is derived from Equation 1.23

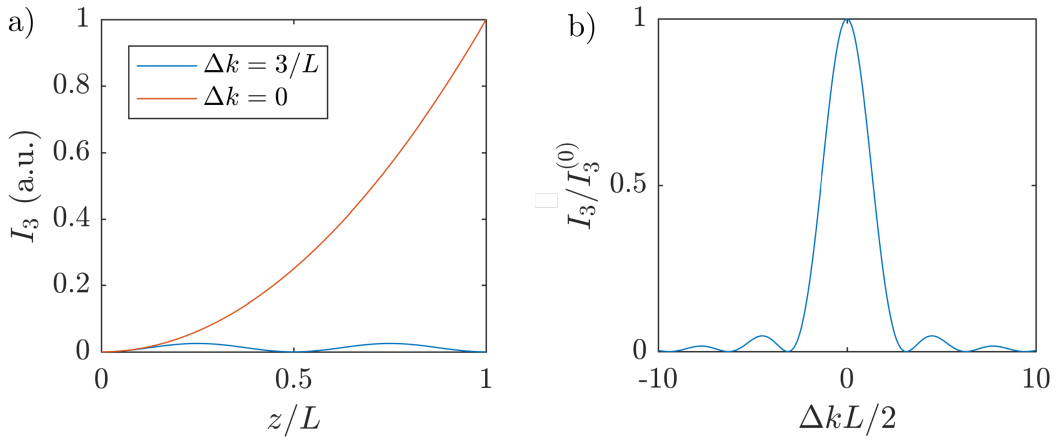

Figure 1.2: (a) Sum-frequency optical intensity at a distance z/L for a perfect phase-matched conversion (red) and with a mismatch $\Delta k = 3/L$ (blue). (b) Effect of the wavevector mismatch on the sum-frequency intensity, normalized to the maximum intensity available $I_3^{(0)}$.

and reads:

$$P_3(L) = \frac{2\, d_{\text{eff}}^2\, \omega_3^2 L^2}{n_1 n_2 n_3 \epsilon_0 c^3 S} P_1 P_2\, \text{sinc}^2\left(\frac{\Delta k L}{2}\right) \tag{1.26}$$

where P_1 and P_2 are the power of the input fields.

The nonlinear conversion efficiency η is then defined as follows:

$$\eta = \frac{P_3(L)}{P_1 P_2} = \frac{2\, d_{\text{eff}}^2\, \omega_3^2 L^2}{n_1 n_2 n_3 \epsilon_0 c^3 S}\, \text{sinc}^2\left(\frac{\Delta k L}{2}\right) \tag{1.27}$$

From this relation we see that, in order to increase the efficiency η, we should:

- employ a medium with a high value of the ratio $\dfrac{d_{\text{eff}}^2}{n_1 n_2 n_3}$;
- satisfy the phase-matching condition (i.e. $\Delta k = 0$);
- increase the medium length L [1] and decrease the effective area S of the fields.

1.2 The guided regime

Until now, we have considered only bulk nonlinear media and non-confined electromagnetic fields. Yet, as a result of diffraction, a light beam with a finite cross section spreads as it propagates. This divergence, which may be different for each interacting field, can decrease the overall efficiency of the nonlinear process. In order to deal with this issue, it is possible to confine the three interacting fields within a waveguide, obtaining to a smaller field section S and conservating a good nonlinear overlap as the fields propagate.

[1] Also the propagation losses must be considered and this leads to an optimal length after which the conversion efficiency does not increase further [130].

A dielectric waveguide is a structure, made of dielectric materials, where the electromagnetic radiation is confined along one or two dimensions while it propagates. Thanks to a core with a higher refractive index compared to that of the surrounding material (cladding), the waveguide "traps" the light by total internal reflection. In a dielectric waveguide the typical dimensions of the core are of the order of the wavelength of the propagating field.

We now analyze more in detail a specific case to highlight the fundamental characteristics of the guided regime. We consider a waveguide that confines light in the x and y directions while it lets it propagate along the z direction. Since the structure is homogeneous along the z axis, the electromagnetic field for a given frequency ω can be written as:

$$\mathbf{E} = A(x, y) \exp(i\omega t - ikz)\, \hat{\mathbf{e}} \tag{1.28}$$

where k is the z component of the wavevectors and is called propagation constant, $\hat{\mathbf{e}}$ is the electric field polarization direction. $A(x, y)$ is the transverse spatial distribution of the electric field and is determined by the following wave equation, derived from Maxwell's laws [131]:

$$\left[\nabla^2 - \frac{\mathrm{d}^2}{\mathrm{d}x^2} + \left(\frac{\omega^2}{c^2} n^2(x, y) - k^2\right)\right] A(x, y) = 0 \tag{1.29}$$

where $n(x, y)$ is the refractive index profile, determined by the waveguide structure and material composition. Note that the previous equation is not valid at the dielectric interfaces, where the boundary conditions of the electromagnetic field apply instead [131]. Each solution of Equation 1.29 represents a guided mode of the waveguide and is characterized by its own propagation constant.

For a guided mode two conditions must apply. First, the field amplitude must fall off exponentially outside the guide structure. Secondly, the field must reach a maximum value, typically inside the core. These two conditions are satisfied only for a discrete set of propagation constants k:

$$\frac{\omega^2}{c^2} n^2(\infty) < k^2 < \frac{\omega^2}{c^2} n^2_{\mathrm{core}}(x, y) \tag{1.30}$$

where $n(\infty)$ is the refractive index of the material surrounding the waveguide.

Each guided mode propagates along the waveguide independently and is characterized by several quantities:

- a polarization direction (transverse electric TE or transverse magnetic TM), defined with respect to the waveguided structure;
- an effective refractive index $n_{eff}(\omega)$, associated to the propagation constant:

$$k(\omega) = \frac{\omega}{c} n_{eff}(\omega) \tag{1.31}$$

- a phase velocity $v_p(\omega)$ which indicates the velocity of the mode as it propagates in the waveguide:

$$v_p(\omega) = \frac{c}{n_{eff}(\omega)} \tag{1.32}$$

- a group velocity $v_g(\omega)$, indicating the velocity of the energy flow:

$$\frac{1}{v_g(\omega)} = \frac{\partial k}{\partial \omega} = \frac{1}{v_p} + \frac{\omega}{c}\frac{\partial n_{eff}}{\partial \omega} \tag{1.33}$$

  from which we can define the group refractive index:

$$n_g(\omega) = \frac{c}{v_g(\omega)} \tag{1.34}$$

- a group velocity dispersion GVD, which gives the dependency of the group velocity on frequency:

$$\text{GVD} = \frac{\partial}{\partial \omega}\frac{1}{v_g} = \frac{\partial^2 k}{\partial \omega^2} \tag{1.35}$$

  Alternatively, it can also be defined with respect to wavelength and called dispersion parameter:

$$D_\lambda = \frac{\partial}{\partial \lambda}\frac{1}{v_g} \tag{1.36}$$

  Where the second definition is more used for optical fibers.

The mode spatial distribution $A(x, y)$ and propagation constant k can be found analytically in the case of a homogeneous one dimensional waveguide or numerically by solving Equation 1.29 for more complex 2D and 3D structures [132].

1.2.1 Nonlinear optics in waveguides

Compared to bulk media, waveguides allow to confine the interacting fields of a nonlinear process in a smaller area and to propagate them for longer distances without diffractive effects. Moreover, by engineering the guided modes it is possible to control the spatial modes of the generated field, thus eliminating walk off and facilitating injection into fibers. Finally, waveguide-based nonlinear sources open to the miniaturization of circuits and devices into integrated chips.

In order to calculate the conversion efficiency for a nonlinear process occurring in a waveguide we introduce the nonlinear overlap integral:

$$\Gamma = \iint_S d_{\text{eff}}(x, y) A_1(x, y) A_2(x, y) A_3(x, y)\, \mathrm{d}x\, \mathrm{d}y \tag{1.37}$$

where $A_i(x, y)$ is the transverse spatial distribution of the mode i and $d_{\text{eff}}(x, y)$ the nonlinear effective coefficient distribution in the x, y plane. We can now rewrite the generated output power $P_3(L)$ (Equation 1.26) as follows:

$$P_3(L) = \frac{2\,\omega_3^2 L^2}{n_1 n_2 n_3 \epsilon_0 c^3} |\Gamma|^2 P_1 P_2\, \text{sinc}^2\left(\frac{\Delta k L}{2}\right) \tag{1.38}$$

Consequently the conversion efficiency η (Equation 1.27) becomes:

$$\eta = \eta_0^{\text{SFG}} \text{sinc}^2\Big(\frac{\Delta k L}{2}\Big) \tag{1.39}$$

where

$$\eta_0^{\text{SFG}} = \frac{2\,\omega_3^2 L^2}{n_1 n_2 n_3 \epsilon_0 c^3}\, |\Gamma|^2 \tag{1.40}$$

In conclusion, in order to increase the conversion efficiency, the nonlinear overlap integral between the interaction fields must be maximized.

1.2.2 Spontaneous Parametric Down-Conversion in waveguides

So far we have we have given a classical description of sum-frequency generation (SFG). Conversely, Spontaneous Parametric Down-Conversion (SPDC), which is the process that we employ in this work to produce photon pairs, is more difficult to model and a quantum mechanical description is necessary. However, it is possible to derive the SPDC conversion efficiency by starting from the SFG process.

In a semiclassical description, SPDC can be viewed as two DFG processes between an intense pump field at frequency ω_p and vacuum fluctuations, generating two photons called signal ad idler, respectively at frequency ω_s and ω_i, constrained by the energy conservation condition $\omega_p = \omega_s + \omega_i$. The process can be modeled by considering that one input idler photon generates the signal output [133, 134]:

$$P_s(L) = \frac{2\omega_s^2 P_i(0) P_p(0) |\Gamma|^2}{\epsilon_0 c^3 n_s n_i n_p} \mathrm{sinc}^2\left(\frac{\Delta k L}{2}\right) \tag{1.41}$$

where $P_i(0) = \hbar\omega_i \Delta\omega / 2\pi$ is the idler input power, calculated considering one photon in each idler mode, with the number of modes determined by $\Delta\omega$, the linewidth of the idler spectrum. The generated idler power $P_i(L)$ can be defined analogously.

The number of generated photon pairs per time unit can be then determined as follows:

$$N_{\mathrm{pairs}} = \frac{P_s(L)}{\hbar\omega_s} = \frac{P_i(L)}{\hbar\omega_i} = \frac{2\,\hbar\,\omega_s\,\omega_i\,\omega_p}{\epsilon_0 c^3 n_s\, n_i\, n_p} |\Gamma|^2 N_p \frac{\Delta\omega}{2\pi} L^2 \tag{1.42}$$

where we have considered a perfect phase-matching ($\Delta k = 0$) and $N_p = P_p(0)/\hbar\omega_p$ is the number of pump photons.

The SPDC conversion efficiency η^{SPDC}, defined as the ratio between number of generated pairs N_{pairs} and the number of pump photons N_p, is then given by:

$$\begin{aligned} \eta^{\mathrm{SPDC}} &= \frac{N_{\mathrm{pairs}}}{N_p} = \frac{2\hbar\ \omega_s\ \omega_i\ \omega_p\ L^2}{\epsilon_0\ c^3\ n_s\, n_i\, n_p} \frac{\Delta\omega}{2\pi} |\Gamma|^2 \\ &= \eta_0^{\mathrm{SFG}}\ \frac{\hbar\omega_s\omega_i}{\omega_p} \frac{\Delta\omega}{2\pi} \end{aligned} \tag{1.43}$$

In conclusion, the SPDC conversion efficiency can be evaluated from the SFG conversion efficiency and the photon pair bandwidth.

1.3 Optical properties of GaAs and AlGaAs

Gallium arsenide (GaAs) is a III-V semiconductor compound formed by Gallium (Ga) and Arsenic (As). GaAs is a material widely employed for microwave electronics, infrared light-emitting diodes, laser diodes and solar cells. For this reason its clean room processing techniques are well established. This material, thanks to its physical properties, enables:

- second-order and third-order nonlinear processes;

- electro-optical modulation;
- laser emission (direct band gap $E_g = 1.441$ eV, $\lambda_g = 872$ nm).

GaAs has a non-centrosymmetric zincblende structure which imposes a $\bar{4}3m$ symmetry. If we deal with fields far away from the resonance, the nonlinear susceptibility, $\chi^{(2)}_{ijk}$, can be considered frequency-independent. In this situation the Kleinman's symmetry condition is valid and all the permutations (i, j, k) are equivalent [127].

In order to simplify the notation, we introduce the tensor d_{ijk}:

$$d_{ijk} = \frac{1}{2}\chi^{(2)}_{ijk} \tag{1.44}$$

By taking advantage of the permutation symmetry we can define a contracted matrix d_{il} according to:

jk	11	22	33	23/32	31/13	12/21
l	1	2	3	4	5	6

Thus, the second-order susceptibility tensor reduces to a 3x6 matrix:

$$d_{il} = \begin{pmatrix} d_{11} & d_{12} & d_{13} & d_{14} & d_{15} & d_{16} \\ d_{16} & d_{22} & d_{23} & d_{24} & d_{14} & d_{12} \\ d_{15} & d_{24} & d_{33} & d_{23} & d_{13} & d_{14} \end{pmatrix} \tag{1.45}$$

with only ten independent elements. Finally, the $\bar{4}3m$ symmetry leads to a unique non zero element d_{14}:

$$d = \begin{pmatrix} 0 & 0 & 0 & d_{14} & 0 & 0 \\ 0 & 0 & 0 & 0 & d_{14} & 0 \\ 0 & 0 & 0 & 0 & 0 & d_{14} \end{pmatrix} \tag{1.46}$$

This matrix constrains the allowed polarizations of the interacting fields, in particular d_{14} corresponds, in the crystal principal axis reference systems (X,Y,Z), to d_{XYZ} and all the permutation of these indices; it thus always involves three different polarization directions of the fields.

The AlGaAs samples that we employ in this thesis are grown via Molecular Beam Epitaxy along the (001) direction. The waveguides propagation direction is oriented along the $(1\bar{1}0)$ direction and we call Transverse electric (TE) the mode in which the electric field oscillates along the $(\bar{1}\bar{1}0)$ direction and Transverse Magnetic (TM) mode the one for which the electric field oscillates along along (001). Figure 1.3 summarizes this geometry, reporting the AlGaAs crystallographic axes in black (X, Y, Z) and in blue the corresponding waveguide reference system (x, y, z), employed in this thesis. This geometry enables the nonlinear frequency conversion between TE and TM polarized fields by means of the d_{14} coefficient. In the following we will analyze the allowed nonlinear processes of the studied devices.

Figure 1.4 reports the GaAs refractive index in the range 700-1700 nm, calculated using the Afromowitz model [135]. In the whole wavelength range, the refractive index is real and the chromatic dispersion is normal, with the exception of the surroundings of the resonance at 872 nm.

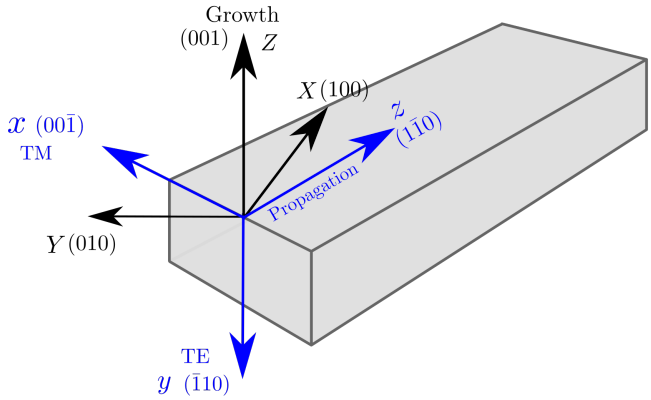

Figure 1.3: Waveguide reference system (x, y, z) (in blue) and AlGaAs crystallographic axes (X, Y, Z) (in black). The waveguide propagation direction is oriented along the z axis, $(1\bar{1}0)$ direction.

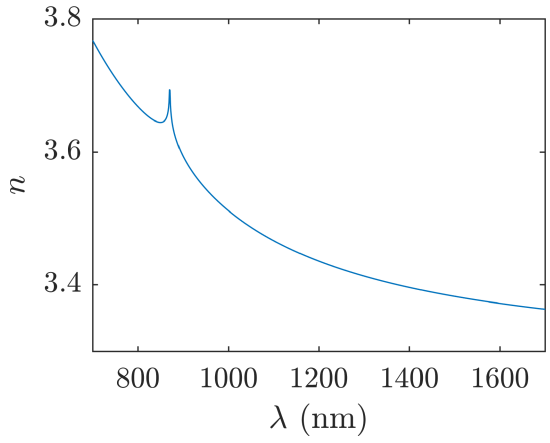

Figure 1.4: GaAs chromatic dispersion at 20 °C, calculated using the Afromowitz model [135]. The peak at 872 nm is due to the material resonance.

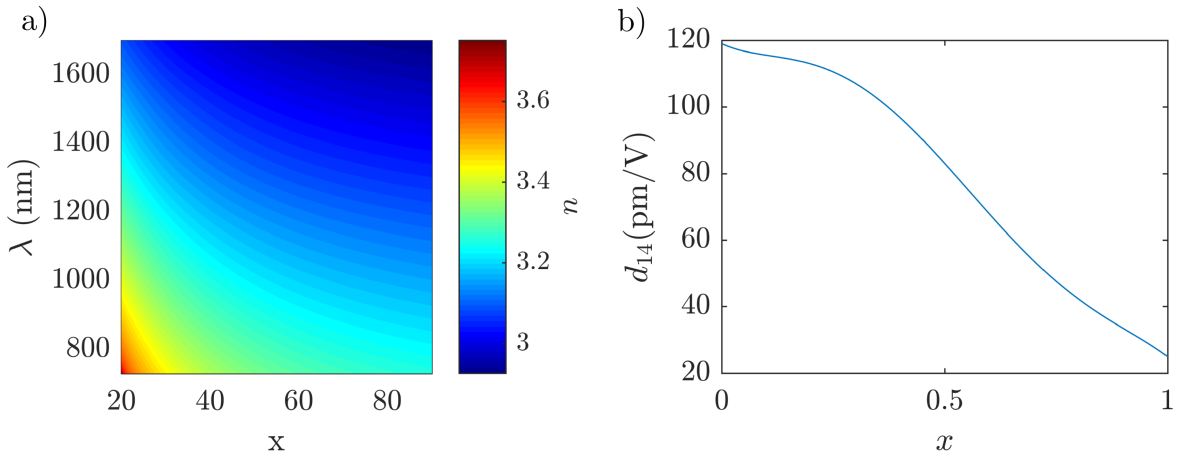

Figure 1.5: $Al_xGa_{1-x}As$ optical properties vs Al concentration: (a) refractive index n, calculated using the Gehrsitz model [136]. (b) Second-order nonlinear effective coefficient d_{14}, calculated using the Ohashi model [137].

The strong lattice similarities between GaAs and AlAs allow to realize heterostructures by replacing part of Gallium atoms of GaAs with Aluminum atoms. The resulting alloy is $Al_xGa_{1-x}As$ where the ratio of Aluminum atoms to Gallium atoms can be varied to achieve specific optical characteristics.

Figure 1.5a shows the AlGaAs refractive index as a function of Al concentration, calculated using the Gehrsitz model [136]. For a given wavelength, increasing the Al content decreases the refractive index. Therefore, during the fabrication process, it is possible to tune the refractive index layer by layer, by changing the Al concentration. The refractive index values span from 2.9 to 3.4 for an Al concentration from $x = 0.9$ to $x = 0.2$.

Figure 1.5b reports the AlGaAs second-order nonlinear effective coefficient d_{14} as a function of Al concentration, calculated using the Ohashi model [137] and the experimentally measured value $d_{14} = 119$ pm/V at $\lambda_s = \lambda_i = 1533$ nm, obtained by Shoji et al. [138]. We observe that d_{14} decreases as the Al content x is increased in a range [119 pm/V, 27 pm/V]. This variation of the nonlinear coefficient can be employed to engineer and optimize the nonlinear process, as we shall see in the case of the counter-propagating source.

1.3.1 Fulfilling the phase-matching condition in AlGaAs devices

As we have already seen, phase-matching, contrary to energy conservation, is not automatically verified and it is not trivial to obtain. The two conditions read:

$$\begin{cases} \omega_3 = \omega_1 + \omega_2 \\ \mathbf{k}_3 = \mathbf{k}_1 + \mathbf{k}_2 \end{cases} \tag{1.47}$$

In a dispersive material:

$$k_i = n(\omega_i)\frac{\omega_i}{c} \tag{1.48}$$

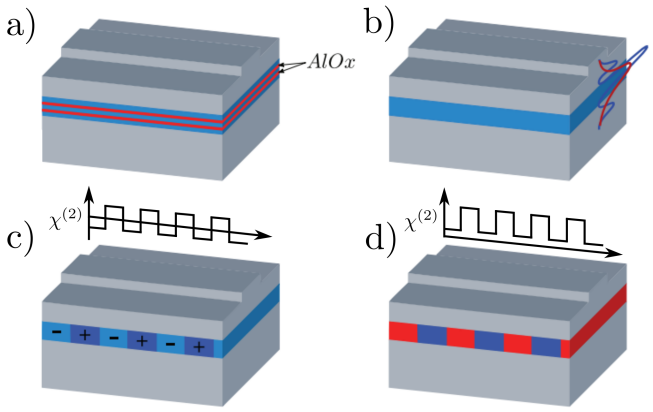

Figure 1.6: Phase-matching strategies in AlGaAs waveguides: (a) form birefringence, (b) modal phase-matching, (c) quasi-phase-matching obtained by completely inverting the sign of the nonlinear coefficient and (d) quasi-phase-matching obtained alternating a high and a low nonlinear coefficient.

where for a normal dispersion $n(\omega)$ is a monotonic increasing function of ω, as we have seen for AlGaAs in Figure 1.5. In this case it is clear that the phase-matching condition cannot be satisfied.

In principle it would be possible to achieve phase-matching by employing anomalous dispersion (i.e. n decreases when the frequency increases), however the most common method to satisfy the condition is to exploit the birefringence (i.e. dependence of the refractive index from the field polarization) displayed by many crystals. The highest frequency field has to be polarized along the direction that gives the lower of the two possible refractive indices [139]. Yet, since AlGaAs is not a birefringent material, other strategies have been developed.

An artificial birefringence can be induced by inserting small Aluminum oxide (AlOx) layers into the AlGaAs waveguide. The refractive index difference between the two material breaks the original symmetry, resulting in an artificial birefringent material [140, 141], as shown in Figure 1.6.

On the other hand, by periodically modulating the effective nonlinear coefficient of the medium it is possible to achieve quasi-phase-matching (QPM) (Figure 1.6c), which is less efficient than perfect phase-matching. The modulation compensates for the wave-vector mismatch accumulated in adjacent sections of the material, leading to a constructive interaction between the interacting fields. QPM, proposed for the first time by Armstrong et al. [142], has been employed in crystals and waveguides, by inverting the sign of the nonlinear coefficient through periodically poling techniques in ferroelectric nonlinear crystal materials, such as lithium niobate [143], lithium tantalate [144] and potassium titanyl phosphate [145].

In AlGaAs inverting the nonlinear effective coefficient is technologically challenging; it can be obtained by wafer bonding, which however induces significant optical losses [146]. An easier, but less efficient, approach to obtain QPM is to alternate sections with low and high nonlinear coefficient (Figure 1.6d), leading to an imperfect phase-matching [147]. Figure 1.7 illustrates the difference between

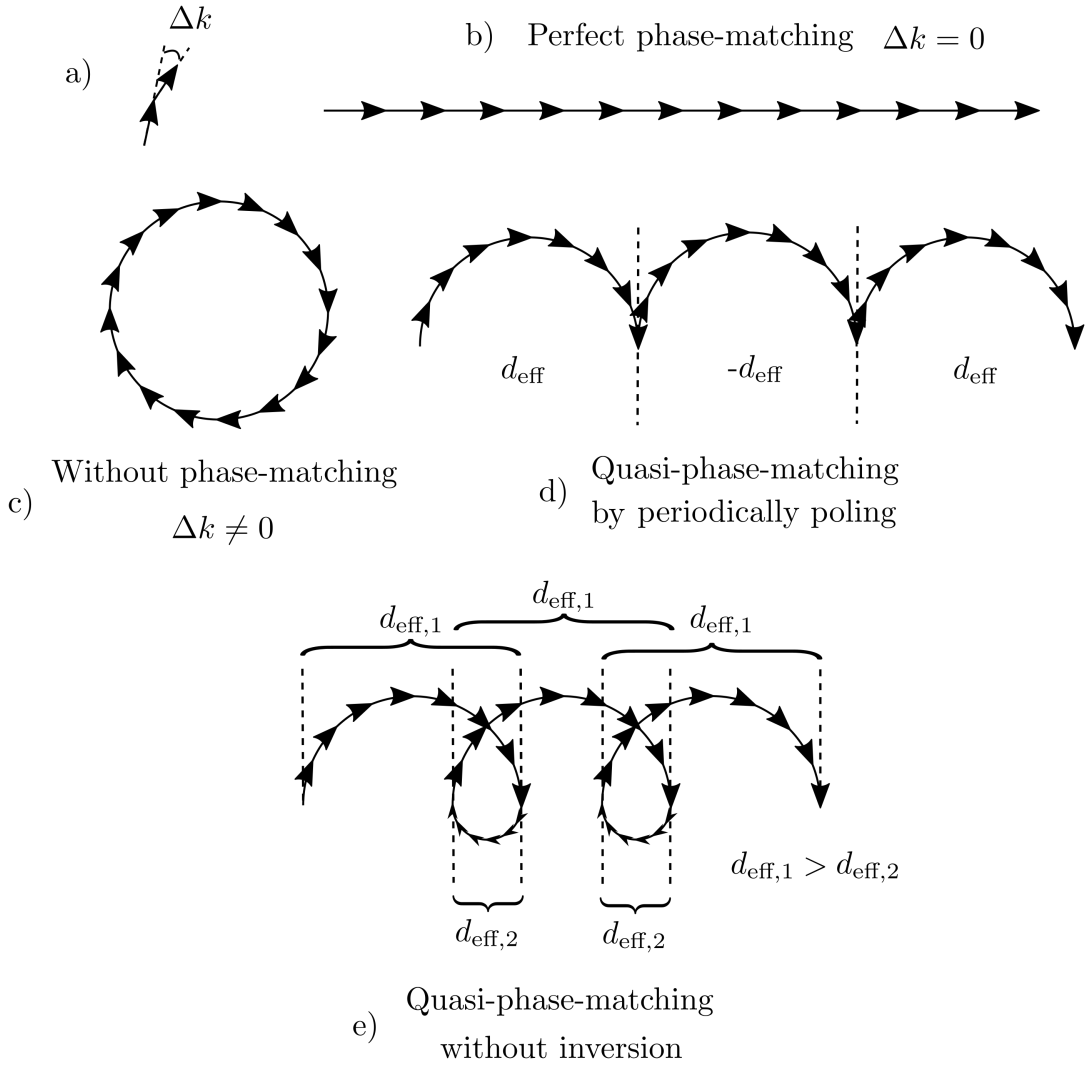

Figure 1.7: Illustration of the phase-matching process: addition of amplitude contributions from different parts of the nonlinear crystal; (a) each arrow represents the amplitude phasor while the angle it forms with the previous phasor is the phase-mismatch Δk. (b) Perfect phase-matching: the conversion efficiency is maximized. (c) Without phase-matching: there is no constructive interference and the energy transfer changes periodically. (d) Quasi-phase-matching obtained by inverting d_{eff} when the wave has traveled for half a wavelength. (e) Quasi-phase-matching obtained by alternating materials with low and high nonlinear coefficient ($d_{\text{eff,1}} > d_{\text{eff,2}}$): $d_{\text{eff,2}}$ generates smaller phasor amplitudes and thus the destructive interference is only partial and the converted field builds up; the overall conversion efficiency is lower than (d).

these QPM techniques by reporting the phasor of each amplitude contribution from different parts of the crystal: when the nonlinear coefficient is inverted after half wavelength the constructive interference continues (Figure 1.7d). Conversely by employing a material with a lower nonlinear coefficient the destructive interference is minimized (Figure 1.7e), even if the overall conversion efficiency is lower compared to the previous case (periodically poling).

Finally, it is possible to engineer the chromatic dispersion of the involved guided modes in a multimode waveguide to fulfill the phase-matching condition (modal phase-matching, see Figure 1.6b) [59].

In the following two sections we describe the two AlGaAs nonlinear waveguides employed in this thesis, which generate photon pairs in the telecom range (1550 nm) by means of SPDC. The first source is based on a counter-propagating phase-matching scheme under transverse pumping in a ridge waveguide, while the second is based on modal phase-matching in a Bragg reflection waveguide.

1.4 SPDC source based on a counter-propagating phase-matching scheme

Counter-propagating phase-matching for Spontaneous Parametric Down Conversion (SPDC) has been proposed by De Rossi and Berger [148] and by Ding et al. [149], and it has been experimentally demonstrated by our team in 2006 [150].

The general scheme for the production of photon pairs with a counter-propagating geometry is the following: a pump beam impinges on the top of a nonlinear waveguide and generates by SPDC two photons propagating in opposite directions into the waveguide, as sketched in Figure 1.8.

The guided regime is a strong advantage compared to non-collinear SPDC in bulk crystals, since the photon emission direction is degenerate for all frequencies, simplifying their collection. Moreover, by engineering the spatial profile of the guided modes it is possible to maximize their coupling into monomode telecom optical fibers [151].

In this section we first describe the design of the AlGaAs nonlinear waveguide based on counter-propagating phase-matching, developed by our team. Then, we study in detail the characteristics of this particular phase-matching scheme.

1.4.1 Source structure

The device is a ridge waveguide made of horizontal AlGaAs layers, with alternating Al content. It consists of a high refractive index core surrounded by a lower refractive index cladding; its nominal epitaxial structure is reported in Table 1.1.

The core consists of AlGaAs layers with alternate concentration of Al (25% and 80%) which leads to alternate values of nonlinear susceptibility along the x direction. This structure implements the Quasi Phase-Matching condition in the vertical direction. Indeed, the device is optimized to have the positive half periods of the electric field amplitude in the layers with a high $\chi^{(2)}$ (25% of Al) and the negative half periods in the layers with a lower $\chi^{(2)}$ (80% of Al). Therefore, the

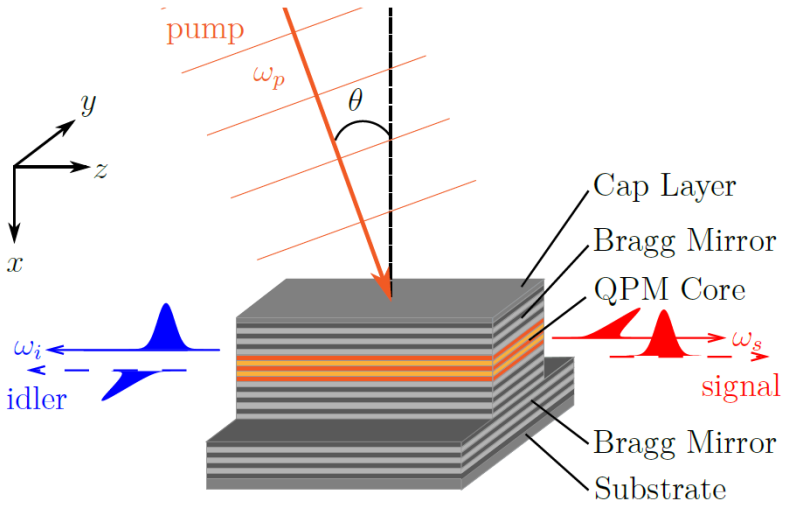

Figure 1.8: Sketch of the source based on the counter-propagating phase-matching scheme under transverse pumping and its working principle.

nonlinear interaction is constructive along the vertical direction, as illustrated in Figure 1.7e.

On the other hand, the cladding consists of Bragg mirrors made of AlGaAs layers with 35% and 90% Aluminum contents. These mirrors play several roles. First, they confine the modes of the generated photon pairs at 1550 nm by total intern reflection. Second, they create around the core a vertical microcavity whose resonance matches the pump field wavelength (775 nm). Third, since the bottom mirror is more reflective than the top one ($R_{\text{top}} = 0.9435$ and $R_{\text{bottom}} = 0.9974$ from our numerical simulations [134]), it avoids penetration of the pump field into the substrate and the consequent absorption and incoherent photon re-emission. Figure 1.9 reports the transverse amplitude distribution of the three interacting fields within the heterostructure.

The pump microcavity is designed to deal with the main drawback of counter-propagating phase-matching scheme, which is the limited interaction volume. Indeed, the interaction length of the nonlinear process is defined by the pump beam size on the ridge. The cavity enhances the pump field, thus leading to a higher nonlinear overlap integral Γ. In particular, the sources we employ in this work have a conversion efficiency [134]:

$$\eta \approx 10^{-11} \quad \text{photon pairs/pump photon} \tag{1.49}$$

which has to be compared to $\eta \approx 10^{-13}$ photon pairs per pump photon for a source without microcavity [152]. On the other hand, the microcavity has a theoretical bandwidth of 280 pm, which imposes a lower bound of a few picoseconds to the time duration of pump pulses.

Figure 1.10 reports the reflectivity spectrum of the device measured with Fourier-transform infrared spectroscopy (FTIR); in the center of the stop-band we notice the microcavity resonance. From its value of reflectivity we evaluate that approximately 50% of the intensity of an incident pump beam is coupled inside the cavity.

Finally, we can tune the microcavity resonance wavelength by changing its

Number of periods	Role	Al content (%)	Thickness h (nm)
1	Substrate	0	
36	Bottom Bragg	90	70.8
		35	50.1
1	Buffer	90	125.1
4	Core	25	129.1
	Core	80	104.3
1	Core	25	129.1
1	Buffer	90	125.1
14	Top Bragg	35	50.1
		90	70.8
1	Cap	0	46.2

Table 1.1: Nominal epitaxial structure for the wafer **F3W083** (April 2015), from which the counter-propagating geometry sources employed in this thesis have been processed.

temperature. Indeed in this way, the size of the layers is altered through thermal expansion and, more importantly, the refractive indices are modified [136]. G. Boucher in its PhD thesis [153] reports numerical simulations showing that the tuning is of two nanometers for a temperature variation of 40°C.

Infrared guided modes

Figure 1.11 reports the intensity profile of both TE- and TM-polarized fundamental guided modes at 1550 nm.

It is worth noting that, due to the source structure, the two guided modes have different intensity profiles. Indeed, the TM guided mode, having its electric field polarized along the x axis, is not continuous at the dielectric interfaces. On the other hand, the TE guided mode electric field is polarized along the y direction and therefore has a continuous profile. This effect can also be noticed in Figure 1.9.

The following table summarizes the major characteristics of the TE and TM fundamental guided modes, for a 5 µm-wide waveguide, calculated performing a 3D numerical simulation with the software Lumerical FDTD:

	n_{eff}	v_g (m/s)	GVD (fs^2/s)	D_λ (ps/nm/km)	R
TE	3.0980	$9.53 \cdot 10^7$	$57.4 \cdot 10^3$	-45	28.5%
TM	3.0855	$9.57 \cdot 10^7$	$62.5 \cdot 10^3$	-49	24.7%

where n_{eff} is the effective refractive index, v_g the group velocity, the group velocity dispersion given by GVD and D_λ, and the modal reflectivity R.

We note that the modal refractive indices for the two guided modes are not equal and thus they induce a slight modal birefringence in the device ($\Delta n \approx 0.0125$). This effect is due to the source aspect ratio (the core is ≈ 1 µm thick and 5 µm wide) and its structure (the stack of layers with different Al content).

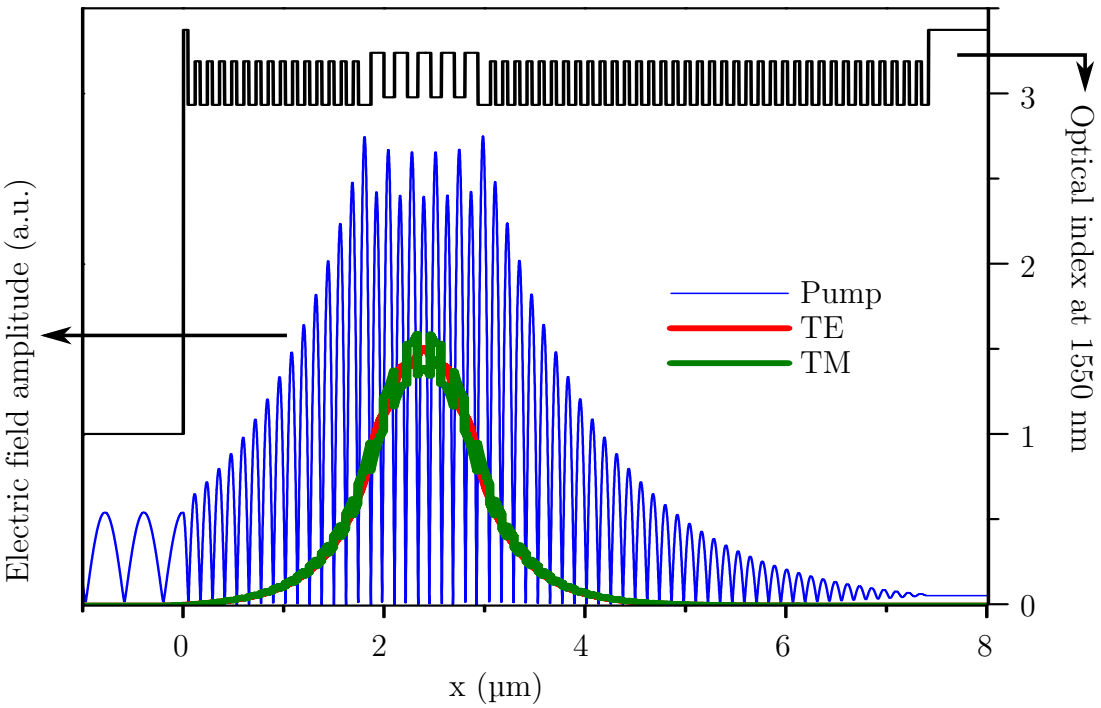

Figure 1.9: Refractive index profile at 1550 nm and amplitude transverse profile for the three interacting fields.

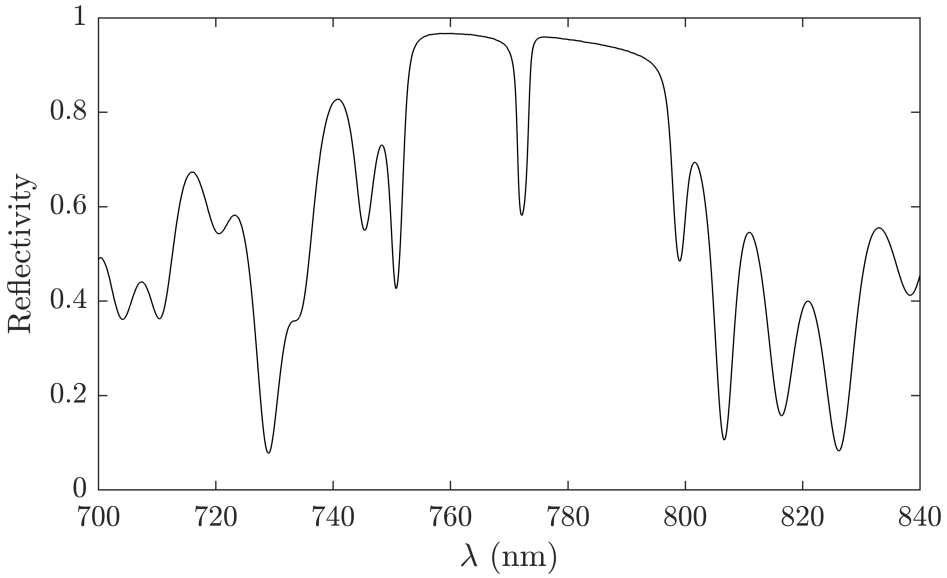

Figure 1.10: Reflectivity spectrum measured with the FTIR on the wafer **F3W083**. In the center we notice the dip due to the presence of the vertical microcavity.

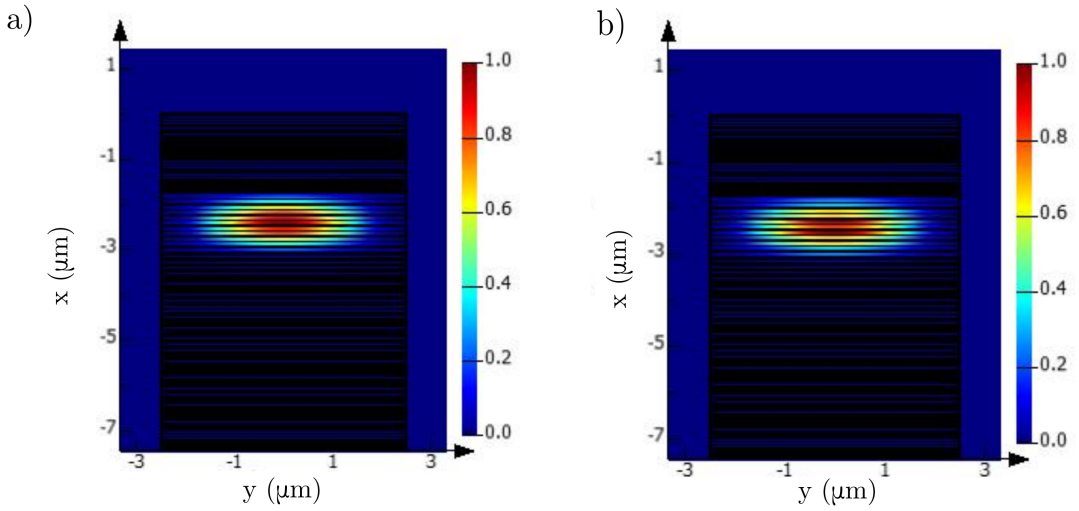

Figure 1.11: Numerical simulation of the intensity profile of the TE- and TM-polarized fundamental guided modes at 1550 nm.

The modal reflectivity R gives the amount of power that is reflected inside the waveguide when the field arrives at the waveguide facet. The reflection is caused by a refractive index mismatch between the waveguide ($n_{eff} \approx 3$) and the air ($n = 1$), as expected from Fresnel's law. We will deal deeply with this subject in chapter 8, proposing some techniques to eliminate the modal reflectivity.

1.4.2 Characteristics of counter-propagating phase-matching scheme

Let us now study more in detail the fundamental characteristics of counter-propagating phase-matching in a ridge waveguide, referring to Figure 1.8 that reports the source scheme.

A pump beam at 775 nm, polarized along the y direction, impinges on the top of the waveguide with an angle θ and generates by SPDC photon pairs at 1550 nm. We call signal the photon propagating to the right (propagating forward along the z axis) and we call idler the one propagating to the left (propagating backward along the z axis), as depicted in Figure 1.8.

In this geometry, due to the AlGaAs nonlinear coefficients, only a type II nonlinear process can take place, in which a pump photon is down-converted into orthogonally polarized photons (TE and TM polarization)[2]. Therefore, two concurrent photon pair generation processes occur simultaneously inside the source: we call interaction HV the process where the signal photon is Transverse Electric (TE), i.e. the electric field is polarized along y axis (H direction), while the idler photon is Transverse Magnetic (TM), i.e. the electric field is polarized along the

[2]Another SPDC process, generating photons with the same polarization, could be obtained by means of the x component of the pump field when the pump beam incidence angle θ is large. However, in our source the quasi-phase-matching is achieved only for small values of θ (of the order of a few degrees) and thus in the following we will neglect this additional process.

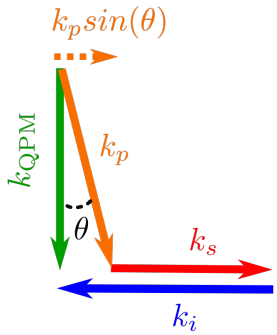

Figure 1.12: Sketch of the phase-matching scheme for counter-propagating photons.

x axis (V direction). On the other hand, we call interaction VH the opposite situation: the signal photon is TM while the idler photon is TE.

We recall the energy conservation and phase-matching conditions:

$$\begin{cases} \omega_p = \omega_s + \omega_i \\ \mathbf{k}_p = \mathbf{k}_s + \mathbf{k}_i \end{cases} \tag{1.50}$$

where ω_p, ω_s and ω_i are, respectively, the angular frequency of the pump, signal and idler fields while $\mathbf{k}_p$, $\mathbf{k}_s$ and $\mathbf{k}_i$ are their wavevectors. In the case of counter-propagating phase-matching, as sketched in Figure 1.12, we can decompose the momentum conservation along the horizontal direction (z-axis) and along the vertical direction (x-axis). In this case the previous equations become:

$$\begin{cases} \omega_p = \omega_s + \omega_i \\ \dfrac{\omega_p}{c} \sin\theta = k_s - k_i \\ \dfrac{n_p(\omega_p, x)\, \omega_p}{c} \cos\theta = k_{QPM} \end{cases} \tag{1.51}$$

where k_s and k_i are the modulus of the wavevectors of the signal and idler photons within the sample, θ is the incidence angle of the pump beam and $n_p(\omega_p, x)$ is the value of the refractive index at frequency ω_p and depth x in the layered structure.

From the third equation we can see that the vertical component of the pump beam wavevector is not compensated and this would lead to a weak efficiency. In order to counterbalance it, a Quasi-Phase Matching (QPM) is implemented in the core of the waveguide, by alternating layers with high and low refractive index, which is described by $k_{\mathrm{QPM}} = \dfrac{2\pi}{\Lambda}$ where $\Lambda = \lambda_p/2n$ is the layers thickness[3]. Figure 1.7e illustrates the phase-matching process.

It is worth noting that, if the waveguide thickness is smaller than half a pump wavelength (approximately 125 nm in our case), counter-propagating phase-matching does not requires phase-matching in the vertical direction [148]. However,

[3]The equation is valid only for a perpendicular pump beam. When the beam is tilted (i.e. $\theta \neq 0$) it becomes $\Lambda = \lambda_p/2n\cos\theta$, thus requiring a different QPM period. In practice, however, we always employ small incidence angles ($\theta < 1°$) and the phase-matching is satisfied.

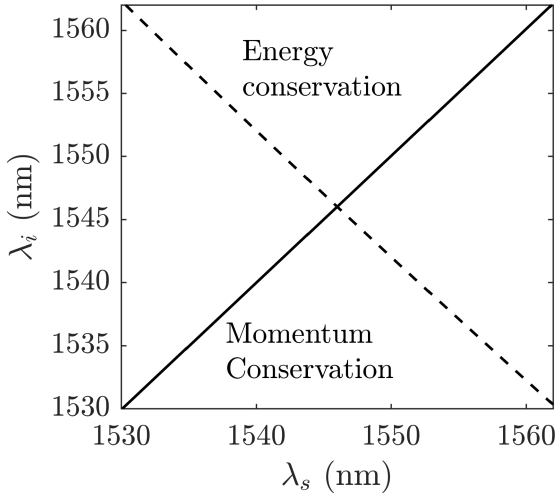

Figure 1.13: Energy conservation (dashed line) and momentum conservation (solid line) condition in a SPDC process based on a counter-propagating phase-matching scheme. The intersection point represents the pair of wavelengths at which the process can take place. In this simulation the pump field has a wavelength $\lambda_p = 773$ nm and impinges onto the device at the degeneracy angle, $\theta_{\text{deg}} = 0.384°$ for the considered structure, and thus the emitted photons have the same wavelength.

in order to increase the conversion efficiency, it is convenient to employ a thicker waveguide, as in our case, and thus QPM has to be implemented in order to keep the generation of the photons in each layer phased with the other.

Source Tunability

Having fulfilled the phase-matching condition in the x direction, we focus on the the propagation direction (z-axis). From Equation 1.51 the involved expressions are:

$$\begin{cases} \omega_p = \omega_s + \omega_i \\ \omega_p \sin\theta = \omega_s n_s(\omega_s) - \omega_i n_i(\omega_i) \end{cases} \tag{1.52}$$

where $n_{s/i}$ are the effective indices of the guided signal and idler modes. We can rewrite the previous equations expressing the idler frequency ω_i as a function of the signal frequency ω_s:

$$\begin{cases} \omega_i = \omega_p - \omega_s \\ \omega_i = \dfrac{n_s}{n_i}\omega_s - \dfrac{\omega_p}{n_i}\sin\theta \end{cases} \tag{1.53}$$

Figure 1.13 reports the plot (in the wavelength space) of these two functions for a given pump incidence angle. We can see that the first (energy conservation) is oriented along the negative diagonal while the second (phase-matching) is orthogonal to it (positive diagonal). The intersection point between the two lines gives the wavelengths of the emitted photons.

Equation 1.53 shows also that, by tilting the incidence angle θ, it is possible to tune the frequency of the generated photons. The equation solutions are plotted

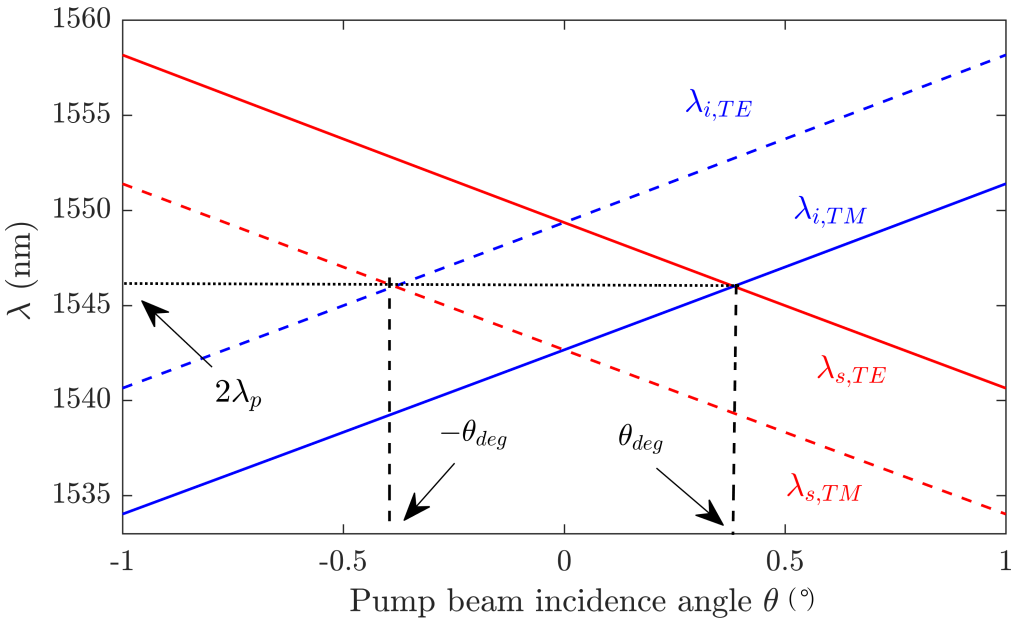

Figure 1.14: Angular dependence of the signal (red) and idler (blue) wavelengths for interaction HV (solid lines) and interaction VH (dashed lines) for a pump wavelength of $\lambda_p = 773$ nm. Where the lines intersect, the signal and idler photons have the same wavelength; the corresponding value of θ is called degeneracy angle. The two degeneracy angles, one for each interaction, are symmetric with respect to the $\theta = 0°$ position and thus the degeneracy wavelength is the same for both interactions ($2\lambda_p$).

in Figure 1.14. This graph, called *accordability curves*, represents the generated signal and idler wavelengths as a function of the pump beam incidence angle θ, for both interactions (HV and VH). We see that, for a given interaction, there is a degeneracy angle at which the produced photons have the same wavelength, given by:

$$\pm\,\theta_{deg} = \pm \arcsin \frac{n_s - n_i}{2} \tag{1.54}$$

where θ_{deg} is for the HV interaction and $-\theta_{\text{deg}}$ for the VH interaction.

The degeneracy angle slightly differs from zero due to the birefringence of the source: as we have seen, bulk AlGaAs is not a birefringent medium, but the device structure induces a small modal refractive index difference between the two polarizations.

Since the graph in Figure 1.14 is symmetric with respect to the $\theta = 0°$ position, the degeneracy frequency is the same for both interactions. This enables the source to generate polarization entangled photons by simply pumping simultaneously at both the degeneracy angles, as has been proved by our group in Ref. [57], or to directly emit hybrid polarization-frequency entangled state as we will report in chapter 7.

1.5 SPDC source based on a co-propagating phase-matching scheme

In this section we detail another type of source developed by our team, which we employ to generate spatially entangled photon pairs, as we will see in Part III of this thesis.

The source is based on modal phase-matching: the pump guided mode at 775 nm is engineered and guided in a Bragg mode, by means of Bragg reflectors, in order to have the same effective refractive index than the fundamental guided modes at 1550 nm.

Bragg reflection waveguides have been proposed by Yeh and Yariv [154] in 1976 and started to be experimentally investigated only in 2006 [155, 156]. In these last years, this phase-matching scheme has led to many important results for the development of photon pair sources working at room temperature and in the telecom range. In particular, our group has demonstrated the electrical injection of the photon pair generation [60], as well as the generation of highly indistinguishable and energy-time entangled photon pairs in a passive device [59] and the generation of biphoton frequency combs [126].

Figure 1.15 is a sketch of the device developed by our group: it consists of a core surrounded by two Bragg mirrors, playing the role of cladding layers and made of six stacks of alternating high and low refractive index bilayers, correspondig to a low (25%) and a high (80%) Al concentration, respectively. By properly choosing the composition and the thickness of these layers (i.e. each layer is a quarter of the pump wavelength in the medium), a constructive interference can take place and a Bragg mode is supported in the waveguide, in addition to the fundamental Gaussian modes.

The vertical profile has been designed to support two Bragg modes around 775 nm (TE and TM polarized) and two fundamental Gaussian modes (TE and TM polarized) centered at 1550 nm, whose modal refractive indices satisfy the phase-matching condition and lead to a high nonlinear overlap integral[4]. Table 1.2 reports the epitaxial structure of the source, which has been designed and optimized by A. Orieux [133], a previous PhD student in our group.

Figure 1.16 shows the numerically simulated electric field intensity of the guided modes, for a 2 µm-wide ridge waveguide with perpendicular sidewalls and the core partially etched. The Bragg modes feature the typical alternating out-of-phase lobes. As for the counter-propagating geometry source, the fundamental TE mode electric field is continuous at the interfaces between high and low refractive index materials, contrary to the TM mode which is not continuous. This and the source aspect ratio lead to a slight difference between the two effective refractive indices: $n_{\mathrm{TE}} = 3.098$ and $n_{\mathrm{TM}} = 3.081$, thus inducing a small form birefringence $\Delta n = 0.017$.

Similarly to the counter-propagating source, also in this case the facets of the waveguide have a non-zero modal reflecitivity, which differs notably between the fundamental Gaussian modes at 1550 nm and the Bragg modes at 775 nm, as

[4]The utilization of Bragg mirrors allows also to reduce the Al content, avoiding the device oxidation and aging.

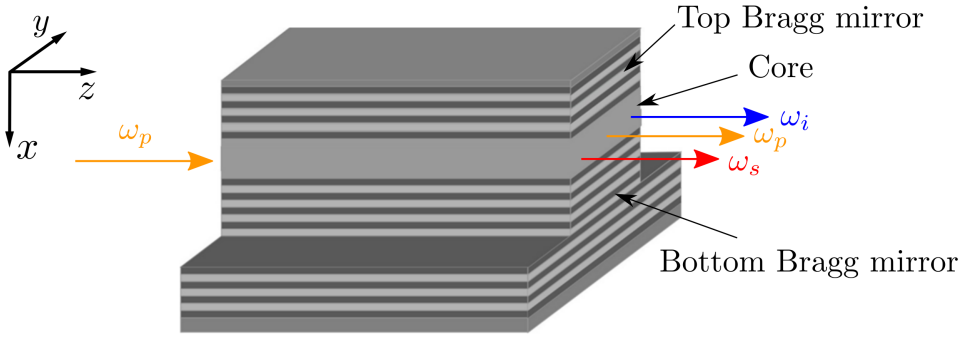

Figure 1.15: Sketch of the Bragg reflection waveguide, indicating the different regions.

Number of periods	Role	Al content (%)	Thickness h (nm)
1	Substrate	0	
6	Bottom Bragg	80	276
		25	114
1	Core	45	355.5
6	Top Bragg	25	114
		80	276
1	Cap	0	250

Table 1.2: Nominal epitaxial structure for the wafers **EBW002**, from which the co-propagating sources have been processed.

reported in the following table:

	R_{TE}	R_{TM}
Bragg mode at 775 nm	88.8%	70.5%
Fundamental mode at 1550 nm	28.2%	27.8%

numerically calculated for a 2 µm-wide waveguide with the core partially etched.

1.5.1 Modal phase-matching

The source achieves phase-matching by engineering the modal chromatic dispersion of the guided modes. In order to show that, we recall the energy conservation and phase-matching conditions:

$$\begin{cases} \omega_p = \omega_s + \omega_i \\ \mathbf{k}_p = \mathbf{k}_s + \mathbf{k}_i \end{cases} \tag{1.55}$$

and we project the phase-matching along the propagation direction (z axis):

$$\omega_p n_p(\omega_p) = \omega_s n_s(\omega_s) + \omega_i n_i(\omega_i) \tag{1.56}$$

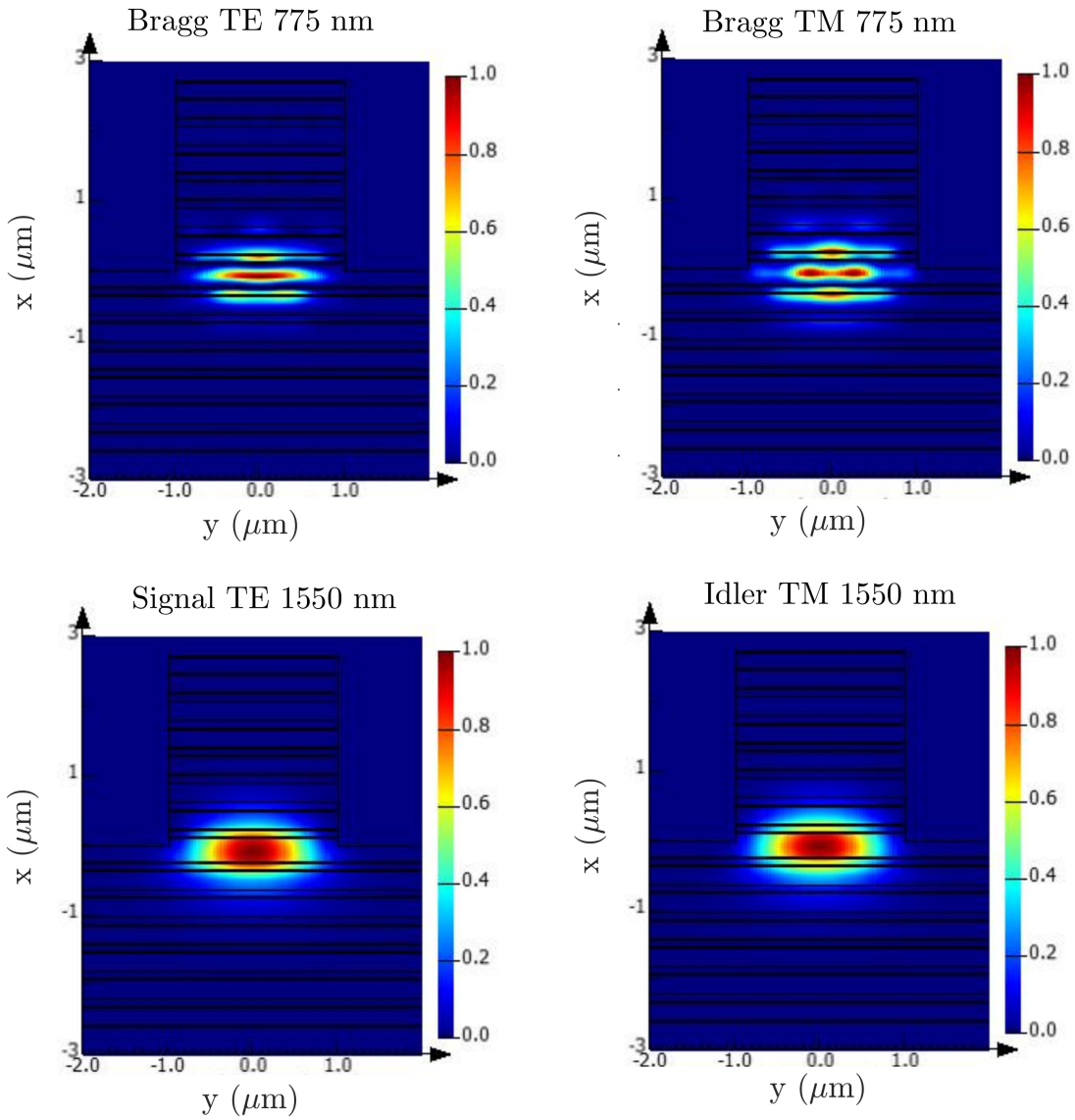

Figure 1.16: Numerical simulations of the intensity profile of the TE- and TM-polarized guided modes supported by a 2 µm-wide waveguide: Bragg modes at 775 nm and fundamental guided modes at 1550 nm.

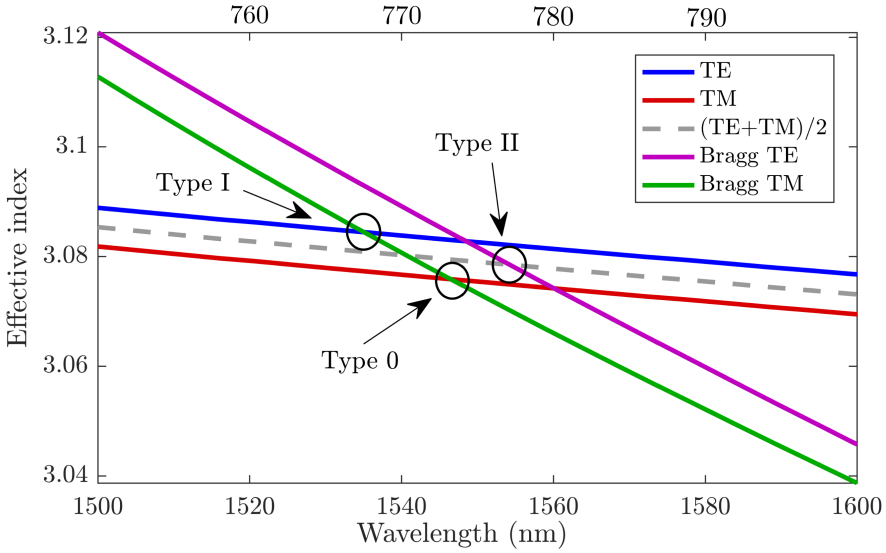

Figure 1.17: Numerically calculated dispersion of the modal effective refractive index of TE and TM Bragg modes (top horizontal axis) and TE and TM fundamental Gaussian modes (bottom horizontal axis). The simulations have been done for a 2 µm-wide ridge waveguide, with the core partially etched.

where $n_j(\omega_j)$ is the modal refractive index of the mode j. From that it is clear that, in order to fulfill the phase-matching condition, the pump guided mode must have the same value of modal refractive index than the signal and idler modes, at their respective frequencies.

Figure 1.17 is a plot of the numerically simulated modal dispersion of the Bragg and fundamental modes of Figure 1.16. Depending on the field polarizations and given the nonlinear susceptibility tensor, three different types of phase-matching can be achieved.

In a type 0 process a TM pump photon is down-converted in two TM polarized photons, the phase-matching condition is:

$$\text{Type 0} \qquad \omega_p n_{\text{Bragg, TM}}(\omega_p) = \omega_s n_{\text{TM}}(\omega_s) + \omega_i n_{\text{TM}}(\omega_i) \tag{1.57}$$

where $n_{\text{Bragg, TM}}$ is the effective index of the TM Bragg mode. This nonlinear process is enabled by the guided regime. Indeed, both TM fundamental and TM Bragg modes have a component of their electric field directed along the propagation direction (z axis), situation that cannot occur in the free space. These longitudinal components of the fields can interact, enabling a type 0 process [157].

In a type I process a TM pump photon is down-converted to two TE polarized photons. The phase-matching condition is:

$$\text{Type I} \qquad \omega_p n_{\text{Bragg, TM}}(\omega_p) = \omega_s n_{\text{TE}}(\omega_s) + \omega_i n_{\text{TE}}(\omega_i) \tag{1.58}$$

This process is directly enabled by the d_{XYZ} nonlinear coefficient, which couples the TE and the TM modes. In order to explain this, we can examine the corresponding SHG process in which two TE pump photons are converted in one TM photon with double frequency (TE + TE $\rightarrow$ TM). The nonlinear polarization, in the crystal

reference system (X, Y, Z), is:

$$P_{\mathrm{Z}}^{NL,\mathrm{TM}} \propto d_{\mathrm{ZXY}} E_{\mathrm{X}}^{\mathrm{TE}} E_{\mathrm{Y}}^{\mathrm{TE}} \tag{1.59}$$

which couples the X and Y component of the TE fields to generate a SHG field directed along the Z direction (i.e. TM polarized).

In a type II process a TE pump photon is down-converted to a TE and a TM photons. In this case two interactions can occur: a TE signal photon and a TM idler photon are generated, or vice-versa. Contrary to the counter-propagating source, here the two photons of the pair cannot be distinguished by their propagation direction, which is the same. Therefore, we employ their frequency: we call signal the photon at higher frequency and idler the one at lower frequency.

The phase-matching relation becomes:

$$\text{Type II} \qquad \omega_p n_{\mathrm{Bragg,\ TE}}(\omega_p) = \omega_s n_{\sigma}(\omega_s) + \omega_i n_{\sigma_\perp}(\omega_i) \tag{1.60}$$

where σ and $\sigma_\perp$ denote a given polarization and the orthogonal one, respectively. This process is enabled by the nonlinear coefficients d_{XYZ} and d_{YXZ}. For the corresponding SHG process ($\mathrm{TE} + \mathrm{TM} \rightarrow \mathrm{TE}$), the nonlinear polarization in the crystal reference system (X, Y, Z) reads:

$$\begin{aligned} P_{\mathrm{X}}^{NL,\mathrm{TE}} &\propto d_{\mathrm{XYZ}} E_{\mathrm{Y}}^{\mathrm{TE}} E_{\mathrm{Z}}^{\mathrm{TM}} \\ P_{\mathrm{Y}}^{NL,\mathrm{TE}} &\propto d_{\mathrm{YXZ}} E_{\mathrm{X}}^{\mathrm{TE}} E_{\mathrm{Z}}^{\mathrm{TM}} \end{aligned} \tag{1.61}$$

The first equation couples the Y component of the TE mode and the Z component of the TM one, generating the X component of the SHG field. Meanwhile the Y component of the SHG field is generated by the coupling of the X component of the TE mode and the Z component of the TM mode, as described in the second equation.

From the nonlinear overlap integral Γ we can calculate the device conversion efficiency η for a type II process. For a $L = 2$ mm device we expect [158]:

$$\eta = 1.37 \cdot 10^{-8} \quad \text{photon pairs/pump photons} \tag{1.62}$$

which is considerably higher than the counter-propagating scheme source, for which the conversion efficiency is $\eta \approx 10^{-11}$, mainly due to the higher nonlinear overlap integral.

In Part III of this manuscript we will employ the co-propagating source to develop a novel device that generates spatially entangled biphoton states.

1.6 Sample fabrication and optical characterization

In this section we give a brief overview on the clean room fabrication processes of the sources and on the employed method to evaluate their propagation losses.

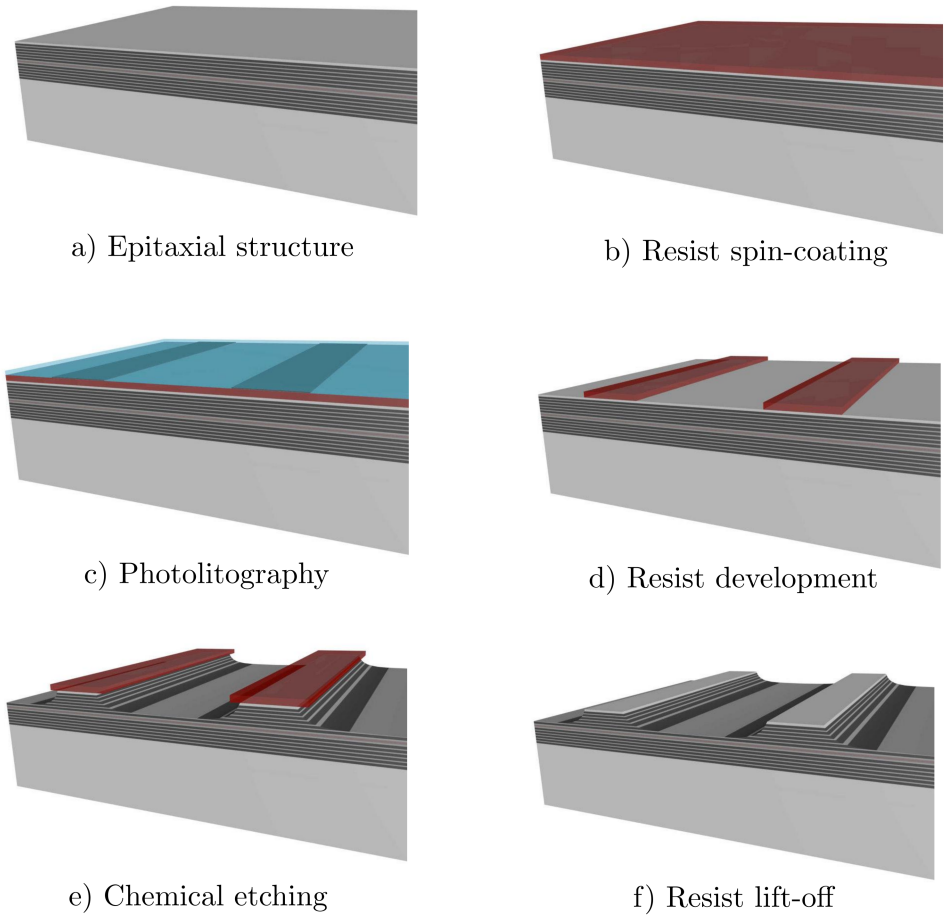

Figure 1.18: Steps for the chemical etching of the waveguides. Adapted from [159].

1.6.1 Fabrication processes

The counter-propagating source that has been employed in this work has been fabricated in the clean room of the MPQ Laboratory employing the epitaxial growth made by A. Lemaitre at C2N by Molecular Beam Epitaxy (wafer **F3W083**). The fabrication is principally divided in two steps: optical lithography with UV light and wet etching using a chemical solution. Figure 1.18 summarizes the procedure. This process has already been optimized by previous PhD students of the team and thus refer to their PhD theses for more information [134, 159].

The processed waveguide is 1.9 mm long and 5 µm wide; the side-walls have a curved profile, typical of the wet etching technique (see Figure 1.19a). Vertically the top Bragg mirror and the core are etched while the bottom mirror is not.

The fabrication process described above is a fast technique, which gives satisfactory results when processing single waveguides. However, it presents many drawbacks when more complex designs are envisaged, e.g. the device to generate spatially entangled photon pairs that we will present in Part III. For this reasons, we have developed a new fabrication process based on electron beam lithography

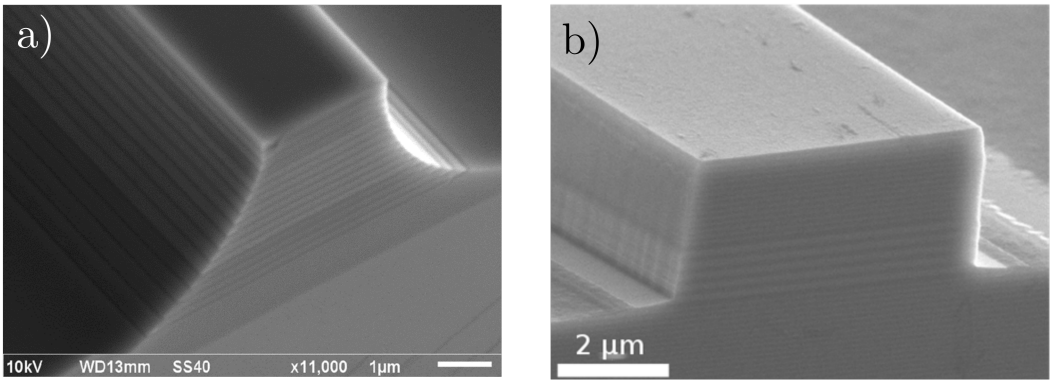

Figure 1.19: Comparison between the facets of a wet etched sample with curved sidewalls (a) and a dry etched one with vertical sidewalls (b).

and inductively coupled plasma etching, which result is more vertical sidewalls (see Figure 1.19b). A detailed description of this fabrication process and its optimization steps will be given in section 9.4.

1.6.2 Propagation loss evaluation

The propagation of a light beam inside a waveguide strongly depends on its fabrication quality. Indeed, if the waveguide suffers from fabrication problems (e.g. defects, free charges or roughness) the beam is attenuated while it propagates.

Let us consider a waveguide of length L and an electromagnetic wave propagating along the z direction. If I_0 is the intensity injected in the device, the intensity at the position z is:

$$I(z) = I_0 e^{-\alpha z} \tag{1.63}$$

where α is the propagation loss coefficient we want to determine.

As we have seen above, the waveguide facets have a non-zero reflectivity (R), due to the refractive index mismatch between the waveguide and the air. Thus, the waveguide behaves like a Fabry-Pérot cavity, modulating the output power. For a monomode waveguide, the transmitted power is described by the Airy function:

$$T_{FP} = \frac{T^2 e^{-\alpha L}}{\left(1-\tilde{R}\right)^2 + 4\tilde{R}\sin^2\left(\frac{\phi}{2}\right)}\eta \tag{1.64}$$

where T is the end-facet transmission, η the coupling efficiency into the waveguide, L is its length and $\tilde{R} = Re^{-\alpha L}$ is the combined loss-reflection coefficient. The phase term $\phi = 2k_0 n_{eff} L + \phi_0$ is the phase accumulated over a round trip: it involves the reflection dephasing ϕ_0, the wave-vector in free space k_0, and the effective refractive index n_{eff} of the guided mode. We can tune the phase term ϕ by changing the temperature, applying an electric field (electro-optic effect) or simply continuously varying the input wavelength. Measuring the contrast C of the Fabry-Pérot fringes

allows to extract the value of $\tilde{R}$. Indeed,

$$C = \frac{T_{\max} - T_{\min}}{T_{\max} + T_{\min}} \tag{1.65}$$

and thus

$$\tilde{R} = \frac{1}{C}\left(1 - \sqrt{1 - C^2}\right) \tag{1.66}$$

Knowing the reflectivity of the facets and the waveguide length we can extract the loss coefficient:

$$\alpha = \frac{\ln\left(R/\tilde{R}\right)}{L} \tag{1.67}$$

where R is the waveguide modal reflectivity, which can be evaluated through numerical simulations.

This method has been proposed for the first time by Park et al. [160] in 1995 for a monomode waveguide. In case of multimode waveguides, if the higher-order guided modes have higher (or equal) propagation losses compared to the fundamental one, the relation above gives an upper bound for the propagation losses, as demonstrated in [161]. Indeed, in this case, the different modes propagating in the waveguide beat and, when they are in phase, the contrast is maximal and closest to the real propagation losses. In addition, if all the involved modes have the same modal reflectivity and propagation losses, the method still provides their exact value.

In the following paragraph we apply this technique to evaluate the propagation losses of the counter-propagating source that will employed in Part II of this thesis. On the contrary, the analysis of the co-propagating source optical losses will be presented after its fabrication process, in section 9.5.

Counter-propagating source propagation losses

To implement the method described above, we inject a CW infrared laser inside the waveguide and we measure the output power. By scanning the laser wavelength we reconstruct the Fabry-Pérot oscillations and calculate the propagation losses. Figure 1.20 reports experimentally measured Fabry-Pérot fringes for both TE and TM polarization. The fringe free spectral range (FSR) is related to the sample length L by the following formula:

$$\Delta\lambda_{\mathrm{FSR}} = \frac{\lambda^2}{2L\, n_g} \tag{1.68}$$

where n_g is the group refractive index of the involved guided mode. The experimentally measured value ($\Delta\lambda_{\mathrm{FSR}} = 190$ pm) confirms the source length value ($L = 1.9$ cm).

Finally, from the fringes contrast we derive the propagation losses: $\alpha = 0.48$ cm^{-1} (-2 dB/cm) for the TE polarization and $\alpha = 0.65$ cm^{-1} (-2.8 dB/cm) for the TM polarization. These loss values are higher than the best one obtained with such structure ($\alpha = 0.2$ cm^{-1}) [134] with the same nominal epitaxial growth, but fabricated from a different wafer (**88P14**). We suppose that the higher losses may be due to a difference in the epitaxial growth.

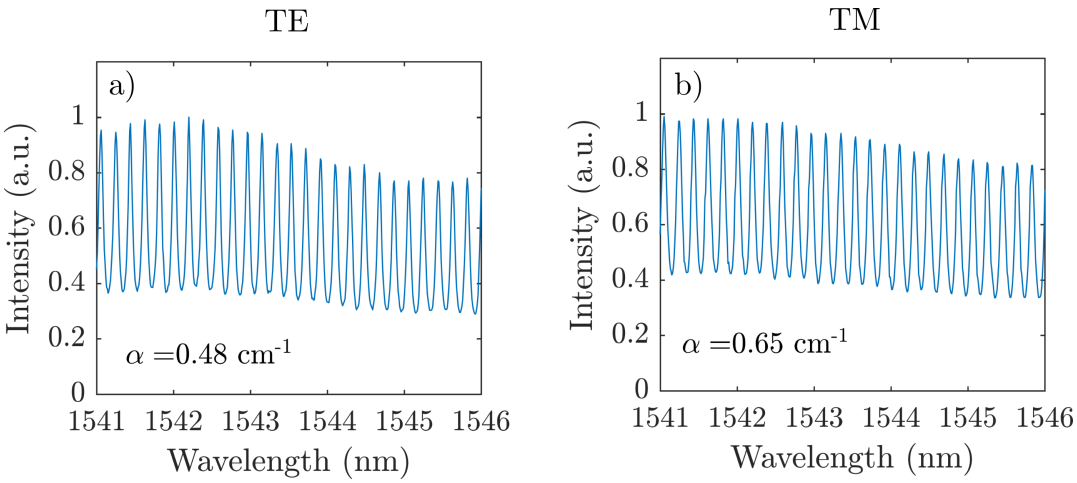

Figure 1.20: Normalized power for TE (a) and TM polarized (b) waves through the waveguide. From the contrast of the Fabry-Pérot oscillations we derive the optical losses.

Chapter 2

Quantum Theory of SPDC in a Counter-propagating Phase-Matching Scheme

In this chapter we present a quantum theory of light describing the generation of photon pairs in a counter-propagating phase-matching source, focusing on photon frequency-time properties.

Different approaches can be employed depending on the situation [162, 163]. Here, since we are interested in low power pumping regime, in which the probability of generating multiple pairs per pump photon is negligible, we follow the analysis, based on perturbation theory, proposed by Guillaume Boucher in his PhD manuscript [153].

The goal is to derive the Joint Spectral Amplitude JSA $\phi(\omega_s, \omega_i)$, a function giving the joint probability that the signal and idler photons are emitted at frequencies ω_s and ω_i, respectively. In particular, we will connect the JSA to the pump beam spatial and temporal properties, showing how those can be engineered in order to control the frequency correlations between the photons of the pair, as it has been pointed out for the first time by Walton et al. [164].

In the second part of the chapter we will analyze the frequency-time properties

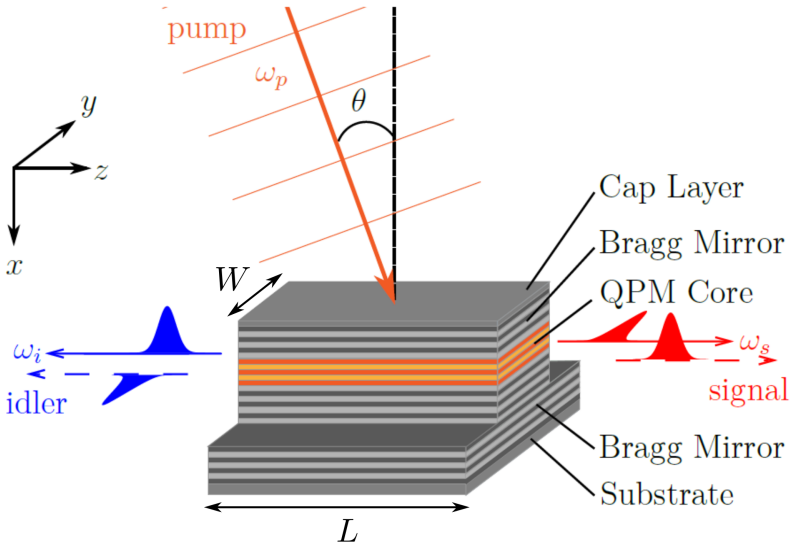

Figure 2.1: Sketch of the source based on the counter-propagating phase-matching scheme under transverse pumping and its working principle.

of the quantum state emitted by the source by introducing concepts such as the Schmidt decomposition and the Chronocyclic Wigner Function.

The results are derived for a counter-propagating phase-matching scheme but they can be easily generalized to a co-propagating scheme. For a detailed calculation of this particular case we refer to G. Maltese PhD thesis [158].

2.1 Joint Spectral Amplitude derivation

In this section we derive the JSA of the generated state by employing the following procedure. We rely on the Heisenberg picture (i.e. the state wavefunction is constant in time, while the operators acting on it evolve) and we start by identifying the fields involved in the process, expressed in their quantized forms. Then we define the perturbation term to the linear Hamiltonian, given by the SPDC nonlinear Hamiltonian. As a last step, we derive the biphoton state generated by the source by solving the Schrödinger equation including the perturbation term.

In the calculation we employ the same reference system introduced in the previous chapter (here reported in Figure 2.1), namely the x axis corresponds to the growth direction, the z axis is the propagation direction and the y axis is orthogonal to the first two. The produced photons can be distinguished by their propagation direction: we call signal the photon propagating to the right (positive z) and idler the photon propagating to the left (negative z). Moreover, we focus only on the fundamental guided modes and on the HV interaction: the one emitting a horizontally polarized signal photon (TE polarized, i.e. its electric field is directed along the y axis) and a vertically polarized idler photon (TM polarized, i.e. its electric field is directed along the x axis). The result can be easily generalized to the other interaction (VH) or to higher order guided modes. From now on we will use only H and V to indicate the polarization directions.

2.1.1 Interacting fields

Pump field

SPDC-based sources generally have a low conversion efficiency ($\approx 10^{-11}$ generated pairs per pump photon, in our case) and the pump beam is very bright. Therefore, the latter can be assumed as undepleted and described classically:

$$\hat{\mathbf{E}}_p(\mathbf{r},t) \sim \mathbf{E}_p(\mathbf{r},t) = (2\pi)^{-3/2} \int_0^{+\infty} \mathrm{d}\mathbf{k}\, \hat{\mathbf{u}}_y E_p(\mathbf{k},t)\, e^{i(\mathbf{k}\cdot\mathbf{r}-\omega_{\mathbf{k}}t)} + \text{c.c.} \tag{2.1}$$

where we have assumed a H polarization, so as to fulfill the conditions for a type II phase-matching (as detailed in section 1.4). The pump beam electric field is thus directed along the y direction, indicated by the unit vector $\hat{\mathbf{u}}_y$, and $E_p(\mathbf{k},t)$ represents the electric field amplitude at a given wavevector $\mathbf{k}$, as it will be detailed later.

Idler and Signal Fields

The waveguide confines the produced photons along the vertical and horizontal directions by total internal reflection and thus the number of allowed modes is discretized (see section 1.2). As stated above, in this analysis we consider, for the signal and idler fields, only the fundamental guided modes, but it can be easily generalized to higher-order modes.

The produced photon pairs propagate along the z axis, where the waveguide length L is much larger than the wavelength in the range we work in, therefore we have a continuum of k-vectors. We can thus write the electric field operator inside the waveguide using the usual quantization procedure [165]:

$$\begin{aligned}\hat{\mathbf{E}}(\mathbf{r},t) = &\overbrace{\sqrt{\frac{L}{2\pi}}\sum_\sigma \int_0^{+\infty} \mathrm{d}k\, \mathbf{E}_\sigma(x,y) e^{i(k_\sigma z-\omega_k t)} \hat{\mathrm{a}}_{\sigma,k}}^{\hat{\mathbf{E}}_s^{(+)}(\mathbf{r},t)} + \overbrace{\text{h.c.}}^{\hat{\mathbf{E}}_s^{(-)}(\mathbf{r},t)} \\ &\underbrace{+\sqrt{\frac{L}{2\pi}}\sum_\sigma \int_{-\infty}^{0} \mathrm{d}k\, \mathbf{E}_\sigma(x,y) e^{i(k_\sigma z-\omega_k t)} \hat{\mathrm{a}}_{\sigma,k}}_{\hat{\mathbf{E}}_i^{(+)}(\mathbf{r},t)} + \underbrace{\text{h.c.}}_{\hat{\mathbf{E}}_i^{(-)}(\mathbf{r},t)}\end{aligned} \tag{2.2}$$

where the label σ indicates the polarization of the field (H or V), $\hat{\mathrm{a}}_{\sigma,k}$ is the annihilation operator of a photon with polarization σ and wavevector k, and $\mathbf{E}_\sigma(x,y)$ is its transverse profile. We have split the integral in two terms: the first $\hat{\mathbf{E}}_s^{(+)}(\mathbf{r},t)$, with positive k, represents the signal modes (propagating forward) while the second $\hat{\mathbf{E}}_i^{(+)}(\mathbf{r},t)$, with negative k, represents the idler modes (propagating backward). The creation and annihilation operators, $\hat{\mathrm{a}}^\dagger$ and $\hat{\mathrm{a}}$, satisfy the usual commutation relations.

The guided regime also implies a direct relation between the wavevector k and the frequency ω:

$$|k_\sigma| = \frac{n_\sigma \omega}{c} \tag{2.3}$$

where n_σ is the effective index of the mode, for a given polarization. This relation allows us to change the integration variable from k-vector to frequency [165], which is more intuitive to describe the frequency correlations between the generated photons. We employ the following transformations:

$$\mathrm{d}k \to \frac{\mathrm{d}\omega}{v_g(\omega)} \qquad \hat{a}_k \to \sqrt{v_g(\omega)}\,\hat{a}(\omega) \tag{2.4}$$

where $v_g(\omega)$ is the group velocity of the involved guided mode at frequency ω. The fields can now be written as follows:

$$\hat{\mathbf{E}}^{(+)}_{s/i}(\mathbf{r},t) = \sqrt{\frac{L}{2\pi}}\sum_\sigma \int_0^{+\infty} \mathrm{d}\omega\, \frac{\mathbf{E}_\sigma(x,y;\omega)}{\sqrt{v_g^\sigma(\omega)}} e^{i(\pm|k_\sigma(\omega)|z-\omega_k t)}\hat{\mathrm{a}}_{s/i,\sigma}(\omega) + \mathrm{h.c.} \tag{2.5}$$

The exponential has a + for the signal field (propagating forward) and a - for the idler field (propagating backwards).

2.1.2 Nonlinear Hamiltonian

The nonlinear interaction between the three interacting fields is expressed by the following nonlinear Hamiltonian:

$$\hat{H}_{\mathrm{NL}}(t) = \epsilon_0 \int \mathrm{d}\mathbf{r}\chi^{(2)}(\mathbf{r})\hat{E}_p(\mathbf{r},t)\hat{E}_s(\mathbf{r},t)\hat{E}_i(\mathbf{r},t) \tag{2.6}$$

with $\chi^{(2)}(\mathbf{r})$ the nonlinear susceptibility tensor of the medium.

As we have seen in section 1.4 the device achieves only type II phase-matching, in which a H pump photon is downconverted in two orthogonally polarized photons (H and V). With this condition the nonlinear Hamiltonian becomes:

$$\begin{aligned}\hat{H}_{\mathrm{NL}}(t) = \epsilon_0 \int \mathrm{d}\mathbf{r}\, \chi^{(2)}(\mathbf{r})\hat{E}_p(\mathbf{r},t)\hat{E}_{s,H}(\mathbf{r},t)\hat{E}_{i,V}(\mathbf{r},t) \\ + \epsilon_0 \int \mathrm{d}\mathbf{r}\, \chi^{(2)}(\mathbf{r})\hat{E}_p(\mathbf{r},t)\hat{E}_{s,V}(\mathbf{r},t)\hat{E}_{i,H}(\mathbf{r},t)\end{aligned} \tag{2.7}$$

The involved fields are all composed of a frequency positive term E^+ and a conjugate negative frequency term E^- (c.f. Equation 2.2). The first contains the annihilation operator and the latter the creation operator. By multiplying the three operators ($\hat{E}_p\ \hat{E}_s\ \hat{E}_i$), we thus obtain eight possible combinations. The energy conservation condition constrains the possible combinations and therefore we keep only the ones where a pump photon is annihilated and a signal and a idler photon are created, and their Hermitian conjugates. With these considerations the nonlinear Hamiltonian simplifies to:

$$\begin{aligned}\hat{H}_{\mathrm{NL}}(t) = \epsilon_0 \int \mathrm{d}\mathbf{r}\, \chi^{(2)}(\mathbf{r})\hat{E}^{(+)}_p(\mathbf{r},t)\hat{E}^{(-)}_{s,H}(\mathbf{r},t)\hat{E}^{(-)}_{i,V}(\mathbf{r},t) + \mathrm{h.c.} \\ + \epsilon_0 \int \mathrm{d}\mathbf{r}\, \chi^{(2)}(\mathbf{r})\hat{E}^{(+)}_p(\mathbf{r},t)\hat{E}^{(-)}_{s,V}(\mathbf{r},t)\hat{E}^{(-)}_{i,H}(\mathbf{r},t) + \mathrm{h.c.}\end{aligned} \tag{2.8}$$

2.1.3 The biphoton state

So far we have identified the interacting fields and the nonlinear Hamiltonian, now we derive the output state of the source (a long time after the pump pulse has left the medium) by solving the Schrödinger equation for the nonlinear term $\hat{H}_{\mathrm{NL}}(t)$:

$$i\hbar\frac{\mathrm{d}}{\mathrm{d}t}\left|\Psi(t)\right\rangle = \hat{H}_{\mathrm{NL}}(t)\left|\Psi(t)\right\rangle \tag{2.9}$$

In a low pump regime, with low generation probability per pulse, the output state can be approximated as:

$$\left|\Psi(t)\right\rangle = \left|0\right\rangle - \frac{i}{\hbar}\int_{-\infty}^{t}\hat{H}_{\mathrm{NL}}(t)\,\mathrm{d}t\left|0\right\rangle \tag{2.10}$$

where the initial state is the vacuum ($\left|\Psi(t\to 0)\right\rangle = \left|0\right\rangle$). Here we have applied a first order expansion, neglecting the eventual multiple photon pair events. The output is thus the superposition of the vacuum and a biphoton state, which can be rewritten as:

$$\left|\Psi(t)\right\rangle = \left|0\right\rangle + \beta\left|\psi\right\rangle \tag{2.11}$$

with β the probability amplitude of generating a biphoton state $\left|\psi\right\rangle$.

Since we are interested in the output state after the disappearance of the pump pulse we can extend the time integral of Equation 2.10 to infinity. By plugging in the nonlinear Hamiltonian, Equation 2.8, and restriciting only to one interaction (signal H and idler V) the state becomes:

$$\left|\psi\right\rangle = \frac{\epsilon_0}{i\beta\hbar}\int\mathrm{d}t\int\mathrm{d}\mathbf{r}\chi^{(2)}(\mathbf{r})\hat{E}_p^{(+)}(\mathbf{r},t)\hat{E}_{s,H}^{(-)}(\mathbf{r},t)\hat{E}_{i,V}^{(-)}(\mathbf{r},t)\left|0\right\rangle \tag{2.12}$$

Inserting the definition of the involved states derived above, we find:

$$\begin{aligned}\left|\psi\right\rangle =& \frac{1}{\beta}\frac{\epsilon_0 L}{i2\pi\hbar}\int\mathrm{d}t\iiint\mathrm{d}\omega_p\,\mathrm{d}\omega_s\,\mathrm{d}\omega_i\int\mathrm{d}\mathbf{r}\,\frac{1}{\sqrt{v_g^H(\omega_s)v_g^V(\omega_i)}}\chi^{(2)}(\mathbf{r})\\ &\times E_p(\mathbf{r},\omega_p)E_H(x,y;\omega_s)E_V(x,y;\omega_i)\,e^{-i\Delta kz}e^{i\Delta\omega t}\hat{a}_H^\dagger(\omega_s)\hat{a}_V^\dagger(\omega_i)\left|0\right\rangle\end{aligned} \tag{2.13}$$

where $\Delta\omega = (\omega_s+\omega_i)-\omega_p$ represents the energy difference between the three fields and $\Delta k = k_H(\omega_s) - k_V(\omega_i)$ the wavevector mismatch between the signal and idler fields. Integrating over time yields the energy conservation condition:

$$\int\mathrm{d}t\,e^{i\Delta\omega t} = 2\pi\delta(\Delta\omega) \tag{2.14}$$

which justifies a posteriori the removal of terms from the Hamiltonian that we made. We can now integrate over the pump frequency ω_p, yielding:

$$\boxed{\left|\psi\right\rangle = \iint\mathrm{d}\omega_s\,\mathrm{d}\omega_i\,\phi(\omega_s,\omega_i)\,\hat{\mathrm{a}}_H^\dagger(\omega_s)\hat{\mathrm{a}}_V^\dagger(\omega_i)\left|0\right\rangle} \tag{2.15}$$

with $\phi(\omega_s,\omega_i)$ the Joint Spectral Amplitude (JSA) or biphoton wavefunction:

$$\begin{aligned}\phi(\omega_s,\omega_i) =& \frac{\epsilon_0 L}{i\beta\hbar\sqrt{v_g^H(\omega_s)v_g^V(\omega_i)}}\\ &\times\int\mathrm{d}\mathbf{r}\,\chi^{(2)}E_p(\mathbf{r},\omega_s+\omega_i)\,E_H(x,y,\omega_s)E_V(x,y,\omega_i)e^{-i\Delta kz}\end{aligned} \tag{2.16}$$

As a final remark we want to relate the JSA with the frequency correlations that we experimentally measure. In the calculation we have already extracted the probability β of generation of a pair and thus the normalization of the JSA is simply:

$$\langle\psi|\psi\rangle = \iint \mathrm{d}\omega_s \, \mathrm{d}\omega_i \, |\phi(\omega_s, \omega_i)|^2 = 1 \tag{2.17}$$

Therefore, the squared modulus of the JSA, called Joint Spectral Intensity (JSI), can be viewed as the probability of finding a pair of photons in a given couple of frequencies and for this reason the JSA is usually called biphoton spectral wavefunction.

Treating the photons individually, we can obtain the spectral marginal amplitude for the signal by integrating the JSA $\phi(\omega_s, \omega_i)$ over the idler frequencies:

$$\phi_s(\omega_s) = \frac{1}{\sqrt{2\pi}} \int \mathrm{d}\omega_i \, \phi(\omega_s, \omega_i) \tag{2.18}$$

It can be interpreted as the probability amplitude of detecting a signal photon of frequency ω_s. For the idler photon, $\phi_i(\omega_i)$ is defined analogously.

2.2 Joint Spectral Amplitude characteristics

We now continue our study by making some assumptions and establishing a link between the JSA and the pump beam characteristics.

2.2.1 Phase mismatch

First of all, we analyze the wavevector mismatch term (Δk) of Equation 2.16 and simplify it by making some approximations. We can Taylor expand the refractive indices of the signal and the idler around the degeneracy frequency $\omega_{\mathrm{deg}} = \omega_p/2$ to the second order in $\delta\omega = \dfrac{\omega_s - \omega_i}{2} \equiv \dfrac{\omega_-}{2}$. Doing so the wavevector mismatch becomes:

$$\Delta k = k_{\mathrm{deg}}(\omega_p) + \frac{\omega_-}{\bar{v}_g} + \left(\frac{\omega_-}{2}\right)^2 \delta_{\mathrm{GVD}} \tag{2.19}$$

The first term corresponds to the projection along the z-axis of the wavevector that the pump should have to produce frequency-degenerate photons. It can be written as:

$$k_{\mathrm{deg}}(\omega_p) = \frac{\omega_p}{c} \frac{n_s - n_i}{2} = \frac{\omega_p}{c} \sin\theta_{\mathrm{deg}} \tag{2.20}$$

This term is linked to the birefringence of the device: in order to produce frequency degenerate photons the pump beam must impinge on the waveguide with an angle θ_{deg} different from zero, as we have already commented in Figure 1.14 (see also Equation 1.54). From this formula we see that the opposite interaction (signal V and idler H) will have the opposite degeneracy angle ($-\theta_{\mathrm{deg}}$).

The second term in Equation 2.19 depends on the mean group velocity of the two involved guided modes, defined as:

$$\bar{v}_g^{-1} = \left(\frac{v_g^H + v_g^V}{2}\right)^{-1} = \frac{1}{c}\left[\frac{n_H + n_V}{2} + \frac{\omega_{\mathrm{deg}}}{2} \frac{\mathrm{d}(n_H + n_V)}{\mathrm{d}\omega}\right] \tag{2.21}$$

This term is an important feature of the counter-propagating phase-matching scheme; as we will see in the next section, it connects the pump beam spatial properties to the biphoton spectral correlations.

The last term is controlled by δ_{GVD} which is the difference between the Group-Velocity Dispersions (GVD) of the two guided modes:

$$\begin{aligned}\delta_{\mathrm{GVD}} &= \frac{1}{2}\left(\frac{\mathrm{d}^2 k_H}{\mathrm{d}\omega^2} - \frac{\mathrm{d}^2 k_V}{\mathrm{d}\omega^2}\right) \\ &= \frac{1}{2c}\left[2\frac{\mathrm{d}(n_H + n_V)}{\mathrm{d}\omega} + \omega_{\mathrm{deg}}\frac{\mathrm{d}^2(n_H + n_V)}{\mathrm{d}\omega^2}\right]\end{aligned} \tag{2.22}$$

For our device the GVDs for H (TE) and V (TM) modes are almost equal, see section 1.4, and therefore their difference can be neglected. Neglecting this term the wavevector mismatch becomes:

$$\boxed{\Delta k = \frac{\omega_p}{c}\sin\theta_{\mathrm{deg}} + \frac{\omega_-}{\bar{v}_g}} \tag{2.23}$$

2.2.2 Connection between JSA and pump beam properties

In order to further study the Joint Spectral Amplitude we need to make some assumptions on the pump field $E_p(\mathbf{r}, \omega_p)$. We assume that:

- the pump field propagates only in the (x, z) plane, thus having k_y component equal to zero;
- its transverse spatial profile is separable along the z and y directions,

  $$\phi_p(x, y; \omega_+) = \phi_p(y) \times \phi_p(z, \omega_+) \tag{2.24}$$

  where $\omega_+ = \omega_p = \omega_s + \omega_i$ and with a possible dependence on the pump frequency ω_+ of the z spatial profile.
- the effect of the vertical microcavity on its shape along the x axis and on its spectrum can be decoupled in two terms: $f_{\mu\mathrm{cav}}(x) \times f_{\mu\mathrm{cav}}(\omega_+)$. They represent respectively the effect of the refractive index variation along the x direction and the microcavity filtering effect on the pump beam spectrum.

Therefore, we can write the pump field amplitude as:

$$E_p(\mathbf{r}, \omega_+) = \varepsilon_p^{(0)} f_{\mu\mathrm{cav}}(x) f_{\mu\mathrm{cav}}(\omega_+) f_{\mathrm{spectrum}}(\omega_+) \phi_p(y) \phi_p(z, \omega_+) \tag{2.25}$$

where $f_{\mathrm{spectrum}}(\omega_+)$ describes the spectral amplitude of the field and $\varepsilon_p^{(0)}$ is a normalization constant.

We now introduce an explicit expression of the second order susceptibility coefficient, by taking advantage of the device geometry:

$$\chi^{(2)}(\mathbf{r}) = \chi^{(2)}(x) \times \Pi_W(y) \times \Pi_L(z) \tag{2.26}$$

where $\chi^{(2)}(x)$ is the susceptibility value at a given x position, and the last two terms are rectangular gate functions defined as:

$$\Pi_L(z) = \begin{cases} 1 & \text{if } |z| \leq \dfrac{L}{2} \\ 0 & \text{elsewhere} \end{cases} \tag{2.27}$$

$$\Pi_W(y) = \begin{cases} 1 & \text{if } |y| \leq \dfrac{W}{2} \\ 0 & \text{elsewhere} \end{cases} \tag{2.28}$$

where L and W are respectevely the length and the width of the waveguide.

With all these considerations, the general expression of the JSA (Equation 2.16) becomes:

$$\begin{aligned} \phi(\omega_s, \omega_i) =& \frac{\epsilon_0 L}{i\beta\hbar\sqrt{v_g^H(\omega_s)v_g^V(\omega_i)}} \varepsilon_p^{(0)} f_{\text{spectrum}}(\omega_+) f_{\mu\text{cav}}(\omega_+) \\ & \times \int \mathrm{d}x\, \chi^{(2)}(x) f_{\mu\text{cav}}(x) E_H(x, \omega_s) E_V(x, \omega_i) \\ & \times \int \mathrm{d}y\, \Pi_W(y) \phi_p(y) E_H(y, \omega_s) E_V(y, \omega_i) \\ & \times \int \mathrm{d}z\, \Pi_L(z) \phi_p(z, \omega_+) e^{-i\Delta k z} \end{aligned} \tag{2.29}$$

The first two integrals represent the spatial overlap between the three fields in the waveguide cross-section. The third integral, performed along z, takes into account the phase mismatch Δk between the three fields.

This expression of the JSA (Equation 2.29) can be divided into three different factors :

$$\boxed{\phi(\omega_s, \omega_i) = \chi_\Gamma(\omega_s, \omega_i) \cdot \text{PM}(\omega_s, \omega_i) \cdot \phi_{\text{spectral}}(\omega_s, \omega_i)} \tag{2.30}$$

The first term, χ_Γ, is the overlap integral between the interacting fields and the non linear medium, including all the multiplicative constants:

$$\begin{aligned} \chi_\Gamma(\omega_s, \omega_i) =& \frac{\epsilon_0 L \varepsilon_p^{(0)}}{i\beta\hbar\sqrt{v_g^H(\omega_s)v_g^V(\omega_i)}} \\ & \times \iint \mathrm{d}x\, \mathrm{d}y\, \chi^{(2)}(x) \Pi_W(y) f_{\mu\text{cav}}(x) \phi_p(y) E_H(x, y, \omega_s) E_V(x, y, \omega_i) \end{aligned} \tag{2.31}$$

This term is proportional to the nonlinear overlap integral defined in the previous chapter, Equation 1.37. During the design of the device, this quantity has been optimized in order to maximize the conversion efficiency [134, 152].

The quantum states generated by our device have a Joint Spectral Amplitude which does not exceed a few nanometers in width, remaining in the telecom c-band. For this reason, due to the small GVD of the involved guided modes, we can neglect the frequency dependence of the effective group velocities. Moreover, the profiles of the guided modes can be considered as a constant, for such frequency ranges. Thus, for the analytic discussion, we can consider χ_Γ as frequency-independent and hence the y and x profiles of the pump beam do not affect the JSA. However, it is important to note that, even if χ_Γ does not have a role on the frequency

engineering, it is of paramount importance for the device because it determines its conversion efficiency.

The second term of Equation 2.29, containing the integral along the z direction, describes the phase-matching:

$$\mathrm{PM}(\omega_s, \omega_i) = \int \mathrm{d}z\, \Pi_L(z) \phi_p(z, \omega_+) e^{-ik_{\mathrm{deg}}(\omega_+)z - i\frac{\omega_-}{v_g}z} \tag{2.32}$$

where we have used Equation 2.23 to express the wavevector mismatch Δk. Differently from the previous term, here the pump beam profile, $\phi_p(z, \omega_+)$, influences the frequency dependency of the JSA. In particular, the phase-matching term contains the projection of the pump field wavevector $\mathbf{k}$ along the z axis, thus linking the incidence angle θ to the JSA. This point highlights a very important feature of the counter-propagating phase-matching scheme: tailoring the pump beam profile along z, $\phi_p(z, \omega_+)$, gives a direct and flexible control over the JSA shape, as we will see in details in the second part of this thesis (chapter 5).

Finally, the third term of Equation 2.30 is related to the energy conservation and depends on the frequency spectrum of the pump beam multiplied by the filtering effect of the microcavity:

$$\phi_{\mathrm{spectral}}(\omega_+) = f_{\mathrm{spectrum}}(\omega_+) f_{\mu\mathrm{cav}}(\omega_+) \tag{2.33}$$

The microcavity has a bandwidth of 280 pm and thus it imposes a lower bound of 3 ps to the duration of the pump pulses. Since in this thesis we will always consider longer pulses, we can neglect the microcavity filtering effect on the pump beam spectrum. For a more detailed analysis on this topic refer to [153].

JSA dependency on ω_+ and ω_-

In the previous analysis we have divided the JSA in the product of three terms: χ_Γ, which does not depend on the frequency, and two frequency dependent terms (PM and ϕ_{spectral}). We now move a step further and investigate the JSA dependency from the $\omega_+ = \omega_s + \omega_i$ and $\omega_- = \omega_s - \omega_i$ variables.

First of all, we note that the spectral term ϕ_{spectral} depends only on the pump laser frequency $\omega_p = \omega_+ = \omega_s + \omega_i$ and therefore it is directed along the JSA anti-diagonal (ω_- axis). This direction is constrained by the energy conservation condition and cannot be changed in any way.

On the other hand, the phase-matching term PM is generally a function of both ω_s and ω_i; however, depending on the pump beam properties, specific directions can be chosen. Indeed, in the usual case where there is no frequency dispersion in the angular spectrum (θ is independent from ω_p), the phase-matching term depends only from $\omega_- = \omega_s - \omega_i$ and therefore it is directed along the JSA principal diagonal (ω_+ axis)[1], as we have seen in chapter 1(Figure 1.13). In this case the JSA can be factorized along the ω_+ and ω_- axes:

$$\phi(\omega_s, \omega_i) = \chi_\Gamma\, \mathrm{PM}(\omega_-)\, \phi_{\mathrm{spectral}}(\omega_+) \tag{2.34}$$

[1]This is strictly true only if we consider a monochromatic pump beam. However, as we will see in section 5.2, in our case experimental case (picosecond pulsed pump beam) this approximation is valid up to a precision <1%.

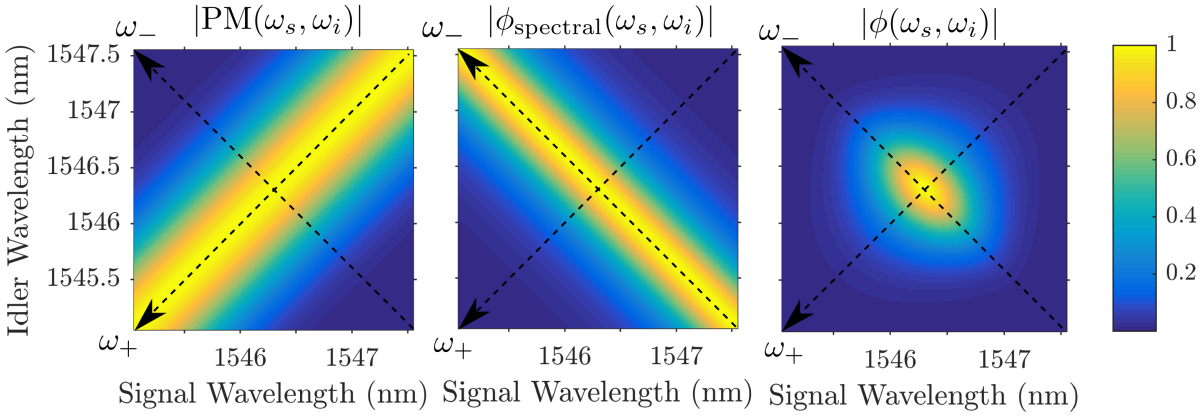

Figure 2.2: Example of JSA separable along the ω_- and ω_+ axes. From left to right: norm of the phase-matching $|\mathrm{PM}(\omega_s,\omega_i)|$, of the spectral function $|\phi_{\mathrm{spectral}}(\omega_s,\omega_i)|$ and of the resulting JSA $|\phi(\omega_s,\omega_i)|$. Simulation parameters: $L = 1.9$ mm, $w_z = 0.3$ mm, $\tau_p = 4.5$ ps and $R_H = R_V = 0$.

Figure 2.2 is an example of this situation. It reports numerical simulations of the norm of the phase-matching, spectral function and resulting JSA[2].

Conversely, if a dispersive element (e.g. a prism) is introduced in the pump beam, the incidence angle is frequency-dependent (in general $\mathbf{k_p} \cdot \hat{\mathbf{u}}_z = f(\omega_p)\omega_p/c$) and thus the phase-matching term rotates in the (ω_s,ω_i) plane [164]. In this manuscript we will analyze only biphoton states that are separable along the ω_+ and ω_- axes and thus we do not detail further this case.

In the remaining part of this chapter we continue our study of the JSA by analyzing its general properties, i.e. without giving an explicit expression of the pump beam.

2.2.3 Frequency correlations and Schmidt decomposition

A biphoton state can be classified by its frequency-time properties, more in particular by its frequency correlations. We will here analyze the JSA in a qualitative way, identifying different types of correlations, and then we will introduce the Schmidt decomposition to quantify the amount of spectral correlations.

First of all we define the notion of spectral correlation. A photon pair is spectrally correlated when its JSA cannot be written as the product of the single-photon spectra, i.e. $\phi(\omega_s,\omega_i) \neq \phi_s(\omega_s)\phi_i(\omega_i)$. Depending on the shape of the JSA we can then identify:

- *frequency anti-correlated states*: in this case the two photons of the pair have negatively correlated frequencies and the JSA is directed along the anti-diagonal, i.e. the ω_- direction, as in Figure 2.3a;

- *frequency correlated states*: in this case the two photons of the pair have positively correlated frequencies and the JSA is oriented along the principal

[2]In all the JSA/JSI plots of this thesis we employ the normalization $\max(|\phi(\omega_s,\omega_i)|)=1$ instead of $\iint \mathrm{d}\omega_s\,\mathrm{d}\omega_i\,|\phi(\omega_s,\omega_i)|^2 = 1$, for a better visualization.

diagonal, i.e. the ω_+ direction, as in Figure 2.3b;

- *frequency-separable states*: in this case the signal and idler photons are not spectrally correlated and their JSA is simply given by the product of their spectra, as in Figure 2.3c;

In order to give a more quantitative analysis of the frequency correlations of a biphoton state, we now introduce the Schmidt decomposition of the JSA [166], which consist in finding two complete sets of orthonormal functions $\{u_m(\omega)\}$, $\{v_m(\omega)\}$ such that the JSA $\phi(\omega_s, \omega_i)$ may be written:

$$\phi(\omega_s, \omega_i) = \sum_m \sqrt{\lambda_m} u_m(\omega_s) v_m(\omega_i) \tag{2.35}$$

where λ_m, $u_m(\omega)$ and $v_m(\omega)$ satisfy the integral eigenvalue equations:

$$\begin{aligned} \iint \mathrm{d}\omega' \mathrm{d}\omega_2 \, \phi(\omega, \omega_2) \, \phi^*(\omega', \omega_2) \, u_m(\omega') &= \lambda_m u_m(\omega) \\ \iint \mathrm{d}\omega' \mathrm{d}\omega_1 \, \phi(\omega_1, \omega) \, \phi^*(\omega_1, \omega') \, v_m(\omega') &= \lambda_m v_m(\omega) \end{aligned} \tag{2.36}$$

The expansion parameters λ_m are real and positive and obey the normalization condition $\sum_m \lambda_m = 1$. The existence of the Schmidt decomposition has been demonstrated for a large class of systems under very general assumptions [167].

The Schmidt functions $u_m(\omega)$ and $v_m(\omega)$ can be thought of as building blocks of entanglement. Indeed, if the signal photon is projected into the function u_n, the idler photon is known with certainty to be described by the corresponding function v_n. The probability of finding the photon pair in this specific pair of modes is given by λ_n.

The level of spectral entanglement can be quantified by the cooperativity parameter, or Schmidt number K, defined as:

$$K = \frac{1}{\sum_m \lambda_m^2} \tag{2.37}$$

The value of K gives the effective numbers of separable modes needed to perform the decomposition. A biphoton state with $K = 1$ represents a state with only a pair of Schmidt modes and therefore it is separable, exhibiting no spectral entanglement.

In Figure 2.3 we reports the numerically calculated Schmidt number K for each case described above (frequency correlated, anti-correlated and separable JSA). It is worth noting that the Schmidt number quantifies the level of frequency entanglement, but it cannot identify the type of frequency correlation (positive or negative).

2.2.4 Joint Temporal Amplitude

In order to further study the properties of the biphoton state, we now introduce the Joint Temporal Amplitude (JTA) $\tilde{\phi}(t_s, t_i)$, which gives the joint probability amplitude of detecting the photons of the pair at times t_s and t_i. Since the JSA has a narrow bandwidth, we can safely define the JTA as its Fourier Transform:

$$\tilde{\phi}(t_s, t_i) = \frac{1}{2\pi} \iint \mathrm{d}\omega_s \mathrm{d}\omega_i \, \phi(\omega_s, \omega_i) e^{-i\omega_s t_s} e^{-i\omega_i t_i} \tag{2.38}$$

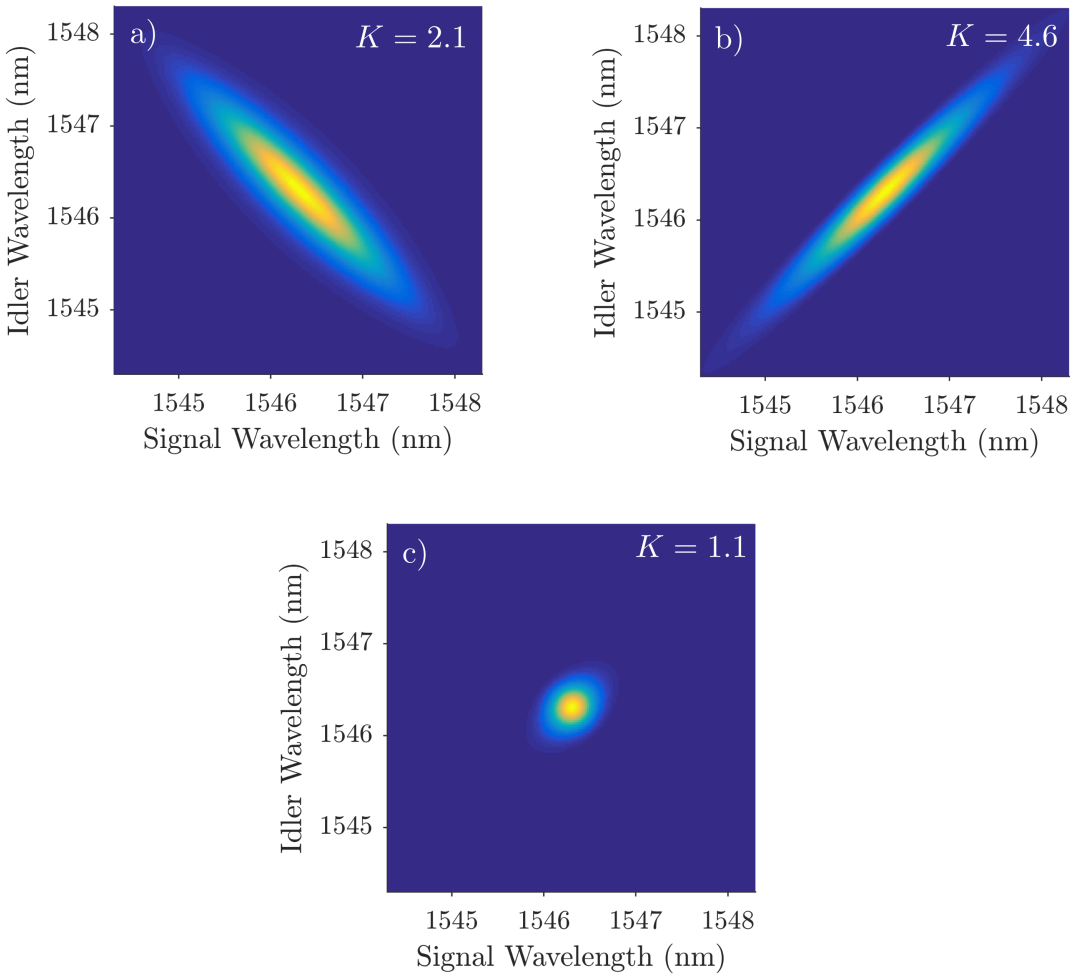

Figure 2.3: Norm of the JSA $|\phi(\omega_s, \omega_i)|$ of an anti-correlated (a), a correlated (b) and a separable (c) frequency state, with the corresponding Schmidt number K, which quantifies the amount of frequency entanglement. Simulation parameters: $L = 1.9$ mm, $R_H = R_V = 0$. (a) $w_z = 0.1$ mm and $\tau_p = 4.5$ ps; (b) $w_z = 1$ mm and $\tau_p = 1$ ps; (c) $w_z = 0.6$ mm and $\tau_p = 4.5$ ps.

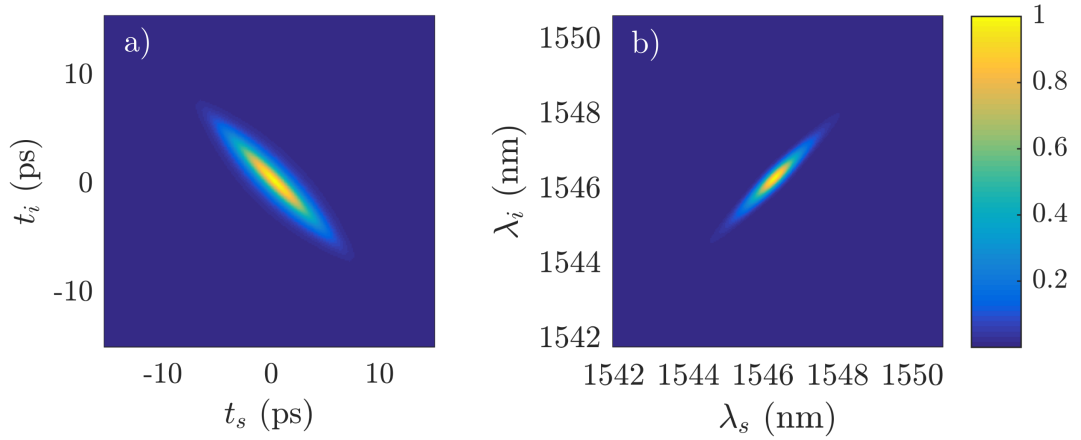

Figure 2.4: (a) Norm of the JTA and (b) norm of the JSA of a frequency correlated state. The JTA shows temporal anti-correlation. Simulation parameters: $L = 4$ mm, $R_H = R_V = 0$, $w_z = 1$ mm and $\tau_p = 2$ ps.

where we have applied the definition of the Fourier-transformed operator $\hat{a}^\dagger(t)$ [165]:

$$\hat{a}^\dagger(\omega) = \frac{1}{\sqrt{2\pi}} \int \mathrm{d}t\, \hat{a}^\dagger(t) e^{-i\omega t} \tag{2.39}$$

The squared modulus of the JTA, called Joint Temporal Intensity JTI, gives the joint probability of detecting the photons at times t_s and t_i.

Similarly to the JSA, it is possible to define the temporal amplitude of the photons taken individually by integrating the JTA over the time variable of the other photon:

$$\tilde{\phi}_s(t_s) = \frac{1}{\sqrt{2\pi}} \int \mathrm{d}t_i\, \tilde{\phi}(t_s, t_i) \tag{2.40}$$

$\tilde{\phi}_s(t_s)$ gives the probability amplitude of measuring a signal photon at the time t_s, and analogously for the idler photon.

Figure 2.4 reports the norm of the JSA and of the JTA for a frequency correlated state. The JTA shows temporal anti-correlation, due to the Fourier Transform. Conversely, a frequency anti-correlated state would display temporal correlation.

From the knowledge of both the JTI and the JSI, it is possible to determine whether or not the biphoton state is entangled in energy-time by measuring their standard deviations along the diagonal $\omega_s + \omega_i$ and $t_s - t_i$ directions. Indeed, two classical pulses or two separable photons must satisfy the following relation:

$$\Delta(\omega_s + \omega_i)\, \Delta(t_s - t_i) \geq 1 \tag{2.41}$$

while, for energy-time entangled photons, this inequality can be violated and can reach 0 [168].

2.2.5 Fabry-Pérot cavity effect on the JSA

As we have seen in the previous chapter, in particular in section 1.4, the refractive index contrast between the waveguide ($n \approx 3$) and the air ($n = 1$) induces a modal

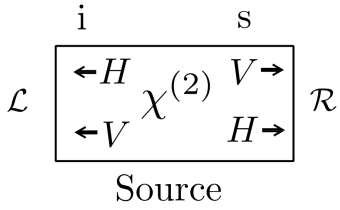

Figure 2.5: Symbolic sketch of the source ($\chi^{(2)}$ medium) placed in a cavity. Both SPDC interactions are represented, we call signal s and idler i the photons inside the cavity and right $\mathcal{R}$ and left $\mathcal{L}$ the photons outside the cavity.

reflectivity of the waveguide facets. The 3D numerical simulations that we have performed for a 5µm-wide ridge waveguide yield a modal reflectivity of $R_H = 28.5\%$ for the horizontally polarized fundamental mode (TE) and $R_V = 24.7\%$ for the vertically polarized fundamental mode (TM), at 1550 nm. As a result, the two facets create a Fabry-Pérot cavity for the signal and idler fields, which has a non negligible influence on the JSA of the generated biphoton state, as we shall see.

Jeronimo-Moreno et al. [169] studied the SPDC pair generation process in a nonlinear Fabry-Pérot cavity. The authors demonstrated that, if the source remains in the spontaneous regime, i.e. the generated photons do not stimulate the emission of new photons, the effect of the cavity reduces to the multiplication of the original JSA by the Fabry-Pérot transfer functions. G. Boucher applied this approach to the counter-propagating source and here we report only the final results; for the complete calculation refer to his PhD thesis [153].

Let us consider a photon pair generated in the center (along the z axis) of the source; the transmission ($f_{t,\sigma}(\omega)$) and reflection ($f_{r,\sigma}(\omega)$) cavity functions can be written:

$$\begin{aligned} f_{t,\sigma}(\omega) &= \frac{\sqrt{1-R_\sigma}\ \exp\left(i\frac{\omega n L}{2c}\right)}{1-R_\sigma\ \exp\left(i\frac{2\omega n L}{c}\right)} \\ f_{r,\sigma}(\omega) &= \frac{\sqrt{R_\sigma(1-R_\sigma)}\ \exp\left(i\frac{3\omega n L}{2c}\right)}{1-R_\sigma\ \exp\left(i\frac{2\omega n L}{c}\right)} \end{aligned} \tag{2.42}$$

for a modal reflectivity R_σ and a mode polarization σ (H or V). These are the usual Fabry-Pérot functions, up to a half-length propagation phase factor (given by the photon propagation from the center to the facets, which corresponds to a distance $L/2$).

Each waveguide facet can be modeled as a frequency-dependent beamsplitter, where photons can either be reflected or transmitted [170]. Referring to Figure 2.5 we call signal s and idler i the photons inside the cavity, while we call right $\mathcal{R}$ and left $\mathcal{L}$ the photons exiting the cavity respectively from the right and left side. It is important to note that, due to the cavity, a signal photon may now exit from the left side and vice-versa. Using this notation the transformations for the $\hat{a}$ and $\hat{a}^\dagger$

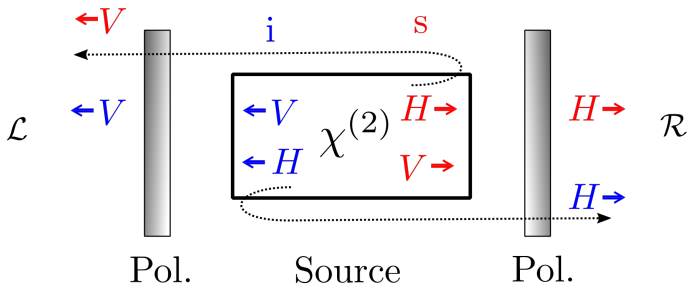

Figure 2.6: Interaction selection with polarizers. Here the polarizers (Pol.) are set to select the HV interaction (signal H-polarized and idler v-polarized). However, they do not suppress the reflections: a H-polarized idler photon that is reflected by the cavity is then transmitted by the polarizer, and vice versa for the V-polarized signal photon. Therefore to completely suppress one interaction both frequency filters and polarizers are required.

operators become:

$$\begin{aligned}\hat{a}^{\dagger}_{s,\sigma}(\omega) &\rightarrow f_{t,\sigma}(\omega)\hat{a}^{\dagger}_{\mathcal{R},\sigma}(\omega) + f_{r,\sigma}(\omega)\hat{a}^{\dagger}_{\mathcal{L},\sigma}(\omega)\\ \hat{a}^{\dagger}_{i,\sigma}(\omega) &\rightarrow f_{t,\sigma}(\omega)\hat{a}^{\dagger}_{\mathcal{L},\sigma}(\omega) + f_{r,\sigma}(\omega)\hat{a}^{\dagger}_{\mathcal{R},\sigma}(\omega)\end{aligned} \tag{2.43}$$

We will employ the above transformations in chapter 7 in order to demonstrate the generation of hybrid polarization/frequency entanglement. For the moment we consider a simpler case, to understand how the cavity effect modifies the JSA. By using both polarizers and frequency filters on each side of the cavity we select only the HV interaction. Note that polarizers are not sufficient to select one interaction and completely suppress the other one. Indeed, for example, an idler H photon, emitted by the unwanted VH interaction, can be reflected from the left side and then transmitted from the right one and therefore it contribute to the events of the HV interaction, unless a frequency filter is used in conjunction with the polarizers, as illustrated in Figure 2.6.

Using such conjunction of filters and polarizers, the photons are forced to exit only from one side, eventually after multiple round-trips, therefore we can continue to call signal the photon propagating to the right and idler the one propagating to the left. As a consequence Equation 2.43 reduces to:

$$\begin{aligned}\hat{a}^{\dagger}_{s,H}(\omega) &\rightarrow f_{t,H}(\omega)\hat{a}^{\dagger}_{s,H}(\omega)\\ \hat{a}^{\dagger}_{i,V}(\omega) &\rightarrow f_{t,V}(\omega)\hat{a}^{\dagger}_{i,V}(\omega)\end{aligned} \tag{2.44}$$

Consequently, the JSA of the biphoton state emitted by the source, considering the reflecting facets and selecting only the HV interaction, becomes:

$$\boxed{\phi_{FP}(\omega_s,\omega_i) = f_{t,H}(\omega_s) f_{t,V}(\omega_i)\phi(\omega_s,\omega_i)} \tag{2.45}$$

which corresponds to the original JSA multiplied by the Fabry-Pérot function of the infrared modes. The JSA of the VH interaction has an analogous expression.

Figure 2.7 reports numerical simulations of the JSA norm for a source without cavity effect (Figure 2.7a) and for a source having $R_H = 28.5\%$ and $R_V = 24.7\%$

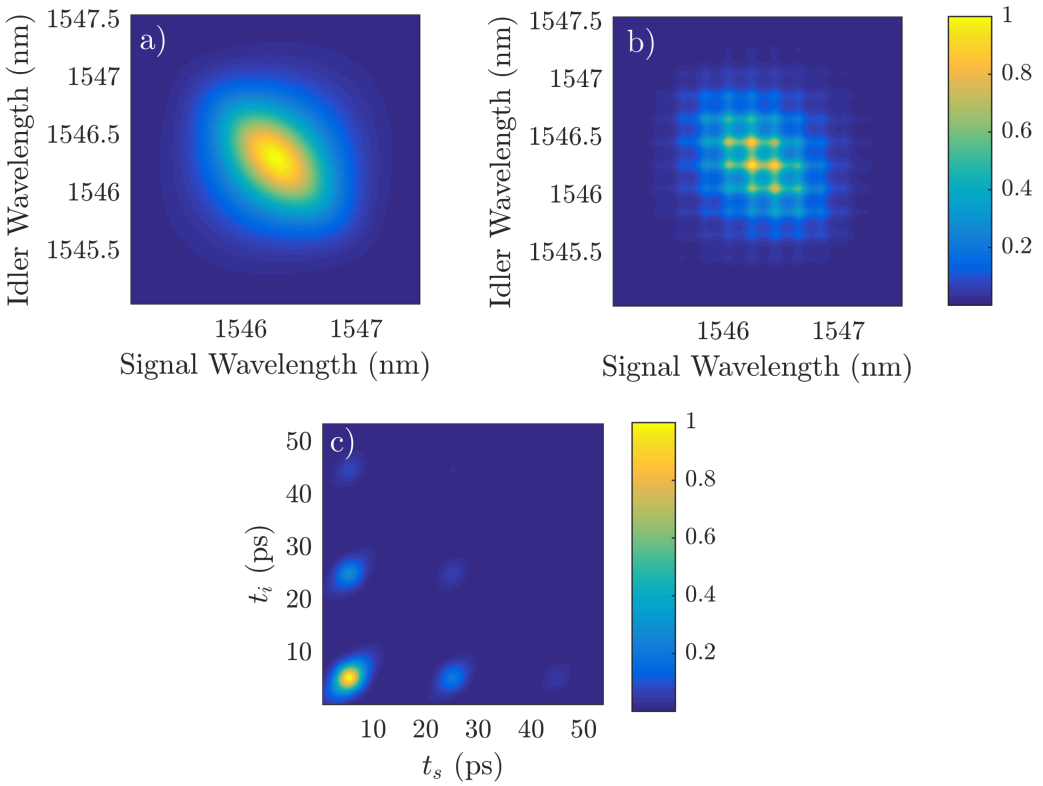

Figure 2.7: Numerically simulated norm of the JSA: (a) for a 1.9 mm-long sample without cavity effect and (b) for facets reflectivity $R_H = 28.5\%$ and $R_V = 24.7\%$. (c) Norm of the JTA corresponding to the state reported in (b). Simulation parameters: $w_z = 0.3$ mm and $\tau_p = 4.5$ ps, $L = 1.9$ mm.

(Figure 2.7b). The cavity effect introduces a chessboard modulation of the JSA, with a spacing between the Fabry-Pérot peaks of approximately 180 pm, for our 1.9 mm-long waveguide.

In Figure 2.7c we show the norm of the JTA for the state reported in Figure 2.7b. The cavity introduces several additional peaks along the signal and idler temporal axes. The most intense peak (in the bottom left) corresponds to the case in which both photons are directly transmitted, while the secondary peaks correspond to a given number of complete round-trips of the photons, where the round-trip period is $\tau_{\mathrm{FP}} = 2L/v_g \approx 41$ ps for the considered sample.

2.3 Chronocyclic Wigner Function

So far we have analyzed the biphoton state by means of its JSA and JTA, which are both complex functions and therefore of difficult visualization. Indeed, their phase distribution can be very rich and contain critical features for the characterization of frequency entanglement. This information is lost if we only examine the JSI or the JTI. An easier and more direct method is to employ the Wigner function, which is real valued and, thanks to its nature, is naturally suited to describe pulsed SPDC processes.

The concept of quasi-probability Wigner function has been borrowed by the ultrafast optics community to describe the characteristics of ultrashort pulses with a real function, in the time-frequency phase space [171]. In this context, the function is called Chronocyclic Wigner Function (CWF) and the usual $\hat{X}$ and $\hat{P}$ operators are replaced by the time t and the frequency ω, its conjugate variable.

The CWF has then been applied to fully describe the frequency-time properties of a biphoton state by Grice and Walmsley [172]. Even if the CWF was originally meant for single photons, the authors extended the definition to describe both signal and idler photons. The Joint Chronocyclic Wigner Function, which from now on for simplicity we will call CWF, is thus a four-dimensional real function that depends on the frequencies ω_s, ω_i and on the detection times t_s, t_i of the signal and idler photons. The CWF can be retrieved from the state density operator $\hat{\rho}$ [173]:

$$W(\omega_s, t_s, \omega_i, t_i) = \frac{1}{2\pi} \iint \mathrm{d}\omega'_s \mathrm{d}\omega'_i \, e^{-i(\omega'_s t_s + \omega'_i t_i)} \times \left\langle \omega_s + \frac{\omega'_s}{2}, \omega_i + \frac{\omega'_i}{2} \middle| \, \hat{\rho} \, \middle| \omega_s - \frac{\omega'_s}{2}, \omega_i - \frac{\omega'_i}{2} \right\rangle \tag{2.46}$$

In the case of a pure state $\rho = |\psi\rangle\langle\psi|$, the CWF can be expressed as a function of the JSA $\phi(\omega_s, \omega_i)$:

$$W(\omega_s, t_s, \omega_i, t_i) = \frac{1}{2\pi} \iint \mathrm{d}\omega'_s \mathrm{d}\omega'_i \, e^{-i(\omega'_s t_s + \omega'_i t_i)} \times \phi\left(\omega_s + \frac{\omega'_s}{2}, \omega_i + \frac{\omega'_i}{2}\right) \phi^*\left(\omega_s - \frac{\omega'_s}{2}, \omega_i - \frac{\omega'_i}{2}\right) \tag{2.47}$$

Despite the complexity of four dimensions that makes this function less intuitive than the JSA or the JTA, the CWF has a number of useful properties. First of all, the JSI and the JTI are obtained by integrating $W(\omega_s, t_s, \omega_i, t_i)$ over the conjugate variables; e.g. for the signal photon, this reads respectively:

$$\begin{aligned} |\phi(\omega_s, \omega_i)|^2 &= \frac{1}{2\pi} \iint \mathrm{d}t_s \mathrm{d}t_i \, W(\omega_s, t_s, \omega_i, t_i) \\ |\tilde{\phi}(t_s, t_i)|^2 &= \frac{1}{2\pi} \iint \mathrm{d}\omega_s \mathrm{d}\omega_i \, W(\omega_s, t_s, \omega_i, t_i) \end{aligned} \tag{2.48}$$

Moreover, the Chronocyclic Wigner Function for the individual photons are given by the marginal of the Joint Chronocyclic Wigner Function, obtained by integrating over the conjugate time and frequency variables, e.g. for the signal photon this reads:

$$W_s(\omega_s, t_s) = \frac{1}{2\pi} \int \mathrm{d}\omega_i \int \mathrm{d}t_i W(\omega_s, t_s, \omega_i, t_i) \tag{2.49}$$

Finally, the single-photon spectra or temporal profiles are retrieved by integrating the single-photon CWF W_s over the conjugate variables:

$$\begin{aligned} I_s(\omega_s) &= \frac{1}{\sqrt{2\pi}} \int \mathrm{d}t_s \, W_s(\omega_s, t_s) \\ I_s(t_s) &= \frac{1}{\sqrt{2\pi}} \int \mathrm{d}\omega_s \, W_s(\omega_s, t_s) \end{aligned} \tag{2.50}$$

and analogously for the idler photon.

In conclusion, the four-dimensional Chronocyclic Wigner function is a real-valued function that fully describes the frequency-time properties of a biphoton state, from which it is possible to retrieve all the properties of the individual photons and their joint functions (JSI and JTI).

2.3.1 Separable Chronocyclic Wigner Function

We now consider a JSA separable in ω_+ and ω_-, as naturally obtained when pumping the source with a beam having no frequency dependency of the angular spectrum (i.e. θ is independent from ω_+, we refer to subsection 2.2.2). In this way the CWF can be further simplified and split into two terms: one depending on ω_+ and one on ω_-.

Indeed, a JSA separable in ω_+ and ω_- can be written as follows (see Equation 2.34):

$$\phi(\omega_s, \omega_i) = \chi_\Gamma \, \mathrm{PM}(\omega_-) \, \phi_{\mathrm{spectral}}(\omega_+) \tag{2.51}$$

From this the CWF can be factorized as:

$$W(\omega_s, t_s, \omega_i, t_i) = |\chi_\Gamma|^2 \, W_+(\omega_+, t_+) \, W_-(\omega_-, t_-) \tag{2.52}$$

with $\omega_\pm = \omega_s \pm \omega_i$ and $t_\pm = \dfrac{t_s \pm t_i}{2}$. The two-dimensional CWFs read:

$$\begin{aligned} W_+(\omega_+, t_+) &= \frac{1}{\sqrt{2\pi}} \int \mathrm{d}\omega'_+ \, \phi_{\mathrm{spectral}}(\omega_+ + \frac{\omega'_+}{2}) \, \phi^*_{\mathrm{spectral}}(\omega_+ - \frac{\omega'_+}{2}) \, e^{-i\omega'_+ t_+} \\ W_-(\omega_-, t_-) &= \frac{1}{\sqrt{2\pi}} \int \mathrm{d}\omega'_- \, \mathrm{PM}(\omega_- + \frac{\omega'_-}{2}) \, \mathrm{PM}^*(\omega_- - \frac{\omega'_-}{2}) \, e^{-i\omega'_- t_-} \end{aligned} \tag{2.53}$$

where the first one $W_+(\omega_+, t_+)$ is governed by the pump spectrum (energy conservation), while the second one $W_-(\omega_-, t_-)$ is governed by the phase-matching function.

Figure 2.8 reports numerically simulated W_+ and W_- functions for the frequency anti-correlated (first row) and separable state (second row), corresponding to the ones whose JSA have been plotted in Figure 2.3a and Figure 2.3c. The two different states have been obtained by modifying only the phase-matching function and leaving unchanged the spectral function. Consistently, we observe that W_+ is the same for both cases states while W_- changes.

Thanks to the separability of the JSA in ω_+ and ω_-, which is a very common situation, we have simplified the CWF into the product of two bi-dimensional real-valued functions, which are considerably easier to visualize compared to the complex-valued JSA or JTA. This justifies the use of the CWF to analyze the frequency-time properties of biphoton states.

In this thesis we will focus mainly on $W_-(\omega_-, t_-)$, which is governed only by the phase-matching function, the main tool we will use to engineer the frequency correlations of the biphoton state.

During this analysis, since we have considered Gaussian states, the Chronocyclic Wigner function always assumed positive values. However, in a more broad

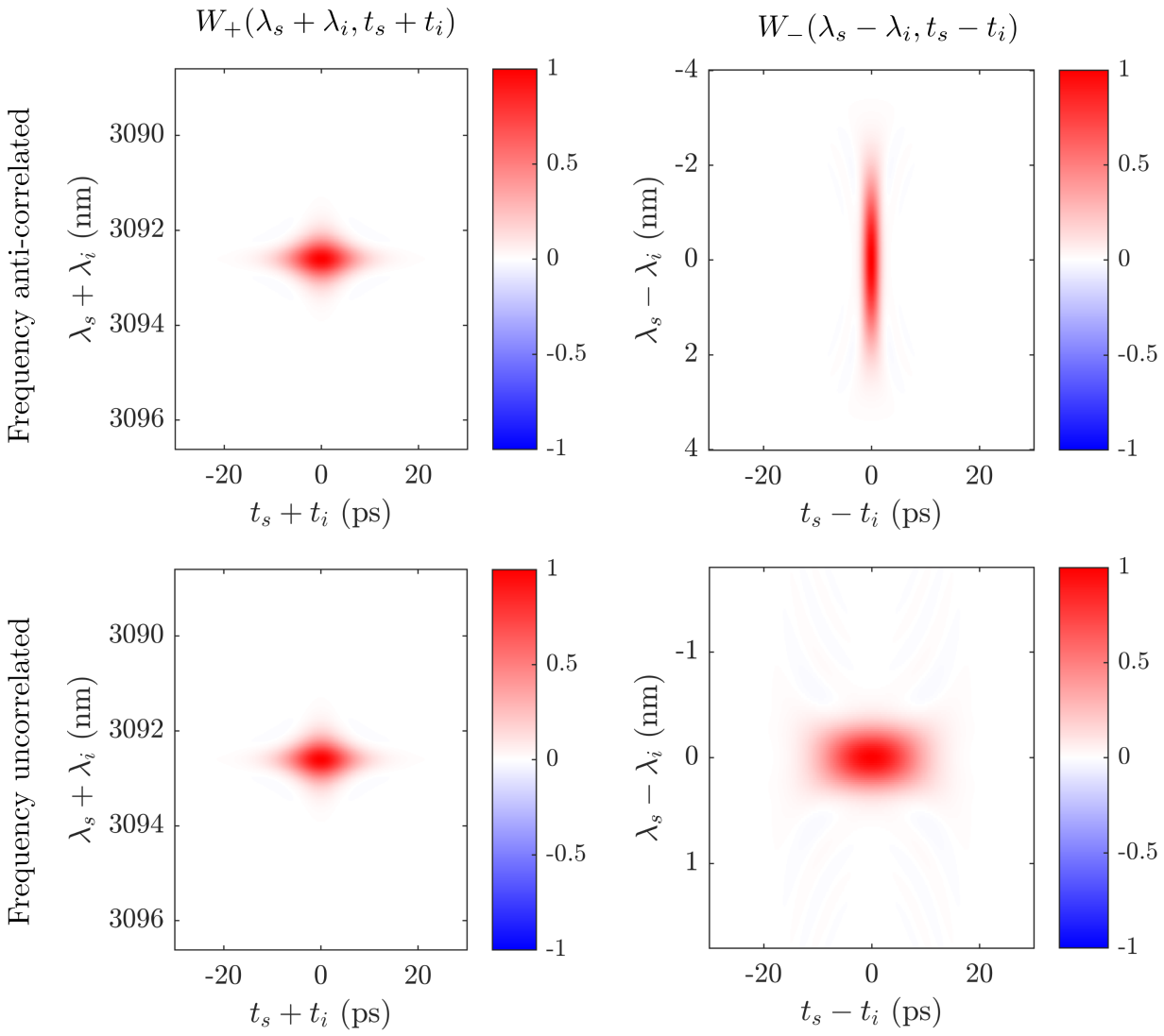

Figure 2.8: Numerically simulated W_+ (left side) and W_- (right side) chronocyclic Wigner functions for a frequency anti-correlated state (first row, corresponding to Figure 2.3a) and a frequency uncorrelated state (second row, corresponding to Figure 2.3c). To pass from the first case to the second we have changed only the phase-matching and not the spectral function, thus W_+ is the same for both cases. Simulation parameters: $L = 1.9$ mm, $R_H = R_V = 0$. First row: $w_z = 0.1$ mm and $\tau_p = 4.5$ ps; second row $w_z = 0.6$ mm and $\tau_p = 4.5$ ps. The Wigner functions are plotted normalized to 1.

perspective, the generation of non-Gaussian states, featuring negative Wigner functions, is a subject of growing interest. Indeed, quantum states with non-Gaussian statics are fundamental bricks for the realization of quantum information protocols in the continuous variable regime (e.g. in the quadrature phase space [174] or in the position-momentum phase space [175]). In analogy, in this work we will study the generation of non-Gaussian states in the frequency-time phase space, featuring a negative Chronocyclic Wigner Function.

2.4 Conclusions

In this chapter we have given a theoretical description of the biphoton state emitted by a SPDC source in a counter-propagating scheme. The state is fully characterized by its Joint Spectral Amplitude (JSA), a complex-valued function giving the joint probability amplitude of detecting the photons with frequency ω_s and ω_i.

We have shown that the JSA can be factorized into two frequency dependent terms: the energy conservation and the phase-matching terms. In particular, since the latter directly depends on the pump beam spatial profile along the z axis, it allows a direct and flexible control over the JSA shape. In the next part of this thesis we will exploit this property to engineer the frequency correlations by tailoring the pump beam profile (chapter 3) and measuring the resulting squared modulus of the JSA (chapter 4 and chapter 5).

We have then analyzed the general characteristics of the JSA by detailing the different types of frequency states (frequency correlated, anti-correlated and separable), and we have quantified the level of frequency entanglement via the Schmidt decomposition.

Finally we have introduced alternative descriptions of the biphoton state. The Joint Temporal Amplitude (JTA), derived by performing a Fourier Transform of the JSA, allows to visualize the state in the temporal domain. On the other hand, the Chronocyclic Wigner Function (CWF) of a biphoton state is a four-dimensional real valued function showing both the temporal and spectral characteristics of the state. Interestingly, when the JSA is separable in the ω_+ and ω_- axes, the CWF can be simplified into the product of two real-valued bi-dimensional functions, which can be easier to visualize than the JSA or JTA.

Part II

Frequency-time correlations engineering

Chapter 3

Pump Beam Shaping Techniques

In the first part of this manuscript we have studied the process of photon pair generation through SPCD in nonlinear ridge waveguides. In particular, for a nonlinear source based on the counter-propagating phase-matching scheme under transverse pumping, we have detailed the peculiar connection between the pump beam spatial profile and the frequency correlations of the photon pairs, represented by the joint spectral amplitude (JSA). This property permits to flexibly control the biphoton spectrum by shaping the pump beam spatial profile.

Tailoring a laser beam transverse profile, in both intensity and phase, is a challenging task and can require an accurate level of control at the micrometer scale. Nevertheless, different systems have been developed to achieve this goal, in particular digital micromirror devices (DMDs) [176] and spatial light modulators (SLMs) [177]. Both devices feature a fundamental characteristic: they are re-configurable, allowing a dynamic and versatile shaping of a light beam. Their usages are various: atom trapping [178], wavefront correction [179], super-resolution microscopy [180], holography [181] and many others.

The firsts, DMDs, are an evolution of deformable mirrors and, thanks to millions of tiny switchable mirrors, enable to locally shape an incident beam by choosing which mirrors to tilt and which not. Even if the device acts only on the beam intensity, algorithms have been proposed to effectively gain full control over the amplitude and the phase of the beam. For instance, Goorden et al. [182] proposed a superpixels approach in which adjacent pixels are merged to obtain only one "superpixel", which can modulate independently phase and amplitude. DMDs

have two important advantages compared to SLMs: they can display static images and they are spectrally broadband.

On the other hand, SLMs consist of an array of pixels, each of which can locally modify the amplitude or the phase of a light beam. Therefore, by employing diffraction effects, it is possible to shape the beam wavefront. SLMs can be divided into amplitude-only and phase-only modulators, the first acting only on the amplitude and the second only on the phase. In the recent years, the latter have become the principal solution to generate complex phase patterns: for example tailoring Laguerre-Gaussian beams [183] or frequency pulse shaping (after a frequency to space mapping using a dispersive element)[184]. Compared to DMDs, SLMs have a far bigger dynamic range, indeed each pixel can be addressed with a grey scale modulation and not only with a binary modulation; but they suffer from flickering at a frequency of hundreds of Hertz caused by their digital addressing, which makes them unable to display a true static image [185]. In our case, since we are interested in time-integrated measurements of tens of seconds, this problem is not relevant.

In this chapter we present the experimental setup for beam shaping that will be used in chapter 5 and chapter 6 to control the joint spectrum and wavefunction symmetry of photon pairs. Its core blocks are a phase-only modulator and a wavefront analyzer. The first section is dedicated to the setup and its characterization. Then we present the employed modulation technique, which allows to shape the intensity or the phase of a beam, but not both simultaneously. At the end of the chapter we introduce a more complex technique to achieve a simultaneous modulation and we comment on its implementation in our experimental situation.

3.1 Experimental setup

Our experimental setup for beam shaping is illustrated in Figure 3.1; it is composed of a phase-only SLM in a 4f configuration and a wavefront analyzer. The source laser beam is produced by a Ti:sapphire laser (Coherent Mira) pulsed at 76 MHz repetition rate with 6 ps pulse duration, with a central wavelength of 775 nm. In this section we describe in detail the SLM and the wavefront analyzer, while in the next section we focus on the employed shaping technique.

3.1.1 The spatial light modulator

The spatial light modulator we use is a Leto from the company HoloEye (Figure 3.2a), a reflective phase-only modulator. We have chosen this SLM for its excellent resolution of 1920x1080 pixels of size 6.4 µm x 6.4 µm and a modulation depth of 256 grey levels (8 bit addressing); it provides a minimum phase shift of 2π in the range 400-850 nm. The device is fabricated with the LCOS technology (Liquid-Crystals-on-Silicon): each pixel is a liquid crystal whose orientation can be modified by applying a voltage. Rotating the liquid crystal locally modifies the birefringence of the pixel medium and thus the phase shift locally experienced by the reflected beam. The SLM is connected to a computer from which we control the phase pattern encoded on it: these "phase masks" are encoded in 256 grey

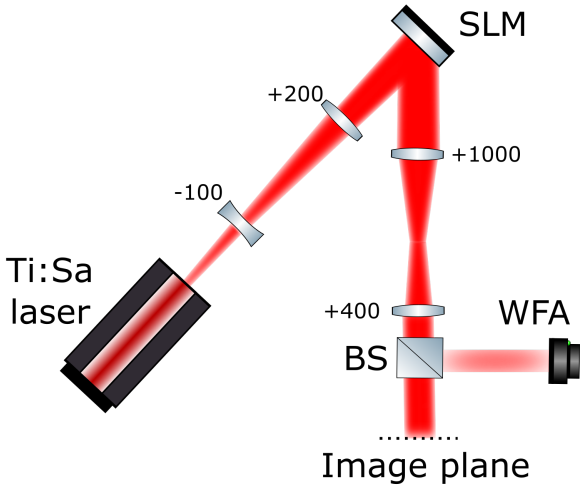

Figure 3.1: Experimental setup for shaping the pump beam transverse profile. A first telescope enlarges the beam to match the SLM screen dimension, while a second one shrinks the reflected beam to match the sample width. A wavefront analyzer (WFA), placed after a 99:1 beamsplitter (BS), constantly monitors the beam. Focal lengths are given in millimeters

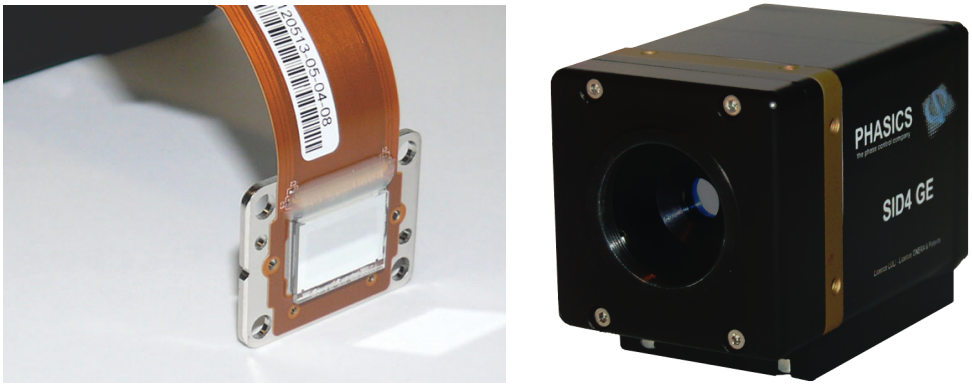

(a) **(b)**

Figure 3.2: (a) Holoeye Leto spatial light modulator and (b) Phasics SID4 wavefront analyzer

.

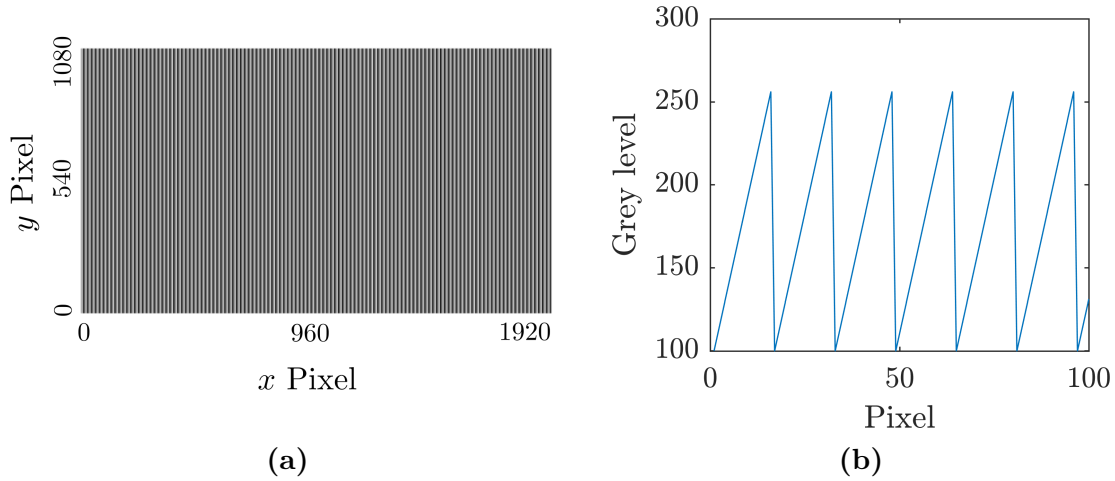

Figure 3.3: (a) 16 level blazed grating phase mask and (b) close-up of the corresponding modulation along the x axis.

levels and generated using a Matlab script.

Before characterizing the device, let us first describe the behavior of a beam when it reflects on a largely used type of phase masks: the blazed grating, as illustrated in Figure 3.3. This phase mask is composed of stripes, and in each stripe pixels linearly increase from 0 to 256 grey level. As a result the beam acquires the same phase modulation, and when it passes through a converging lens, which performs the Fourier Transform (FT) of its spatial profile in its focal plane, a diffraction peak is formed. The lateral position of this peak, with respect to non-diffracted one (zero order), depends on the spatial periodicity of the phase imposed by the SLM. We can think of this peak as the (in theory unique) spatial frequency component of the reflected beam. For example, if we add two blazed grating modulations with different periods, having therefore two different spatial frequencies, the diffracted beam would display two distinct peaks, one for each frequency. This diffraction effect is a core component of the SLM working principle and we will employ it different times: first in the device characterization and then in the beam shaping technique.

Prior to the device calibration we characterize its properties: the reflectivity and the total diffraction efficiency at two different wavelengths (663 nm, where device specifications are given and 775 nm, our working wavelength). Table 3.1 reports the experimental results. The first parameter, the reflectivity, is simply given by the ratio between the incident power of a beam and the reflected one; it mainly depends on the reflectivity of the aluminum mirror placed behind the pixel grid, inside the device. From the experimental values we note that the reflectivity falls by 15% from a wavelength of 663 nm to 775 nm. This issue is mainly due to a drop of the aluminum reflectivity and it cannot be circumvented.

The total diffraction efficiency is given by the composed effect of the reflectivity and the diffraction efficiency. It is experimentally evaluated by applying a 16-level blazed grating phase mask to the SLM and using a converging lens to focus the diffracted beam. From the ratio between the incident power and the diffracted one

	Wavelength	Reflectivity	Diffraction Efficiency	Total Efficiency
Specifications	633 nm	75%	85%	64%
Experimental Results	633 nm	73%	79%	57%
	775 nm	58%	79%	46%

Table 3.1: SLM characteristics, measured at 633 nm and 775 nm.

we obtain the total diffraction efficiency, which is 57% at 663 nm (a bit lower than the specification) and 46% at our working wavelength of 775 nm. By dividing the total efficiency by the reflectivity we can also access the diffraction efficiency itself. The values, reported in Table 3.1, show that the diffraction efficiency is the same for both wavelengths, while, the reflectivity being lower at 775 nm, we obtain a decrease of the total efficiency.

Calibration

The device works properly when the maximum grey level (255) induces a 2π phase shift, compared to the 0 grey level. The phase shift induced by the birefringent pixels depends on the wavelength of the incident beam and therefore the SLM must use a different calibration for each wavelength. We have thus calibrated the device for our working wavelength (775 nm), as follows.

First of all, we measure the induced phase shift as a function of the applied grey level. Then, we determine the voltage needed to induce a 2π phase shift and finally, if the phase shift is not linear as a function of the grey level, we modify the LookUpTable (LUT): this is the numerical table containing the one to one relation between each grey level and the voltage applied to the liquid crystals.

In order to evaluate the relative phase shift between two different grey levels, we build a Mach-Zender interforemeter (see Figure 3.4): the input beam is divided in two parts and each of them is sent to a half of the SLM panel. Then, the two beams are recombined in a microscope objective and interference fringes are observed with a camera. By modifying the phase of one beam (by changing the pixel value) while keeping the other fixed, the shift of the spatial fringes allows to retrieve the relative phase shift between the two addressed grey levels.

Figure 3.5 illustrates this calibration procedure and reports the results: each row of the figure is a step. First of all, we apply a linear LUT and measure the induced phase shift for each grey level from the interference fringes (left to right in the figure). The maximum phase shift we obtain is only 1.5π and thus we modify the applied voltages to the liquid crystals. The second row shows the phase shift measurement after this voltage correction: now the phase shift reaches 2π, but it shows a nonlinear dependency from the grey level. Therefore, as illustrated in the third row, by modifying the LUT we obtain a linear phase shift. This correct LUT is retrieved by inverting the measured phase as a function of the grey level of the previous step.

With this procedure we have calibrated the spatial light modulator, in order to induce a complete 2π phase shift at our working wavelength of 775 nm. This

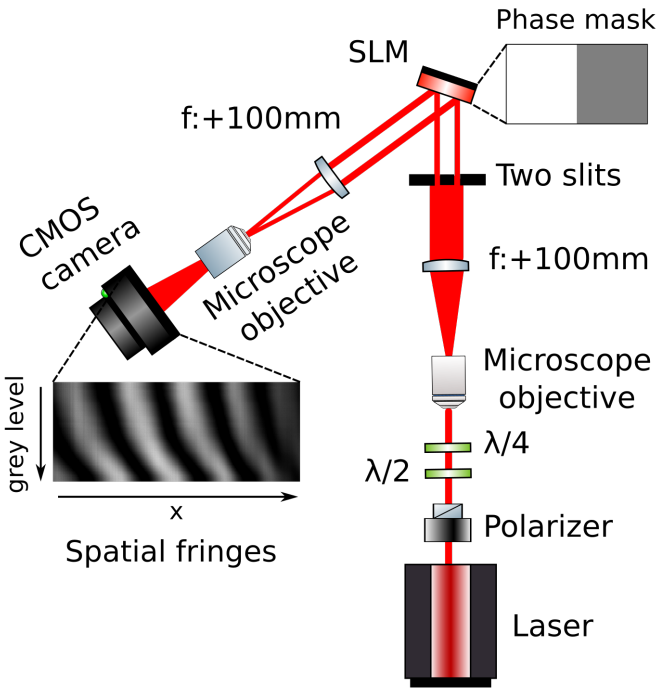

Figure 3.4: Experimental setup to calibrate the SLM. It is based on a Mach-Zender interferometer: the two beams impinge on the two halves of the SLM where two different grey level are addressed. By varying one of the two grey levels, the spatial interference fringes measured by the camera move and from their shift we evaluate the relative phase shift between the two addressed grey levels.

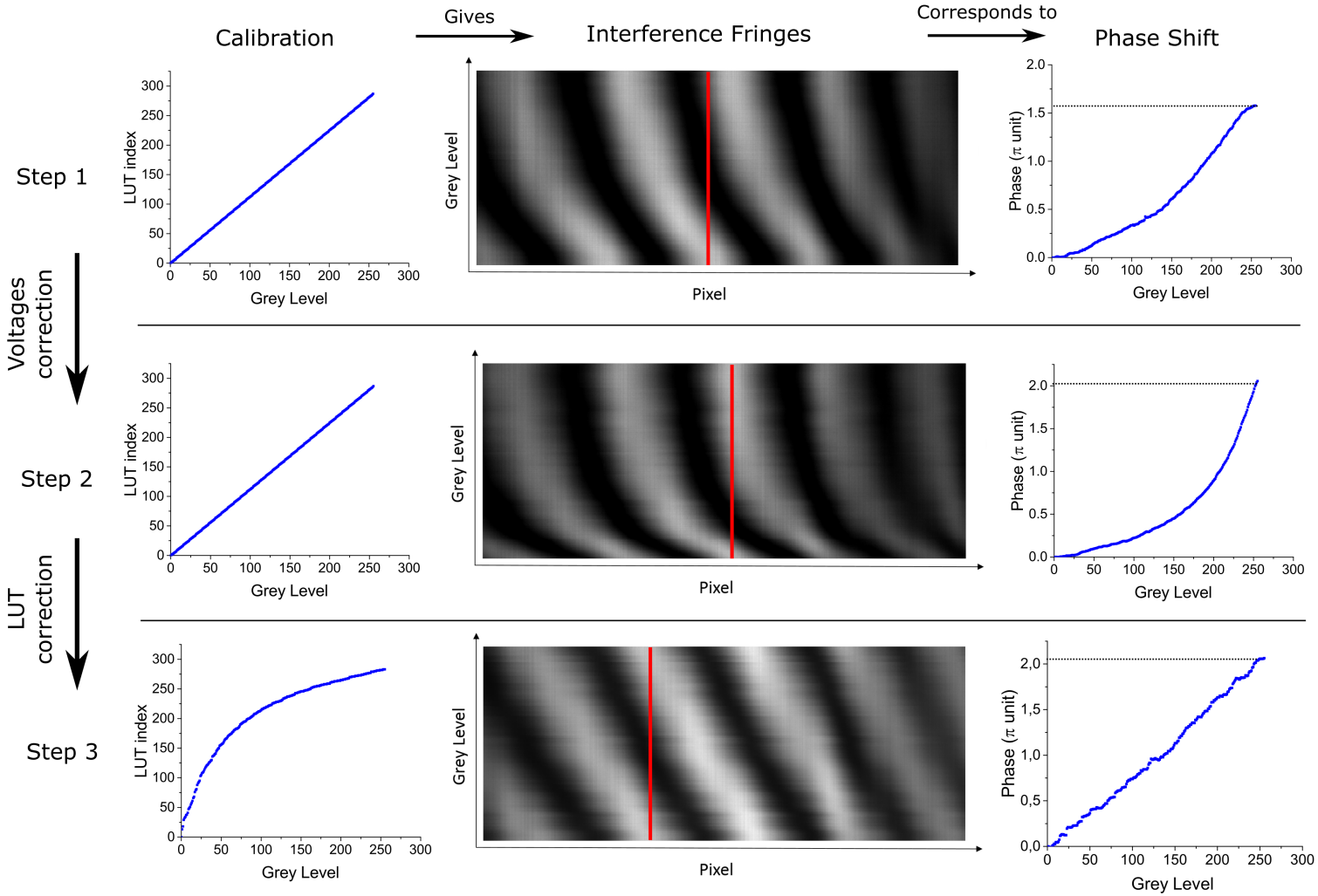

Figure 3.5: SLM calibration steps (working wavelength 775 nm). In the first column we report the used LUT file which generates the interference fringes shown in the second column. From the latter we evaluate the induced phase shift for each grey level (third column). The red line in the pictures highlight the range of the phase shift: a 2π phase shift is obtained when the interference fringes shift of one period. The three rows illustrate the steps of the calibration procedure, see text for the description.

characteristic is of fundamental importance in order to employ beam shaping algorithms.

3.1.2 The wavefront analyzer

So far we have described the spatial light modulator, but in order to ensure that the device works properly and that the chosen shaping technique performs correctly, we need to employ a wavefront analyzer.

A wavefront analyzer is a device capable of measuring, at the same time, the spatial profile of both the intensity and phase of a beam. In principle, this measurement could be done using a reference field and detecting the interference fringes with a camera. However, the necessity of having a phase stabilization between the signal and the reference makes this technique challenging and time consuming. For this reason, reference-free methods have been developed, in particular the Shack-Hartmann wave-front sensor, which employs arrays of micro-lenses to image the wavefront deformation [186].

For our scope, we have chosen the SID4 wavefront analyzer of the company Phasics (Figure 3.2b) for its excellent spatial resolution of 30 µm and high sampling 160 x 120 pixels map. The instrument relies on a development of the Shack-Hartmann wavefront analyzer with an improved spatial resolution. It employs spatial interferometry to measure the phase: an hexagonal diffraction grating is placed before a CCD sensor and each hole produces four replicas of the impinging beam that interfere with the neighboring ones; the resulting interferogram is detected by the camera and analyzed by a software, retrieving both intensity and phase profiles. In particular the phase is derived from the interference fringes deformation; this technique is called *"Multiple- wave shearing interferometry"* [187].

The main limitation of this device is the impossibility to measure the relative phase between two non-adjacent regions. In other words, if the beam is composed of two distinct halves, separated by a zero-intensity area, their relative phase cannot be measured. Indeed, the instrument measures the phase gradients among adjacent pixels and from them it reconstructs the phase profile. In a zero-intensity area, the phase is not defined and it is not possible to apply the reconstruction algorithm. Therefore, the phase of the two regions is properly measured, but their relative phase is not. In subsection 3.2.2 we will see how this issue influences our phase shaping technique and how it can be circumvented.

3.2 Intensity or phase shaping technique

We now describe the experimental procedure that we have employed in this work to shape either the amplitude or phase of the pump beam, in order to control the biphoton spectrum.

The technique relies on the optical setup sketched in Figure 3.1: the laser beam is enlarged by a first telescope (f:-100 mm and f:+200 mm) and impinges on the SLM. After the reflection, a second telescope (f:+1000 mm and f:+400 mm) reduces the beam dimension to match the waveguide width ($\approx$ 2 mm). This second telescope, placed in a 4f configuration, images the SLM on the sample and

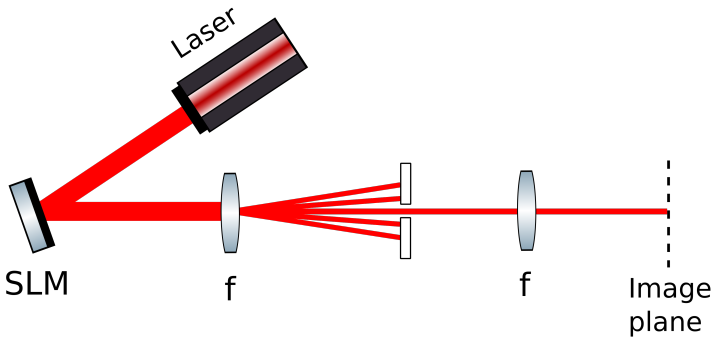

Figure 3.6: Sketch of the setup used to perform intensity or phase shaping. The second lens of the 4f system is aligned only with the zero-order peak. The diffraction angles have been emphasized.

realizes, in the focal plane of the first lens, the Fourier Transform (FT) of the beam reflected by the SLM. This point is of fundamental importance because, when a blazed grating is applied, the FT creates diffraction peaks, spatially separated. The second lens of the telescope is aligned only with the zero-order peak, discarding all the others, as depicted in Figure 3.6.

3.2.1 Intensity shaping

The setup presented in Figure 3.6 can be used to shape a beam in intensity. Indeed, since the first-order diffraction peak is not aligned with the second lens of the telescope, it is sufficient to apply a blazed grating to the region of the beam that we want to remove.

We now describe the steps to generate a phase mask to obtain a Gaussian beam with waist dimension w:

- a 16-level blazed grating is generated for the whole phase mask;
- the target waist dimension w is divided by the magnification of the 4f system to calculate the waist dimension at the SLM position. In our case the magnification is 0.4, thus the waist on the SLM has to be 2.5 times bigger.
- the physical dimension of the waist is converted in pixels of the SLM (1920 x 1080 pixels for a screen of 12.5 mm x 7.1 mm) and a Gaussian beam profile is calculated.
- the Gaussian profile is subtracted from the blazed grating and the final phase mask is converted to a bmp image in grey levels from 0 to 255.

This simple procedure allows to obtain a shaped beam fairly in agreement with the target one. The intensity, indeed, is correctly modulated but the phase suffers from the optical aberrations of the setup.

The first column of Figure 3.7 reports the shaping process to generate a Gaussian beam with 1 mm waist: a phase mask (a), calculated with the previously described procedure, is applied to the SLM and the intensity (b) and phase (c) of

the shaped beam are measured on the 4f system image plane with the wavefront analyzer. The resulting intensity profile is almost a Gaussian distribution, with the target waist of 1 mm (as shown in Figure 3.8a). On the other hand, the phase is not flat as it should be but features optical aberrations, in particular vertical astigmatism. Phase aberrations are generally due to misalignment of the optical system or to low quality optical components. However, the SLM is perfectly suited to solve this problem: by subtracting from the phase mask the opposite of the measured phase, the aberrations are compensated and a flat phase is obtained. The second column of Figure 3.7 details the results after this phase aberration correction: when the corrected phase mask (d) is applied, the intensity (e) is not modified while the phase (f) becomes flat.

In order to experimentally validate this technique we generate Gaussian beams with different waist dimensions. Figure 3.8 shows the results (intensity in blue, phase in red), for the following values: 1 mm (a), 0.8 mm (b), 0.5 mm (c), 0.3 mm (d). In all cases the intensity is almost Gaussian with the target waist and the phase is flat, with fluctuations of the order of 0.1π only.

As a last remark, let us mention some limitations of the technique. The most evident one is the not perfect diffraction efficiency of the SLM, which prevents part of the reflected light to be modulated. This means that a portion of the reflected light, which should be shifted in the first order and eliminated from the beam, stays in the zero order and pollutes the intensity profile. In addition, it is possible to calculate that, if a Gaussian profile is subtracted from the phase mask, the shaped beam in the zero order is not perfectly Gaussian [188], as we shall see in the next section. Nevertheless, the results presented in this paragraph entirely satisfy our experimental needs and thus we have employed this technique to shape the pump beam.

3.2.2 Phase shaping

The setup presented in Figure 3.6 can also be employed to shape the beam in phase, without modifying the optical components. Indeed, by applying a phase mask that does not contain periodic modulation (no blazed grating), the phase pattern is directly encoded in the beam, which remains in the zero diffraction order.

Let us start by generating a Gaussian beam with a phase profile featuring a single or double phase step. The most natural phase masks that can be employed are composed of two or three regions of a constant value of grey level; the phase step is then induced by the grey level difference between adjacent regions. However this approach has an important drawback. Indeed, an abrupt phase step causes a phase discontinuity point with zero intensity, thus splitting the intensity in two regions and preventing the wavefront analyzer to measure the relative phase step (as we have commented in the description of the device).

For this reason, we decide to employ a linear phase step instead of an abrupt one. In other words, rather than applying an abrupt step between two different grey levels, we design a phase mask in which the step is completed in 30 pixels, with a linear slope. Figure 3.9a and Figure 3.9c display the two phase masks, one for a single π phase step and the second a double π phase step; the inset in the

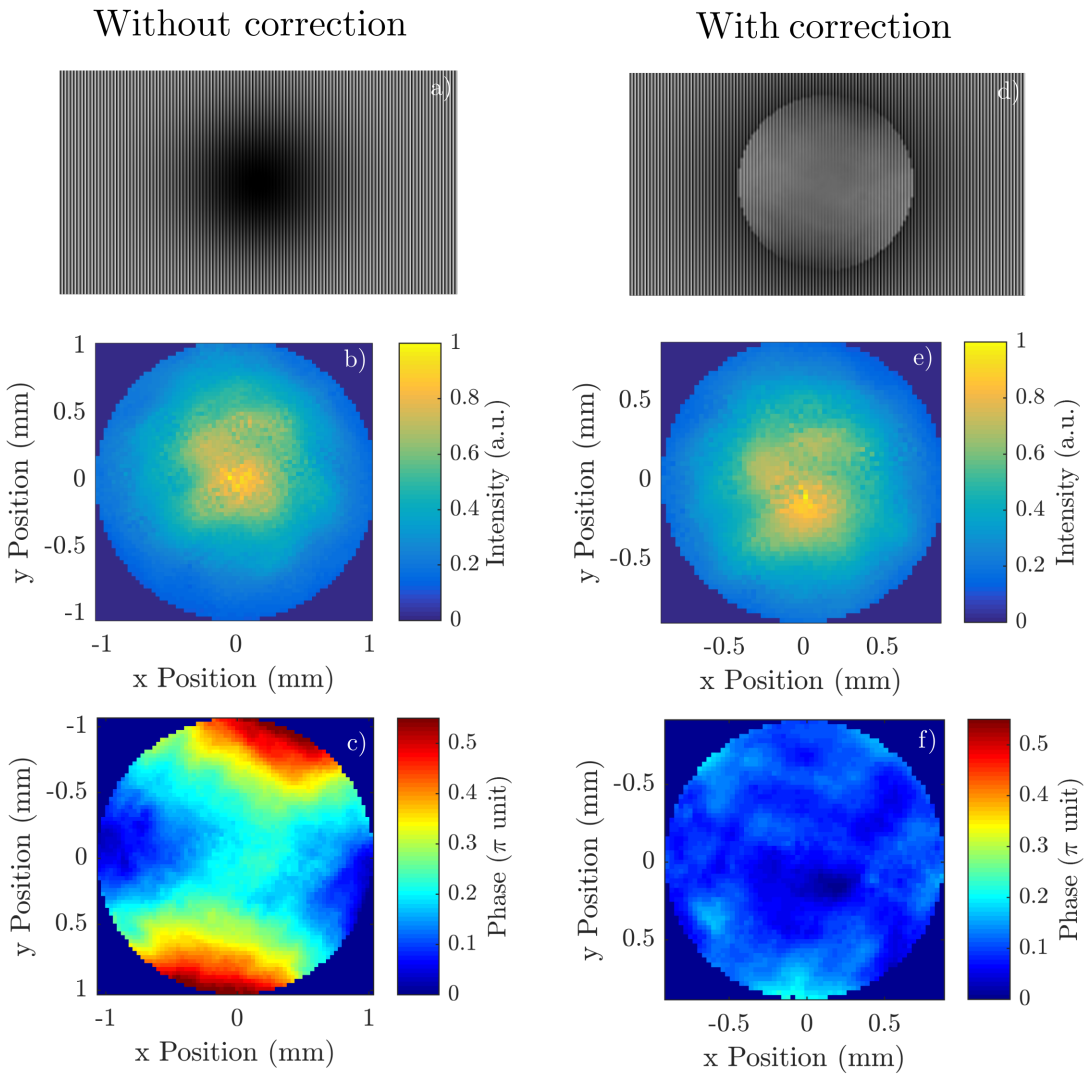

Figure 3.7: Intensity shaping procedure: a 1 mm-waist beam is obtained using a blazed grating and optical aberration correction. Initially a blazed grating is addressed to the SML (a) and the resulting intensity (b) and phase (c) profiles of the reflected beam are measured. Note that, while the intensity is almost Gaussian the phase shows a 0.5 π astigmatism. Then, the phase mask is modified (d) in order to obtain the same intensity profile (e) but with a flat phase (f).

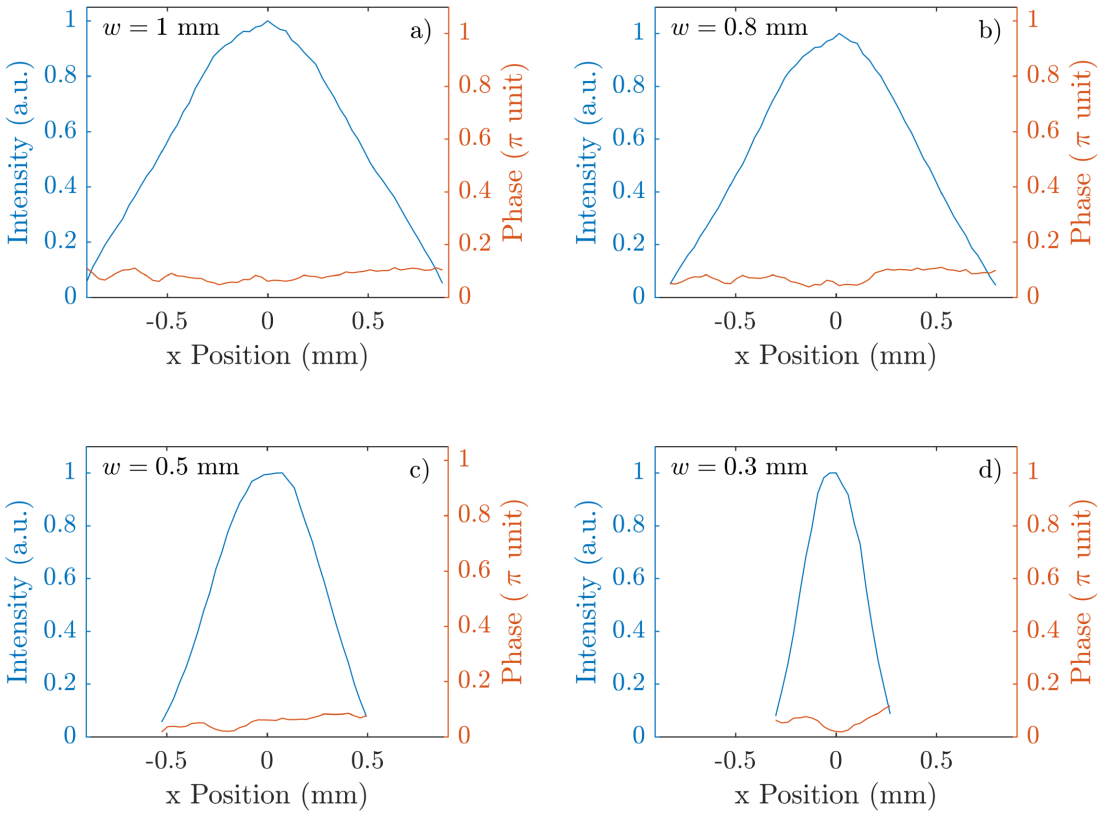

Figure 3.8: Examples of experimental shaping of the beam intensity: from (a) to (d) horizontal central sections of four Gaussian beams (intensity in blue, phase in red) with different waists (respectively 1 mm, 0.8 mm, 0.5 mm and 0.3 mm).

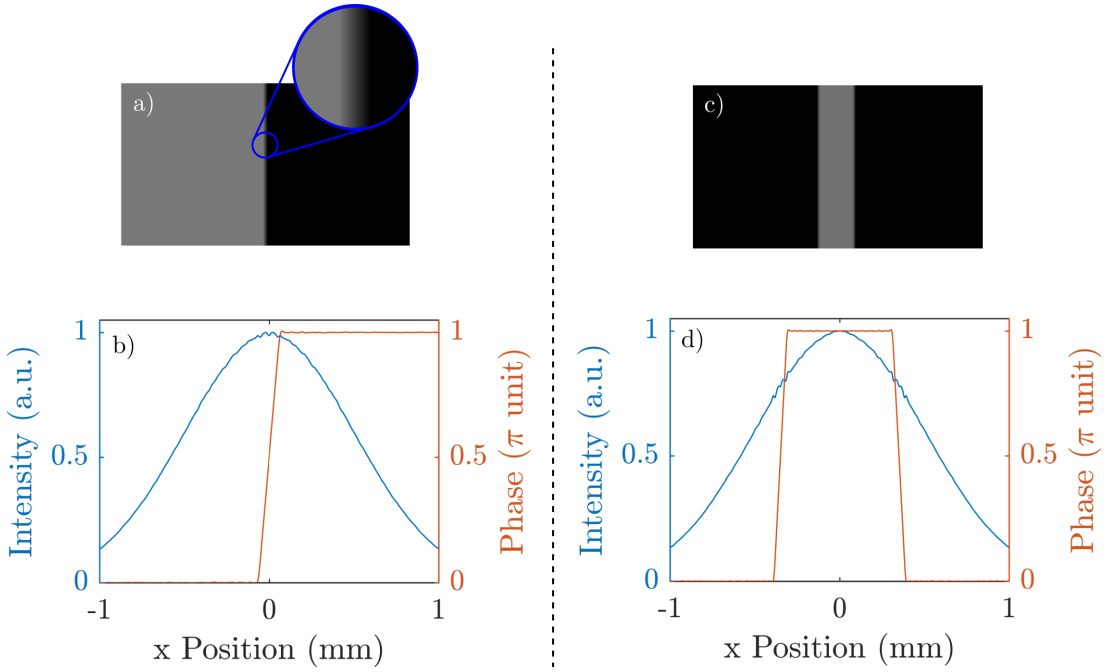

Figure 3.9: Phase masks used to generate a Gaussian beam featuring a single (a) and a double phase (c) step profile; (b) and (d) corresponding simulated intensity and phase at the sample position.

first figure shows the linear variation of the phase step.

Before experimentally generating the beam, we numerically check the behavior of these phase masks. The simulations are performed by taking a Gaussian beam as input and adding the phase mask. Then we calculate the effect of the 4f system by applying two successive Fourier Transform, one for each lens, obtaining the field on its image plane (where the sample will be placed later, see to Figure 3.6). Figure 3.9b and Figure 3.9d report the resulting simulated intensity and phase for both a single and a double phase step profile. We note that the phase is well encoded; the intensities undergo very slight fluctuations, in the positions where the phase shift have been added, but the profiles are Gaussian up to an excellent approximation.

We now proceed to the experimental shaping of the laser beam with the single and the double phase step. Figure 3.10 reports the measurements performed with the wavefront analyzer: on the left column the case of a single phase step and on the right column the case of a double phase step. For each case two phase shift values are reported: π (first row) and $\pi/2$ (second row). In both cases the beam intensity is still Gaussian and the phase has acquired the desired phase step. However, when a single phase step is applied (Figure 3.10a and Figure 3.10b) the phase displays a linear gradient superimposed to the phase step. Fortunately, this is not a problem for the engineering of the biphoton spectrum. Indeed, in the counter-propagating phase-matching scheme, a linear phase gradient of the pump beam corresponds to a tilt of the pump beam incidence angle and therefore it can be simply corrected by implementing the opposite tilt.

So far, we have generated and measured a circular Gaussian beam with 1 mm

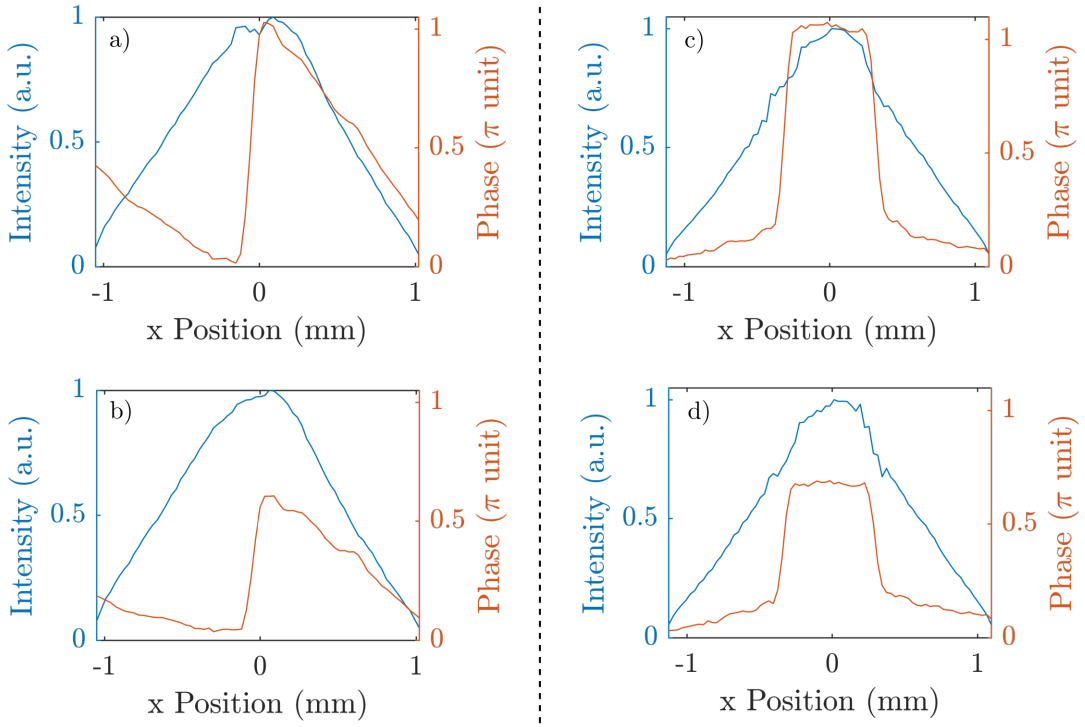

Figure 3.10: Experimentally measured phase and intensity profiles for a 1.1 mm-waist Gaussian beam modulated with a single phase step (first column) and a double phase step (second column): in (a) and (c) a phase shift of π is applied, while in (c) and (d) a phase shift of π/2 is applied.

waist in both transverse directions, but, to actually use the beam to pump the nonlinear waveguide source, it has to be focused in the vertical direction to match the ridge width (5 µm). This can be done by employing a cylindrical lens and we have verified that the focusing does not alter the phase profile along the horizontal direction.

In conclusion, we have demonstrated that this shaping technique allows to generate Gaussian beams with arbitrary waist or to encode phase steps, but not to do both simultaneously. However, it satisfies entirely our experimental needs and it has thus been be employed to control the joint spectrum and wavefunction symmetry of photon pairs, as we will detail in chapter 5 and chapter 6.

3.3 Simultaneous shaping of intensity and phase

Until now we have dealt with the task of shaping either the intensity or the phase of a laser beam. Now we move a step further and introduce a technique allowing to shape both intensity and phase simultaneously that could be implemented in our optical setup in the future if more complex beam profiles are required.

Generating an arbitrary beam requires an accurate engineering over both amplitude and phase, but no existing device enables a direct simultaneous control of both. Combining a phase-only SLM and an amplitude-only SLM is a possible solution [189, 190], but alternative and more complex techniques exist allowing to modulate both properties with a single pass phase-only SLM [188, 191–193].

Clark et al. [177] compared and tested several of these methods, both numerically and experimentally, by generating different types of beams likely to be used in applications: fundamental Gaussian, Laguerre-Gaussian modes, ring lattices and photographic images. However, only the intensity of the resulting fields have been measured and not the phase, thus this study does not exactly compare with our experimental needs.

3.3.1 Analytic formula

Here we follow the proposal of Bolduc et al. [188] which provides the analytic exact solution to the problem. The method connects the target beam (intensity and phase) to the phase mask addressed on the SLM.

We start by writing the SLM phase-only transmission function as:

$$T(m,n) = e^{i\phi(m,n)} \tag{3.1}$$

where $\phi(m,n)$ is the phase mask distribution as a function of SLM pixel position (m,n). For simplicity, we consider the incident beam on the SLM as a plane wave (flat intensity and flat phase). After the reflection, a converging lens focuses the diffracted field, which can be calculated, in the lens focal plane, by taking the Fourier Transform (FT) of the SLM phase mask, since the input beam is a plane wave.

To understand the shaping procedure we first consider the simple case of a

blazed grating of period Λ along the m coordinate:

$$T(m) = \exp\left(i \,\mathrm{Mod}(\frac{2\pi m M}{\Lambda}, 2\pi)\right) \tag{3.2}$$

where $\mathrm{Mod}(x, 2\pi)$ stands for modulo 2π of x.

The parameter M (with $0 \leq M \leq 1$) defines the extent of the phase shift over each grating period. For $M = 1$ we have a normal blazed grating, otherwise the phase maximum value is less than 2π. This periodic function can be expanded in a Fourier series as:

$$T(m) = \sum_{k=-\infty}^{\infty} T_k \exp\left(ik\frac{2\pi m}{\Lambda}\right) \tag{3.3}$$

where the coefficients T_k are given by

$$T_k = \exp[i\pi(M-k)]\frac{\sin[\pi(M-k)]}{\pi(M-k)} \tag{3.4}$$

The diffracted field can be calculated by taking the FT of Equation 3.3:

$$t(x) = \sum_{k=-\infty}^{\infty} T_k \,\delta(x - \frac{k}{\Lambda}) \tag{3.5}$$

where $x = \dfrac{m}{\Lambda f}$ and f is the focal length of the lens. Thus, the diffraction pattern consists of a series of delta functions whose amplitudes are given by Equation 3.4. For $M = 1$ we recover the blazed grating diffraction pattern.

After this preliminary example, let us now consider a more general phase function:

$$T(m,n) = \exp\left(iM(m,n)\,\mathrm{Mod}\Big[\phi(m,n) + \frac{2\pi m}{\Lambda}, 2\pi\Big]\right) \tag{3.6}$$

Here $M(m,n)$ is a normalized amplitude function ($0 \leq M \leq 1$), while the second part has two terms: a generic one $\phi(m,n)$ and a blazed grating $\dfrac{2\pi m}{\Lambda}$. This expression can be expanded in a mixed Fourier-Taylor series, as reported in Ref. [192]:

$$T(m,n) = \sum_{k=-\infty}^{\infty} T_k(m,n) \exp\left(ik\phi(m,n) + ik\frac{2\pi m}{\Lambda}\right) \tag{3.7}$$

The coefficients $T_k(m,n)$ are given by:

$$T_k = \exp\{i\pi[M(m,n)-k]\}\frac{\sin\{\pi[M(m,n)-k]\}}{\pi[M(m,n)-k]} \tag{3.8}$$

To calculate the Fraunhofer diffraction pattern we take the FT of Equation 3.7:

$$t(x,y) = \sum_{k=-\infty}^{\infty} FT(T_k) * FT(e^{ik\phi(m,n)}) \cdot \delta(x - \frac{k}{\Lambda}) \tag{3.9}$$

where (x,y) are the spatial frequencies of the Fourier Transform depending on (m,n) and the lens focal length f: $x = \dfrac{m}{\Lambda f}$ and $y = \dfrac{n}{\Lambda f}$.

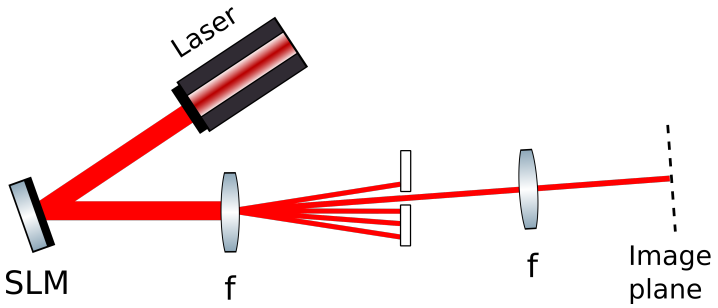

Figure 3.11: Sketch of the setup to shape simultaneously intensity and phase of a laser beam. The second lens of the 4f system is aligned only with the first-order diffraction peak. The diffraction angles have been emphasized.

Now we insert a spatial filter that selects only the first diffraction order ($k = 1$) and a second lens in order to form a 4f system. Therefore, in the second lens focal plane we obtain the FT of only the first order. Considering the two lenses to be identical, we obtain:

$$T_1'(m,n) = \exp\Big[i\pi(M(m,n)-1) + i\phi(m,n)\Big]\,\mathrm{sinc}[\pi M(m,n) - \pi] \tag{3.10}$$

Equation 3.10 describes the complex field in the image plane of the second lens. It is a function of $M(m,n)$, the extent of the phase modulation, and of $\phi(m,n)$, the phase modulation itself. If $E(m,n) = A(m,n)\exp[i\psi(m,n)]$ is the target field to be encoded, we find:

$$\begin{aligned} M(m,n) &= 1 + \frac{1}{\pi}\mathrm{sinc}^{-1}[A(m,n)] \\ \phi(m,n) &= \psi(m,n) - \pi M(m,n) \end{aligned} \tag{3.11}$$

where $\mathrm{sinc}[A(m,n)]$ is the sinc function in the domain $[-\pi, 0]$ (we have taken this form in order to directly account for the minus sign in Equation 3.10).

In conclusion, we have established an analytic connection between the target complex field at the image plane of the 4f system (keeping only the first-order peak and discarding the other) and the phase mask addressed to the SLM (Equation 3.6). Figure 3.11 illustrates the situation.

Let us analyze the method in order to highlight its characteristics. First of all, the modulated beam is not in the zero diffraction order but in the first one, and therefore the non-unitary diffraction efficiency of the SLM does not spoil the beam profile (the unreflected energy is in the zero order). Moreover, the method takes into account all the optical modifications caused by the 4f system, which were not considered in section 3.2. For example, if a Gaussian profile is addressed into the SLM the resulting beam is not Gaussian, but has an added sinc modulation than slightly deforms its profile. Equation 3.11 considers this issue and allows to apply the necessary correction to the phase mask.

On the other hand, the main limitation of this approach is the assumption of a plane wave input beam, in particular for the intensity (because the phase, if the setup is properly aligned, should be flat). However, this issue can be easily overcome by applying a correction to the phase mask taking into account the input beam intensity profile.

3.3.2 Numerical simulations

In order to validate this shaping method we now perform a numerical analysis: we consider a Gaussian input field, we add the phase modulation induced by the SLM, and then we propagate the field into the 4f system, by employing twice the Fast Fourier Transform (FTT) and spatially filtering out all the diffraction peaks but the first order.

Let us consider a 5 mm-waist Gaussian input beam and examine two cases: first, we generate a 1 mm-waist beam with an abrupt π phase step and then a 1 mm waist beam with a gradual π phase step. Figure 3.12a and Figure 3.12d display the corresponding phase masks, calculated employing Equation 3.11. Both feature a central Gaussian peak (actually not perfectly Gaussian, as they are corrected to take into account the sinc modulation) modulated by a 16-level blazed grating, plus the phase step.

The second row of the figure contains the simulated intensities and the third one the simulated phases. In both cases the intensity has the target waist, even if it is split in two halves by the phase step; for the abrupt step this effect is sharper while for the gradual step slightly less, even if it is still present. On the other hand, the phases (Figure 3.12c and Figure 3.12f) are properly modulated.

To conclude this section, the numerical simulations point out that obtaining a Gaussian beam with an arbitrary waist is doable, but adding a phase shift splits the intensity in two halves. As we have already explained in the previous sections, the wavefront analyzer cannot resolve the relative phase between two distinct regions and thus with the current setup it is not possible to control the result. However, if in future experiments simultaneous shaping of intensity and phase would be required, this technique may be employed, adapting the measurement stage (for example interfering the shaped beam with a reference one). Moreover, since more complex phase masks are used, a meticulous characterization of the SLM would be needed: the flatness of its screen, the crosstalk between adjacent pixels and, of course, all the optical aberrations of the setup have to be measured.

3.4 Conclusions

In this chapter we have dealt with the task of shaping the pump beam intensity and phase, employing a spatial light modulator and a wavefront analyzer. We have started with the SLM characterization and calibration at our working wavelength. By setting up a Mach-Zender interfrometer we have evaluated the induced phase shift as a function of the the addressed grey level and consequently modified the LookUpTable to obtain a linear 2π phase shift at 775 nm.

Afterwards, we have presented the shaping technique that we have employed in this work to shape the pump beam and engineer the biphoton spectrum. It enables to shape the intensity or the phase of a laser beam (but not both simultaneously). The beam, which lies in the zero diffraction order, has been modulated first in intensity, by generating Gaussian beams with an arbitrary waist, and then in phase by encoding phase steps in its center with a π and a $\pi/2$ phase shifts. In particular, we have shown that an abrupt phase step splits the intensity in two halves, while a

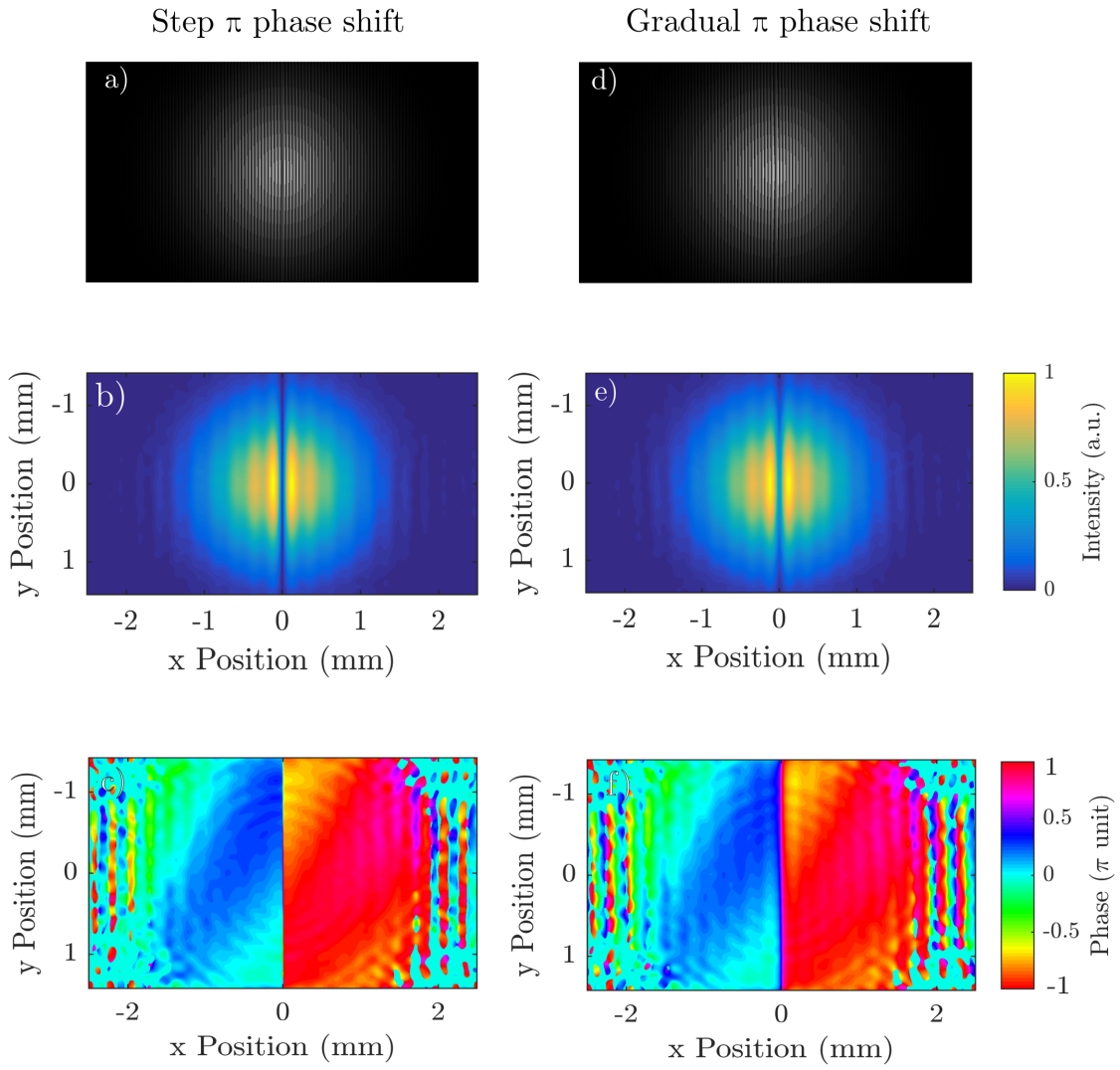

Figure 3.12: Numerical simulations of the method detailed in subsection 3.3.1: we consider a 5 mm-waist Gaussian beam as input and generate, in the image plane, a 1 mm-waist Gaussian beam with: an abrupt π phase step (first column) and a π gradual phase step (second column). Corresponding phase mask (a, d), intensity profiles (b, e) and phase profiles (c, f). In this figure, in order to highlight the phase steps we have employed a cyclic color scale for the phase. In the zero-intensity area the phase is not defined leading to numerical artifacts.

gradual phase step does not and thus it can be checked by the wavefront analyzer.

Finally following Bolduc et al. [188], we have introduced another technique which enables to simultaneously shape the beam intensity and phase and that could be employed in future experiments if more complex beam profiles are needed. The method relies on an analytic formula that relates the target field in the image plane of the 4f system with the phase mask addressed on the SLM. In order to validate the formula, we have performed numerical simulations.

Chapter 4

Joint Spectral Intensity Reconstruction

Reconstructing the full wavefunction of a photon pair is a challenging task, in particular concerning the spectral and temporal properties, i.e the Joint Spectral Amplitude (JSA) and the Joint Temporal Amplitude (JTA), since they are complex valued.

Most reconstruction techniques are limited to the squared modulus of the JSA and the JTA, i.e. the Joint Spectral Intensity (JSI) and the Joint Temporal Intensity (JTI). Concerning the spectral characteristics, the most obvious technique would register the signal and idler frequencies over many events to estimate the biphoton JSI. This can be done, pixel by pixel, by using scanning monochromators [194, 195], in a simple and accurate approach, that however requires long integration times, depending on the considered sampling of the JSI.

Another possibility is to use two-dimensional Fourier spectroscopy, measuring frequency information in the time domain [196]. This technique is not ideal because it requires two scanning interferometers and its measurement time scales as the square of the sampling resolution.

Dispersive fiber spectrography resolves both these problems by mapping frequency information into photon arrival times by using highly dispersive fibers before the single-photon detectors [197]. The resolution of this technique is then set by the combination of the fiber dispersion and the accuracy with which the

single-photon arrival times can be measured.

Another interesting approach, called stimulated emission tomography, uses the classical counterpart of the spontaneous photon-pair generation process to characterize the source, relying on the relationship between the spontaneous and stimulated process [198, 199]. This technique is one of the most efficient and high-resolution methods, since it does not requires single-photon detectors but only standard spectrometers (such as an optical spectrum analyzer).

Concerning now the JTI, since for many nonlinear sources, including ours, the time scale is orders of magnitude smaller than the typical single-photon detector temporal resolution (which is of the order of 100 ps), a direct measurement of photon arrival times is not envisageable, for now. Therefore other techniques have been developed. Maclean et al. [168] employed an optical gating technique at the single-photon level to reconstruct the JTI, using a non-collinear sum-frequency generation process between the single photons and a classical gating pulse. The two upconverted photons (one for the signal and on for the idler) are then detected in coincidence, reconstructing the JTI.

Mittal et al. [200] proposed a different approach, using a "time-lens" to magnify the relative time delay between the photons up to the detector time resolution. They employed a dispersive material and an electro-optic phase modulator to introduce a quadratic time-varying phase to both signal and idler photons: the photon relative time delay is then converted to a linear frequency shift, measurable with a dispersive fiber spectrograph, for instance.

In this chapter we focus on the two techniques employed in this thesis to measure the JSI of biphoton states: a dispersive fiber spectrograph and the Stimulated Emission Tomography (SET). Finally, in the last section we quickly describe two methods, reported in the literature, to completely reconstruct the JSA (both amplitude and phase information) and we analyze the possibility of adapting them to our experimental setup.

4.1 JSI reconstruction with a fiber spectrograph

When an optical pulse travels through a medium it is subject to the chromatic dispersion of the material: different frequency components of the pulse have different phase and group velocities and therefore propagate with different speeds. This can lead to a change of the pulse shape and to a spreading of the pulse.

Considering a pulse with the central frequency ω_0, far away from eventual medium resonances, we can Taylor expand the chromatic dispersion as follows:

$$k(\omega) = k_0 + \frac{\partial k}{\partial \omega}(\omega - \omega_0) + \frac{1}{2}\frac{\partial^2 k}{\partial \omega^2}(\omega - \omega_0)^2 + ... \tag{4.1}$$

where k_0 corresponds to a constant phase. The second term is proportional to the inverse of the group velocity ($\frac{\partial k}{\partial \omega} = v_g^{-1}$) and it results in a time delay due to the propagation inside the medium. The third term accounts for the fact that the group velocity may not be the same for each frequency component of the pulse. This phenomenon, called Group Velocity Dispersion (GVD), leads to a spreading of the optical pulse: the frequency components propagate at different speeds and reach the detector at different times.

Coming back to the biphoton wavefunction, media with high GVD can be employed to stretch its spectrum and convert the frequency information in arrival time information [201]. The dispersive medium is thus used to Fourier Transform the JTI into the JSI, if the propagation is long enough to separate the frequency components, in a sort of "far field condition" [202].

In the following we employ Dispersion Compensating Fibers (DCFs) to measure the JSI of the biphoton state, realizing a single-photon fiber spectrograph. This kind of fibers, generally used in telecommunications, have a high GVD of opposite sign compared to standard fibers and thus are usually employed to compensate the frequency spreading due to propagation; here instead we use them to maximize the pulse spreading phenomenon.

4.1.1 Experimental setup

The setup we have used in our laboratory to measure the biphoton JSI is illustrated in Figure 4.1. The Ti:sapphire laser is set at the nonlinear source resonance ($\lambda_p =$ 773.15 nm for the considered sample) and with a beam average power of 150 mW. The laser is pulsed at 76 MHz with a 6 ps pulse duration. The laser beam is shaped with the setup described in chapter 3, by a SLM and a 4f system. Please refer to that chapter for a complete description. The properly shaped pump beam is then focused on the source through a cylindrical lens (+20 mm), which shrinks the beam in one direction in order to match the waveguide width (5 µm). We estimate that about 30% of the incident power on the sample is coupled inside the vertical microcavity[1], thus only 50 mW are employed in the nonlinear process.

The emitted SPDC photons are collected by two microscope objectives (x40, NA=0.65) and coupled into single mode telecom fibers. Two polarizers (P) are placed before the fiber couplers to select only one interaction (signal TE and idler TM, or the opposite). Subsequently, each photon of the pair travels inside a DCF spool where its frequency components are spread. The DCF spool lengths have been chosen to obtain a sufficient frequency spreading with an acceptable level of optical losses (7.3 dB). Figure 4.2 reports the calibration curves of the two DCF spools used. The group velocity dispersion is defined as:

$$D = -\frac{2\pi c}{\lambda^2}\frac{\partial^2 k}{\partial \omega^2} \cdot L \tag{4.2}$$

and it has been measured as a function of the wavelength (L is the fiber length). The linear fits give an average value of dispersion $D = -1650$ ps/nm for the two spools at the degeneracy wavlength of SPDC photons ($2\lambda_p =$1546.3 nm).

Two free-running InGaAs Single-Photon Avalanche Photodiodes (SPADs), Id220 from IdQuantique™, detect the photons with a quantum efficiency of 25% and a dead time of 10 µs. Their arrival times t_s and t_i are recorded by a time-to-digital

[1]The pump beam is focused by the cylindrical lens on the sample obtaining a lateral waist of 5µm. The resulting overlap between the the sample (5 µm wide) and the beam is about 60%, while from the FTIR measurement reported in Figure 1.10 we evaluate a cavity transmission of about 50%. In conclusion approximately 30% of the incident pump power is coupled inside the cavity.

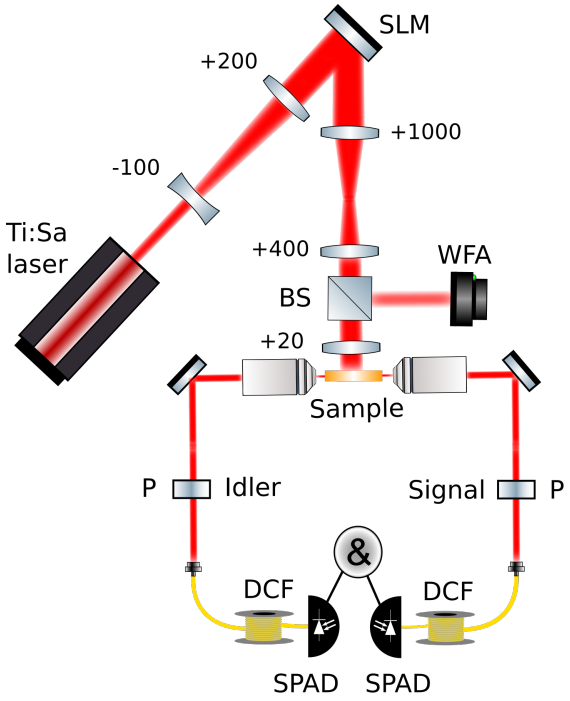

Figure 4.1: Experimental setup for the reconstruction of the JSI of a biphoton state via a fiber spectrograph. Focal lengths are given in millimeters. Abbreviations: SLM, spatial light modulator; BS, beamsplitter; WFA, wavefront analyzer; P, polarizer; DCF, dispersive compensating fiber; SPAD, single-photon avalanche photodiode.

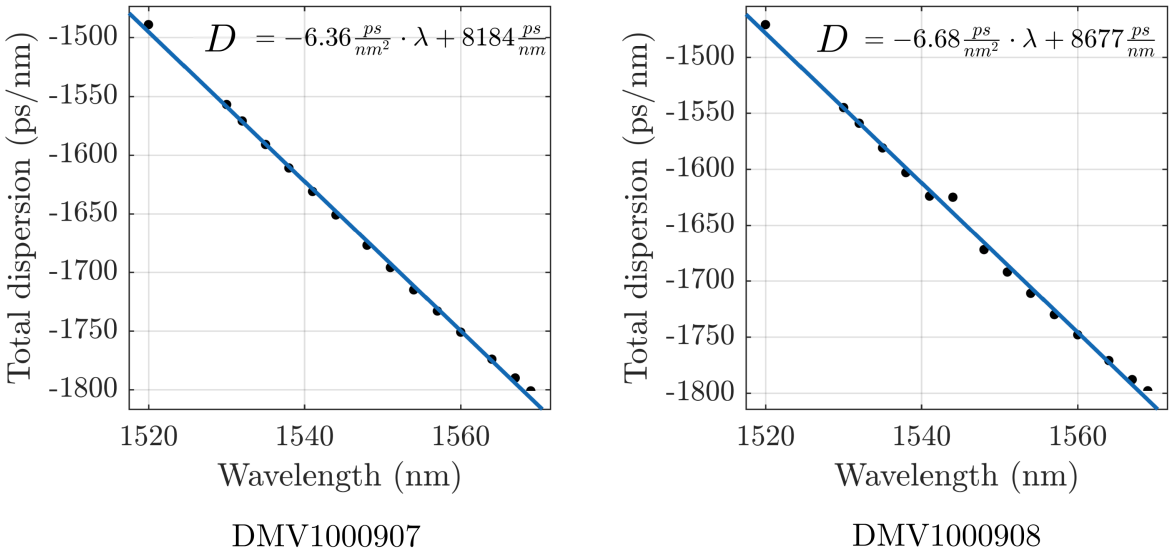

Figure 4.2: DCF calibration curves: the fiber group velocity dispersion D has been measured varying the wavelength. For each fiber spool we report the calibration curve obtained with a linear fit.

converter (TDC), QuTau from QuTools™, and compared with laser trigger t_t, retrieving the relative arrival times $\tau_{s/i} = t_{s/i} - t_t$. Once the systems is calibrated, $\tau_{s/i}$ can be converted the photon wavelength $\lambda_{s/i}$, allowing to measure the marginal spectra. Finally, by detecting coincidence photon events after a laser trigger, we perform the JSI reconstruction.

As a side note, let us analyze the coincidence detection. The laser is pulsed at 76 MHz, but the triggers are generated only at a twenty times smaller repetition rate (3.8 MHz) so as not to saturate the TDC, which cannot record more than ten millions events per second. This is not a problem because the laser is an almost perfect oscillator and therefore correlating a coincidence detection to an other trigger does not modify the timing information (we checked that the laser jitter is approximately 1 ps). In addition, this technique is widely employed in most TDC modules.

The spectral resolution of the reconstruction depends on the dispersion introduced by the DCF and on the detector electronic jitter, $\delta_{s/i} = 250$ ps. In addition, also the TDC temporal bin size has to be accounted for; in our case the minimum bin size is $\delta_{\mathrm{TDC}} = 81$ ps. Considering all these factors, the spectral resolution we can achieve is:

$$\delta\lambda = \frac{\sqrt{\delta_{s/i}^2 + \delta_{\mathrm{TDC}}^2}}{|D|} \approx 160\,\mathrm{pm} \tag{4.3}$$

Obviously, $\Delta\lambda$ can be increased by employing longer DCFs, but at the cost of greater optical losses and thus a longer integration time. Moreover, it is important to notice that the pump power cannot be arbitrary intensified, in order to limit the generation of double pairs.

Note that an alternative to DCFs to increase the system dispersion D are chirped fiber Bragg gratings. Davis et al. [203] reconstructed a single-photon marginal spectrum of 10 nm spectral width, with a resolution of 55 pm. However, this technique is limited by the bandwidth of such device, less than 10 nm, and its cost.

4.1.2 Calibration of the spectrograph

To convert the photon arrival times into their corresponding wavelength values, the spectrograph must be calibrated. In order to do so, we take advantage from the source characteristics themselves. As we have already described, the waveguide facets have a non-zero reflectivity, which creates a Fabry-Pérot cavity. Thus the photons can be reflected from a facet and transmitted from the opposite one, after a half round trip. If the pump beam is not at normal incidence, the two interactions generate photons at four different wavelengths (see the accordability graph, Figure 1.14) and therefore in the marginal spectrum we identify four peaks: two major peaks associated to the directly transmitted photons and two minor peaks associated to the photons that have traveled a half round trip. Note that in order to measure both interactions it is necessary to remove the polarizers from the setup shown in Figure 4.1.

Figure 4.3a reports the signal marginal spectrum between two laser triggers at 3.8 MHz, while the laser pulses are emitted at 76 MHz. The graph contains thus

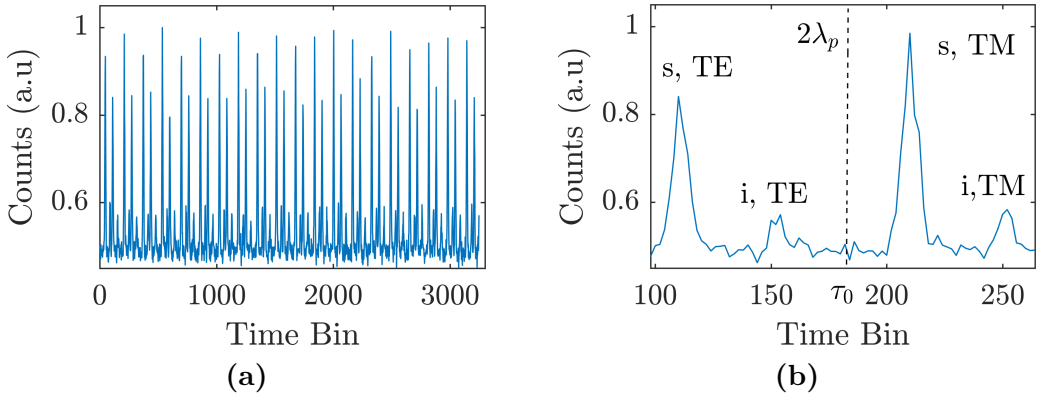

Figure 4.3: Signal side marginal spectra: (a) between two consequent trigger events, containing twenty laser pulses, and (b) close-up on the first spectrum. In (b) each peak has been identified (s=signal, i=idler, for both polarizations TE and TM) and the central bin τ_0, corresponding to the degeneracy wavelength $2\lambda_p$, is highlighted. The time delay between two consequent laser pulses is 13 ns, corresponding to 160 time bins, while the spectral distance between two major or minor peaks is approximately 4.9 nm (fixed by the birefringence) and it corresponds to approximately 97 time bins, with the employed DCFs.

twenty marginal spectra of the signal side. Figure 4.3b is a close-up showing only the detection peaks generated by the first pulse after the trigger: the four peaks detailed above are identified.

From the accordability graph it is possible to notice that, for all pump angles and each interaction, the two emitted wavelengths are always symmetric with respect to $2\lambda_p$, because of the energy conservation condition. Therefore, once the peaks have been identified, the central bin τ_0 (highlighted in Figure 4.3b by a dashed line) can be associated to the degeneracy wavelength $2\lambda_p$. Consequently, knowing the DCF dispersion, we obtain the calibration relation:

$$\lambda_{s/i} = \frac{\tau_{s/i} - \tau_0}{D} + 2\lambda_p \tag{4.4}$$

Once the axes have been calibrated and the central bin has been found for each spectrum between two consequent triggers, we need to merge the twenty 2D histograms contained in the graph. This is done by selecting an enough wide area around each central bin and summing up all of them. We finally obtain a single 2D histogram, with calibrated axes.

Time bin correction

The employed TDC features even and odd time bins with different sizes and thus a numerical analysis is needed. Once the 2D coincidence histogram has been obtained, we create artificial time bins in the shared corners of four neighboring raw bins, with the same temporal dimension (81 ps). For each new bin the number of coincidences is calculated as the average of the counts of the four raw bins,

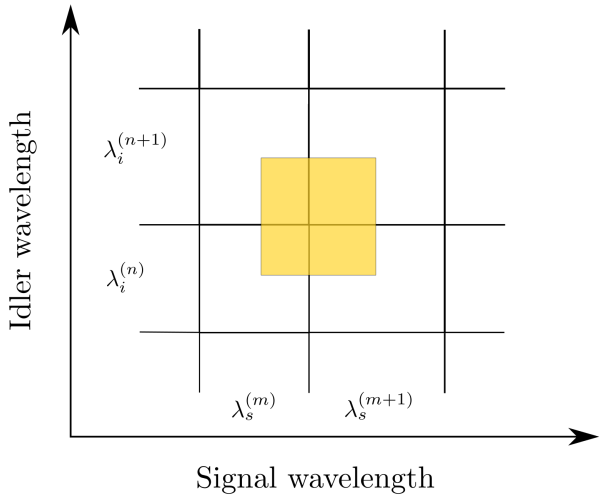

Figure 4.4: Sketch of the correction procedure of the TDC bin size. Since even and odd time bins have different sizes, we create artificial bins in their shared corners (in yellow).

following the formula:

$$|\phi|^2\Big(\frac{\lambda_s^{(m)}+\lambda_s^{(m+1)}}{2},\frac{\lambda_i^{(n)}+\lambda_i^{(n+1)}}{2}\Big)=\frac{|\phi|^2_{m,n}+|\phi|^2_{m+1,n}+|\phi|^2_{m,n+1}+|\phi|^2_{m+1,n+1}}{4} \tag{4.5}$$

where the new artificial bin is created between the wavelength bin m and $m+1$ on the signal side, and between the bin n and $n+1$ on the idler side. $|\phi|^2_{i,j}$ are the recorded coincidence counts in the signal bin i and in the idler bin j. Figure 4.4 illustrates this procedure.

4.1.3 Experimental JSI reconstruction

We now present a typical reconstructed JSI obtained via the fiber spectrograph, comparing it with a numerical simulation. Figure 4.5a shows the experimental reconstruction of a biphoton JSI for a 773.15 nm pump beam, incident at the degeneracy angle, with a 1 mm-waist Gaussian profile. By using the polarizers we select only the interaction emitting TM-polarized signal photons and TE-polarized idler photons. The measurement has been carried out integrating for 24 minutes.

Figure 4.5b reports the corresponding numerical simulation for which all the parameters have been independently determined, apart from the incidence angle and the Fabry-Pérot phases. The pump central wavelength and its spectral width have been determined experimentally with an optical spectrum analyzer, while its spatial properties have been measured with the wavefront analyzer, as detailed in chapter 3. The effective indices n_{TE} and n_{TM} have been numerically simulated on the nominal structure with the transfer matrix method [132].

We notice that the experimental measurement succeeds in resolving the biphoton spectrum. On the other hand, even though some structuring is present, the spectral resolution of the fiber spectrograph is not sufficient to resolve the Fabry-Pérot fringes due to the waveguide facet reflectivity. Indeed, the free spectral range

of the modulation (FSR) is $\Delta\lambda_{\mathrm{FSR}} = 190$ pm (for a 1.9 mm-long waveguide) which is of the same order than the spectrograph resolution $\delta\lambda = 160$ pm.

The resolution in the experiment could be improved by using Superconductive Nanowire Single-Photon Detectors (SNSPDs), which have a higher quantum efficiency, allowing to afford greater collection losses and hence to employ longer DCF spools. Instead of using longer DCFs, a different approach could be envisaged: both photons can be sent in a single fiber, obtained by stacking the two spools together. However, in this case the separation of the photons at the output of the fiber has to be performed probabilistically with a 50:50 beamsplitter, losing half of the coincidences [204]. In our case we prefer to avoid this problem by using two distinct DCF spools.

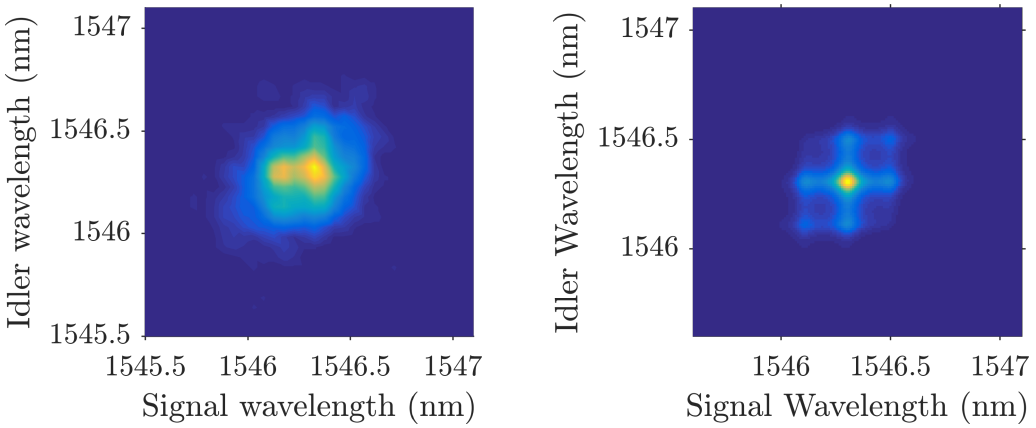

(a) Experimental JSI **(b)** Simulated JSI

Figure 4.5: (a) Experimental reconstructed JSI via the fiber spectrograph, for a 773.15 nm pump beam with a 1 mm waist, incident at the degeneracy angle on a 1.9 mm-long waveguide. (b) Corresponding numerical simulation.

4.2 JSI reconstruction by Stimulated Emission Tomography (SET)

In the previous section we have analyzed the fiber spectrograph technique as a means to reconstruct the biphoton JSI. In practice, this technique is mainly limited by the low biphoton generation probability, demanding long integration time, and by the spectral resolution, as we have just seen. These limitations can be overcome by a different approach, called Stimulated Emission Tomography (SET).

Let us start by recalling that SPDC can be seen as the quantum counterpart of Difference Frequency Generation (DFG). Indeed, in the latter process, the conversion of pump photons to signal and idler photons is stimulated by a seed beam; thus SPDC can be interpreted as a DFG process stimulated by vacuum fluctuations, as sketched in Figure 4.6.

Liscidini and Sipe [198] pointed out that, since DFG and SPDC are governed by the same phase-matching and energy conservation equations, in a DFG process the biphoton wavefunction plays the role of response function for the generation of the

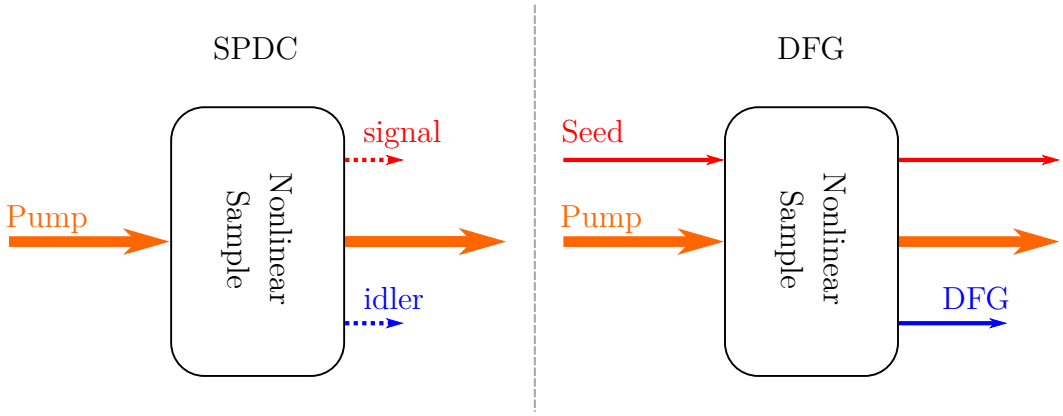

Figure 4.6: Comparison between SPDC (left) and DFG (right) processes. SPDC can be considered as the quantum limit of DFG: the seed beam is replaced by vacuum fluctuations. Adapted from [153].

idler field. From this approach, they proposed the SET technique, which enables to reconstruct the JSI of a biphoton pair by performing classical measurements on the DFG photons. As one passes from single photons to a classical field, the intensity increases by several orders of magnitude, allowing to speed up the measurement and to directly characterize the spectrum using a classical detector such as an optical spectrum analyzer, which can have a better resolution than the fiber spectrograph detailed before.

The technique has been experimentally demonstrated for the first time by Eckstein et al. [199], showing a significant improvement both in integration time and spectral resolution.

4.2.1 Experimental setup

In this section we detail the experimental setup employed to reconstruct the JSI via the SET technique, as depicted in Figure 4.7. The pump scheme and its shaping stage is similar to the one used for the fiber spectrograph in section 4.1. In addition, a tunable infrared CW laser (Tunics-Plus™) provides the seed beam with a linewidth $\delta\omega_s = 100$ kHz; it is filtered by a fibered filter (FF) with 1.2 nm bandwidth (OzOptics™), in order to remove eventual sidebands of the laser. Indeed, the DFG power that will be measured is of the order of tens of picoWatts (for 10 mW of seed power) and therefore even a very weak sidebands could spoil the measurement.

In order to couple the seed telecom beam inside the waveguide and to be able, at the same time, to collect the DFG photons, we use a fibered polarization beam splitter (PBS) as a polarizator circulator. The telecom laser is set TM polarized with a fibered polarization controller (FPC), sent through the PBS and coupled inside the source. On the other hand, the generated DFG signal, which is TE polarized, is sent by the PBS to the optical spectrum analyzer (OSA), Yokogawa™ 6730C. This instrument has a spectral resolution of 20 pm and a sufficient sensitivity to detect the DFG signal. Note that, differently from the fiber spectrograph technique, here we do not employ polarizers to select the nonlinear interaction: it

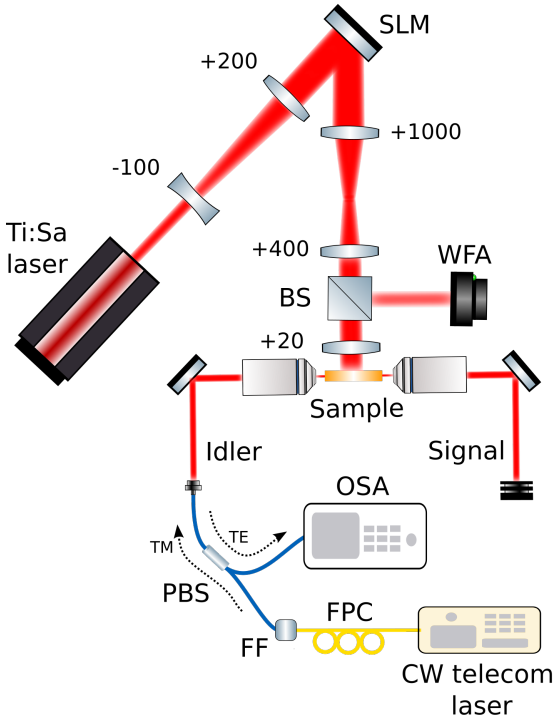

Figure 4.7: Experimental setup for the reconstruction of the JSI of a biphoton state employing the SET technique. Focal lengths are given in millimeters. See text for description. Abbreviations: SLM, spatial light modulator; WFA, wavefront analyzer; OSA, optical spectrum analyzer; PBS, polarizing beamsplitter; FF, fibered filter; FPC, fibered polarization controller.

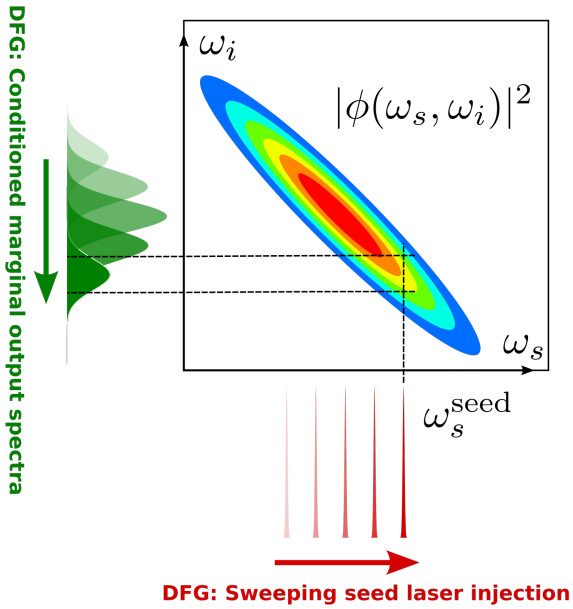

Figure 4.8: JSI reconstruction scheme by SET. Scanning the laser wavelength, each JSI "slice" is acquired by the OSA. Adapted from [153].

is directly chosen by the seed beam polarization.

Figure 4.8 illustrates the measurement scheme. Once the seed wavelength $\lambda_s^{(0)}$ is chosen, the DFG, measured by the optical spectrum analyzer, corresponds to a slice of the JSI: $|\phi(\lambda_s^{(0)}, \lambda_i)|$. By scanning the seed laser, the whole JSI can thus be reconstructed. As a last step, each slice has to be corrected for the transmission of the fibered filter used to purify the seed laser, which has a Gaussian profile rather that a flat one.

4.2.2 Experimental JSI reconstruction

Figure 4.9a reports the experimental reconstruction of the JSI with the SET technique, for a 1 mm-waist pump beam at 773.15 nm wavelength. The experimental conditions are identical to the ones of the measurement reported in Figure 4.5, reconstructed via fiber spectrograph, except for the incidence angle and the Fabry-Pérot peak position.

The OSA is set at its best spectral resolution, namely 20 pm, and at a sensitivity of tens of pW. Compared to the measurement reported in [153] here we use the pump laser at its full repetition rate (76 MHz), resulting in a more intense DFG signal, which enables to speed up the measurement.

The reconstructed JSI reported in Figure 4.9 has been acquired in 5 minutes and proves a remarkable improvement of the spectral resolution, compared with the fiber spectrograph (see Figure 4.5a). Along the idler wavelength, measured by the OSA, the spectral resolution is 20 pm, while for the signal wavelength the resolution is given by the tunics laser sampling (10 pm), an order of magnitude

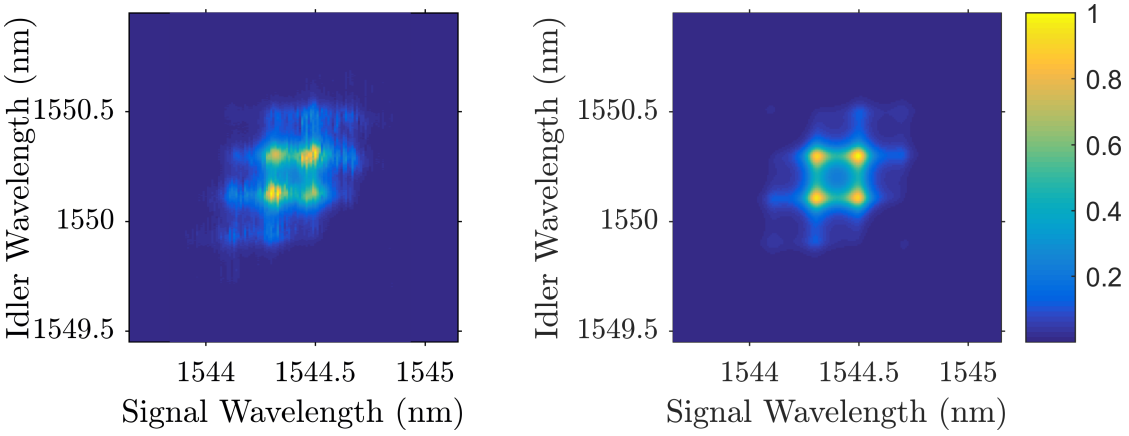

(a) Experimental JSI **(b)** Simulated JSI

Figure 4.9: (a) Experimental reconstructed JSI via Stimulated Emission Tomography, for a 773.15 nm pump beam with a 1 mm beams waist incident on a 1.9 mm waveguide. (b) Corresponding numerical simulation.

better than the 160 pm resolution of the fiber spectrograph.

Figure 4.9b shows the numerically simulated JSI, corresponding to the experimental situation of Figure 4.9a. Comparing the two, we note that the better spectral resolution has here allowed to resolve the Fabry-Pérot modulation. Note that the only free parameter of the simulations are the Fabry-Pérot peak positions, which have been adjusted to match the experimental data[2].

4.2.3 SET limitations

Stimulated Emission Tomography enables to speed up the JSI reconstruction and to obtain a better spectral resolution, compared to the fiber spectrograph. However, in our experimental implementation, it presents a main limitation: the PBS used to route the seed beam to the source and the DFG signal to the OSA has not a perfect extinction ratio (20 dB), thus impeding to reconstruct degenerate JSIs. Indeed, at degeneracy, a non-negligible part of the seed beam would pollute the DFG signal and a frequency filtering cannot be performed. A solution to this issue would be a PBS with a better extinction ratio (e.g. a free-space PBS cube whose extinction rate can reach 40 dB).

4.3 A phase sensitive JSA reconstruction

So far we have dealt with techniques capable of measuring the squared modulus of the JSA, but not its phase. The full reconstruction of a JSA is an extremely hard task, which has been carried out only in particular situations, and it lacks a

[2]Since we are considering high resonance orders, it is not possible to determine the exact Fabry-Pérot peak positions from an experimental measurement of the waveguide length L. For this reason they have been adjusted by introducing artificial Fabry-Pérot phases in the numerical simulation. On the other hand, the cavity free spectral range can be easily determined from L.

general technique. In the following we analyze some possible solutions that have been reported in the literature.

Two-photon interference on a beamsplitter, i.e. the Hong-Ou-Mandel (HOM) effect [205], is sensitive to the symmetry of the biphoton wavefunction with respect to the degenerate frequency. Therefore, it could be employed to measure the relative phase of symmetric points of the JSA, but not to obtain the full reconstruction. As we will see in chapter 6, a generalization of the HOM experiment has been proposed [206] to enable the full reconstruction of the Chronocliclyc Wigner function, from which the JSA can be retrieved.

Another viable technique to obtain a full reconstruction is to extend Stimulated Emission Tomography to measure also the phase. Indeed, the DFG spectrum contains both intensity and phase information. Jizan et al. [207] experimentally demonstrated an implementation of this technique employing Four Wave Mixing (FWM) in a Silicon Nanowire. In FWM the emitted photon pairs are the same wavelength than the pump and therefore it is possible to interfere the pump beam with the stimulated photons (in this case it is not DFG but stimulated FWM). A broadband pulsed beam (30 nm) is spectrally shaped and the pump beam, the seed beam and a reference beam are carved out from it. When these beams travel inside the nonlinear medium the stimulated photons are generated exactly at the frequency of the reference beam and interfere with it. By varying their relative phase and measuring the interference pattern with an OSA, the full JSA of the biphoton state can be reconstructed, with a demonstrated spectral resolution of 30 pm [207].

This technique can be employed also in our experimental case but with additional modifications. Indeed, the SPDC generated photons are not at the same frequency than the pump beam, requiring therefore a second laser as reference beam in the telecom range. This laser has to be spectrally broad enough to cover the whole JSA and to be phase-locked with the pump beam. Maintaining the same experimental setup presented in subsection 4.2.1, the reference beam should be coupled inside the waveguide from the signal side and crossed polarized with respect to the seed beam. In this way the OSA would directly record the interference pattern.

Maclean et al. [208] proposed a different technique, based on the experimental reconstruction of both JSI and JTI of the biphoton state. The first is reconstructed with dual single-photon monochromators, while the second via optical gating with a noncollinear sum-frequency generation process between the signal/idler photon and a strong gate pulse [168]. Since the JSA is the Fourier Transfor of the JTA, they employed a modified version of the Gerchberg-Saxton algorithm [209] to retrieve the JSA phase, from the knowledge of their squared moduli (JSI and JTI). Compared to the previous one, for our experimental situation, this technique is more costly in term of both resources and integration time, since it is based on single-photon coincidence detection rather than classical measurements.

4.4 Conclusions

This chapter has begun with an overview of the experimental techniques to reconstruct the JSI and the JTI of a biphoton state. Then, we have focused our attention on the two techniques we will employ in the next chapters: the fiber spectrograph technique, which uses fibers with high group velocity dispersion (GVD) to convert the frequency information in arrival time information, and the Stimulated Emission Tomography (SET) technique, which takes advantage of the relationship between SPDC and DFG to "classically" retrieve the JSI. For both techniques we have detailed the experimental implementation and compared the reconstructed JSI with the corresponding numerical simulations.

We have proven that SET enables to reconstruct the JSI with a better spectral resolution, 20 pm compared to 200 pm for the fiber spectrograph, and in a shorter integration time. We have mentioned however that, with our experimental implementation, SET does not permit the reconstruction of degenerate JSIs. Depending on the experimental situation both techniques will thus be useful for our experiments.

Finally, in the last section of the chapter, we have analyzed two proposals that allow to completely reconstruct the JSA, both amplitude and phase information, focusing on the possibility to adapt them to our experimental situation in the future. We have identified an interferometric version of SET, as a promising method that would allow to fully reconstruct the JSA with only an additional laser beam.

Chapter 5

Joint Spectral Amplitude Engineering

So far we have described the quantum state of the photon pairs emitted by our nonlinear source and illustrated two experimental techniques to measure its Joint Spectral Intensity (JSI). In order to exploit such biphoton state in various quantum information protocols, a deep control over frequency correlations is preferable, which means manipulating the joint spectrum in both amplitude and phase.

In this chapter we start by giving an overview of the techniques that have been proposed so far in the literature to tailor the biphoton spectrum, dividing them in two categories: post-manipulation and direct shaping. The first category modifies the JSA once the state is emitted, while the latter directly shapes the JSA at the generation stage.

We then describe how the counter-propagating phase-matching scheme under transverse pumping enables to directly shape the JSA of the emitted photon pairs. This is achieved by controlling the pump beam spatial profile, which is directly connected with the JSA. We provide numerical simulations and experimental measurements of the JSI, in various situations: first we show how to manipulate the frequency correlations by modifying the pump beam waist; then we show how to control the state's symmetry by shaping the pump beam phase.

5.1 Joint spectrum engineering: an overview

Frequency entangled photon pairs have a large variety of applications, but for each of them a precise control of the type of correlation is preferable, or even required. For example, non-correlated states are required for heralded single photon sources [194], while correlated states are key resources for clock synchronization [115] or dispersion cancellation in long distance quantum communications [117]. However, under CW pumping, energy conservation naturally leads to frequency anti-correlated states, which limits the possible applications of the source. By contrast, a tunable source of frequency entangled photon pairs, capable of emitting quantum states with arbitrary JSA, would allow to target several applications.

Post-manipulation techniques

We start by reviewing post-manipulation techniques, in which the quantum states are shaped after the generation stage, inevitably reducing the integrability of the source into chip-based photonic circuits. The simplest method is spectral filtering, which is widely used to obtain non-correlated photon pairs for heralded single-photon sources [210]. It allows to obtain very high single-photon purity at the cost of a great brightness reduction. Nevertheless, programmable spectral filters and phase modulators have been demonstrated as a viable method to implement quantum gates for manipulating high-dimensional frequency combs [104].

The phase of the JSA can be post-manipulated by performing spectral-phase shaping, a basic technique used in the pulsed laser community: the photon pair spectral components are spatially separated with dispersion prisms and their phase is then controlled with a spatial light modulator. This method allows to gain control over the spectro-temporal properties of the photon pairs, as demontrated in [211] and [212].

Another technique that has been adapted from classical optics is time-lensing: a quadratic time-varying phase is imposed to the photon pair through an electro-optic phase modulator and a dispersive material. This enables to convert the time delay to a linear frequency shift and to measure the JTI (as pointed out in chapter 4), but also to shape the joint spectrum. Donohue et al. [213] demonstrated that a time-lens can convert strongly frequency anti-correlated photon pairs to frequency correlated ones.

Direct generation techniques

Direct shaping at the generation stage is preferable, with respect to to post-manipulation, because it allows to fully exploit the brightness of the source while keeping the door open to its integration on chip-based photonic circuits. Several techniques have been proposed in the literature, acting either on the source or on the pump beam parameters.

We start with the techniques achieving spectral shaping by modifying the phase-matching conditions of the source. As we have already said, energy conservation naturally leads to strongly frequency anti-correlated states, particularly in a collinear geometry (Figure 5.1a), and this situation is not a desirable condition

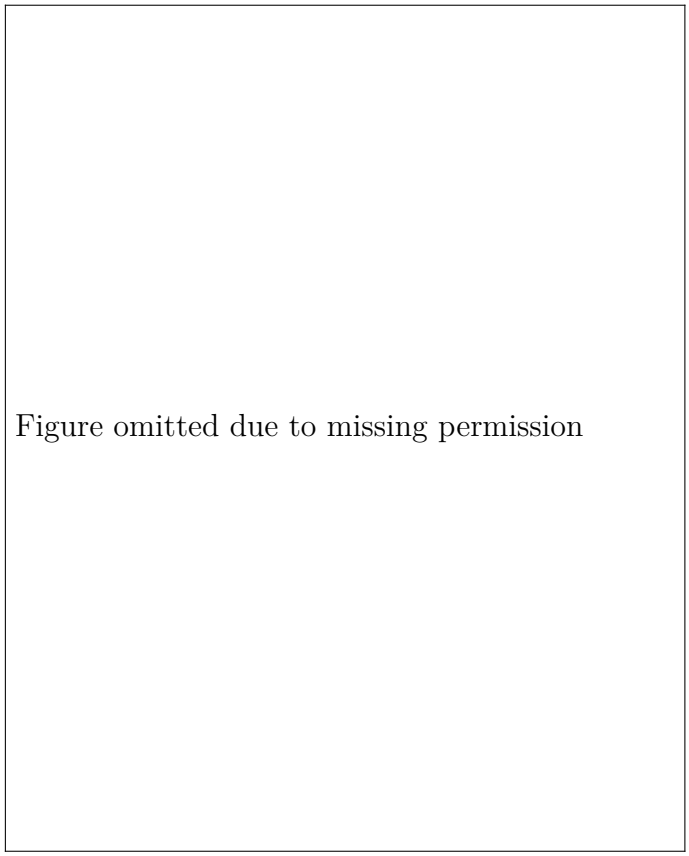

Figure 5.1: Three group-velocity matching conditions: the JSA of each case is plotted on the left with the respective group velocities v_g on the right. (a) Without dispersion engineering, the phase-matching function is oriented with a negative angle and the JSA is anti-correlated. (b) The signal photon propagates at the same velocity of the pump, leading to a phase-matching function aligned with the signal axis. (c) The pump group velocity lies in between the group velocities of the signal and idler, yielding a phase-matching function directed along the principal diagonal. Adapted from [216].

for some applications, for example for heralded single photon sources. Single-mode emission (i.e. non-correlated frequency states) has been reached by properly matching the group velocity of the signal, idler and pump field (group-velocity matching GVM)[214–216]. In particular, if the pump propagates at the same velocity than the signal (idler) photons, the phase-matching function is aligned along the signal (idler) frequency axis, as shown in Figure 5.1b. In this condition, if the spectral bandwidth is broader than the phase-matching bandwidth, a nearly separable JSA is generated. On the other hand, if the pump group velocity lies in between the ones of signal and idler photons, the phase-matching function is oriented along the principal diagonal, as in the case of the counter-propagating phase-matching scheme. If the spectral bandwidth matches the phase-matching bandwidth, a separable JSA is obtained (Figure 5.1c) [216].

A step further has been done by tailoring the nonlinearities of the source with domain engineering, by employing group velocity matching in periodically poled

crystal [217]. It has been demonstrated that the phase-matching function can be transformed from a sinc^2 function to purely Gaussian, eliminating the side lobes and thus resulting in a very high spectral purity [218–220]. In addition, this technique enables to design sources with arbitrary phase-matching functions. Graffitti et al. engineered the nonlinear domains of periodically poled potassium titanyl phosphate (PPKTP) waveguides to shape the phase-matching as a first order Hermite-Gaussian function, demonstrating the generation of non-Gaussian frequency entanglement [65].

Engineering the phase-matching conditions through GVM results in a high-quality shaping of the joint spectrum, but it has a non negligible drawback: the emitted biphoton state is fixed and cannot be tuned.

On the contrary, tuning the pump beam properties (spatial and spectral profile) enables, under certain phase-matching geometries, to tailor the joint spectrum and control the frequency correlations. Valencia et al. [221] shaped the joint spectrum of a non-collinear Type I SPDC nonlinear crystal, by tuning the spatial width of the pump beam. Conversely, in a collinear geometry, only the spectral profile of the pump beam and not the spatial one has an effect on the joint spectrum. Ansari et al., employing a periodically poled lithium niobate (PPLN) waveguide, demonstrated the JSA shaping by modifying the pump beam spectrum and generated correlated, non-correlated, anti-correlated frequency states [41].

Finally, several methods have been proposed to tune the frequency correlations by reversibly changing the source properties (e.g. with a temperature variation), even if this enables only a partial control of the JSA [222–224]. For example, Kumar et al. [222] employed a silicon chip composed of a periodic sequence of coupled microring resonators, generating photon pairs in the supermodes of the combined structures, through spontaneous four-wave mixing. The result is a chessboard-like patterning of the phase-matching function, on the top of which the energy conservation condition selects only one diagonal stripe at the time, when the laser is pulsed with a smaller spectral width than the resonance distance. Tuning the pump central wavelength or the source temperature enables to select different resonances and thus to change the frequency correlations of the photon pairs, as shown in Figure 5.2. Even if the device allows a certain tunability, the joint spectrum is always anti-correlated and the source cannot generate correlated or non-correlated frequency states.

During the last years many efforts have been devoted to implement joint spectrum engineering in integrated devices, for the realization of fully on-chip quantum information applications. The most exploited platforms are PPKTP [65] and PPLN [41] waveguides and silicon microring resonators [222].

In this chapter we show how our counter-propagating source allows to shape directly on-chip the biphoton joint spectrum, in a tunable manner.

5.2 Joint spectrum engineering in the counter-propagating phase-matching scheme

After the overview on the methods proposed in the literature to shape the joint spectrum of a photon pair, we now focus our attention on the tunability of the

Figure omitted due to missing permission

Figure 5.2: Numerical simulations of the JSI produced by the device proposed by Kumar et al. [222]. The pump wavelength determines which diagonal oriented slice is selected, allowing to control the level of spectral correlation as shown in (b), (c) and (d) by the Schmidt number K. Adapted from [222].

quantum states produced by our counter-propagating source.

The counter-propating phase-matching scheme under transverse pumping has already been proposed as an interesting situation for engineering of the joint spectrum [225]. Indeed, a source exploiting this geometry features many physical properties that can be independently tuned in order to arbitrary shape the JSA of the emitted state, in particular the pump beam spatial and spectral profile.

In chapter 2 we derived that, under some approximations, the quantum state emitted by the source can be written as:

$$|\psi\rangle = \iint \mathrm{d}\omega_s \, \mathrm{d}\omega_i \, \phi(\omega_s, \omega_i) \, \hat{\mathrm{a}}_H^\dagger(\omega_s) \hat{\mathrm{a}}_V^\dagger(\omega_i) \, |0\rangle \tag{5.1}$$

where $\phi(\omega_s, \omega_i)$ is the Joint Spectral Amplitude (JSA), which can be factorized in four terms (considering also the Fabry-Pérot cavity created by the facet reflectivity):

$$\phi(\omega_s, \omega_i) = \chi_\Gamma \cdot \mathrm{PM}(\omega_s, \omega_i) \cdot \phi_{\mathrm{spectral}}(\omega_s, \omega_i) \cdot \phi_{\mathrm{FP}}(\omega_s, \omega_i) \tag{5.2}$$

Let us recall the analytic expression of each term. The first one is the overlap integral between the interacting fields and the nonlinear medium, including also all the multiplicative constants:

$$\begin{aligned} \chi_\Gamma(\omega_s, \omega_i) = & \frac{\epsilon_0 L \varepsilon_p^{(0)}}{i\beta\hbar\sqrt{v_g^H(\omega_s) v_g^V(\omega_i)}} \\ & \times \iint \mathrm{d}x \, \mathrm{d}y \, \chi^{(2)}(x) \Pi_W(y) \phi_p(y) E_H(x, y, \omega_s) E_V(x, y, \omega_i) \end{aligned} \tag{5.3}$$

This term, under the approximations we have considered in chapter 2 (small GVDs and no frequency dependency of the guided mode spatial profile), can be considered frequency independent and therefore it has no influence on the frequency correlations.

The second term, containing the integral along the z-direction, describes the phase-matching condition:

$$\mathrm{PM}(\omega_s, \omega_i) = \int \mathrm{d}z\, \Pi_L(z) \phi_p(z, \omega_+) e^{-ik_{\mathrm{deg}}(\omega_+)z - i\frac{\omega_-}{\bar{v}_g}z} \tag{5.4}$$

where $\phi_p(z, \omega_+)$ is the pump spatial profile along z and $\omega_\pm = \omega_s \pm \omega_i$. Here we can already see a peculiarity of this geometry: the phase-matching integral is along z, the same direction than the pump spatial profile. Conversely, in a waveguided collinear source, since the pump beam propagates in the same direction than the generated photons, its spatial profile is constant along the integration direction and therefore it has no influence on the joint spectrum.

The third term corresponds the energy conservation relation:

$$\phi_{\mathrm{spectral}}(\omega_+) = f_{\mathrm{spectrum}}(\omega_+) \tag{5.5}$$

where $f_{\mathrm{spectrum}}(\omega_+)$ is the pump beam spectral profile. In our work, since we do not employ pump pulses shorter than 4 ps, we have neglected the filtering effect of the vertical microcavity on the pump beam spectrum (see section 1.4).

Finally, the last term describes the chess-board pattern induced by the longitudinal Fabry-Pérot cavity and it depends only on the source structure, as described in subsection 2.2.5:

$$\phi_{\mathrm{FP}}(\omega_s, \omega_i) = f_{\mathrm{H}}(\omega_s) f_{\mathrm{V}}(\omega_i) \tag{5.6}$$

where we have chosen to describe the interaction HV, with TE-polarized signal photon and TM-polarized idler photon.

5.2.1 Gaussian pump beam

In order to analyse the relationship between the JSA and the pump beam spatial and spectral profile, we start by considering the simple case of a Gaussian pulsed pump.

Figure 5.3 reports a sketch of the situation. The pump beam has a Gaussian spatial profile, with w_z and w_y the projections of its waist along the z and y directions. It impinges on the source with an incidence angle θ, very small and with no frequency dependency ($\mathbf{k} \cdot \hat{\mathbf{u}}_z = \dfrac{\omega_p}{c}\sin(\theta)$). The beam is pulsed and has a hyperbolic secant spectral profile (typical of a Ti:Sa laser) centered at $\omega_p^{(0)}$, matching the microcavity resonant frequency, and pulse duration $\Delta\tau_p = \dfrac{1.978}{\omega_p}$, for a Fourier-Transform-limited pulses.

Taking into account all this, the electric field of the pump beam reads then:

$$\begin{aligned} E_p(\mathbf{r}, \omega_+) = \varepsilon_p^{(0)} & \overbrace{\exp\left(-\frac{z^2}{w_z^2}\right)\exp\left(i\frac{\omega_+ \sin\theta}{c}z\right)}^{\phi_p(z)} \\ & \times \underbrace{\exp\left(-\frac{y^2}{w_y^2}\right)}_{\phi_p(y)} \underbrace{\mathrm{sech}\left(\frac{\omega_+ - \omega_p^{(0)}}{\Delta\omega_p}\right)}_{f_{\mathrm{spectrum}}(\omega_+)} \end{aligned} \tag{5.7}$$

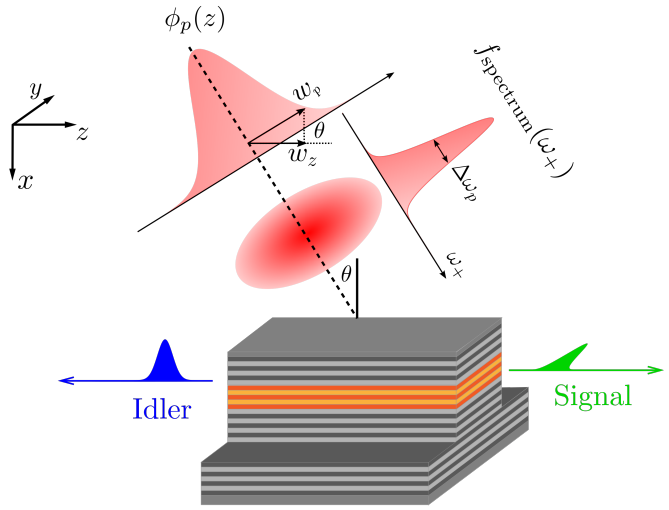

Figure 5.3: Sketch of a Gaussian pump beam impinging on the device, only the spatial section of the beam along z and its spectral profile are shown.

Using this analytic expression of the pump beam, we can derive the phase-matching and the spectral functions. The first is given by:

$$\begin{aligned} \mathrm{PM}(\omega_s,\omega_i) = &\int \mathrm{d}z\, \Pi_L(z) \exp\left(-\frac{z^2}{w_z^2}\right) \\ &\times \exp\left[-i\frac{\omega_+}{c}\left(\sin\theta - \sin\theta_{\text{deg}}\right)z\right] \exp\left(-iz\frac{\omega_-}{\bar{v}_g}\right) \end{aligned} \tag{5.8}$$

If now we make the approximation of a monochromatic pump beam, the phase-matching function depends only on ω_-. Indeed, the pump frequency ($\omega_+ = \omega_p^{(0)}$) acts just as a parameter, setting the position of the phase-matching function in the (ω_s,ω_i) space, without having any role in the shaping process. By performing complete numerical simulations we have verified that this approximation is valid for our experimental situation up to a precision <1%, even if we will employ a picosecond pulsed laser and not a monochromatic one[1].

Depending on the relative value of the pump beam waist along z (w_z) with respect to the source length (L), we find different situations for the phase-matching function $\mathrm{PM}(\omega_-)$:

- $w_z \ll L$
  If the waist is smaller that the waveguide length, the gate function $\Pi_L(z)$ can

[1]More precisely the phase-matching function depends exactly only on ω_- if the following conditions are satisfied:

- the pump beam has no angular dispersion ($\mathbf{k}\cdot\hat{\mathbf{u}}_z = \frac{\omega_p}{c}\sin(\theta)$),
- it has a monochromatic spectrum ($\omega_+ = \omega_p^{(0)}$),
- the signal and idler guided modes have the same group velocity dispersion GVD ($\delta_{\text{GVD}} = 0$, c.f. section 2.2).

be neglected and the phase-matching function is simply the Fourier Transform of the beam spatial profile:

$$\mathrm{PM}(\omega_-) = \sqrt{\pi} w_z \exp\left[-\left(\frac{\omega_- - \omega_-^{(0)}}{\Delta\omega_-}\right)^2\right] \tag{5.9}$$

This is a Gaussian function of width $\Delta\omega_- = 2\bar{v}_g/w_z$, shifted from the degeneracy frequency by an amount $\omega_-^{(0)} = \omega_p^{(0)}(\sin\theta - \sin\theta_{\mathrm{deg}})\bar{v}_g/c$. This last equation reproduces, for small angles, the linear dependency of the frequencies of the photons with the incidence angle θ that we have seen in Figure 1.14: $\omega_-^{(0)} \approx \omega_p^{(0)}(\theta - \theta_{\mathrm{deg}})\bar{v}_g/c$.

- $w_z \gg L$
  In the opposite case, when the waist is larger than the waveguide length, the Gaussian shape can be approximated with the gate function itself. Therefore the phase-matching function is just the Fourier transform of the gate function $\Pi_L(z)$:

$$\mathrm{PM}(\omega_-) = L\,\mathrm{sinc}\left(\frac{\omega_- - \omega_-^{(0)}}{\Delta\omega_-}\right) \tag{5.10}$$

- $w_z \approx L$
  In the intermediate situation, the phase-matching function is given by the convolution of the cardinal sine function and the Fourier Transform of the pump spatial profile.

These results have been derived for a Gaussian pump beam, but from them we can infer the general behavior of the phase-matching function. In particular, in the case where the pump beam typical dimension is much smaller than the waveguide length, the phase-matching function corresponds to the Fourier Transform of the projection along z of the pump spatial profile multiplied by a phase term given by the waveguide birefringence, $\varphi(z,\omega_+) = \phi_p(z,\omega_+)e^{-ik_{\mathrm{deg}}z}$:

$$\mathrm{PM}(\omega_s,\omega_i) = \int_{-L/2}^{+L/2} \mathrm{d}z\, \varphi(z,\omega_+)e^{-i(\omega_s-\omega_i)z/\bar{v}_g} \approx \sqrt{2\pi}\,\tilde{\varphi}(\frac{\omega_-}{\bar{v}_g},\omega_+) \tag{5.11}$$

In conclusion, the phase-matching function depends only on ω_- and it is therefore directed along the ω_+ direction.

On the other hand, for the spectral function, if the pulse spectrum matches the microcavity, we simply have the pump spectrum itself:

$$\phi_{\mathrm{spectral}}(\omega_+) = \mathrm{sech}\left(\frac{\omega_+ - \omega_p^{(0)}}{\Delta\omega_p}\right) \tag{5.12}$$

This term depends only on ω_+ and thus it is directed along the ω_- axis. Moreover, its width is directly related to the pump beam pulse temporal duration $\Delta\omega_p = 1.978/\tau_p$, for Fourier-Transform-limited pulses.

Figure 5.4 reports an example of a numerically simulated JSA for a Gaussian pump beam: from left to right we report the norm of the phase-matching function, of the spectral function and the norm of the JSA. The figure illustrates also the characteristics of each term.

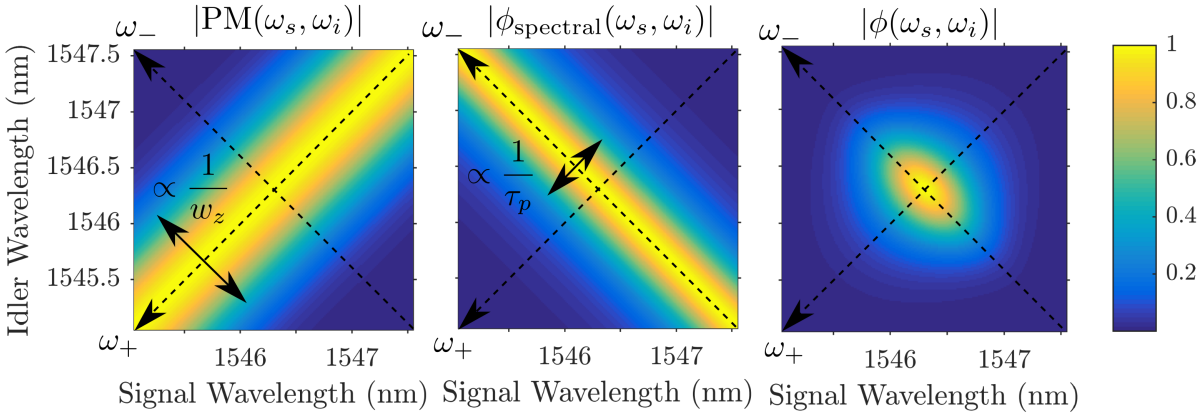

Figure 5.4: Numerically simulated norm of the phase-matching function, spectral function and norm of the resulting JSA, for a 0.3 mm-waist Gaussian pump beam with pulse duration $\tau_p = 4.5$ ps.

5.2.2 Shaping the JSA along the ω_+ and ω_- axes

We have seen that, in our approximations, the spectral function is directed along the ω_- axis, while the phase-matching function is directed along the ω_+ axis; these direction are orthogonal. Therefore, it is possible to tune the JSA along these two axes, encoding arbitrary shapes. This point illustrates the richness of the counter-propagating phase-matching under transverse pumping. Indeed, in a collinear geometry the phase-matching and the spectral function are both directed essentially along the ω_- axis (with the exception of the group velocity matching techniques described in section 5.1).

We now analyze a possible method to shape the JSA along the ω_+ and ω_- axes. To modify the JSA dimension along the ω_+ direction, it is sufficient to change the pump beam spectrum. Arbitrary spectral functions can be obtained by employing a pulse shaper, a device composed by dispersive elements and a spatial light modulator (SLM).

On the other hand, the phase-matching function is governed by the projection along z of the pump beam spatial profile, through a Fourier Transform. Therefore, a SLM can be employed to shape the beam spatial profile, thus tuning the JSA along the ω_- direction.

Both the phase matching and the spectral function are complex and take real values only if the pump spectrum and spatial profiles are real. Therefore, it is possible to control also the JSA phase by adding imaginary terms to the pump spatial and spectral profile (i.e. non-constant spatial and spectral phases).

In the following section, we apply this technique to shape the phase-matching function by acting on the pump beam spatial profile. We first modify the pump beam intensity profile to control the frequency correlations of the biphoton state. Then, by adding one or two phase steps to the spatial profile we control also the JSA phase.

5.3 JSA engineering via the pump beam intensity

In this section we experimentally demonstrate the JSA shaping via the pump beam intensity. The pump beam is tailored in intensity by using the method described in chapter 3, obtaining a Gaussian beam with arbitrary waist and a flat phase profile; the spatial phase profile along the z axis can be written as follows:

$$\phi_p(z, \omega_+) = \exp\left(-\frac{z^2}{w_z^2} + i\frac{\omega_+ \sin\theta\, z}{c}\right) \tag{5.13}$$

where the linear phase term is given by the pump incidence angle θ and has the only effect of translating the JSA along the ω_- axis from the degeneracy frequency.

Since the tailored pump beam has a waist projection along z ($w_z \leq 1$ mm) small compared to the waveguided length ($L = 1.9$ mm), the phase-matching function is approximately the Fourier Transform of the pump profile. It corresponds, in the biphoton frequency plane (ω_s, ω_i), to a stripe aligned along the diagonal, with a width ($\Delta\omega_-$) inversely proportional to the pump waist (w_z), as already illustrated in Figure 5.4. On the other hand, the pump beam is pulsed at 76 MHz with 6 ps pulses and, since the pulses are unchirped (Fourier-Transform limited), the spectral function is real valued. The resulting JSA is given by product of these two terms.

The first column of Figure 5.5 shows the experimentally measured JSIs, for four different values of pump beam waist w_z (from $w_z = 0.25$ mm to $w_z = 1$ mm), via the SET technique for a pump incidence angle θ slightly offset from the degenerate position θ_{deg}, as required by this reconstruction technique (see subsection 4.2.1 for a detailed description of the SET technique). The corresponding numerical simulations, reported in the second column of the figure, are in excellent agreement with the experimental data. Note that the only free parameters in the simulations are the positions of the Fabry-Pérot resonances, which have been adjusted on the experimental data.

Figure 5.5a reports the experimental JSI for a waist $w_z = 1$ mm. The joint spectrum is aligned along the principal diagonal (ω_+ axis), corresponding to a frequency correlated state. The rows below report the JSIs obtained for decreasing waist dimensions. We observe that the joint spectrum progressively stretches along the ω_- axis, reaching a frequency anti-correlated state in Figure 5.5g. For the intermediate value of waist $w_z = 0.6$ mm (Figure 5.5c), the width of the phase-matching and spectral functions are nearly equal, resulting in a frequency separable state.

In each panel of Figure 5.5 we show the calculated Schmidt number K, which quantifies the effective number of orthogonal frequency modes spanned by the biphoton wavefunction (see subsection 2.2.3 for a detailed description). For the simulations, the Schmidt number is directly calculated from the JSA, from its amplitude and phase. For the experimental JSIs we have deduced K assuming a flat phase (a reasonable approximation, since we are using unchirped pulses with flat spatial phase profile) so that the JSA can be retrieved as the squared root of the JSI. K initially decreases, reaches $K \approx 1$ for a frequency separable state, and increases again for a frequency anti-correlated state.

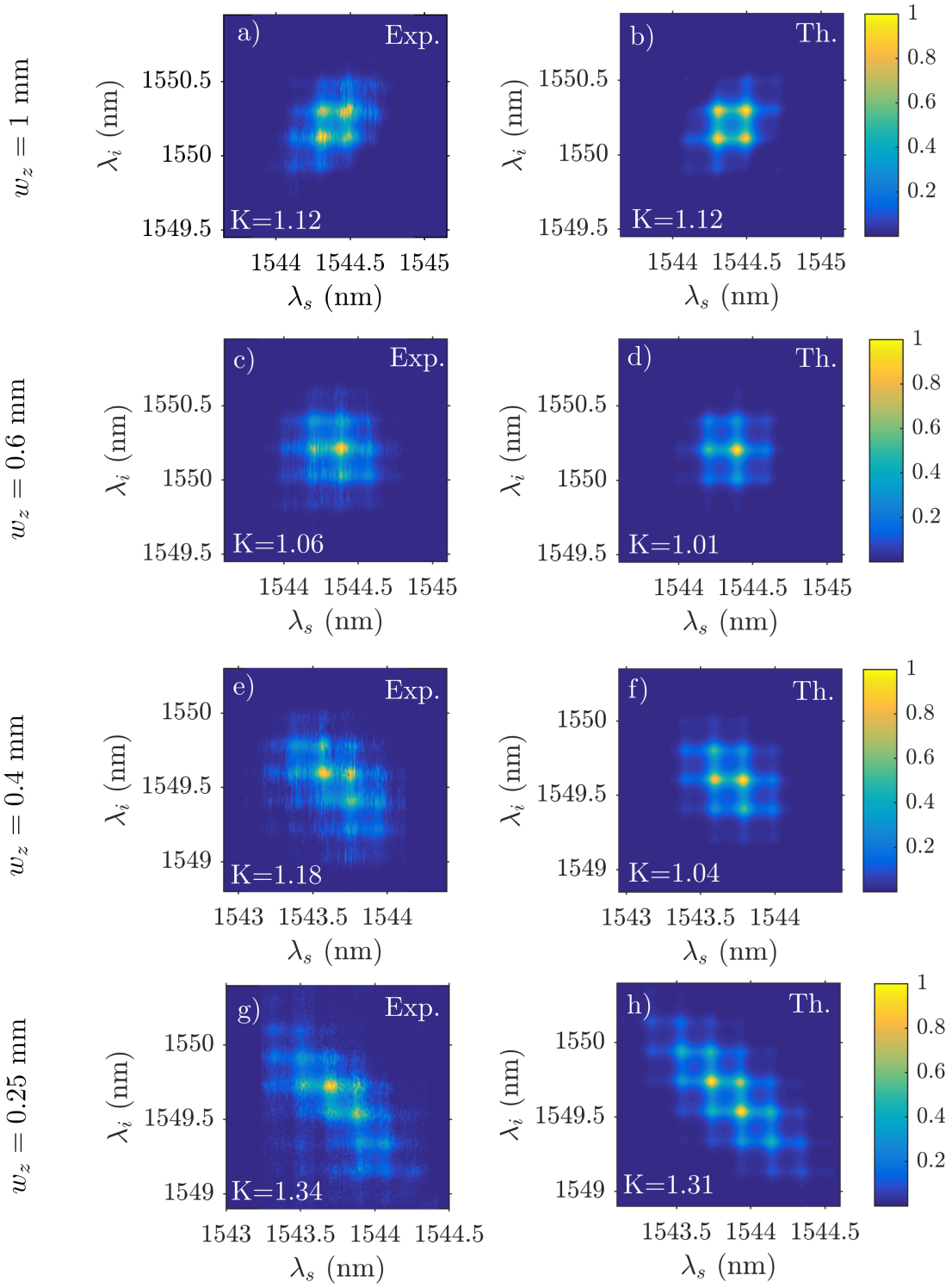

Figure 5.5: Experimentally measured JSIs, via the SET technique (first column) and corresponding numerical simulations (second column), for four different values of the pump beam waist. The pump is centered at 773.15 nm with 6 ps pulse duration and 150 mW average pump power incident on the sample.

Overall, the presented results demonstrate a flexible technique to frequency engineer the biphoton quantum state, generating correlated, non-correlated and anti-correlated frequency states. This flexibility allows to adapt the source to several quantum information applications [115, 117, 194], requiring a given type of frequency correlations.

5.3.1 Producing frequency state with a high dimensionality

For the biphoton states reported in Figure 5.5, the Schmidt number K does not exceed $K = 1.35$, meaning that the states contain only one dominant frequency mode. In the introduction of this thesis we have highlighted the interest of producing high-dimensional states of light; we now show that our technique can be used to combine flexibility and high dimensionality. To achieve this, two main paths can be followed: reducing the spectral function width while increasing the phase-matching function width, in order to generate frequency anti-correlated states, or the opposite way to generate frequency correlated states.

Let us start by considering the case of frequency anti-correlated states. A larger phase-matching function width can be obtained by pumping the sample with a smaller pump waist (e.g. 0.1 mm is easily achievable), while a smaller width of the spectral function can be achieved with longer pump pulses, corresponding to a narrower pump spectrum. Achievable values are 10 ps, using the same Ti:Sa laser, or 1 ns with a nanosecond pulsed laser. In these two cases the estimated Schmidt numbers are:

Waist 0.1 mm	Pulse Duration 10 ps	$K = 4.5$
Waist 0.1 mm	Pulse Duration 1 ns	$K = 440$

On the other hand, a frequency correlated state with high Schmidt number can be generated by pumping with a bigger waist and by using shorter pulses. Nonetheless, in both cases there are fundamental limitations. The waist is limited by the waveguide length ($\approx$ 2 mm), while the finesse of the vertical microcavity currently limits the pulse duration to a minimum of about 2 ps. However, fabricating a sample with a lower finesse is possible, even though it would slightly reduce the conversion efficiency of the source. Let us consider an easily achievable value of 0.5 ps. In these two cases the estimated Schmidt numbers are:

Waist 2 mm	Pulse Duration 2 ps	$K = 3.0$
Waist 2 mm	Pulse Duration 0.5 ps	$K = 11$

Another possibility is to focus the beam, making its spatial phase profile parabolic. For instance, starting from the non-correlated situation of Figure 5.5c (a 0.6 mm waist pump beam with 6 ps pulse duration) using a pump beam spot with a curvature radius of 10 cm would yield $K \approx 7$.

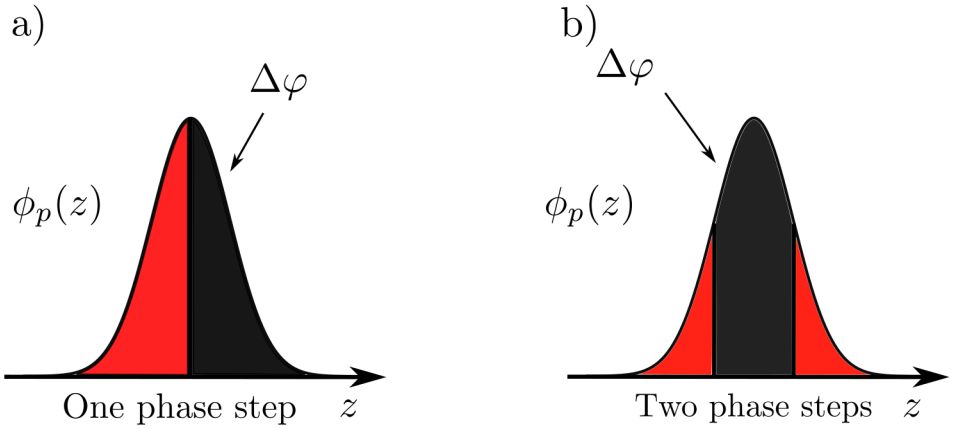

Figure 5.6: Pump beam spatial profile along z, $\phi_p(z)$: (a) for a single phase step and (b) for a double phase step.

5.4 JSA engineering via the pump beam spatial phase profile

So far, we have shaped the JSA by modifying the pump beam waist. However also the phase spatial profile influences the phase-matching function.

In this section we study the behavior of frequency correlations when phase steps are added to the beam spatial profile: first we consider the case of one single phase step and then of two equal and symmetric phase steps (double phase step).

5.4.1 Single phase step

Let us start by the case of a single phase step $\Delta\varphi$ between the two halves of the pump beam, as sketched in Figure 5.6a. Placing the pump spot at the center of the waveguide, the pump amplitude profile reads:

$$\phi_p(z) = \begin{cases} \exp\left(-\dfrac{z^2}{w_z^2} + i\dfrac{\omega_+ \sin\theta\, z}{c}\right) & z < 0 \\ \exp\left(-\dfrac{z^2}{w_z^2} + i\dfrac{\omega_+ \sin\theta\, z}{c} + i\Delta\varphi\right) & z > 0 \end{cases} \tag{5.14}$$

We fix the waist value to $w_z = 1$ mm and generate this spatial amplitude profile, by using the technique analyzed in subsection 3.2.2, for five different values of $\Delta\varphi$ $(0, \frac{1}{4}\pi, \frac{1}{2}\pi, \frac{3}{4}\pi, \pi)$.

The first column of Figure 5.7 reports the experimentally measured JSIs for these values of $\Delta\varphi$, via the SET technique for a pump incidence angle θ slightly offset from the degenerate position θ_{deg}. The pump beam is centered at 773.15 nm

with 4 ps pulse duration[2] and has an average pump power of 150 mW incident on the sample. Starting from a frequency correlated state (Figure 5.7a), for $\Delta\varphi = 0$, as $\Delta\varphi$ increases we observe the progressive appearance of a second lobe in the joint spectrum. When $\Delta\varphi = \pi$ the JSI is split into two lobes of equal intensity and vanishes along the diagonal axis between them.

These results are in good agreement with the numerical simulations, reported in the second column of Figure 5.7, for which we show also the calculated Schmidt number K. The Schmidt number increases when $\Delta\varphi$ increases and reaches $K = 2.24$ for $\Delta\varphi = \pi$, meaning that the states contains more than two dominant frequency modes. Here it is not possible to determine K from the experimental measurement of JSI, since the JSA has a non-flat phase structure, which cannot be measured by the SET technique.

The third column of Figure 5.7 shows the numerically simulated Chronocyclic Wigner Function W_- (CWF, introduced in section 2.3), corresponding to each phase step value. Starting from an almost Gaussian Wigner function when $\Delta\varphi = 0$, we observe the gradual appearance of a negative dip as $\Delta\varphi$ increases. Negative values of CWF are a signature of entanglement with non-Gaussian statistics [175, 206] as we will see more in detail in the next chapter. The residual small negativity (≈ -0.05) observed when $\Delta\varphi = 0$, Figure 5.7c, is due to the finite waveguide length which acts as a filter on the pump spatial profile and modifies the phase-matching function. In the case of a purely Gaussian phase-matching function the CWF is always positive.

5.4.2 Double phase step

We now shape the pump spatial profile with two equal and symmetric phase steps, as sketched in Figure 5.6b. The amplitude spatial profile can be written as:

$$\phi_p(z) = \begin{cases} \exp\left(-\dfrac{z^2}{w_z^2} + i\dfrac{\omega_+ \sin\theta\, z}{c}\right) & z < -\dfrac{L}{4} \\ \exp\left(-\dfrac{z^2}{w_z^2} + i\dfrac{\omega_+ \sin\theta\, z}{c} + i\Delta\varphi\right) & -\dfrac{L}{4} < z < +\dfrac{L}{4} \\ \exp\left(-\dfrac{z^2}{w_z^2} + i\dfrac{\omega_+ \sin\theta\, z}{c}\right) & z > +\dfrac{L}{4} \end{cases} \tag{5.15}$$

We keep the same waist as in the case of a single phase step ($w_z = 1$ mm) and we generate the pump beam for five values of $\Delta\varphi$ $(0, \frac{1}{4}\pi, \frac{1}{2}\pi, \frac{3}{4}\pi, \pi)$.

The first column of Figure 5.8 reports the experimentally measured JSI via the SET technique with the same experimental conditions as for the single phase step. The pump beam impinges on the sample slightly offset from the degenerate position, is centered at 773.15 nm with 6 ps pulse duration and has an average

[2]The pulse duration of the pump laser depends slightly on the mode-locking conditions and thus it may vary from one experiment to the other (in the range 4-6 ps). However this effect does not influence the overall results.

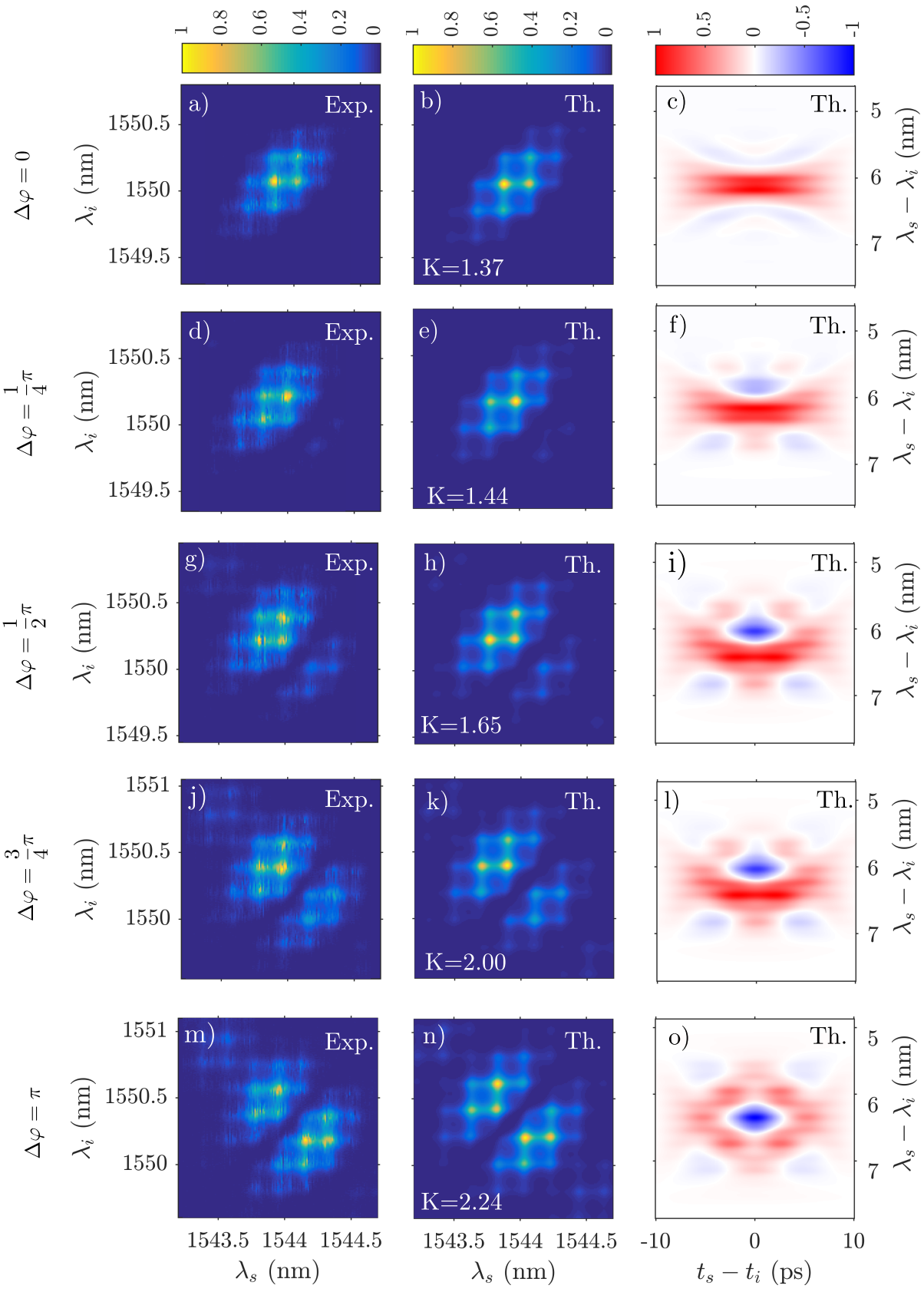

Figure 5.7: Gaussian pump beam with single phase step: experimentally measured JSIs via the SET technique (first column) and corresponding numerical simulations of the JSI (second column) and CWF W_- (third column). Each row corresponds to a phase step value $\Delta\varphi$.

pump power of 150 mW incident on the sample. Starting from an almost separable state (Figure 5.8a), the JSI gradually acquires two lateral peaks while the central one disappears. When $\Delta\varphi = \pi$ the JSI is split into two lobes of equal intensity and vanishes along the diagonal axis between them, as in the case of a single phase step (Figure 5.7m). The two JSIs look similar but the corresponding JSAs are very different, mostly due to their phase structure. In the following section and in the next chapter we will deeply analyze this feature, dealing with the biphoton state symmetry with respect to particle exchange.

The second column of Figure 5.8 displays the corresponding numerically simulated JSI for each value of $\Delta\varphi$, which are in good agreement with the experimental results. We report also the calculated Schmidt number K, deduced from the simulations. Looking at the obtained K values, we note that adding a single phase step or a double phase step produces essentially the same number of effective frequency modes.

Concerning the CWF W_-, whose simulations are reported in the third column of Figure 5.8, we note that, starting from an almost Gaussian function, two lateral negative dips gradually appear. As for the single phase step, the negativity of the CWF is a signature of non-Gaussian entanglement.

5.5 Effects of the JSA phase

As we have seen in the previous chapter, in our experimental situation, it is not possible to fully reconstruct the JSA, in both amplitude and phase. Indeed, so far we have experimentally measured only the JSA squared modulus, the JSI, but evidently also the phase is a parameter of paramount importance for frequency correlations.

Let us investigate three cases, reported in Figure 5.9, in which we employ the same experimental conditions (1 mm-waist Gaussian pump beam with 4 ps pulse duration and same incidence angle) except for the pump spatial phase profile. The first row displays the experimental JSI, measured via the SET technique, and the expected phase distribution of the JSA for a pump beam with a flat phase profile; the second row corresponds to the case with a single π phase step, while the third one to the case with a double π phase step. The simulated phases are calculated neglecting the Fabry-Pérot modulation which complicates the distribution but does not influence the frequency correlations because it affects the signal and idler photons independently[3].

We observe that the JSA phase distributions for these three cases directly reflect the pump spatial phase profile: in the first case the phase of the JSA is flat, in the second case it features a π step along the principal diagonal between the upper and lower part, while in the third case it presents a double π step on the sides of the principal diagonal, dividing the JSA phase in three regions. In particular, the

[3]In addition, if the pump beam has a large waist, compared to the waveguide dimension, also the sinc modulation of the phase-matching function modifies the JSA phase structure, because of the relative π phase shift between its peaks. However, since the lateral peaks have very small amplitudes with respect the principal one, they have a negligible influence on the frequency correlations.

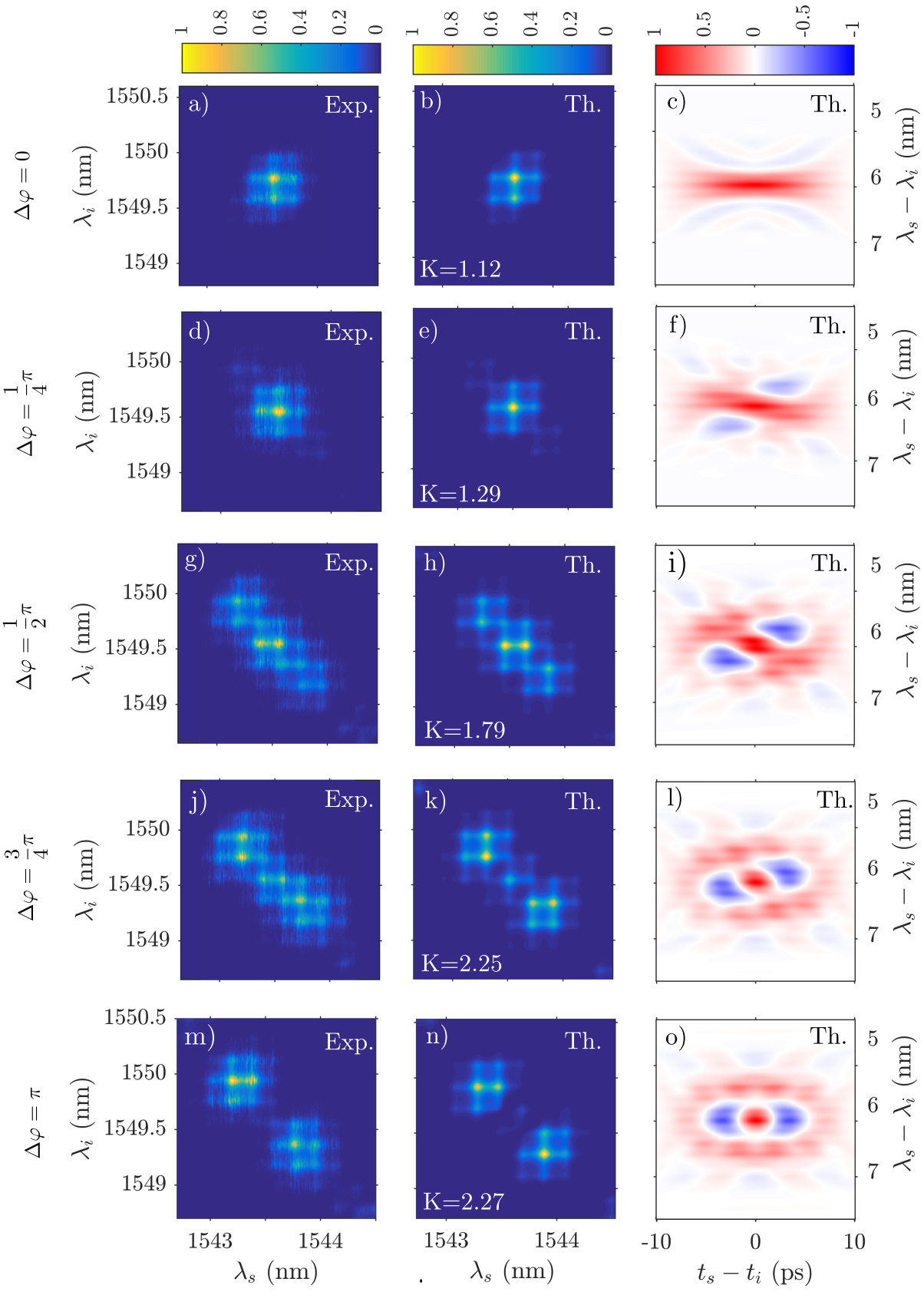

Figure 5.8: Gaussian pump beam with double phase step: experimentally measured JSIs via the SET technique (first column) and corresponding numerical simulations of the JSI (second column) and CWF W_- (third column). Each row corresponds to a phase step value $\Delta\varphi$.

second and third cases have fairly similar JSIs, but the phase distributions are very different. Indeed, in Figure 5.9e the two lobes have opposite phase values (0 and π), while in Figure 5.9h the two lobes have the same phase value.

In the previous chapter we have presented some techniques that should enable to reconstruct these phase distributions, even if until now they have been employed to measure only parabolic phase profiles and not phase steps. However, since they require complex optical setups, for the moment we choose to adopt another strategy: it is possible to retrieve the relative phase between the JSI lobes by taking advantage of the state symmetry with respect to particle exchange. In the next chapter we will deal extensively with this notion and we will detail how it can be measured; here we give only a quick introduction.

Let us consider the case in which we pump the sample at the frequency degeneracy angle θ_{deg}, in this case the flat phase and the double phase step cases would have symmetric JSAs with respect to the ω_+ diagonal, while the single phase step case would have an anti-symmetric JSA, with the two lobes having a relative phase of π. The symmetry or anti-symmetry of the JSA with respect to the diagonal characterize the behavior of the quantum state when the two photons are exchanged; therefore we speak of symmetry or anti-symmetry of the wavefunction under particle exchange.

In the next chapter we will show how the symmetry or the anti-symmetry of the wavefunction under particle exchange determines the output of a Hong-Ou-Mandel interferometer [205], which can be therefore used to retrieve partial information on the JSA phase.

5.6 Conclusions

In the first part of this chapter we have given an overview of the techniques, proposed in the literature, to control the frequency correlations of a biphoton state. We have stressed the differences between post-manipulation techniques, which modify the quantum state after the generation, and direct generation techniques, which modify the source or the pump beam characteristics to directly obtain the target state. A particular attention has been given to the techniques that can be integrated into chip-based devices.

Afterwards, we have analyzed the counter-propagating phase-matching geometry under transverse pumping, highlighting the relation between the pump spectral and spatial properties and the generated biphoton state, which allows to directly shape the JSA along the ω_- and ω_+ axes. An experimental demonstration of this shaping technique has then been performed by shaping the pump spatial profile and reconstructing the JSI via the SET technique.

As a first step, we have tailored the pump beam waist and demonstrated the generation of frequency correlated, separable and anti-correlated biphoton states. The second degree of freedom we have employed to shape the JSA is the pump beam spatial phase profile: by applying one or two variable phase steps to it, the JSA acquires the same phase step and splits into two lobes, as demonstrated by the experimental measurements. However, the JSA phase cannot be directly retrieved with our implementation of the SET technique, therefore in the next chapter we

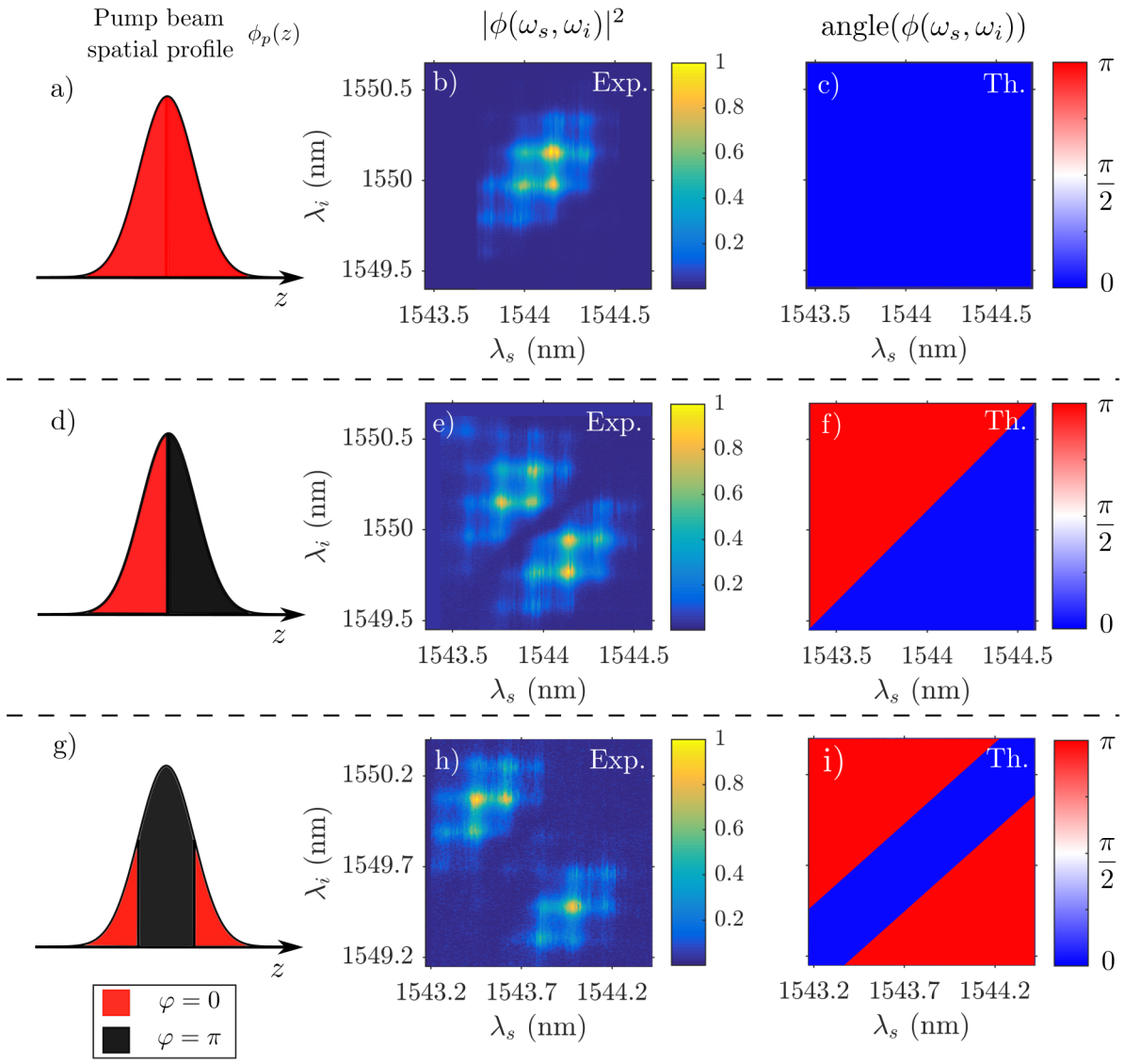

Figure 5.9: Pump beam spatial profile $\phi_p(z)$ (first column), experimental JSI (second column) measured by the SET technique and simulated JSA phase (third column) for three different phase profiles: a flat phase profile in the first row, a single π phase step in the second row and a double π phase step in the third one. The pump beam has a waist of 1 mm, is centered at 773.15 nm and its pulse duration is 4 ps.

will employ a Hong-Ou-Mandel interformeter to further characterize the generated biphoton states and validate the engineering of the JSA phase.

As conclusive remarks, we want to note that here we have tuned the JSA, both in phase and amplitude, but only along the ω_- axis, by modifying the phase-matching function. A simultaneous control along both axes can be obtained by tailoring both the spectral and the spatial profile of the pump beam. This can be easily realized with a pulse shaper, composed by a SLM and a diffractive grating, and the setup described in chapter 3 to shape the pump spatial profile. Once the spectral and phase-matching functions of the target JSA have been decided, it is easy to retrieve the corresponding pump spatial and spectral profile to generate such JSA. Doing so, it would be possible to obtain an almost arbitrary JSA distribution.

In conclusion, in this chapter we have demonstrated that the counter-propagating phase-matching scheme under transverse pumping enables the shaping of the wavefunction of the generated biphoton state, in a flexible, re-programmable and tunable way. The experimental demonstration, carried out in a semiconductor integrated device at room temperature, opens the way to the source integration and employment in more complex photonic chips.

Chapter 6

Control of the Spectral Wavefunction Symmetry and Exchange Statistics

In the previous chapter we have demonstrated the shaping of the joint spectrum of the biphoton state emitted by our counter-propagating source, by tuning the pump beam spatial profile. In particular, we have shown with numerical simulations that, by adding a phase step to the pump beam spatial profile, the symmetry of the JSA of the corresponding biphoton state can be controlled, passing from symmetric to anti-symmetric.

Anti-symmetric high-dimensional biphoton states have several applications in quantum information, for example to study the effect of exchange statistics in quantum simulation problems [86, 110, 226] and in communication and computation protocols [227, 228].

The symmetry control of high-dimensional entangled states has been demonstrated previously in the spatial degree of freedom [120, 229], but using bulk sources only. In the frequency domain, a recent work demonstrated the on-chip generation of anti-symmetric biphoton frequency states, by tailoring the nonlinearity of a

PPKTP crystal with domain engineering [65]. This approach leads to sources producing very high-quality quantum states, but without the possibility of tuning it. Another work developed a method to control two-color entanglement and generate frequency anti-symmtric states [224], but this approach requires two passages in a bulk source and post-manipulation with a dispersive element, and it is limited to the production of two-color entangled states. On the other hand, Ansari et al. demonstrated the integrated and post-manipulation-free control of the spectrum of biphotons by engineering the spectrum of the pump field [41]. However, this approach tailors the spectral part of the joint spectrum, which is directed along the ω_- direction, and therefore always produces spectral wavefunctions that are symmetric under particle exchange.

In this chapter we will employ two-photon interference on a beamsplitter (Hong-Ou-Mandel effect) as a means to experimentally characterize the symmetry of the biphoton state generated by our counter-propagating source and demonstrate the direct generation of anti-symmetric biphoton frequency states.

We first study theoretically the behavior of a biphoton state in a Hong-Ou-Mandel (HOM) interferometer, detailing the relation between the resulting interferogram and the symmetry of the wavefunction, which is related to its JSA in case of biphoton frequency states. Then, we show that the HOM interferogram is proportional to the cut at $\omega_- = \omega_s - \omega_i = 0$ of the Chronocyclic Wigner Function W_-, and that it is possible to generalize the HOM experiment to retrieve the entire W_- function.

Finally, we report experimental HOM measurements and the corresponding numerical simulations relative to the two cases studied in the previous chapter: the biphoton state generated by a Gaussian pump beam with a flat phase and that generated by a Gaussian beam with a phase step.

6.1 Hong-Ou-Mandel experiment

The Hong-Ou-Mandel experiment [205] is the most popular arrangement of two-photon interference: two photons enter in a 50:50 beamsplitter and interfere. Depending on their global wavefunction they may exit from the same output port (bunching) or from different output ports (anti-bunching).

Let us start with a simple situation to demonstrate the physical principle of the effect. Figure 6.1 shows a sketch of the HOM interferometer. We consider two independent single photons, entering the beamsplitter from port 1 and port 2, indistinguishable in all their degrees of freedom. We will thus employ the creation and annihilation operators $\hat{a}_1^\dagger$, $\hat{a}_1$ for the first photon and $\hat{a}_2^\dagger$, $\hat{a}_2$ for the second photon. The input wavefunction reads:

$$|\Psi\rangle = \hat{a}_1^\dagger \hat{a}_2^\dagger |0\rangle \tag{6.1}$$

We now focus on the beamsplitter, which is the core of the HOM interferometer: it mixes the two photons according to its transformation matrix M. Considering a lossless symmetric 50:50 beamsplitter, the matrix M can be written as [230]:

$$M = \frac{1}{\sqrt{2}} \begin{pmatrix} 1 & i \\ i & 1 \end{pmatrix} \tag{6.2}$$

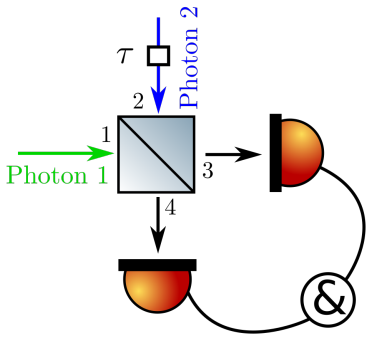

Figure 6.1: Sketch of the HOM interferometer. The photons impinge on a 50:50 beamsplitter, from the ports 1 and 2. The interference is observed by recording the coincidences between the counts at the output ports 3 and 4 as a function of the relative delay τ.

Applying this matrix to the $\hat{a}$ operators of the input ports 1 and 2 we find:

$$\begin{pmatrix} \hat{a}_3 \\ \hat{a}_4 \end{pmatrix} = \frac{1}{\sqrt{2}} \begin{pmatrix} 1 & i \\ i & 1 \end{pmatrix} \begin{pmatrix} \hat{a}_1 \\ \hat{a}_2 \end{pmatrix} \tag{6.3}$$

which gives the output operators 3 and 4, as a function of the input operators. From this relation we retrieve the relation between the $\hat{a}^\dagger$ operators:

$$\begin{pmatrix} \hat{a}_1^\dagger \\ \hat{a}_2^\dagger \end{pmatrix} = \frac{1}{\sqrt{2}} \begin{pmatrix} 1 & i \\ i & 1 \end{pmatrix} \begin{pmatrix} \hat{a}_3^\dagger \\ \hat{a}_4^\dagger \end{pmatrix} \tag{6.4}$$

Transforming the input wavefunction (Equation 6.1) with the beamsplitter transformation (Equation 6.4) we retrieve:

$$|\Psi\rangle = \frac{1}{2}(\underbrace{i\hat{a}_3^\dagger\hat{a}_3^\dagger + i\hat{a}_4^\dagger\hat{a}_4^\dagger}_{\text{I}} + \underbrace{\hat{a}_3^\dagger\hat{a}_4^\dagger - \hat{a}_4^\dagger\hat{a}_3^\dagger}_{\text{II}})\,|0\rangle = \frac{1}{2}i(\hat{a}_3^\dagger\hat{a}_3^\dagger + \hat{a}_4^\dagger\hat{a}_4^\dagger)\,|0\rangle \tag{6.5}$$

where the probability amplitudes related to case II cancel out, since the photons are indistinguishable in all degrees of freedom and thus $\hat{a}_3$ and $\hat{a}_4$ commute, $[\hat{a}_3, \hat{a}_4] = 0$. This is the bunching effect: the two photons always exit from the same port.

It is interesting to note that in a HOM interferometer the interference does not arise between the two photons, but between the probability amplitudes associated to the four possible paths (both photons are reflected, both are transmitted, or one is reflected while the other is transmitted). This point highlights an important feature of the HOM interference: since it is a second-order interference effect, it is phase-independent. Indeed, an eventual phase shift in one of the two paths would affect the probability amplitudes of the four situations described above, without any effect on the interference.

So far we have considered the two photons as indistinguishable in all their degrees of freedom. Nonetheless, it is possible to tune their distinguishability level by adding a time delay τ in one of the two arms, thus modifying their relative arrival times. As the time delay τ increases, the interference effect gradually disappears

and the coincidence rate exhibits a characteristic dip, whose width is related to the photon coherence time.

All the previous considerations are valid for two independent single photons. In case of an entangled biphoton state, the HOM interference is not simply the interference of two single photons. It is the interference of the whole quantum state itself: it is not possible to describe the effect in the "two photons picture" and it is necessary to shift the description in a "biphoton picture". The entangled photon pair has to be taken as whole. One striking example of this property is the work of Pittman et al. [231], in which the authors observed an interference effect even when the time delay between the photons is compensated after the beamsplitter. This result cannot be explained simply as the interference between two photons, as they do not "arrive" at the same time on the beamsplitter.

The HOM effect has been employed in the last decades in a wide range of applications, such as single-photon emitter characterizations [232], implementation of photonic Bell state measurement for entanglement swapping or teleportation [233], tailoring high-dimensional photonic entangled states [229] and time delay measurements [234, 235].

6.2 Biphoton frequency state in a HOM interferometer

In the previous section we have taken in consideration the single-mode version of the HOM, with independent photons. Here, we consider an arbitrary frequency entangled biphoton state emitted by our source and we calculate the HOM coincidence probability, highlighting some generic features.

The state emitted by the source can be written as:

$$|\Psi\rangle = \iint \mathrm{d}\omega_s \mathrm{d}\omega_i \phi(\omega_s, \omega_i) \hat{a}^\dagger_{s,V}(\omega_s) \hat{a}^\dagger_{i,H}(\omega_i) \, |0\rangle \tag{6.6}$$

where we consider the VH interaction, with TM-polarized signal photon and TE-polarized idler photon, and $\phi(\omega_s, \omega_i)$ is a generic JSA, whose normalization condition reads:

$$\iint \mathrm{d}\omega_s \mathrm{d}\omega_i |\phi(\omega_s, \omega_i)|^2 = 1 \tag{6.7}$$

In order to obtain interference, the signal and idler paths must be indistinguishable and thus we rotate the polarization of the idler photon to align it with that of the idler photon. From now on, to keep a lighter notation, we neglect the polarization subscript for the $\hat{a}^\dagger$ and $\hat{a}$ operators.

The delay line, placed in the idler path, induces a time delay τ. At the beamsplitter the wavefunction reads:

$$|\Psi\rangle = \iint \mathrm{d}\omega_s \mathrm{d}\omega_i \phi(\omega_s, \omega_i) \hat{a}^\dagger_1(\omega_s) \hat{a}^\dagger_2(\omega_i) e^{-i\omega_i \tau} \, |0\rangle \tag{6.8}$$

where we have identified the signal (idler) photon with the input port 1 (port 2) of the beamsplitter. By applying Equation 6.4, we express the wavefunction as a

function of the beamsplitter output operators:

$$|\Psi\rangle = \frac{1}{2}\iint \mathrm{d}\omega_s \mathrm{d}\omega_i\, \phi(\omega_s,\omega_i)\Big(\hat{a}_3^\dagger(\omega_s)\hat{a}_4^\dagger(\omega_i) + i\hat{a}_3^\dagger(\omega_s)\hat{a}_3^\dagger(\omega_i) + i\hat{a}_4^\dagger(\omega_s)\hat{a}_4^\dagger(\omega_i) - \hat{a}_3^\dagger(\omega_i)\hat{a}_4^\dagger(\omega_s)e^{-i\omega_i\tau}\Big)|0\rangle \tag{6.9}$$

At this point, to calculate the coincidence probability at the detectors we need to introduce the projection operator which models each detector, assuming a flat frequency response. Following [236] we define the projector operator $\hat{P}_3$ for the output port 3:

$$\hat{P}_3 = \int \mathrm{d}\omega_3\, \hat{a}_3^\dagger(\omega_3)\,|0\rangle\,\langle 0|\,\hat{a}_3(\omega_3) \tag{6.10}$$

and $\hat{P}_4$ for the output mode 4:

$$\hat{P}_4 = \int \mathrm{d}\omega_4\, \hat{a}_4^\dagger(\omega_4)\,|0\rangle\,\langle 0|\,\hat{a}_4(\omega_4) \tag{6.11}$$

The coincidence probability of detecting one photon in each mode is:

$$P_c = \mathrm{Tr}\Big[|\Psi\rangle\,\langle\Psi|\,\hat{P}_3\otimes\hat{P}_4\Big] = \langle\Psi|\hat{P}_3\otimes\hat{P}_4|\Psi\rangle \tag{6.12}$$

Therefore, we can define the coincidence operator $\hat{M}$:

$$\hat{M} = \hat{P}_3\otimes\hat{P}_4 = \int \mathrm{d}\omega_3\, \hat{a}_3^\dagger(\omega_3)\,|0\rangle\,\langle 0|\,\hat{a}_3(\omega_3)\int \mathrm{d}\omega_4\, \hat{a}_4^\dagger(\omega_4)\,|0\rangle\,\langle 0|\,\hat{a}_4(\omega_4) \tag{6.13}$$

The coincidence probability becomes:

$$\begin{aligned} P_c(\tau) = \langle\Psi|\hat{M}|\Psi\rangle = \\ &\langle 0|\,\frac{1}{2}\iint \mathrm{d}\omega_s'\mathrm{d}\omega_i'\,\phi^*(\omega_s',\omega_i')\Big(\hat{a}_3(\omega_s')\hat{a}_4(\omega_i') - \hat{a}_3(\omega_i')\hat{a}_4(\omega_s')e^{+i\omega_i'\tau}\Big) \\ &\times \int \mathrm{d}\omega_3\, \hat{a}_3^\dagger(\omega_3)\,|0\rangle\,\langle 0|\,\hat{a}_3(\omega_3)\int \mathrm{d}\omega_4\, \hat{a}_4^\dagger(\omega_4)\,|0\rangle\,\langle 0|\,\hat{a}_4(\omega_4) \\ &\times \frac{1}{2}\iint \mathrm{d}\omega_s\mathrm{d}\omega_i\,\phi(\omega_s,\omega_i)\Big(\hat{a}_3^\dagger(\omega_s)\hat{a}_4^\dagger(\omega_i) - \hat{a}_3^\dagger(\omega_i)\hat{a}_4^\dagger(\omega_s)e^{-i\omega_i\tau}\Big)|0\rangle \end{aligned} \tag{6.14}$$

where for each wavefunction we have kept only the cross terms ($\hat{a}_3^\dagger\hat{a}_4^\dagger$), which give rise to a coincidence count. By applying the $\hat{a}$ and $\hat{a}^\dagger$ operators to the vacuum state we obtain:

$$\begin{aligned} P_c(\tau) =& \frac{1}{4}\int \mathrm{d}\omega_s'\int \mathrm{d}\omega_i'\int \mathrm{d}\omega_s\int \mathrm{d}\omega_i\int \mathrm{d}\omega_3\int \mathrm{d}\omega_4 \\ &\phi^*(\omega_s',\omega_i')e^{+i\omega_i'\tau}\Big[\delta(\omega_s'-\omega_3)(\omega_i'-\omega_4) - \delta(\omega_i'-\omega_3)(\omega_s'-\omega_4)\Big] \\ &\phi(\omega_s,\omega_i)e^{-i\omega_i\tau}\Big[\delta(\omega_s-\omega_3)(\omega_i-\omega_4) - \delta(\omega_i-\omega_3)(\omega_s-\omega_4)\Big] \end{aligned} \tag{6.15}$$

Integrating over $\omega_s', \omega_i', \omega_s, \omega_i$ and applying the Dirac deltas yields:

$$\begin{aligned} P_c(\tau) =& \frac{1}{4}\iint \mathrm{d}\omega_3\mathrm{d}\omega_4\Big[|\phi(\omega_3,\omega_4)|^2 + |\phi(\omega_4,\omega_3)|^2 \\ &- \phi^*(\omega_3,\omega_4)\phi(\omega_4,\omega_3)e^{i(\omega_4-\omega_3)\tau} - \phi^*(\omega_4,\omega_3)\phi(\omega_3,\omega_4)e^{i(\omega_3-\omega_4)\tau}\Big] \end{aligned} \tag{6.16}$$

and by employing the normalization of the JSA (Equation 6.7) we obtain:

$$\begin{aligned} P_c(\tau) =& \frac{1}{2} - \frac{1}{4}\iint \mathrm{d}\omega_3\mathrm{d}\omega_4\Big(\phi^*(\omega_3,\omega_4)\phi(\omega_4,\omega_3)e^{i(\omega_4-\omega_3)\tau} + \mathrm{c.c.}\Big) \\ =& \frac{1}{2} - \frac{1}{2}\,\mathrm{Re}\left[\iint \mathrm{d}\omega_3\mathrm{d}\omega_4\phi^*(\omega_4,\omega_3)\phi(\omega_3,\omega_4)e^{i(\omega_4-\omega_3)\tau}\right] \end{aligned} \tag{6.17}$$

This expression gives the probability of a coincidence count at the detectors, when the input state is a biphoton with the JSA $\phi(\omega_3, \omega_4)$. Since the calculation has been performed in the frequency framework and we have considered detectors with flat frequency response, the result includes coincidence counts with arbitrary time difference. A more detailed calculation should take into account also the detector time resolution, which impacts the detector frequency response. However, since we are interested in time-integrated HOM measurements and not time-resolved ones, the result we have obtained is sufficient for our experimental needs.

Equation 6.17 shows that the coincidence probability $P_c(\tau)$ is the difference between the constant term 1/2 and an interference term, governed by the relative delay τ between the two paths. This term can increase the coincidence probability, leading to a bunching effect ($P_c(\tau) < 1/2$), or decrease it, leading to an anti-bunching effect ($P_c(\tau) > 1/2$), depending on the JSA.

6.2.1 Interference conditions

We start with a general analysis, following [237], on the interference behavior for $\tau = 0$, by looking at the joint spectrum of the biphoton state. From Equation 6.17 we note that the necessary and sufficient condition for the absence of interference is:

$$\iint \mathrm{d}\omega_3\mathrm{d}\omega_4\Big(\phi^*(\omega_3,\omega_4)\phi(\omega_4,\omega_3) + \mathrm{c.c.}\Big) = 0 \tag{6.18}$$

This conditions corresponds to an equal probability of the two photons exiting from the same output and the two photons exiting from different outputs (i.e. $P_c(\tau = 0) = 1/2$). From the previous equation we can derive a sufficient but not necessary condition for the absence of interference:

$$|\phi(\omega_3,\omega_4)\phi(\omega_4,\omega_3)| = 0 \tag{6.19}$$

which means that, if the joint spectrum of the biphoton state has no overlap with its symmetric with respect to the principal diagonal (ω_+ axis), the interference cannot occur.

On the other hand, a sufficient and necessary condition for perfect bunching (i.e. $P_c(\tau = 0) = 0$) is that the joint spectrum of the biphoton state is mirror symmetric over the entire frequency range:

$$\phi(\omega_3,\omega_4) = \phi(\omega_4,\omega_3) \tag{6.20}$$

This condition can be satisfied by either a frequency entangled state or a separable state. Let us consider two examples to better clarify:

- a frequency separable state centered along the degeneracy would lead to a perfect bunching;

- an anti-correlated state, stretched along the ω_- axis, with a mirror symmetric spectrum, would also lead to a perfect bunching.

In conclusion a perfect bunching proves that the biphoton state has a perfectly symmetric joint spectrum, but it does not give information about the frequency entanglement.

In the case of a mirror symmetric JSA, the HOM coincidence probability (Equation 6.17) becomes the Fourier Transform of the JSI along $\omega_- = \omega_3 - \omega_4$:

$$P_c(\tau) = \frac{1}{2} - \frac{1}{2}\iint \mathrm{d}\omega_3 \mathrm{d}\omega_4 |\phi(\omega_3, \omega_4)|^2 e^{i(\omega_4 - \omega_3)\tau} \tag{6.21}$$

Therefore, the shape of the interferogram is governed by the shape of the JSI: a Gaussian JSI gives rise to a Gaussian dip, while a sinc^2 shaped JSI gives rise to a triangular dip. In the next paragraph we will analyze extensively the link between the JSA and the HOM interferogram, in the case of a Gaussian pump beam.

Coming back to the general analysis of Equation 6.17, we note that the necessary and sufficient condition for perfect anti-bunching (i.e. $P_c(\tau = 0) = 1$) is that the biphoton spectrum is anti-symmetric over the whole frequency range:

$$\phi(\omega_3, \omega_4) = -\phi(\omega_4, \omega_3) \tag{6.22}$$

Contrary to the case of perfect bunching, a frequency separable state (e.g. two non-entangled single photons) cannot give anti-bunching in any way. This property can be easily demonstrated analytically by considering two independent single photons and showing that $P_c(\tau = 0) \leq 1/2$ [237]. Therefore, anti-bunching $P_c > 1/2$ at $\tau = 0$ is a signature of entanglement of the biphoton state [238].

6.2.2 Gaussian phase-matching function

So far we have analyzed the coincidence probability, Equation 6.17, from a general point of view. Here we introduce the specific biphoton state emitted by our source. As we have seen in section 2.2, under our experimental conditions, the JSA is separable along the ω_+ and ω_- directions:

$$\phi(\omega_3, \omega_4) = \chi_\Gamma \, \mathrm{PM}(\omega_-) \, \phi_{\mathrm{spectral}}(\omega_+) \tag{6.23}$$

where, for the moment, we neglect the Fabry-Pérot modulation induced by the waveguide facet reflectivity. Substituting the above expression in the HOM coincidence probability (Equation 6.17) and changing the integration variables form ω_3, ω_4 to ω_+, ω_- yields:

$$\begin{aligned} P_c(\tau) = & \frac{1}{2} - \frac{1}{2}|\chi_\Gamma|^2 \int \mathrm{d}\omega_+ |\phi_{\mathrm{spectral}}(\omega_+)|^2 \\ & \times \mathrm{Re}\left[\int \mathrm{d}\omega_- \mathrm{PM}^*(-\omega_-)\mathrm{PM}(\omega_-)\, e^{-i\omega_-\tau}\right] \end{aligned} \tag{6.24}$$

By plugging in the normalization condition we obtain:

$$P_c(\tau) = \frac{1}{2} - \frac{1}{2}\frac{\mathrm{Re}\left[\int \mathrm{d}\omega_- \, \mathrm{PM}^*(-\omega_-)\mathrm{PM}(\omega_-)\, e^{-i\omega_-\tau}\right]}{\int \mathrm{d}\omega_- \, |\mathrm{PM}(\omega_-)|^2} \tag{6.25}$$

where we note that the two-photon interference is governed only by the phase-matching function, which is directed along ω_-.

In order to illustrate this result, we now consider a Gaussian pump beam of waist w_z impinging on the waveguide with an angle θ; we refer to Figure 2.1. The resulting phase-matching function, if the waist w_z is smaller than the waveguide length L, is given by Equation 5.9:

$$\mathrm{PM}(\omega_-) = \sqrt{\pi} w_z \exp\left[-\left(\frac{\omega_- - \omega_-^{(0)}}{\Delta\omega_-}\right)^2\right] \tag{6.26}$$

where $\Delta\omega_- = 2\bar{v}_g/w_z$ is the phase-matching width and $\omega_-^{(0)} = \omega_p(\sin\theta - \sin\theta_{\mathrm{deg}})\bar{v}_g/c$ is its central position on the ω_- axis. By inserting this phase-matching function into Equation 6.25 the coincidence probability becomes:

$$P_c(\tau) = \frac{1}{2} - \frac{1}{2}\exp\left[-\left(\frac{\tau}{\Delta\tau}\right)^2\right]\exp\left[-2\left(\frac{\omega_-^{(0)}}{\Delta\omega_-}\right)^2\right] \tag{6.27}$$

with $\Delta\tau = \dfrac{2\sqrt{2}}{\Delta\omega_-} = \dfrac{\sqrt{2}w_z}{\bar{v}_g}$. When the two photons are degenerate in frequency ($\omega_-^{(0)} = 0$) the JSA is perfectly mirror symmetric: the HOM interferogram then features a dip, which reaches zero for $\tau = 0$ and it is described by the first exponential. In this particular case, the dip has a Gaussian shape of width $\Delta\tau$, controlled by the pump beam waist w_z. Conversely, when the two photons have different central frequencies (i.e. the JSA is offset from the degeneracy, $\omega_-^{(0)} \neq 0$) the shape of the dip is preserved but with a reduced visibility, given by the value of the second exponential in Equation 6.27.

The solid blue curve in Figure 6.2 reports the simulation of the HOM interferogram for the biphoton state generated by a Gaussian pump beam with a 1 mm waist, impinging at the degeneracy angle on our source.

Fabry-Pérot cavity effect

In the previous analysis of the HOM interferogram the Fabry-Pérot cavity has not been considered. The cavity effect modulates the JSA by creating resonance peaks, which corresponds, in the time domain, to the possibility for the photons to exit from the cavity after a half-integer or an integer number of round trips. Here we do not consider the case in which a signal photon exits from the idler side and viceversa (i.e. after half-integer number of round trips), because we employ polarizers together with frequency passband filters to select only one interaction, thus discarding this type of events.

In this configuration, the dashed curve in Figure 6.2 reports the numerically simulated HOM interferogram for the biphoton state generated by a Gaussian pump beam with a 1 mm waist, impinging at the degeneracy angle on a 1.9 mm-long waveguide, considering the Fabry-Pérot effect. The satellite dips at ± 40 ps are due to the interference between a doubly reflected photon (i.e. a photon having done a complete round trip) and a directly transmitted one. More satellite dips

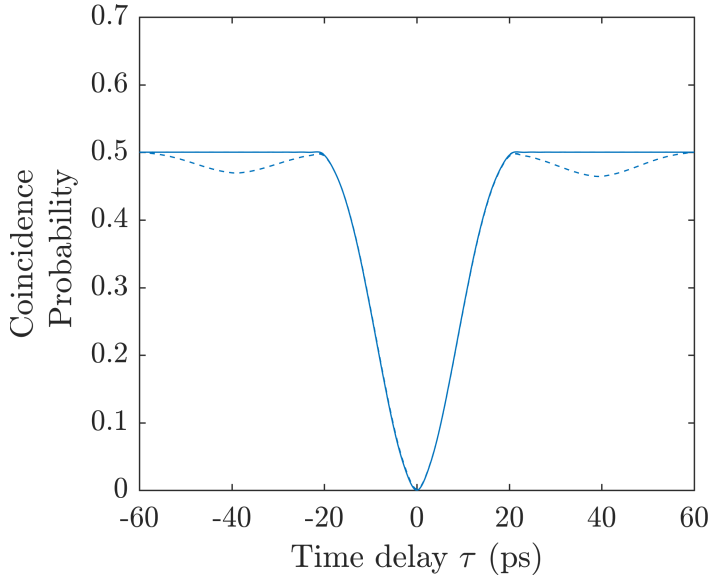

Figure 6.2: Numerically simulated HOM interferogram for a biphoton state generated by a Gaussian pump beam of 1 mm waist, impinging at the degeneracy angle on a 1.9 mm-long waveguide. Solid blue line: without the Fabry-Pérot cavity effect. Dashed blue line: with the Fabry-Pérot cavity effect.

are present at integer multiples of the round trip period (outside the plotting region of Figure 6.2), but, since the probability of higher-order reflections is low, their amplitude is very weak. Note that these satellite dips are present because the HOM interference is not resolved in time. If the detectors could distinguish the directly transmitted photon from the reflected one (i.e. having sufficient time resolution), the satellite dips would disappear.

We mention that the interpretation given above does not fully take into account the nature of the HOM interference. Indeed, the interference does not take place between photons, but between the probability amplitudes related to each possible path, given that they are indistinguishable. Performing a complete quantum calculation it is possible to show that, depending on the JSA, additional side dips or peaks may appear at half round trip periods. However, it is possible to show that in our case, due to the JSA shape of the biphoton state we consider, there are no satellite dips/peaks at half round trip periods, but only dips at integer round trips (see Giorgio Maltese's PhD Thesis [158]).

In the following, the HOM interferograms are calculated by inserting the numerically simulated JSA, which already includes the Fabry-Pérot modulation, into the HOM coincidence probability (Equation 6.17).

6.2.3 HOM interferogram as a probe of the wavefunction symmetry

As a conclusion of this section on the study of the behavior of a biphoton frequency state in a HOM interferometer, we want to recall the coincidence probability cal-

culated in Equation 6.17:

$$\boxed{P_c(\tau) = \frac{1}{2} - \frac{1}{2}\,\mathrm{Re}\left[\iint \mathrm{d}\omega_i \mathrm{d}\omega_j \phi^*(\omega_j, \omega_i)\phi(\omega_i, \omega_j) e^{i(\omega_j - \omega_i)\tau}\right]} \tag{6.28}$$

This equation establishes a direct link between the HOM interferogram and the biphoton JSA, allowing to employ the HOM interferometer to directly probe the biphoton state. In particular, as we have seen, perfect bunching and perfect anti-bunching effects are related to a mirror symmetric and mirror anti-symmetric JSA, respectively, properties which depend on both the JSA amplitude and phase. This enables to go beyond the JSI reconstruction described in chapter 4 and acquire partial information on the JSA phase.

In this section we have analyzed the HOM interferometer from the point of view of a frequency entangled biphoton state, however it is possible to infer a more general behavior. Before the beamsplitter the two photons are distinguishable by their paths (i.e. the wavefunction spatial part), but when they are mixed by the beamsplitter they become indistinguishable. Since photons are bosonic particles, their total wavefunction must be symmetric under particle exchange. Therefore, if the JSA is anti-symmetric, the spatial part of the wavefunction becomes anti-symmetric too (anti-bunching behavior), in order to preserve the total symmetry of the wavefunction. Conversely, if the JSA is mirror symmetric, the spatial part of the wavefunction becomes symmetric too (bunching behavior).

The explanation above applies also when the symmetry or the anti-symmetry is associated to degrees of freedom other than frequency: some examples are the anti-symmetric polarization Bell state $\left|\Psi^-\right\rangle = \frac{1}{\sqrt{2}}(|HV\rangle - |VH\rangle)$ [239] and the spatial-momentum entangled biphoton states studied in [120], which generate anti-bunching.

6.3 Connection between the HOM experiment and the Chronocyclic Wigner function W_-

Before moving on to the experimental part we want to recall the Chronocyclic Wigner function (CWF), introduced in subsection 2.3.1, and show its relation with the Hong-Ou-Mandel interferometer. This link has been demonstrated by Douce et al. [206], leading to a generalized version of the HOM experiment, that we will quickly introduce.

We have seen that, considering a state with a JSA separable in ω_+ and ω_-:

$$\phi(\omega_s, \omega_i) = \chi_\Gamma\, \mathrm{PM}(\omega_-)\, \phi_{\mathrm{spectral}}(\omega_+) \tag{6.29}$$

the CWF can be factorized into:

$$W(\omega_s, t_s, \omega_i, t_i) = |\chi_\Gamma|^2\, W_+(\omega_+, t_+) W_-(\omega_-, t_-) \tag{6.30}$$

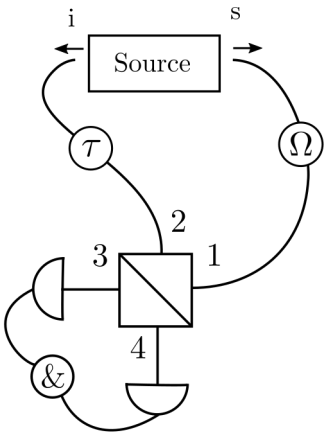

Figure 6.3: Generalized HOM interferometer. The addition of a frequency shift Ω allows to probe the Chronocyclic Wigner function.

with $\omega_\pm = \omega_s \pm \omega_i$ and $t_\pm = \dfrac{t_s \pm t_i}{2}$ and the two-dimensional CWFs:

$$\begin{aligned} W_+(\omega_+, t_+) &= \frac{1}{\sqrt{2\pi}} \int \mathrm{d}\omega'_+ \, \phi_{\text{spectral}}(\omega_+ + \frac{\omega'_+}{2}) \, \phi^*_{\text{spectral}}(\omega_+ - \frac{\omega'_+}{2}) \, e^{-i\omega'_+ t_+} \\ W_-(\omega_-, t_-) &= \frac{1}{\sqrt{2\pi}} \int \mathrm{d}\omega'_- \, \mathrm{PM}(\omega_- + \frac{\omega'_-}{2}) \, \mathrm{PM}^*(\omega_- - \frac{\omega'_-}{2}) \, e^{-i\omega'_- t_-} \end{aligned} \tag{6.31}$$

where $W_+(\omega_+, t_+)$ is governed by the pump spectrum and $W_-(\omega_-, t_-)$ by the phase-matching function.

It is already possible to notice a similarity between $W_-(\omega_-, t_-)$ and the HOM coincidence probability $P_c(\tau)$ (Equation 6.17), both being functions of the phase-matching function. To clarify this link, we now consider the generalized version of the HOM interferometer proposed in [206]: a device (e.g. an electro-optic modulator) introducing a frequency shift Ω is inserted in the signal arm, in addition to the standard time delay line in the idler arm, as illustrated in Figure 6.3. With this arrangement, the coincidence probability becomes:

$$P_c(\Omega, \tau) = \frac{1}{2} - \frac{1}{2} \frac{\int \mathrm{d}\omega_- \, \mathrm{PM}(\Omega + \frac{\omega_-}{2}) \, \mathrm{PM}^*(\Omega - \frac{\omega_-}{2}) \, e^{-i\omega_- \tau}}{\int \mathrm{d}\omega_- \, |\mathrm{PM}(\frac{\omega_-}{2})|^2} \tag{6.32}$$

We notice that Equation 6.31 and Equation 6.32 share the same integral. By employing the normalization $\int \mathrm{d}\omega_- |\mathrm{PM}(\omega_-/2)|^2 = 1$ and recalling that $\tau = t_s - t_i$ and $t_- = \dfrac{t_s - t_i}{2}$ we obtain:

$$W_-(\Omega, \tau) = \frac{1 - 2P_c(\Omega, 2\tau)}{\sqrt{2\pi}} \tag{6.33}$$

This equation relates the cut of the CWF at $\omega_- = \Omega$ with the HOM interferogram measured when a frequency shift Ω is inserted between the photons of the pair[1].

[1] In this thesis we plot the Wigner function normalized to 1 and thus the relation with the HOM coincidence probability becomes: $W_-(\Omega, \tau) = 1 - 2P_c(\Omega, 2\tau)$.

Thus, sweeping the frequency shift allows to reconstruct the Wigner Function in the (Ω, τ) phase space. This generalized version of the HOM experiment provides an alternative and promising route to probe frequency biphoton states, which does not require a direct measurement of the JSA phase.

Interestingly, in our particular case, the counter-propagating phase-matching scheme under transverse pumping enables a simplification of this measurement procedure. Indeed, as we have already discussed, tilting the pump incidence angle corresponds to a frequency shift of the JSA along the ω_- direction, as the frequency shifting device does in Equation 6.32. Therefore, by measuring the HOM interferogram as a function of the pump incidence angle, it is possible to fully reconstruct the Wigner Function $W_-(\Omega, \tau)$ [240].

To conclude this section it is worth remarking that the usual HOM experiment, without any frequency shift, gives access to the cut of the CWF at zero frequency offset:

$$W_-(0, \tau) = \frac{1 - 2P_c(0, 2\tau)}{\sqrt{2\pi}} \tag{6.34}$$

In the next part of the chapter we focus on this "standard" HOM experiment, employing frequency symmetric and anti-symmetric states and measuring the cut of their CWF at zero frequency difference ($\omega_- = 0$).

6.4 Experimental HOM interference

As we have seen, the HOM experiment is a powerful tool to probe the biphoton wavefunction, in particular its symmetry or anti-symmetry with respect to particle exchange. A first HOM measurement on the symmetric state generated by our source based on the counter-propagating phase-matching scheme has been performed by a former PhD student Xavier Caillet [134, 241], obtaining a net visibility $V = 85\%$.

In this section we move a step further by engineering and analyzing two particular biphoton states: one with a symmetric JSA and one with an anti-symmetric JSA. By performing a HOM experiment, we experimentally verify the exchange symmetry of these two states and demonstrate the generation of non-Gaussian entanglement in the time-frequency phase space.

6.4.1 Experimental JSI

Figure 6.4 reports the experimental reconstruction of the two JSIs cited above: the first is obtained with a Gaussian pump beam with a flat phase profile while the second is obtained with a Gaussian beam with a π phase step. The experimental conditions are the following: the pump beam has a waist $w_z = 1$ mm, it is centered at $\lambda_p = 773.15$ nm, with 4 ps pulse duration and it impinges on the waveguide at the degeneracy angle. The states are reconstructed via the fiber spectrograph, because the SET technique cannot be applied at degeneracy (we refer to chapter 4 for a detailed explanation).

We now focus more in detail on the symmetry of the state with respect to particle exchange, which is governed by the symmetry of the JSA with respect

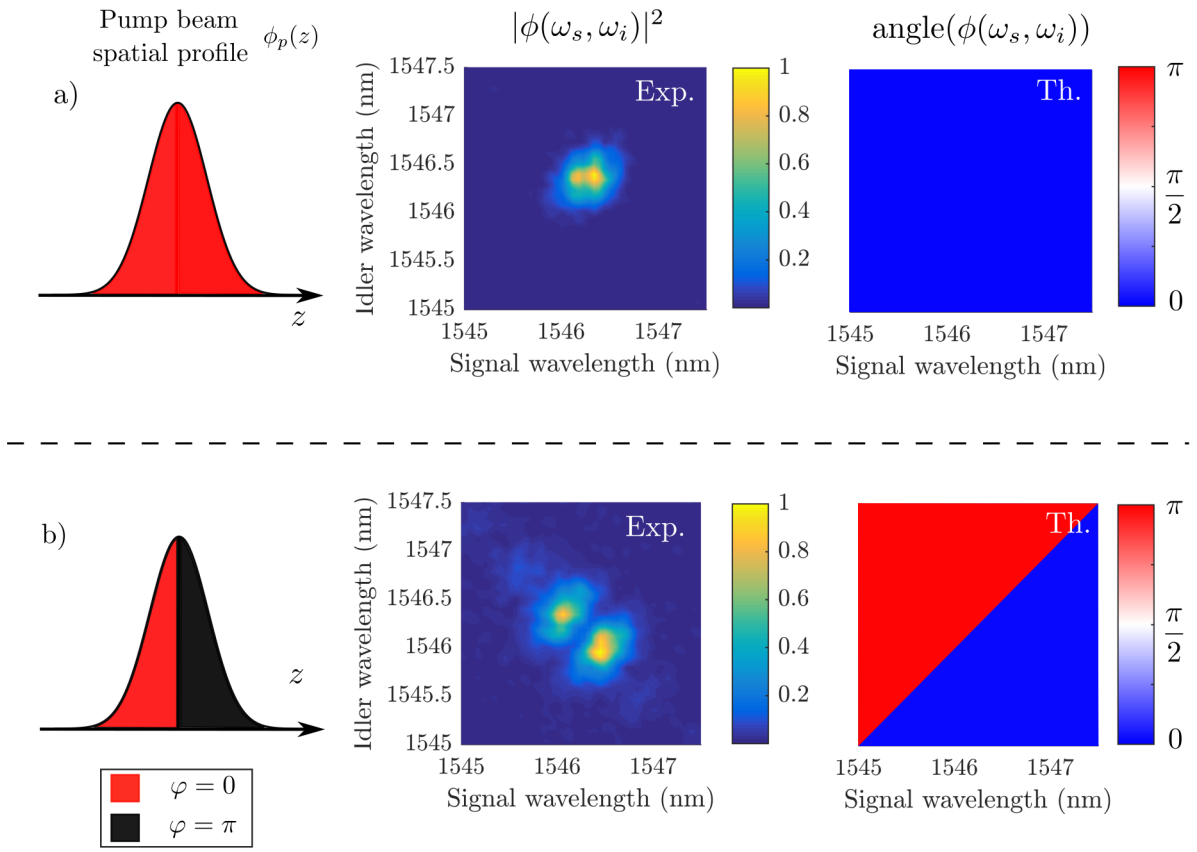

Figure 6.4: Experimental JSIs, reconstructed via a single-photon fiber spectrograph, generated by: (a) a Gaussian pump beam with flat phase and (b) a Gaussian pump beam with π phase step. The pump beam is centered at $\lambda_p = 773.15$ nm, with 4 ps pulse duration and it impinges at the degeneracy angle. The third column reports the corresponding simulated phase of the JSA.

to the diagonal (ω_+ direction). Both the JSIs reported in the second column of Figure 6.4 are symmetric with respect to the diagonal. However, considering also their phase (whose numerical simulations are reported in the third column), we notice that the JSA of the state generated by a pump beam with a flat phase profile (first row) is symmetric and the JSA generated by a pump beam with a π phase step (second row) is anti-symmetric.

In addition, the spectral function depends only on $\omega_+ = \omega_s + \omega_i$ and thus it is always symmetric with respect to ω_-. Therefore, the parity of the phase-matching function directly translates to the JSA (see Equation 6.29).

Let us analyze the two situations considered in Figure 6.4 from an analytic point of view. For both cases the pump beam spatial profile can be written as in Equation 5.14, considering an incidence angle θ and a phase step $\Delta\varphi$:

$$\phi_p(z) = \begin{cases} \exp\left(-\frac{z^2}{w_z^2} + i\frac{\omega_+ \sin\theta\, z}{c}\right) & z < 0 \\ \exp\left(-\frac{z^2}{w_z^2} + i\frac{\omega_+ \sin\theta\, z}{c} + i\Delta\varphi\right) & z > 0 \end{cases} \tag{6.35}$$

From that the phase-matching integral (Equation 5.9) can be split into two terms, under the assumption $L > w_z$:

$$\begin{aligned} \mathrm{PM}(\omega_s, \omega_i) = &\int_{-L/2}^{0} \mathrm{d}z \exp\left(-\frac{z^2}{w_z^2}\right) \exp\left[-i\frac{\omega_+}{c}\big(\sin\theta - \sin\theta_{\mathrm{deg}}\big)z - iz\frac{\omega_-}{\bar{v}_g}\right] \\ &+ e^{i\Delta\varphi} \int_{0}^{L/2} \mathrm{d}z \exp\left(-\frac{z^2}{w_z^2}\right) \exp\left[-i\frac{\omega_+}{c}\big(\sin\theta - \sin\theta_{\mathrm{deg}}\big)z - iz\frac{\omega_-}{\bar{v}_g}\right] \end{aligned} \tag{6.36}$$

When pumping at degeneracy and with a change of variable in the first integral ($z \to -z$) the equation becomes:

$$\mathrm{PM}(\omega_s, \omega_i) = f(\omega_s, \omega_i) + e^{i\Delta\varphi} f(\omega_i, \omega_s) \tag{6.37}$$

with

$$f(\omega_s, \omega_i) = \int_{0}^{L/2} \mathrm{d}z \exp\left(-\frac{z^2}{w_z^2} - iz\frac{\omega_s - \omega_i}{\bar{v}_g}\right) \tag{6.38}$$

From Equation 6.37 we see that for $\Delta\varphi = 0$ the phase-matching function is symmetric, and thus the JSA itself is symmetric with respect to particle exchange:

$$\phi(\omega_s, \omega_i) = \phi(\omega_i, \omega_s) \tag{6.39}$$

On the other hand, for $\Delta\varphi = \pi$ the phase-matching function is anti-symmetric ($\mathrm{PM}(\omega_s, \omega_i) = -\mathrm{PM}(\omega_i, \omega_s)$), translating in an anti-symmetric JSA under particle exchange:

$$\phi(\omega_s, \omega_i) = -\phi(\omega_i, \omega_s) \tag{6.40}$$

In conclusion, we expect the frequency state reported in Figure 6.4a to be symmetric and thus resulting in a HOM dip at $\tau = 0$ and the one reported in Figure 6.4b to be anti-symmetric and therefore resulting in a HOM peak at $\tau = 0$.

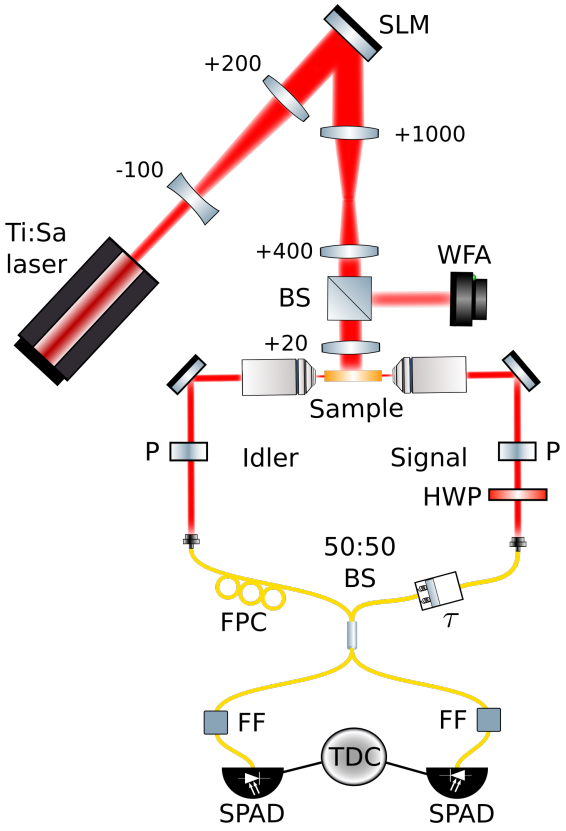

Figure 6.5: Experimental setup of our HOM interferometer; focal lengths are given in millimeters. See text for description.

6.4.2 Experimental setup and results

Figure 6.5 reports a sketch of the experimental setup used to perform the HOM experiment. The first part is the pump beam shaping stage, which has been already detailed in chapter 3. After the photon pair generation, the signal and idler photons are filtered with polarizers (P), in order to select only the VH interaction (signal TM and idler TE). Then they are collected into optical fibers (in yellow in the sketch) and sent into a 50:50 fiber beamsplitter. On the signal side, a fibered motorized delay line adds a tunable time delay τ. By using a half-wave plate (HWP) on the free-space signal arm and a fibered polarization controller (FPC) on the idler arm, the polarizations of the two photons are rotated in order to be parallel.

Prior to detection, two fibered wavelength filters (FF) of 1 nm passband centered at 1546.3 nm are employed to eliminate eventual luminescence noise. Coincidence counts are detected by two SPAD detectors (Id220 by IdQuantique™), with 25% detection efficiency and 10 µs dead time, and a Time-to-Digital converter (TDC, QuTau from QuTools™). The HOM interferogram is acquired by monitoring the coincidence detection rate as a function of the time delay τ.

The results of the HOM experiment (raw coincidence counts) are reported in the first column of Figure 6.6 for both cases $\Delta\varphi = 0$ (situation of first line of Figure 6.4) and $\Delta\varphi = \pi$ (second line of Figure 6.4). The corresponding numerical

simulations are presented in the second column of the figure.

We first comment on the situation of a Gaussian pump beam with flat profile. The experimental HOM interferogram and the corresponding numerical simulation, reported in the first row of the figure, show a coincidence dip (i.e. two-photon bunching), confirming the symmetric nature of the biphoton frequency state. The experimental dip visibility is calculated as:

$$V_{\text{dip}} = \frac{N_\infty - N_0}{N_\infty} \tag{6.41}$$

with $N_\infty(N_0)$ the mean coincidence count at long (zero) time delay, obtained by fitting the HOM interferogram with a modified version[2] of Equation 6.27. For this case we obtain $V_{\text{dip}} = 87.5\%$, using uncorrected coincidence counts. From the same fit we obtain also the value of dip width $\Delta\tau_{\text{exp}} = 10.8$ ps. This parameter has been introduced in Equation 6.27 and in case of a Gaussian phase-matching function can be calculated as $\Delta\tau = \dfrac{\sqrt{2}\bar{v}_g}{\Delta\omega_-} = 14.7$ ps for a 1 mm-waist pump beam. The difference between the experimental value and the theoretical one is due to the fact that the waveguide, which is 1.9 mm long, acts as a spatial filter on the 1 mm-waist pump beam and the phase-matching function is not purely Gaussian, but it is given by the convolution of a Gaussian and a sinc functions.

We now comment on the case of the pump beam with a phase step $\Delta\varphi = \pi$. The HOM interferogram and the corresponding numerical simulation, reported in the second row of Figure 6.6, feature a coincidence peak (two-photon anti-bunching) demonstrating the anti-symmetric nature of the biphoton frequency state. The raw visibility is $V = 77\%$, calculated as:

$$V_{\text{peak}} = \frac{N_0 - N_\infty}{N_\infty} \tag{6.42}$$

where $N_\infty(N_0)$ have the same meaning as before. The two side dips at ± 12 ps are due to the specific shape of the joint spectrum, in particular to the zero probability region between the two lobes of the JSA, see Figure 6.4.

As a side note, we remark that the coincidence probability for long time delay ($\tau > 20$ ps) slightly decrease from 0.5. This effect is due to the Fabry-Pérot side dips situated at ± 40 ps, as already illustrated in Figure 6.2.

Comments on the HOM experiment visibility

The reported visibilities, of $V_{\text{dip}} = 87.5\%$ for the dip and $V_{\text{peak}} = 77\%$ for the peak, are lower than the theoretical value 100%. In this paragraph we detail the possible limiting factors, backing up our analysis by means of some numerical simulations.

A first factor is the pump incidence angle θ, which determines the wavelength of the signal and idler photons. A small offset from the degeneracy angle θ_{deg} induces a frequency shift, making the two photons slightly distinguishable. In the experiment the spectral degeneracy is checked by using dispersive fibers and we estimate a typical precision of 50 pm (wavelength difference between signal and idler photons),

[2]The fit function takes into account a non-unitary visibility and a possible linear offset.

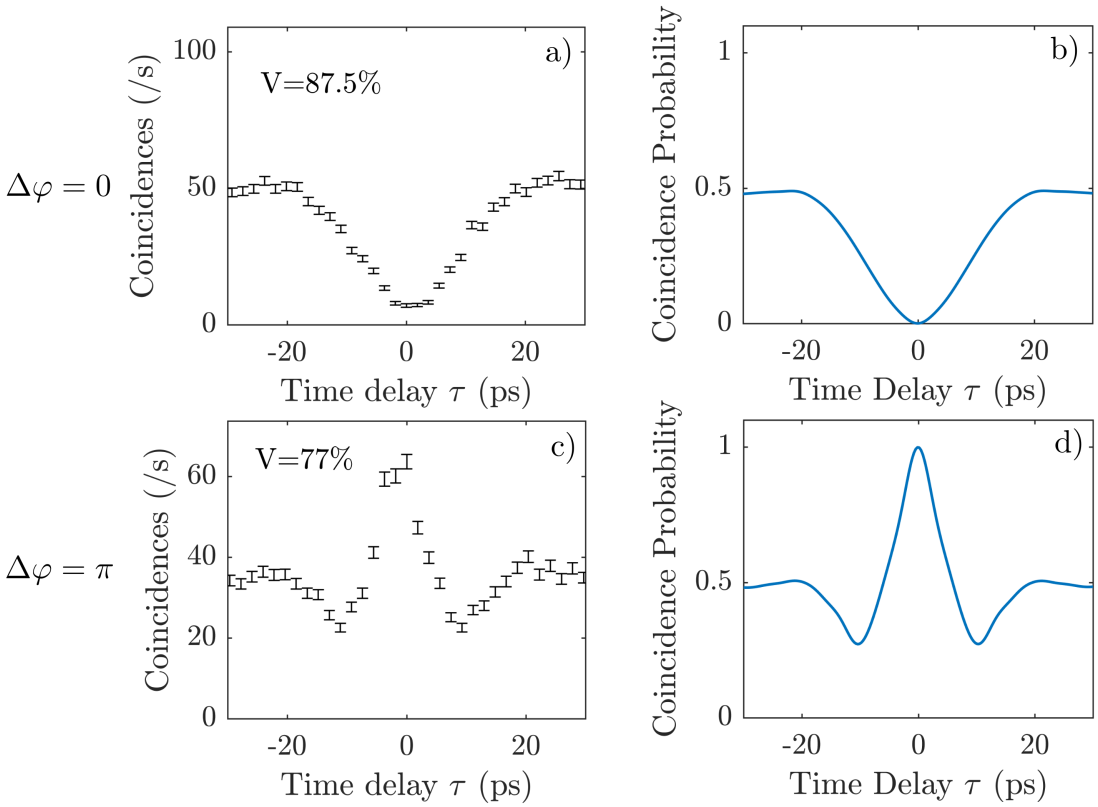

Figure 6.6: (a) Experimental HOM interferogram and (b) corresponding numerical simulation for the state generated by a Gaussian pump beam with $\Delta\varphi = 0$ (first row) and $\Delta\varphi = \pi$ (second row). The experimental data are raw coincidence counts and the errorbars are calculated assuming a Poissonian statistics.

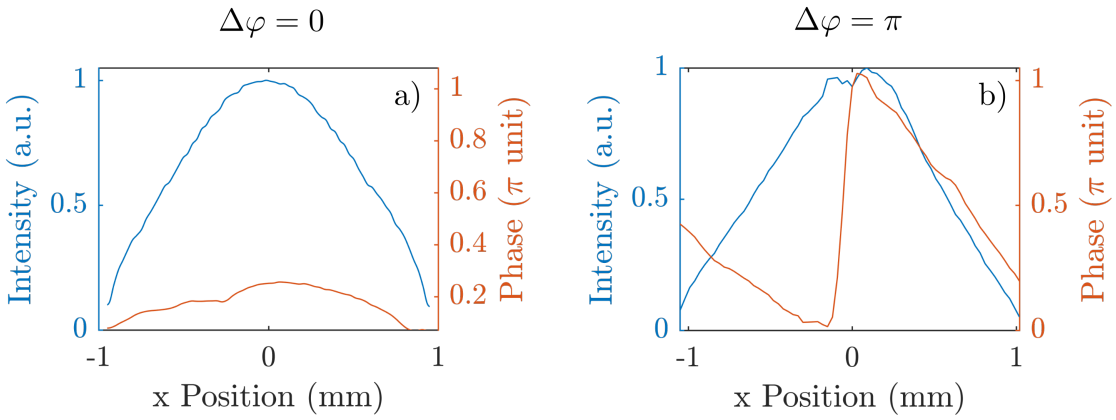

Figure 6.7: Experimentally measured phase (in red) and intensity (in blue) spatial profiles of the pump beam for the case (a) $\Delta\varphi = 0$ and (b) $\Delta\varphi = \pi$. The linear phase gradient superimposed to the π phase step in (b) is due to the shaping technique and cannot be eliminated. However, since it only causes a frequency shift along the ω_- direction, which can be corrected by tilting the pump beam, it does not affect the HOM interferogram.

corresponding to ≈ 10% of the bandwidth of the SPDC photons. Taking into account this factor into our numerical simulations, we estimate a corresponding visibility decrease of 7% for both cases ($\Delta\varphi = 0$ and $\Delta\varphi = \pi$).

In addition to our imperfect setting of the pump angle, also the source modal birefringence plays a role in the spectral distinguishability. Indeed, even when signal and idler central frequencies are equal, their spectral overlap is not perfect due to a slight displacement (15 pm in wavelength) between their Fabry-Pérot resonances. This leads to an additional visibility decrease of 1.5%.

A second series of factors is related to the spatial properties of the pump beam. In order to evaluate these effects we perform a numerical simulation of the HOM interferogram by taking into account the pump intensity and phase spatial profile experimentally measured by the wavefront analyzer, reported in Figure 6.7. The experimental imperfections lead to a visibility drop of 0.5% for the flat phase and of 8% for the π phase step. Finally, the imprecision in the longitudinal centering of pump beam on the waveguide, which is about 200 µm in our setup, leads to an additional 2% visibility drop for both cases.

By taking into account all these factors simultaneously (see Table 6.1), we obtain an expected dip visibility $V_{\text{dip}} = 90\%$ and an expected peak visibility $V_{\text{peak}} = 81.5\%$, which have to be compared to the corresponding experimental values of 88% and 77%. The experimental and expected values are close enough and the remaining 2-5% visibility drop could be due to a slight polarization distinguishability between the two photons, which has not been taken into account into the simulations.

This analysis shows that, in order to increase the HOM visibility for future experiments, we should increase the spectral resolution to adjust the degeneracy condition, gaining up to 7%. This could be done by improving the sensibility of our fiber spectrograph, by using longer DCF spools or superconductive detectors that

Factor	Visibility drop	
	Flat phase profile	π phase step
Incidence angle offset	7%	7%
Modal birefringence	1.5%	1.5%
Pump spatial profile imperfections	0.5%	8%
Pump beam longitudinal position	2%	2%
Total expected visibility	90%	81.5%
Experimental visibility	88%	77%

Table 6.1: Visibility limiting factors, estimated through numerical simulations.

have a shorter jitter, as already commented in section 4.1. On the other hand, implementing a feedback loop on the SLM to correct the pump spatial imperfections could allow an additional 8% gain in the π phase step case.

Source Brightness

We now evaluate the brightness of our source in order to compare it with other similar devices. The measured coincidence rate in the HOM experiment at long time delay is about 50 Hz and, since the coincidences are detected after the HOM beamsplitter only half of them are measured[3]. Therefore the coincidence rate is $C = 100$ Hz. On the other hand, the single-count rate is $S = 35$ kHz. From these values we can deduce the internal pair production rate (PPR) of the source [63]:

$$\mathrm{PPR} = \frac{S^2}{C} \approx 12\,\mathrm{MHz} \tag{6.43}$$

and the total collection efficiency [63]:

$$\eta_{\mathrm{tot}} = \frac{C}{S} = 0.3\% \tag{6.44}$$

The infrared guided modes have transmission losses $\alpha \approx 0.5$ cm^{-1}, so the sample transmission is 90%. Therefore, the pair production rate at the chip output is approximately 11 MHz.

The time-averaged pump power incident on the sample is 150 mW and only one third of it is coupled inside the vertical microcavity[4], resulting in 50 mW employed in the down-conversion. Therefore, the source brightness is approximately 220 kHz/mW, which is, for comparison with a concurrent work, two orders of magnitude higher than the brightness of the PPKTP waveguide source developed by Graffitti et al.[65] to generate anti-symmetric biphoton frequency states.

[3]In absence of the HOM effect (i.e. $\tau \gg \Delta\tau$) the photons have 50% probability of exiting from the same port and thus only one half of the coincidences are measured.

[4]The microcavity transmission is 50% and the overlap between the sample and the pump beam spatial profile is 60%, as we have seen in subsection 4.1.1

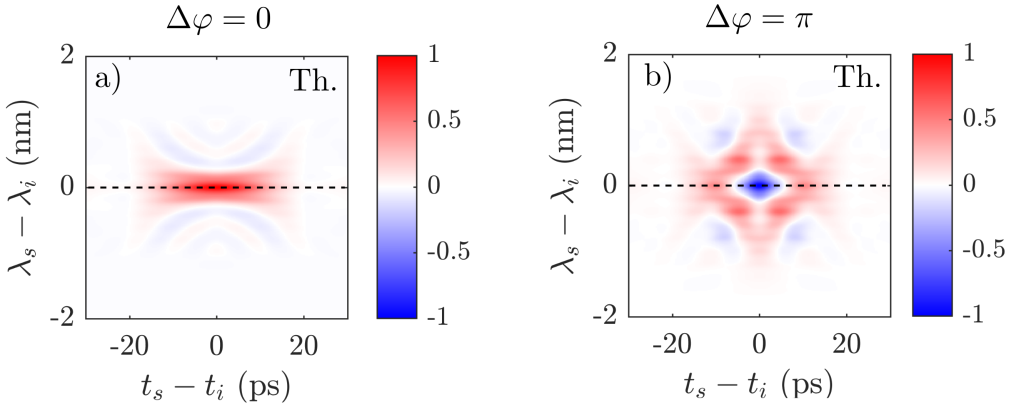

Figure 6.8: Numerical simulated Chronoclyic Wigner Function W_- of the biphoton state generated by (a) a Gaussian pump beam with flat phase ($\Delta\varphi = 0$) and (b) by a Gaussian pump beam with a phase step ($\Delta\varphi = \pi$). The dashed lines indicates the cuts at $\omega_- = 0$, measured by HOM interference.

6.4.3 Particle exchange symmetry and non-Gaussian entanglement

The measured HOM bunching and anti-bunching reported in Figure 6.6, experimentally demonstrate the symmetry and the anti-symmetry with respect to particle exchange of the respective biphoton states. In addition, anti-bunching for $\tau = 0$ is a direct signature of entanglement [238]; indeed a separable state always has $P_c(\tau = 0) \leq 0.5$ (see subsection 6.2.1) [237]. However, we anti-bunching is only a sufficient but not necessary condition for frequency entanglement. Indeed, both quantum states of Figure 6.4 are not separable and therefore frequency entangled, but only the anti-symmetric JSA is certified by the HOM experiment as a frequency entangled state.

In section 6.3 we have shown that the HOM interferogram is directly linked to the cut of the chronocyclic Wigner function W_- at $\omega_- = 0$, as expressed by Equation 6.34. Figure 6.8 reports the numerically simulated CWF W_-, for the case of a Gaussian pump beam with flat phase ($\Delta\varphi = 0$, Figure 6.8a) and the case of a Gaussian pump beam with π phase step ($\Delta\varphi = \pi$, Figure 6.8b). The black dashed lines highlight the cut at $\omega_- = 0$ that is related to the HOM interferogram. The coincidence peak in the HOM interferogram corresponds to a negative value of the Wigner function W_-, which identifies the corresponding state as entangled with non-Gaussian statistics in the time-frequency phase space [206, 242].

Let us now analyze the quantum states focusing on particle exchange. It is interesting to note that the two cases ($\Delta\varphi = 0$ and $\Delta\varphi = \pi$) correspond respectively to the behavior of independent bosons (bunching) and independent fermions (anti-bunching). In addition, it is possible to pass from a situation to the other just by modifying the phase mask addressed on the SLM, without acting on the source itself. This flexible control could be harnessed to study the effect of exchange statistics in various quantum simulation problems [86, 110, 226] with a chip integrated platform.

6.5 Conclusions

In this chapter we have moved a step further in the engineering and the characterization of the states generated by our counter-propagating source, by employing a Hong-Ou-Mandel interferometer.

First of all, we have analytically studied the behavior of a biphoton frequency state in the interferometer, showing when bunching and anti-bunching occur. We have then identified the relation between the HOM interferogram and the Chrocyclic Wigner Function W_-, illustrating how a coincidence peak (two-photon anti-bunching) is associated with a negative value of W_-.

Then, by sending in a HOM interferometer either a symmetric frequency state, generated by pumping the source with a Gaussian beam with flat phase, or an anti-symmetric frequency state, generated by a Gaussian pump beam with a π phase step, we have demonstrated a flexible control over their exchange statistics. Indeed, in the first case the photons bunch together, similarly as independent bosons, while in the second they anti-bunch, similarly as independent fermions. Moreover, the established linked between the HOM interferogram and the Wigner function has allowed to identify the anti-symmetric frequency state as a non-Gaussian entangled state in the time-frequency phase space.

Together with the results described in the previous chapter, these results demonstrate a flexible control over the frequency entanglement and particle statistics of photon pairs, with a chip-integrated source, directly at the generation stage, at room temperature and telecom wavelength. These features are important in view of practical and scalable applications for quantum information technologies. In particular, these results could be harnessed to study the effect of exchange statistics in various quantum simulation problems [86, 110, 226] with a monolithic platform, and to improve communication and computation protocols making use of anti-symmetric high-dimensional quantum states [227, 228].

Moreover, more complex high-dimensional entangled states could also be realized in the employed device by a further engineering of the pump beam [240]. In particular, in the next chapter we will show how the source characteristics can be exploited to generate a biphoton state entangled in the polarization/frequency hybrid degree of freedom. Furthermore, we are currently investigating the possibility of generating biphoton states with anyonic statics, which represents a generalization of fermionic and bosonic statics [86, 243].

The work presented in this chapter and in chapter 5 has been published in [244].

Chapter 7

Direct generation of entanglement in a hybrid degree of freedom

So far we have studied the generation of frequency entangled photon pairs and we have presented some techniques to engineer their frequency correlations and symmetry properties. In this chapter we move a step further and employ the counter-propagating source to generate hybrid polarization/frequency (HPF) entangled states. This particular state is obtained by pumping the source at $\theta = 0°$ (normal incidence) and by keeping both nonlinear interactions.

First we will show that, when a HPF entangled state is analyzed in only one

degree of freedom (DOF), frequency or polarization, it collapses into a mixed state, exhibiting no entanglement. However, we will also show that the two DOFs can be decoupled, obtaining either a polarization Bell state or a two-color entangled state.

In the second part of the chapter, we will employ a HOM interferometer to directly quantify the entanglement in the frequency/polarization hybrid DOF. In particular, we will extensively analyze the effect that the Fabry-Pérot cavity, created by the source facet reflectivity, has on the HPF entangled states.

7.1 Introduction

As we will show in the following section, a HPF entangled state exhibit simultaneous but not independent entanglement in the polarization and frequency DOFs. However, it is possible to project it onto a polarization Bell state or a two-color entangled state, providing our sources with a high level of versatility. For this reason, in this section we introduce briefly these two types of entangled states and the main techniques to generate them, with a particular attention to integrated sources.

7.1.1 Polarization Bell states

Thanks to its easy generation and manipulation, polarization has been one of the first DOFs to be exploited in quantum optics experiments. For example, it has been employed in the first experimental violation of the Bell-CHSH inequality [1, 245], performed by Aspect et al. [85] in 1982.

For two polarization qubits a maximal violation of the Bell-CHSH inequality is provided by the so-called Bell states:

$$\begin{aligned} \left|\Psi^{\pm}\right\rangle &= \frac{|H\rangle_A |V\rangle_B \pm |V\rangle_A |H\rangle_B}{\sqrt{2}} \\ \left|\Phi^{\pm}\right\rangle &= \frac{|H\rangle_A |H\rangle_B \pm |V\rangle_A |V\rangle_B}{\sqrt{2}} \end{aligned} \tag{7.1}$$

where H and V stand for horizontal and vertical polarization respectively, while A and B label the photons (e.g. using their spatial mode). Such states constitute a fundamental building block for quantum information [246] and quantum communication (e.g. quantum teleportation [247] or quantum key distribution protocols [248]).

Polarization Bell state generation

The early quantum optics experiments exploited atomic cascades in calcium to generate polarization entangled photon pairs [85]. In the 1980s and 1990s new sources with higher flux of photon pairs were developed employing parametric processes (i.e. SPDC) in bulk crystals [249–251], which however required external components (e.g. birefringence compensator or Sagnac interferometer) to obtain maximally entangled states. This issue has been overcome via the engineering of

integrated nonlinear sources, both SPDC- and SFWM-based, which can directly generate maximally entangled polarization Bell states, without requiring any compensation stage [57, 58, 252, 253]. On the other hand, quantum dot-based systems can directly generate triggered polarization entangled Bell pairs by exploiting the biexciton cascade process. These systems, working at cryogenic temperatures, require a high level of control and engineering to achieve a high degree of entanglement due to phenomena, such as the fine structure splitting [31–33].

The counter-propagating source studied in this thesis enables the direct generation of polarization Bell states, by exploiting both nonlinear interactions in a double pump beam configuration, as demonstrated in [57].

7.1.2 Two-color entangled states

Frequency is a continuous degree of freedom of photons which can be employed to generate quantum states in a high-dimensional Hilbert space. Nevertheless, it is also possible to discretize this degree of freedom, when the frequency modes have a characteristic width that is small compared to their relative separation. In this way, we can define a set of orthogonal modes, which can be employed to describe a frequency-bin state.

The advantage of discrete frequency states is twofold. On one hand, the discretization allows to generate quantum states with d levels (qudits) and, even if the state does not exhibit entanglement, many quantum information tasks can benefit from this: e.g. clock syncronization [254] and quantum key distribution [107].

On the other hand, when the quantum state is composed of more than one photon, entanglement among their discrete frequency modes becomes an additional valuable resource that can be exploited to increase the data capacity and the robustness of quantum protocols [122, 242, 255].

One of the simplest discrete frequency entangled states is the frequency Bell state $|\Psi\rangle$, which has dimension d=2:

$$|\Psi\rangle = \frac{1}{\sqrt{2}}\Big(|\omega_1\rangle_A\,|\omega_2\rangle_B + e^{i\varphi}\,|\omega_2\rangle_A\,|\omega_1\rangle_B\Big) \tag{7.2}$$

where $|\omega_1\rangle$ and $|\omega_2\rangle$ are well separated single-photon frequency bins. The two photons of this state are in a coherent superposition of two frequencies, as in a polarization Bell state where they are in a superposition of two orthogonal polarizations. For this reason, the state is also called two-color entangled state.

Two-color entanglement generation

Several experimental schemes have been implemented to generate two-color entangled states. The first proposals employed SPDC in bulk crystals to generate photon pairs having a continuous frequency spectrum; a filtering stage was placed before the detection in order to obtain well defined frequency bins [256, 257]. More recently, brighter sources have been demonstrated by using periodically poled crystals in crossed configurations [235, 258], Sagnac loops [259], double passage configurations [224] or by transferring entanglement from the polarization domain to the frequency one [260].

The first integrated photonic device emitting two-color entangled states has been developed by Silverstone et al. [94]. The device exploits the silicon-on-insulator technology and combines two four-wave mixing sources in an interferometer with a reconfigurable phase shifter, allowing to generate two-color entangled states. The great achievement of this work is the ability to obtain quantum interference between photons generated in different sources; however the device suffers from a low efficiency. On the other hand, integrated sources exploiting the process of parametric down conversion in a counter-propagating phase matching scheme have been pointed out as interesting candidates to efficiently generate two-color entangled states [147, 261] at higher rate, but no experimental demonstration has been achieved so far.

7.2 Hybrid polarization/frequency (HPF) entanglement generation

We now illustrate how our counter-propagating source can emit entangled states in the polarization/frequency hybrid degree of freedom, focusing the attention on the fundamental role played in this process by the device form birefringence.

As we have already seen before, the source, thanks to its counter-propagating geometry, has two possible solutions to the phase-matching equation, which differ by the photon polarization. We have called interaction HV the one with a horizontally polarized signal photon and a vertically polarized idler photon, while we have called interaction VH the opposite case (signal V and idler H), where signal and idler stand for the propagation direction (see chapter 1).

The photon central frequency for both interactions can be calculated from the phase-matching and energy conservation equations. Figure 7.1 reports the solutions as a function of the the pump incidence angle, showing the frequency accordability of the source. From this figure we see that the two interactions, reported with solid lines (HV) and dashed lines (VH), have a relative frequency shift and do not overlap. This is due to the form birefringence of the waveguide, caused by its layered structure and by the core aspect ratio, as we have commented in section 1.4. By contrast, in a non-birefringent structure the two interactions would be frequency degenerate, but they would always emit perpendicularly polarized photons. From our numerical simulations we expect a form birefringence of $\Delta n = n_H - n_V = 0.0125$ for the fundamental twin-photon modes. Even if this value is small ($\Delta n/n = 0.4\%$) it has a considerable effect on the source.

The wavelength shift between the two interactions can be calculated from the phase-matching and energy conservation equations (section 1.4) and it does not depend on the pump incidence angle but only on the modal birefringence:

$$\Delta\lambda = \lambda_2 - \lambda_1 = 4\lambda_p \frac{n_H - n_V}{n_H + n_V} \approx \frac{2}{3}\lambda_p (n_{\mathrm{H}} - n_{\mathrm{V}}) \tag{7.3}$$

where λ_p is the pump central wavelength and we have approximated $n_H + n_V \approx 6$, which is reasonable given the modal refractive index values (reported in section 1.4).

Inserting the value of the birefringence, derived from our numerical simulation, and considering a pump at $\lambda_p = 773.15$ nm (the resonant wavelength of the em-

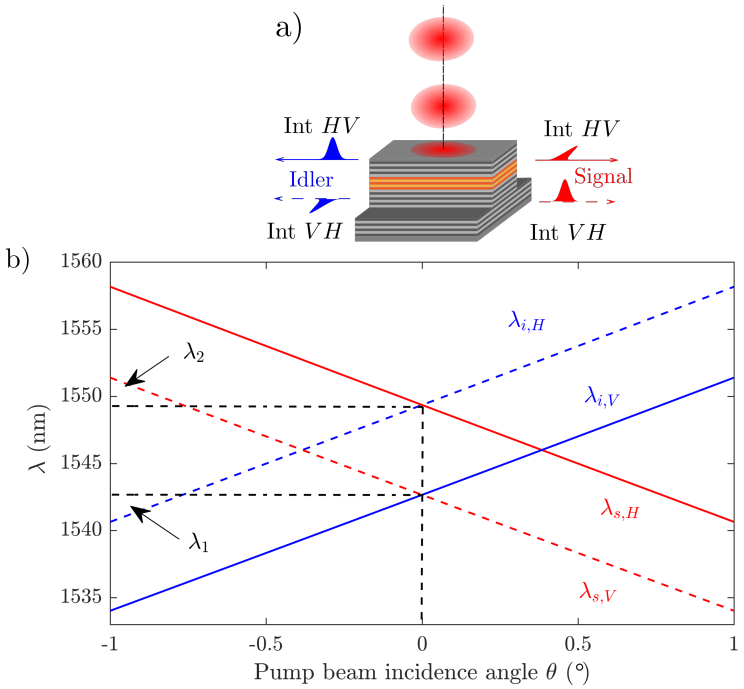

Figure 7.1: (a) Sketch of the counter-propagating source, highlighting the two nonlinear interactions. (b) Numerical simulation of the angular dependency of the signal (red) and idler (blue) wavelength for the interaction HV (solid lines) and the interaction VH (dashed lines), for a pump wavelength $\lambda_p = 773$ nm. The black dashed lines at 0° indicates the position for which the two interactions are symmetric, generating photons of wavelengths λ_1 and λ_2.

ployed sample) we obtain a wavelength shift of about 6.4 nm. This shift is one order of magnitude bigger than the width of the typical JSA of each independent interaction (around 0.5 nm) and thus the two interactions do not overlap.

7.2.1 The emitted quantum state

In the previous chapters we have always considered the quantum state emitted through only one interaction, filtering out the other one (using both frequency filters and polarizers). Here we analyze the situation when both interactions are kept. The wavefunction can be written as follows:

$$|\Psi\rangle = \iint \mathrm{d}\omega_1 \mathrm{d}\omega_2 \left[\phi_{VH}(\omega_1,\omega_2)\hat{a}^\dagger_{s,V}(\omega_1)\hat{a}^\dagger_{i,H}(\omega_2) + \phi_{HV}(\omega_1,\omega_2)\hat{a}^\dagger_{s,H}(\omega_1)\hat{a}^\dagger_{i,V}(\omega_2)\right]|0\rangle \tag{7.4}$$

where $\phi_{HV}(\omega_1,\omega_2)$ ($\phi_{VH}(\omega_1,\omega_2)$) is the JSA for the interaction HV (VH). Here the subscripts "signal" (s) and "idler" (i) still indicate the direction of the photons, while ω_1 and ω_2 do not because we have to take into account both interactions and therefore there are two possible frequencies for each direction.

Equation 7.4 represents the wavefunction of a photon pair that can be created in one interaction or in the other, but not in both simultaneously. Indeed, since we are in a low pump regime, we neglect multiple photon pair generation (e.g. a double pair in one interaction or one pair in each interaction). Therefore, the quantum

state represents a photon pair which is created in the coherent superposition of two possible processes (interaction HV and interaction VH).

From the previous considerations and taking into account that the $\hat{a}$ and $\hat{a}^\dagger$ operators act on orthogonal polarization modes (H and V), the normalization condition becomes:

$$\iint \mathrm{d}\omega_1 \mathrm{d}\omega_2 \left[|\phi_{HV}(\omega_1, \omega_2)|^2 + |\phi_{VH}(\omega_1, \omega_2)|^2 \right] = 1 \tag{7.5}$$

Note that now it is the sum of the squared modulus of the JSA of the two interactions that is normalized to one and not the single JSA.

If now we consider a pump beam perpendicular to the source ($\theta = 0°$), the two interactions will be symmetric with respect to the degeneracy wavelength, as shown in Figure 7.1 by the black dashed lines. Indeed in this situation, the interaction HV has its maximum at (λ_1, λ_2) while the interaction VH has its maximum at the symmetric position (λ_2, λ_1). In addition, assuming that ϕ_{HV} and ϕ_{VH} have the same dependency on (ω_s, ω_i), we have $\phi_{VH}(\omega_1, \omega_2) = \phi_{HV}(\omega_2, \omega_1)$ so we can use the same function $\phi(\omega_1, \omega_2)$ for both interactions:

$$|\Psi\rangle = \iint \mathrm{d}\omega_1 \mathrm{d}\omega_2 \left[\phi(\omega_1, \omega_2) \hat{a}^\dagger_{s,V}(\omega_1) \hat{a}^\dagger_{i,H}(\omega_2) + \phi(\omega_2, \omega_1) \hat{a}^\dagger_{s,H}(\omega_2) \hat{a}^\dagger_{i,V}(\omega_1) \right] |0\rangle \tag{7.6}$$

Figure 7.2 reports the simulated JSI of the generated state considering both interactions and a pump beam perpendicular to the device. We see that the two interactions produce separated peaks which are symmetric with respect to wavelength degeneracy. The modulation of the peaks visible in the figure is due to the Fabry-Pérot effect arising from the facet reflectivity (c.f. subsection 2.2.5).

If we limit our description to the spectral part of the wavefunction, we can deduce that the state is frequency entangled; indeed the JSA has a Schmidt number $K = 2$, meaning that two orthogonal frequency modes are involved, as in a two-color entangled state. However in our case, described by Equation 7.6, since the interactions can be distinguished by the photon polarization, the state does not exhibit two-color entanglement, but a more complex form of hybrid entanglement between the frequency and polarization DOFs, as we shall see in the next paragraph.

7.2.2 Analysis of the HPF entangled state

In order to obtain physical insight into the generated HPF entangled state (Equation 7.6), we now approximate the JSAs with Dirac deltas, $\phi(\omega_1, \omega_2) = \delta(\omega_1 - \omega_1^0, \omega_2 - \omega_2^0)$, which is a reasonable assumption since the two frequency modes are well separated. The wavefunction thus becomes:

$$|\Psi\rangle \sim \left| V, \omega_1^0 \right\rangle_s \left| H, \omega_2^0 \right\rangle_i + \left| H, \omega_2^0 \right\rangle_s \left| V, \omega_1^0 \right\rangle_i \tag{7.7}$$

where the first ket represents the signal photon and the second the idler photon. This state is maximally entangled in the hybrid polarization/frequency degree of freedom, i.e. in the base $\{V, \omega_1^0\}, \{H, \omega_2^0\}$.

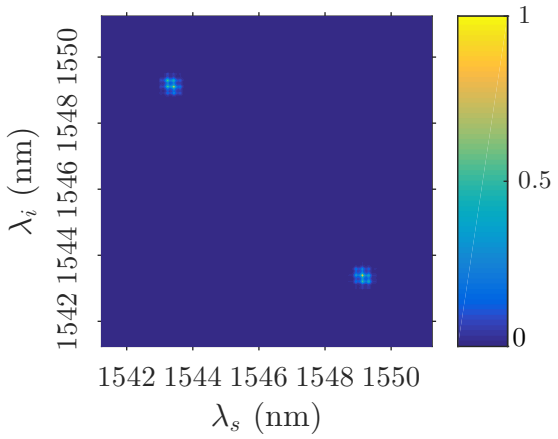

Figure 7.2: Numerical simulation of the expected JSI for the quantum state described by Equation 7.6, taking into account the Fabry-Pérot effect. The pump wavelength is $\lambda_p = 773.15$ nm and the pump beam waist is $w_z = 0.5$ mm with a flat phase profile.

On the other hand, when only the frequency or the polarization is measured the state collapses into a mixed state, which does not exhibit entanglement. Let us show this behavior using the density matrix formalism.

The density operator corresponding to the quantum state reported in Equation 7.7 is:

$$\begin{aligned}\hat{\rho} = |\Psi\rangle\langle\Psi| \sim &\left|V,\omega_1^0\right\rangle_s \left|H,\omega_2^0\right\rangle_i \left\langle V,\omega_1^0\right|_s \left\langle H,\omega_2^0\right| + \left|V,\omega_1^0\right\rangle_s \left|H,\omega_2^0\right\rangle_i \left\langle H,\omega_2^0\right|_s \left\langle V,\omega_1^0\right| \\ &+ \left|H,\omega_2^0\right\rangle_s \left|V,\omega_1^0\right\rangle_i \left\langle V,\omega_1^0\right|_s \left\langle H,\omega_2^0\right| + \left|H,\omega_2^0\right\rangle_s \left|V,\omega_1^0\right\rangle_i \left\langle H,\omega_2^0\right|_s \left\langle V,\omega_1^0\right|\end{aligned} \tag{7.8}$$

If the frequency is measured but the polarization is not, we have to trace over the latter. This leads to:

$$\hat{\rho} \sim \left|\omega_1^0\right\rangle_s \left|\omega_2^0\right\rangle_i \left\langle\omega_2^0\right|_s \left\langle\omega_1^0\right| + \left|\omega_2^0\right\rangle_s \left|\omega_1^0\right\rangle_i \left\langle\omega_1^0\right|_s \left\langle\omega_2^0\right| \tag{7.9}$$

which is a mixed state.

The same thing occurs if we measure polarization instead of frequency. In conclusion, the quantum state described by Equation 7.7 is entangled in the hybrid polarization/frequency degree of freedom, but when only one of the DOFs is observed the state collapses in a mixed state. Thus, the state exhibits simultaneous but not independent entanglement. Such type of entangled state has been previously reported in the literature [262] and called *hypoentangled* state.

It is useful to compare our state to hyperentangled states [263], which display simultaneous and independent entanglement, measurable in each degree of freedom. For polarization and frequency, the strongest hyperentangled state consists of a Bell-type entangled state in each DOF combined in a tensor product, e.g.:

$$\left|\psi_{\text{hyper}}\right\rangle \sim \left(|H\rangle\,|V\rangle + |V\rangle\,|H\rangle\right) \otimes \left(\left|\omega_1^0\right\rangle \left|\omega_2^0\right\rangle + \left|\omega_2^0\right\rangle \left|\omega_1^0\right\rangle\right) \tag{7.10}$$

When one of the two DOFs is ignored (i.e. tracing over it) the other is left in a maximally entangled state: the entanglement in the different DOFs is independently measurable.

7.2.3 Recovering frequency entanglement

We now show that starting from a HPF entangled state it is possible to recover the frequency entanglement by erasing the polarization information. This can be easily done by probabilistically projecting the polarization of both photons onto diagonal directions using polarizers at 45°.

Starting from the wavefunction, Equation 7.6, the polarizers transform the creation and annihilation operators in the following way:

$$\hat{a}^\dagger_{s/i,H/V}(\omega) \rightarrow \frac{1}{\sqrt{2}}\hat{a}^\dagger_{s/i,D}(\omega) \tag{7.11}$$

where D indicates the diagonal polarization direction. Thus the wavefunction becomes:

$$|\Psi\rangle = \frac{1}{2}\iint \mathrm{d}\omega_1\mathrm{d}\omega_2 \left[\phi(\omega_1,\omega_2)\hat{a}^\dagger_s(\omega_1)\hat{a}^\dagger_i(\omega_2) + \phi(\omega_2,\omega_1)\hat{a}^\dagger_s(\omega_2)\hat{a}^\dagger_i(\omega_1)\right]|0\rangle \otimes |D\rangle\,|D\rangle \tag{7.12}$$

which is now a frequency entangled state in which both photons are diagonally polarized; of course this operation leads to the loss of 75% of the produced photon pairs.

By approximating the JSAs with Dirac deltas the state can be written as follows:

$$|\Psi\rangle \sim \left|\omega_1^0\right\rangle_s \left|\omega_2^0\right\rangle_i + \left|\omega_2^0\right\rangle_s \left|\omega_1^0\right\rangle_i \tag{7.13}$$

which is a two-color entangled state.

7.2.4 Recovering polarization entanglement

On the other hand, it is also possible to recover the polarization entanglement by separating the frequency and polarization DOFs.

The scheme that we present has been proposed in 2003 by Kim et al. [264]. As illustrated in Figure 7.3, once the photons of the pair are created, they are sent with equal-length paths to a polarizing beamsplitter (PBS). A half wave plate ($\lambda/2$) is placed in the idler arm to rotate the polarization by 90° and ensure that the photons have the same polarization when they pass through the PBS. Horizontally polarized photons are transmitted while vertically polarized ones are reflected (as shown in the insets of the figure). Applying this transformation to the emitted state, Equation 7.6, yields:

$$|\Psi\rangle = \iint \mathrm{d}\omega_1\mathrm{d}\omega_2 \left[\phi(\omega_1,\omega_2)\hat{a}^\dagger_{4,V}(\omega_1)\hat{a}^\dagger_{3,V}(\omega_2) + \phi(\omega_2,\omega_1)\hat{a}^\dagger_{3,H}(\omega_2)\hat{a}^\dagger_{4,H}(\omega_1)\right]|0\rangle \tag{7.14}$$

where 3 and 4 are the PBS outputs, as illustrated in Figure 7.3. By changing the integration variables in the second term we can factorize the JSA:

$$|\Psi\rangle = \iint \mathrm{d}\omega_1\mathrm{d}\omega_2\, \phi(\omega_1,\omega_2) \left[\hat{a}^\dagger_{4,V}(\omega_1)\hat{a}^\dagger_{3,V}(\omega_2) + \hat{a}^\dagger_{4,H}(\omega_1)\hat{a}^\dagger_{3,H}(\omega_2)\right]|0\rangle \tag{7.15}$$

and thus the frequency and polarization DOFs have been decoupled. If we approximate the JSA with a Dirac delta, the state becomes a polarization entangled Bell state with non-degenerate frequencies:

$$|\Psi\rangle \sim \left(|H\rangle_3\,|H\rangle_4 + |V\rangle_3\,|V\rangle_4\right) \otimes \left|\omega_2^0\right\rangle_3 \left|\omega_1^0\right\rangle_4 \tag{7.16}$$

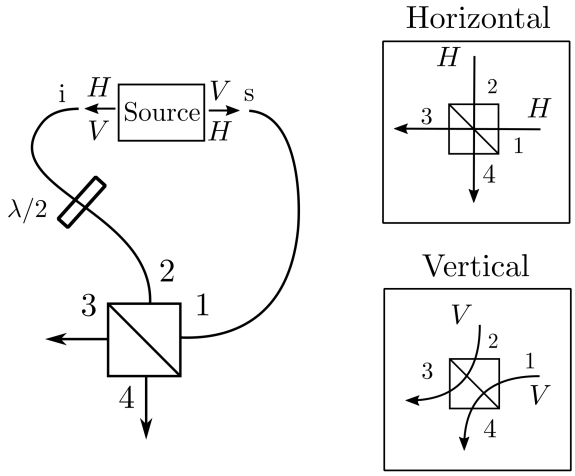

Figure 7.3: Scheme to recover polarization entanglement from the HPF entangled state reported in Equation 7.6. The insets illustrate the behavior of vertically and horizontally polarized photons in the polarizing beamsplitter.

which is a $\left|\Phi^+\right\rangle$ Bell state where the photon in output 3 has frequency ω_2^0 and the one in output 4 has frequency ω_1^0. Contrary to the previous case, this technique has no intrinsic losses.

Utilization of a non-birefringent waveguide

We mention here an alternative solution to generate a polarization Bell state, which is to design a waveguide without modal birefringence. In this case the two interactions would be frequency degenerate for any pump incidence angle and thus the source would directly emit polarization Bell states. In particular, if the pump is at normal incidence the two photons would have the same frequency, while otherwise the frequencies are different.

Figure 7.4 reports the expected modal birefringence of the device as a function of the ridge width, calculated through numerical simulations. We observe that for ridge widths above 3 µm the birefringence is almost constant, while when the ridge width is reduced the birefringence decreases and eventually becomes negative ($\Delta n = n_H - n_V$ changes sign). For a 1.18 µm-wide ridge we obtain a non-birefringent waveguide.

7.3 Theory of a HPF entangled state in a HOM interferometer

In the previous section we have shown that the HPF entangled state produced by our source collapses into a mixed state when only one of the two DOFs is observed. Nonetheless, the entanglement of this particular state can be efficiently characterized by means of a Hong-Ou-Mandel interferometer, as we shall show in this section.

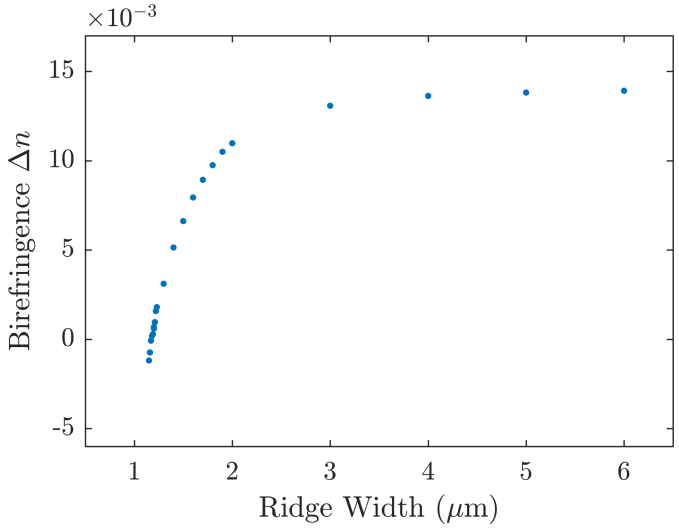

Figure 7.4: Numerical simulations of the source modal birefringence $\Delta n = n_H - n_V$ as a function of the ridge width.

Before starting the analysis we have to differentiate two cases, depending on the source facet reflectivity. Indeed, as we already pointed out, the source facets have a non-zero modal reflectivity that creates a longitudinal Fabry-Pérot cavity. As we will see, this cavity has a non negligible effect on the emitted quantum state and on the resulting HOM interference.

Thus, in the following we will study first a counter-propagating source without the Fabry-Pérot cavity effect (situation that could be obtained with an anti-reflection coating applied to the facets) and then one with the Fabry-Pérot cavity effect (as in the case of a non-coated device).

7.3.1 HPF entangled state without Fabry-Pérot effect

In this section we consider the state emitted by a counter-propagating source and we calculate the HOM coincidence probability, without taking into account the Fabry-Pérot cavity effect. This situation can be easily obtained by depositing an anti-reflection coating on the waveguide facets, as we shall see at the end of this chapter.

Figure 7.5 is a sketch of the setup that we consider: the biphoton state is emitted by the source through both interactions, hence we have both polarizations in either the signal or the idler side. Then the idler photon is delayed with respect to the signal one and eventually the two are mixed in a 50:50 beamsplitter (BS). The figure reports the notation we use in the following calculations.

We start from the emitted state, described by Equation 7.4, where we do not make any assumption on the JSA of each interaction, written as $\phi_{VH}(\omega_1, \omega_2)$ and $\phi_{HV}(\omega_1, \omega_2)$. Considering the delay line, placed in the idler arm, the wavefunction becomes:

$$|\Psi\rangle = \iint \mathrm{d}\omega_1 \mathrm{d}\omega_2 \Big[\phi_{VH}(\omega_1,\omega_2)\hat{a}^\dagger_{s,V}(\omega_1)\hat{a}^\dagger_{i,H}(\omega_2)e^{-i\omega_2\tau} + \phi_{HV}(\omega_1,\omega_2)\hat{a}^\dagger_{s,H}(\omega_1)\hat{a}^\dagger_{i,V}(\omega_2)e^{-i\omega_2\tau}\Big]|0\rangle \tag{7.17}$$

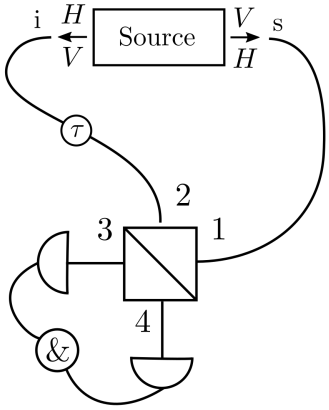

Figure 7.5: Sketch of a Hong-Ou-Mandel interferometer for a counter-propagating source emitting photons through both interactions. The cavity effect is not considered. The labels refer to the subscripts employed in the calculation.

where τ is the delay generated by the delay line.

We now apply the beam-splitter transformation to the creation and annihilation operators, as detailed in section 6.1:

$$\begin{aligned}\hat{a}_1^\dagger(\omega) &\to \frac{1}{\sqrt{2}}\Big(\hat{a}_3^\dagger(\omega) + i\hat{a}_4^\dagger(\omega)\Big)\\ \hat{a}_2^\dagger(\omega) &\to \frac{1}{\sqrt{2}}\Big(\hat{a}_4^\dagger(\omega) + i\hat{a}_3^\dagger(\omega)\Big)\end{aligned} \tag{7.18}$$

where we call 1 the BS input for the signal photon and 2 the input for the idler photon. 3 and 4 are the two BS outputs. The wavefunction becomes:

$$\begin{aligned}|\Psi\rangle =& \frac{1}{2}\iint \mathrm{d}\omega_1 \mathrm{d}\omega_2 \\ &\Big[\phi_{VH}(\omega_1,\omega_2)\Big(\hat{a}_{3,V}^\dagger(\omega_1) + i\hat{a}_{4,V}^\dagger(\omega_1)\Big)\Big(\hat{a}_{4,H}^\dagger(\omega_2) + i\hat{a}_{3,H}^\dagger(\omega_2)\Big)e^{-i\omega_2\tau} \\ &+ \phi_{HV}(\omega_1,\omega_2)\Big(\hat{a}_{3,H}^\dagger(\omega_1) + i\hat{a}_{4,H}^\dagger(\omega_1)\Big)\Big(\hat{a}_{4,V}^\dagger(\omega_2) + i\hat{a}_{3,V}^\dagger(\omega_2)\Big)e^{-i\omega_2\tau}\Big]\,|0\rangle\end{aligned} \tag{7.19}$$

At this point, in order to calculate the coincidence probability at the detectors, we use the coincidence operator $\hat{M}$ (introduced in section 6.2). Note that in this case we also have to consider the polarization degree of freedom: indeed, the $\hat{a}$ and $\hat{a}^\dagger$ operators in Equation 7.19 have a polarization dependency. In general, the coincidence probability will consist of four terms, P_{HH}, P_{VV}, P_{VH} and P_{HV}, but, in our case, the photons are generated through a type II SPDC process; hence they have always crossed polarizations. Thus, only the last two terms are non-zero and the probability of coincidence detection can be written as $P_c = P_{VH} + P_{HV}$. We first consider the latter term P_{HV}, which can be derived by employing the operator $\hat{M}_{HV}$, namely:

$$\hat{M}_{HV} = \int \mathrm{d}\omega_3 \hat{a}_{3,H}^\dagger(\omega_3)\,|0\rangle\langle 0|\,\hat{a}_{3,H}(\omega_3) \int \mathrm{d}\omega_4 \hat{a}_{4,V}^\dagger(\omega_4)\,|0\rangle\langle 0|\,\hat{a}_{4,V}(\omega_4) \tag{7.20}$$

By evaluating the expectation value of this operator on the state $|\Psi\rangle$ we calculate the probability of detecting a horizontally polarized photon in detector 3 and a vertically polarized one in detector 4. The calculation reads:

$$\begin{aligned}
P_{HV}(\tau) = &\langle\Psi|\,\hat{M}_{HV}\,|\Psi\rangle = \\
&\langle 0|\,\frac{1}{2}\iint \mathrm{d}\omega_1'\mathrm{d}\omega_2'\Big[\phi_{VH}^*(\omega_1',\omega_2')e^{i\omega_2'\tau}\Big(\hat{a}_{3,V}(\omega_1')\hat{a}_{4,H}(\omega_2') - \hat{a}_{3,H}(\omega_2')\hat{a}_{4,V}(\omega_1')\Big) \\
&+ \phi_{HV}^*(\omega_1',\omega_2')e^{i\omega_2'\tau}\Big(\hat{a}_{3,H}(\omega_1')\hat{a}_{4,V}(\omega_2') - \hat{a}_{3,V}(\omega_2')\hat{a}_{4,H}(\omega_1')\Big)\Big] \\
&\int \mathrm{d}\omega_3\hat{a}_{3,H}^\dagger(\omega_3)\,|0\rangle\,\langle 0|\,\hat{a}_{3,H}(\omega_3)\int \mathrm{d}\omega_4\hat{a}_{4,V}^\dagger(\omega_4)\,|0\rangle\,\langle 0|\,\hat{a}_{4,V}(\omega_4) \\
&\frac{1}{2}\iint \mathrm{d}\omega_1\mathrm{d}\omega_2\Big[\phi_{VH}(\omega_1,\omega_2)e^{-i\omega_2'\tau}\Big(\hat{a}_{3,V}^\dagger(\omega_1)\hat{a}_{4,H}^\dagger(\omega_2) - \hat{a}_{3,H}^\dagger(\omega_2)\hat{a}_{4,V}^\dagger(\omega_1)\Big) \\
&+ \phi_{HV}(\omega_1,\omega_2)e^{-i\omega_2\tau}\Big(\hat{a}_{3,H}^\dagger(\omega_1)\hat{a}_{4,V}^\dagger(\omega_2) - \hat{a}_{3,V}^\dagger(\omega_2)\hat{a}_{4,H}^\dagger(\omega_1)\Big)\Big]\,|0\rangle
\end{aligned} \tag{7.21}$$

where we have kept only the terms that give rise to a coincidence count ($\hat{a}_3^\dagger\hat{a}_4^\dagger$ or $\hat{a}_4^\dagger\hat{a}_3^\dagger$). By applying those operators on the vacuum state we obtain:

$$\begin{aligned}
P_{HV}(\tau) = &\frac{1}{4}\int \mathrm{d}\omega_1\int \mathrm{d}\omega_2\int \mathrm{d}\omega_1'\int \mathrm{d}\omega_2'\int \mathrm{d}\omega_3\int \mathrm{d}\omega_4 \\
&\Big[\phi_{VH}^*(\omega_1',\omega_2')e^{i\omega_2'\tau}\left(-\delta(\omega_2'-\omega_3)\delta(\omega_1'-\omega_4)\right) \\
&\phi_{HV}^*(\omega_1',\omega_2')e^{i\omega_2'\tau}\left(\delta(\omega_1'-\omega_3)\delta(\omega_2'-\omega_4)\right)\Big] \\
&\cdot\Big[\phi_{VH}(\omega_1,\omega_2)e^{-i\omega_2\tau}\left(-\delta(\omega_2-\omega_3)\delta(\omega_1-\omega_4)\right) \\
&\phi_{HV}(\omega_1,\omega_2)e^{-i\omega_2\tau}\left(\delta(\omega_1-\omega_3)\delta(\omega_2-\omega_4)\right)\Big]
\end{aligned} \tag{7.22}$$

Integrating over ω_1, ω_2, ω_1', ω_2' yields:

$$\begin{aligned}
P_{HV}(\tau) = &\frac{1}{4}\int \mathrm{d}\omega_3\int \mathrm{d}\omega_4\Big[|\phi_{VH}(\omega_4,\omega_3)|^2 + |\phi_{HV}(\omega_3,\omega_4)|^2 \\
&- \phi_{VH}^*(\omega_4,\omega_3)\phi_{HV}(\omega_3,\omega_4)e^{i(\omega_3-\omega_4)\tau} \\
&- \phi_{VH}(\omega_4,\omega_3)\phi_{HV}^*(\omega_3,\omega_4)e^{i(\omega_4-\omega_3)\tau}\Big]
\end{aligned} \tag{7.23}$$

A similar calculation for P_{VH} leads to:

$$\begin{aligned}
P_{VH}(\tau) = &\frac{1}{4}\int \mathrm{d}\omega_3\int \mathrm{d}\omega_4\Big[|\phi_{VH}(\omega_3,\omega_4)|^2 + |\phi_{HV}(\omega_4,\omega_3)|^2 \\
&- \phi_{VH}^*(\omega_3,\omega_4)\phi_{HV}(\omega_4,\omega_3)e^{i(\omega_4-\omega_3)\tau} \\
&- \phi_{VH}(\omega_3,\omega_4)\phi_{HV}^*(\omega_4,\omega_3)e^{i(\omega_3-\omega_4)\tau}\Big]
\end{aligned} \tag{7.24}$$

By adding these two terms we obtain the probability of a coincidence count when a HPF entangled state enters the HOM interferometer:

$$\begin{aligned}
P_c(\tau) &= P_{HV}(\tau) + P_{VH}(\tau) \\
&= \frac{1}{4}\Big\{2 - 2\iint \mathrm{d}\omega_3\mathrm{d}\omega_4\Big[\phi_{VH}^*(\omega_4,\omega_3)\phi_{HV}(\omega_3,\omega_4)e^{-i(\omega_3-\omega_4)\tau} + \text{c.c.}\Big]\Big\} \\
&= \frac{1}{2} - \mathrm{Re}\left[\iint \mathrm{d}\omega_3\mathrm{d}\omega_4\phi_{VH}^*(\omega_4,\omega_3)\phi_{HV}(\omega_3,\omega_4)e^{-i(\omega_3-\omega_4)\tau}\right]
\end{aligned} \tag{7.25}$$

where we have used the normalization condition given by Equation 7.5. This expression shows that, if the total JSA has a non-zero overlap with its mirror symmetric, we have interference.

Figure 7.6 reports the expected coincidence probability for the state whose JSI is reported in Figure 7.2, derived using Equation 7.25. The curve is composed of an envelope, whose shape depends on the phase-matching function, and of a sinusoidal modulation, produced by the interference between the photons emitted by the two interactions.

Notice that in this scheme no half wave plate to rotate the polarization of one arm is present, in contrast with the case where a HOM experiment is done using a single interaction (chapter 6). Indeed, after the beamsplitter, the two interactions are indistinguishable and therefore the photons interfere. On the contrary, if we rotate the polarization in one arm, one interaction will have both photons horizontally polarized and the other interaction will have both photons vertically polarized. It is clear that in this situation the two interactions are distinguishable and the photons cannot interfere.

This remark explains why the HOM interferometer is an efficient tool to quantify the entanglement of a HPF entangled state. Indeed, after the mixing beamsplitter the two interactions are indistinguishable in both frequency and polarization DOFs and the photons can thus interfere. The visibility of the HOM interferogram can be employed to estimate the entanglement level of the experimentally generated state, both in frequency and polarization.

In order to understand the origin of the sinusoidal modulation, let us recall a fundamental concept of the HOM interferometer. As described in chapter 6, when we considered biphoton states with a frequency degenerate JSA, the HOM dip/peak is a phase-independent effect because it is caused by the interference between the situation in which both photons are reflected at the beamsplitter and the one in which both photons are transmitted. Therefore, an eventual phase variation affects both situations and does not influence the interference. Differently, in this case, the sinusoidal modulation arises from the additional phase term due to the frequency difference between the two frequency modes and the temporal delay added by the delay line. This phase term oscillates between 0 and 2π, leading to a modulation. Note that this spatial beating is stationary and not time-dependent. Indeed, it is not an interference between two photons at different frequencies, but between two biphoton wave-packets, one at frequencies (ω_1, ω_2) and the other at (ω_2, ω_1) [170].

We can also analyze the coincidence probability from another point of view. As we have seen in section 6.2, if the JSA of the input state is mirror symmetric with respect to the ω_+ direction, the HOM interferogram is effectively the Fourier Transform of the JSI. Therefore, if the state has only one frequency mode at degeneracy (as in chapter 6) the Fourier Transform has only the zero-frequency component, represented by the dip centered at $\tau = 0$. On the other hand, here the JSI has two non-degenerate frequency modes and thus the FT results in an envelope and a sinusoidal modulation.

To conclude, it is worth noting that a two-color entangled state, with no polarization entanglement, would produce the same sinusoidal oscillation, but, in that case, it would be generated by the interference between the two frequency modes. On the contrary, in our case, the oscillation is generated by the interference between

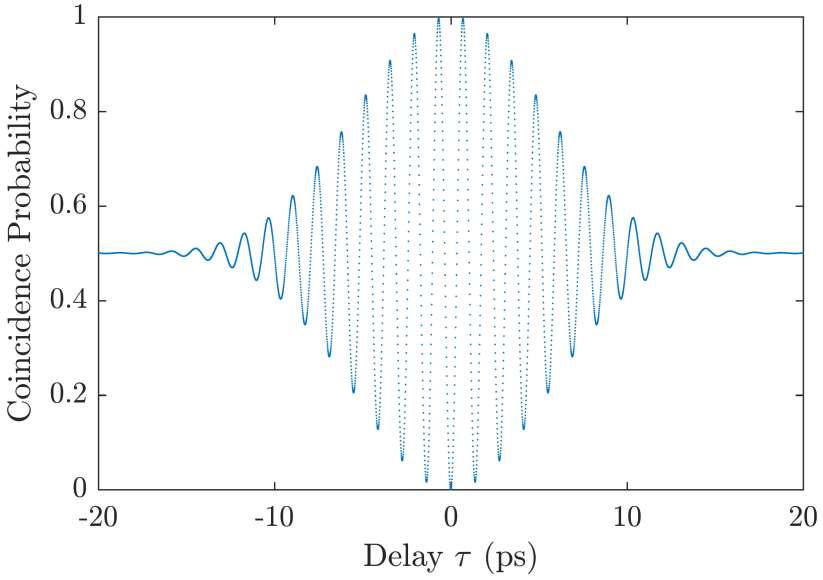

Figure 7.6: Simulated HOM interferogram derived using Equation 7.25 and the state whose JSI is reported in Figure 7.2

the two interactions, in polarization and frequency.

Gaussian phase-matching

In order to gain a physical insight into the parameters influencing the HOM coincidence probability, we now consider a particular case of JSA. We first consider two JSAs separable along $\omega_+ = \omega_3 + \omega_4$ and $\omega_- = \omega_3 - \omega_4$, as commonly produced by our source (see Equation 2.34):

$$\begin{aligned} \phi_{VH}(\omega_3, \omega_4) &= \chi_\Gamma \, \mathrm{PM}_{VH}(\omega_-) \, \phi_{\mathrm{spectral}}(\omega_+) \\ \phi_{HV}(\omega_3, \omega_4) &= \chi_\Gamma \, \mathrm{PM}_{HV}(\omega_-) \, \phi_{\mathrm{spectral}}(\omega_+) \end{aligned} \tag{7.26}$$

In our approximations, the two interactions differ only by the modal refractive indices and therefore they have the same spectral function but different phase-matching functions. Moreover, as we have already seen in Equation 6.27 for the degenerate case, the HOM coincidence probability depends only on the phase-matching function and not on the spectral function. For these reasons we can consider an arbitrary spectral function $\phi_{\mathrm{spectral}}(\omega_+)$ and define only the two phase-matching functions.

Inserting Equation 7.26 into Equation 7.25 and changing the integration variables from ω_3, ω_4 to ω_+, ω_- we obtain:

$$\begin{aligned} P_c(\tau) = &\frac{1}{2} - |\chi_\Gamma|^2 \int \mathrm{d}\omega_+ |\phi_{\mathrm{spectral}}(\omega_+)|^2 \\ &\cdot \mathrm{Re}\left[\int \mathrm{d}\omega_- \mathrm{PM}^*_{VH}(-\omega_-) \mathrm{PM}_{HV}(\omega_-) \, e^{-i\omega_- \tau} \right] \end{aligned} \tag{7.27}$$

where we see that the two-photon interference is governed only the by the phase-

matching function. Using the normalization condition (Equation 7.5) we obtain:

$$P_c(\tau) = \frac{1}{2} - \frac{\mathrm{Re}\left[\int \mathrm{d}\omega_- \, \mathrm{PM}^*_{VH}(-\omega_-)\mathrm{PM}_{HV}(\omega_-)\, e^{-i\omega_-\tau}\right]}{\int \mathrm{d}\omega_- \left[\, |\mathrm{PM}_{VH}(-\omega_-)|^2 + |\mathrm{PM}_{HV}(\omega_-)|^2\right]} \tag{7.28}$$

In order to illustrate this result, we now consider a Gaussian pump beam with a waist w_z, smaller than the waveguide length, impinging perpendicularly to the waveguide. The JSAs of the two interactions are then symmetric with respect to the ω_+ direction and we can write the phase-matching terms as follows:

$$\begin{aligned} \mathrm{PM}_{VH}(\omega_-) &= \sqrt{\pi}\, w_z \, \exp\left[-\left(\frac{\omega_- - \omega_-^{\mathrm{deg}}}{\Delta\omega_-}\right)^2\right] \\ \mathrm{PM}_{HV}(\omega_-) &= \sqrt{\pi}\, w_z \, \exp\left[-\left(\frac{\omega_- + \omega_-^{\mathrm{deg}}}{\Delta\omega_-}\right)^2\right] \end{aligned} \tag{7.29}$$

where $\omega_-^{\mathrm{deg}} = \dfrac{\bar{v}_g}{c}\omega_p \sin\theta_{\mathrm{deg}}$ is the distance of each frequency mode from the degeneracy $\omega_- = 0$. Inserting Equation 7.29 into the expression of the coincidence probability (Equation 7.28) we obtain:

$$P_c(\tau) = \frac{1}{2} - \frac{1}{2}\exp\left[-\frac{\tau^2}{\Delta\tau^2}\right]\cos\left(\omega_-^{\mathrm{deg}}\tau\right) \tag{7.30}$$

Thus, in agreement with the numerical simulation of Figure 7.6, the resulting interferogram is a sinusoidal oscillation with period $\tau_p = \dfrac{2\pi}{\omega_-^{\mathrm{deg}}}$, modulated by a Gaussian envelope, which has the same temporal width $\Delta\tau = \dfrac{2\sqrt{2}}{\Delta\omega_-}$ than in the case of a single interaction (see Equation 6.27). The oscillation period depends on the distance between the two frequency modes, which in our case is proportional to the waveguide modal birefringence.

7.3.2 HPF entangled state with Fabry-Pérot effect

In the previous section we have considered the HOM experiment without taking into account the cavity effect produced by the facet reflectivity. Since our source facets have non-negligible reflectivity ($R_{\mathrm{TE}} = 28.5\%$ and $R_{\mathrm{TM}} = 24.7\%$), we need to consider this effect: due to the counter-propagating geometry of the device, when a signal photon bounces at the facet it can exit the waveguide from the idler side and vice-versa, eventually even after multiple round-trips. For the HOM experiment performed in chapter 6 this effect was not a problem. Indeed, in that case we selected only one interaction with a polarizer and a wavelength bandpass filter in each output arm so that the cavity effect reduced only to a modulation of the JSA, without modifying the photons effective propagation direction (see subsection 2.2.5).

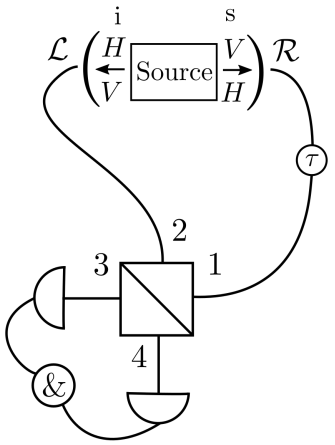

Figure 7.7: Hong-Ou-Mandel scheme for a counter-propagating source emitting photons through both interactions and considering the cavity effect. The letters refer to the subscripts used in the calculations (see text for details).

In the present situation however, since the photons are not polarization selected, there is a non-zero probability to have both signal and idler photons in the right or left side. Even if this is a simplistic corpuscular view, it shows that the study presented in the previous section of this chapter is not complete.

To refine this analysis, we start from the wavefunction of the emitted state (Equation 7.4) and we now consider the cavity, followed by the same steps than in the previous calculation (delay line, 50:50 beamsplitter and detection). For the sake of clarity we refer to Figure 7.7 for the used subscripts: s (signal) and i (idler) label the propagation directions of the generated photons inside the source before the mixing by the cavity, $\mathcal{R}$ (right) and $\mathcal{L}$ (left) are the directions outside the cavity, while 1 and 2 are the two inputs of the beamsplitter, 3 and 4 are the outputs.

As we have already done in subsection 2.2.5, we model the cavity functions as follows:

$$\begin{aligned} f_t(\omega) &= \frac{\sqrt{1-R}\,\exp\left(i\frac{\omega n L}{2c}\right)}{1-R\,\exp\left(i\frac{2\omega n L}{c}\right)} \\ f_r(\omega) &= \frac{\sqrt{R(1-R)}\,\exp\left(i\frac{3\omega n L}{2c}\right)}{1-R\,\exp\left(i\frac{2\omega n L}{c}\right)} \end{aligned} \tag{7.31}$$

where $f_t(\omega)$ ($f_r(\omega)$) is the transmission (reflection) function. Moreover, in order to simplify the calculation, we assume that the cavity has the same reflectivity for both polarization directions (for which we will employ the average value of R_{TE} and R_{TM}, $R \approx 27\%$).

Each waveguide facet can be modeled as a frequency-dependent beamsplitter, where photons can either be reflected or transmitted [170]. The transformations

for the $\hat{a}$ and $\hat{a}^\dagger$ operators are thus:

$$\begin{aligned}\hat{a}^\dagger_{s,\sigma}(\omega) &\to f_t(\omega)\hat{a}^\dagger_{\mathcal{R},\sigma}(\omega) + f_r(\omega)\hat{a}^\dagger_{\mathcal{L},\sigma}(\omega)\\ \hat{a}^\dagger_{i,\sigma}(\omega) &\to f_t(\omega)\hat{a}^\dagger_{\mathcal{L},\sigma}(\omega) + f_r(\omega)\hat{a}^\dagger_{\mathcal{R},\sigma}(\omega)\end{aligned} \tag{7.32}$$

where σ stands for the H or V polarization. The wavefunction becomes:

$$\begin{aligned}|\Psi\rangle = \iint \mathrm{d}\omega_1\mathrm{d}\omega_2\Big[&\phi_{VH}(\omega_1,\omega_2)\Big(\ f_t(\omega_1)\hat{a}^\dagger_{\mathcal{R},V}(\omega_1)e^{-i\omega_1\tau} + f_r(\omega_1)\hat{a}^\dagger_{\mathcal{L},V}(\omega_1)\Big)\\ &\Big(\ f_t(\omega_2)\hat{a}^\dagger_{\mathcal{L},H}(\omega_L) + f_r(\omega_2)\hat{a}^\dagger_{\mathcal{R},H}(\omega_2)e^{-i\omega_2\tau}\Big)\\ +&\phi_{HV}(\omega_1,\omega_2)\Big(\ f_t(\omega_1)\hat{a}^\dagger_{\mathcal{R},H}(\omega_1)e^{-i\omega_1\tau} + f_r(\omega_1)\hat{a}^\dagger_{\mathcal{L},H}(\omega_1)\Big)\\ &\Big(\ f_t(\omega_2)\hat{a}^\dagger_{\mathcal{L},H}(\omega_L) + f_r(\omega_2)\hat{a}^\dagger_{\mathcal{R},H}(\omega_2)e^{-i\omega_2\tau}\Big)\Big]\ |0\rangle\end{aligned} \tag{7.33}$$

where we have also considered the effect of the delay line placed on the right ($\mathcal{R}$) side.

We then apply the beamsplitter transformations, reported in Equation 7.18, and since we are interested only in coincidence events, we keep only the crossed terms (of the kind $\hat{a}^\dagger_3\hat{a}^\dagger_4$ and $\hat{a}^\dagger_4\hat{a}^\dagger_3$). The resulting wavefunction $|\Psi_\mathrm{c}\rangle$ reads:

$$\begin{aligned}|\Psi_\mathrm{c}\rangle = \frac{1}{2}\iint \mathrm{d}\omega_1\mathrm{d}\omega_2\Big[&A(\omega_1,\omega_2)\hat{a}^\dagger_{3,H}(\omega_1)\hat{a}^\dagger_{4,V}(\omega_2) + B(\omega_1,\omega_2)\hat{a}^\dagger_{3,H}(\omega_2)\hat{a}^\dagger_{4,V}(\omega_1)\\ &+C(\omega_1,\omega_2)\hat{a}^\dagger_{3,V}(\omega_1)\hat{a}^\dagger_{4,H}(\omega_2) + D(\omega_1,\omega_2)\hat{a}^\dagger_{3,V}(\omega_2)\hat{a}^\dagger_{4,H}(\omega_1)\Big]\ |0\rangle\end{aligned} \tag{7.34}$$

where the coefficients are:

$$\begin{aligned}A(\omega_1,\omega_2) = \phi_{HV}(\omega_1,\omega_2)\Big[&-f_r(\omega_1)f_r(\omega_2)e^{-i\omega_2\tau} + if_t(\omega_1)f_r(\omega_2)e^{-i(\omega_1+\omega_2)\tau}\\ &+ if_r(\omega_1)f_t(\omega_2) + if_t(\omega_1)f_t(\omega_2)e^{-i\omega_1\tau}\Big]\end{aligned} \tag{7.35}$$

$$\begin{aligned}B(\omega_1,\omega_2) = \phi_{VH}(\omega_1,\omega_2)\Big[&+f_r(\omega_1)f_r(\omega_2)e^{-i\omega_2\tau} + if_t(\omega_1)f_r(\omega_2)e^{-i(\omega_1+\omega_2)\tau}\\ &+ if_r(\omega_1)f_t(\omega_2) - if_t(\omega_1)f_t(\omega_2)e^{-i\omega_1\tau}\Big]\end{aligned} \tag{7.36}$$

$$\begin{aligned}C(\omega_1,\omega_2) = \phi_{VH}(\omega_1,\omega_2)\Big[&-f_r(\omega_1)f_r(\omega_2)e^{-i\omega_2\tau} + if_t(\omega_1)f_r(\omega_2)e^{-i(\omega_1+\omega_2)\tau}\\ &+ if_r(\omega_1)f_t(\omega_2) + if_t(\omega_1)f_t(\omega_2)e^{-i\omega_1\tau}\Big]\end{aligned} \tag{7.37}$$

$$\begin{aligned}D(\omega_1,\omega_2) = \phi_{HV}(\omega_1,\omega_2)\Big[&+f_r(\omega_1)f_r(\omega_2)e^{-i\omega_2\tau} + if_t(\omega_1)f_r(\omega_2)e^{-i(\omega_1+\omega_2)\tau}\\ &+ if_r(\omega_1)f_t(\omega_2) - if_t(\omega_1)f_t(\omega_2)e^{-i\omega_1\tau}\Big]\end{aligned} \tag{7.38}$$

By applying the coincidence operator $\hat{M}$ for the HV and VH cases we then calculate the coincidence probability $P_c(\tau) = P_{HV}(\tau) + P_{VH}(\tau)$, where

$$\begin{aligned}P_{HV}(\tau) = \langle\Psi_\mathrm{c}|\hat{M}_{HV}|\Psi_\mathrm{c}\rangle = &\frac{1}{4}\iint \mathrm{d}\omega_3\,\mathrm{d}\omega_4\Big[|A(\omega_3,\omega_4)|^2 + |B(\omega_3,\omega_4)|^2\\ &+ A^*(\omega_3,\omega_4)B(\omega_4,\omega_3) + A(\omega_4,\omega_3)B^*(\omega_3,\omega_4)\Big]\end{aligned} \tag{7.39}$$

$$\begin{aligned}P_{VH}(\tau) = \langle\Psi_\mathrm{c}|\hat{M}_{VH}|\Psi_\mathrm{c}\rangle = &\frac{1}{4}\iint \mathrm{d}\omega_3\,\mathrm{d}\omega_4\Big[|C(\omega_3,\omega_4)|^2 + |D(\omega_3,\omega_4)|^2\\ &+ C^*(\omega_3,\omega_4)D(\omega_4,\omega_3) + C(\omega_4,\omega_3)D^*(\omega_3,\omega_4)\Big]\end{aligned} \tag{7.40}$$

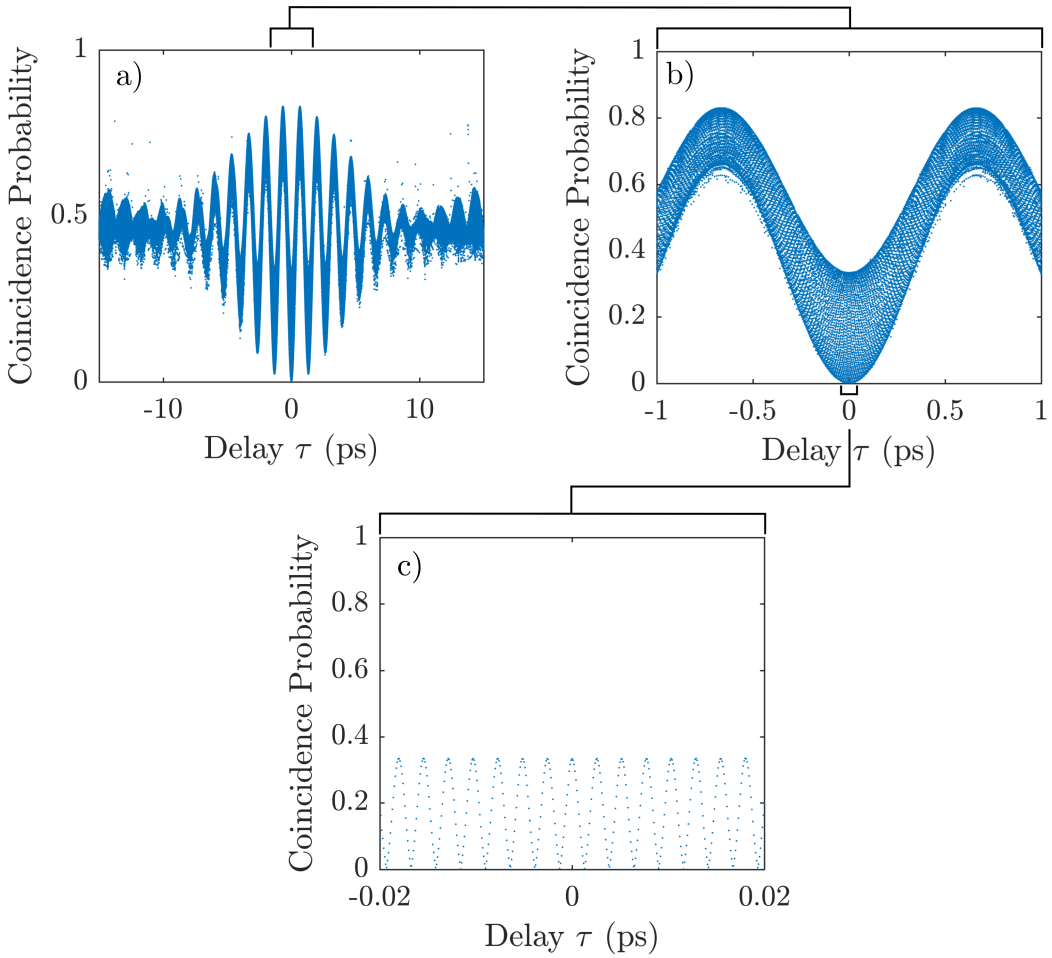

Figure 7.8: Simulated HOM probability for the HPF entangled state considered in Figure 7.2 (facet reflectivity R=27 %). From (a) to (c) the time axis is zoomed around $\tau = 0$, in order to show the additional modulation. The scattered points are caused by numerical artifacts in the integration.

It is worth noting that, even if the photons are mixed by the cavity, they are always generated with crossed polarizations and therefore we can neglect the HH and VV cases.

The resulting integral has been calculated numerically for a JSA composed of two Gaussian peaks centered at 1546 nm having a 0.3 nm width and a relative distance of 6 nm, a situation close to the experimental one reported in the following sections.

Figure 7.8 reports the HOM interferogram for different levels of close-up around the $\tau = 0$ position. The coincidence probability has almost the same shape than in the case without cavity: a Gaussian envelope and a sinusoidal oscillation (Figure 7.8a), but zooming in we note that another oscillation is superimposed to the first one (Figure 7.8b). This modulation has a period of 2.3 fs, corresponding to the inverse of the pump frequency (Figure 7.8c).

This additional oscillation is due to the fact that the cavity does not deterministically separate the two photons, so they have a non-zero probability of exiting

the same facet. The result is a Franson-type two-photon interference scheme [265]: the situation in which the photons are both emitted in the signal arm interferes with the one in which the photons are both emitted in the idler side, producing a $\cos\left(\omega_p \tau\right)$ modulation.

Here the Franson-type interference occurs for a time delay shorter than the photon coherence time and therefore it is superimposed to the HOM interference, as it has already been reported in [266].

Conversely, if the time delay is larger than the photon coherence time, only the Franson-type interference remains and its measurement, in this experimental condition, is widely employed in the literature to prove energy-time entanglement of photon pairs [59, 267, 268].

Another difference of the interferogram of Figure 7.8a with the cavity-free case is that the lower and upper global envelopes are not symmetric anymore. The lower envelope still reaches zero, but the upper envelope does not reach one. We are currently working on the analytic resolution of the integral yielding the coincidence probability, so as to gain more physical insight into this phenomenon.

Our current HOM experimental setup does not have enough resolution (i.e. mechanical stability of the mirrors and of the delay line) to resolve the modulation oscillating at the pump frequency and therefore we can measure only its temporal average, which is numerically evaluated in Figure 7.9. Averaging these oscillations essentially restores the symmetry between the upper and lower envelope, thus resembling the situation in absence of cavity (Figure 7.6); however, the visibility of this averaged interferogram is reduced. In this particular case (facet reflectivity $R = 27\%$) the visibility drops to 60%. By performing several simulations we have verified that, for low reflectivity values ($R < 50\%$), the visibility decays monotonically as a function of R.

In conclusion, our analytic and numerical studies point out that the cavity effect complexifies the quantum state emitted by the source, creating new phenomena that are currently under study. As a first step our objective is to demonstrate the generation of hybrid polarization/frequency entangled states; for this reason we will be interested in the elimination of the cavity effect, by reducing the facet modal reflectivity.

7.4 Experimental demonstration of HPF entanglement generation by an AlGaAs source with built-in cavity

In the previous sections we have analytically and numerically studied HPF entangled states and their typical signature in a HOM interferometer. Now we experimentally demonstrate that our source can effectively emit such states. First of all, we measure the Joint Spectral Intensity (JSI) of the state to ensure that it is in agreement with the simulated one, having two well-separated frequency modes. After that, in order to demonstrate that the state is not only anti-correlated but truly entangled, we measure the HOM interference.

The experimental data and analysis that follow are performed for two different

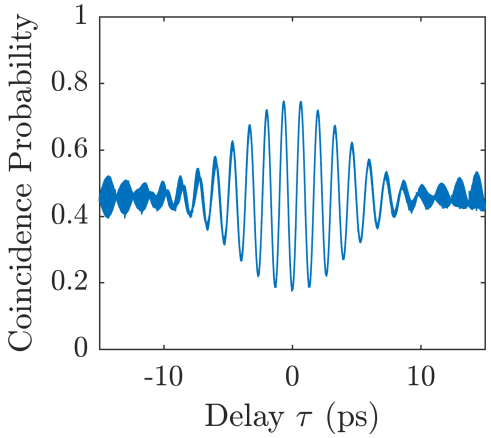

Figure 7.9: Simulated HOM probability for the HPF entangled state considered in Figure 7.2 (facet reflectivity R=27 %), averaging the oscillations of the pump frequency. The visibility of the interferogram is reduced to $V = 60\%$.

samples. In this section we focus on the sample used in the previous chapters, with facet reflectivity about $R \sim 27\%$. In the following section we will present measurements done employing a new device treated with an antireflection coating, with facet reflectivity about $R \sim 10\%$.

7.4.1 JSI measurement via the single-photon fiber spectrograph

At the beginning of this chapter we showed the simulated JSI for a HPF entangled state emitted by our device (Figure 7.2), which is formed by two gaussian lobes separated by 6.4 nm, due to the modal birefringence. We now experimentally reconstruct the JSI and verify the simulations.

The measurement has been done using the single-photon fiber spectrograph technique, already presented in section 4.1, where Figure 4.1 reports a sketch of the setup. In the present case the photons are not selected using polarizers and thus both interactions are kept. In addition, two long-pass filters (cut-off wavelength 1400 nm) are used to remove any residuals of the pump or eventual luminescence.

The measurement, reported in Figure 7.10a, has been performed with the pump beam perpendicular to the waveguide, at a wavelength $\lambda_p = 773.15$ nm, fixed by the microcavity resonance, and with a Gaussian spatial profile (waist of $w_z = 1$ mm and flat phase profile). The result shows two peaks symmetric with respect to degeneracy, with a relative distance ω_-^{deg} greater than their dimension. This ensures the orthogonality of the two frequency modes of the state.

In order to evaluate the distance ω_-^{deg} we analyze the signal marginal spectrum, obtained using only one dispersive fiber. The data, presented in Figure 7.10b, feature two peaks separated by 97 bins. This value corresponds to a wavelength span of about 4.8 nm, obtained using the bin time duration (81 ps) and the DCF dispersion (-1650 ps/nm). The experimental value of ω_-^{deg} slightly differs from the numerical simulation, which gives an expected ω_-^{deg} of about 6.4 nm. This difference is due to the difficulty to have a good estimation of the modal refractive indices

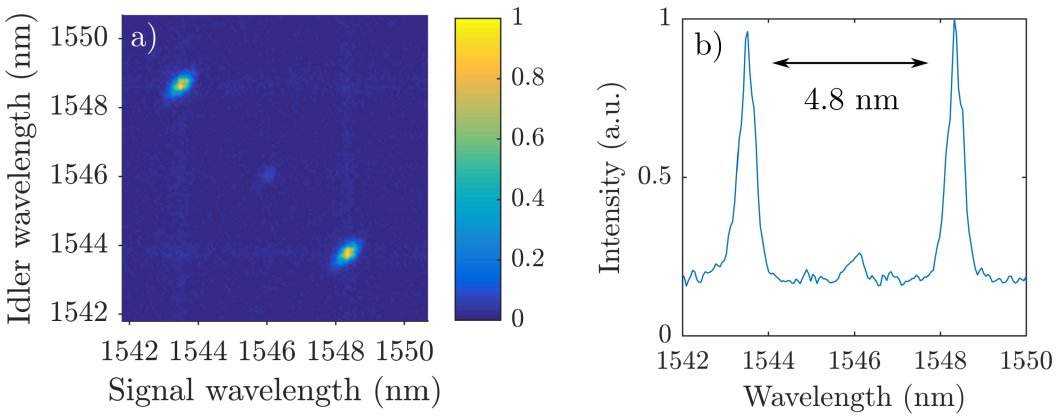

Figure 7.10: JSI (a) and signal marginal spectrum (b) of the HPF entangled state generated by our counter-propagating source, with facet reflectivity $\sim 27\%$. The measurement is done via a single-photon fiber spectrograph with a total integration time of half an hour. The pump beam is set at $\lambda_p = 773.15$ nm, fixed by the microcavity resonance, and it has a Gaussian profile with waist $w_z = 1$ mm and flat phase profile.

and, since the device presents a low modal birefringence (approximately 0.4%), even a small variation of the refractive indices can cause a significant birefringence change.

We can identify two main causes affecting the values of the modal refractive indices. The most probable one is a slight difference between the actual epitaxial growth and the nominal structure. The second is related to the fabrication process: the chemical etching technique is very sensitive to the etching time and does not allow a perfect control of the ridge width. However, the numerical simulations reported in Figure 7.4 show that for a wide enough ridge, a width variation (and therefore a change of the waveguide aspect ratio) has an almost negligible effect on the modal birefringence, while for a smaller ridge width (around 1.5 µm) the variation is significant. Since the device has a 5 µm-wide ridge, we think that the birefringence difference between the actual device and the nominal one comes mainly from the epitaxial growth.

7.4.2 HOM interference measurement

After having ensured that the experimental JSI features two well defined frequency modes, we verify that the state is also HPF entangled by employing a HOM interferometer. The experimental setup is reported in Figure 7.11 and is very similar to the one used in chapter 6. Indeed, the pump scheme is the same: a 1 mm-waist gaussian beam with a flat phase spatial profile is focused on the waveguide and its characteristics are monitored via the wavefront analyzer. The SLM is only used to correct eventual phase aberrations. The main difference with the setup mentioned before is the filtering stage. Due to its nature, the state has a wider spectral range than the 1.2 nm filters that we have employed in chapter 6, therefore here we use instead long pass bulk filters at 1400 nm, inserted in the free space paths before

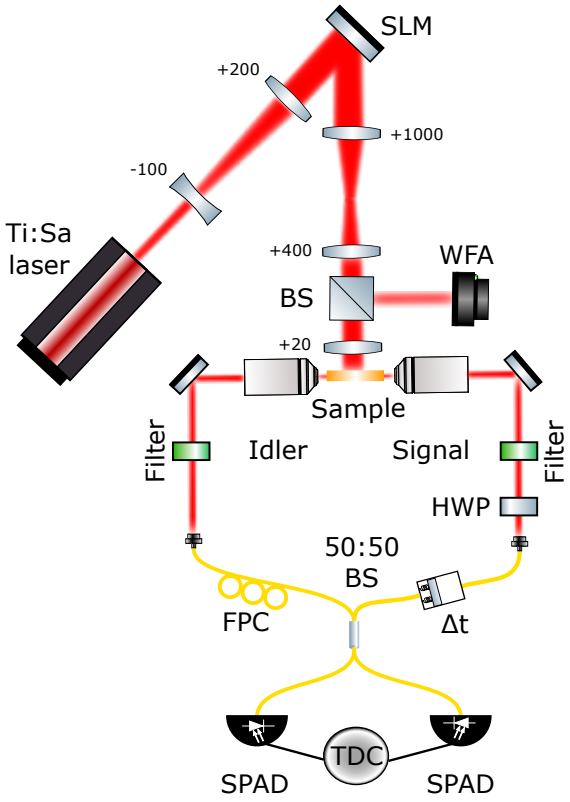

Figure 7.11: Experimental setup used to measure the HOM interference of a HPF entangled state (see text for description). Focal lengths are given in millimeters.

the fiber couplers, so as to remove eventual luminescence noise. For all the other components of the setup we refer to chapter 6.

The polarization is controlled using a half-wave plate (HWP) in the signal arm and a fibered polarization controller (FPC) in the idler arm. As we have noted in section 7.3, in order to obtain the interference effect, the output polarization of the photons has to be maintained and therefore we employ the HWP and the FPC to ensure that the two photons arrive at the beamsplitter with crossed polarizations.

Figure 7.12 reports the experimental interferogram measured in the situation described before. Experimental raw data, in black with error bars, show a clear sinusoidal modulation with a Gaussian envelope. Each point is obtained by a time integration of 20 s and its error bar is calculated assuming a Poissonian statistics. The blue line superimposed to the points is a fit realized using a modified version of Equation 7.30, in order to account for a non-perfect visibility. The employed fitting function is:

$$C(\tau) = a(\tau - \tau_0) + \frac{1}{2}\left[1 - V\exp\left(-\frac{(\tau-\tau_0)^2}{\Delta\tau^2}\right)\sin\left(\frac{2\pi}{\tau_p}(\tau-\tau_0)\right)\right] \tag{7.41}$$

where we have normalized the coincidence rate to one and we have added a possible linear offset with slope a to account for a slight drift of the alignment during the total time of the measurement. Here, V is the interferogram visibility, $\Delta\tau$ the envelope width and τ_p the oscillation period.

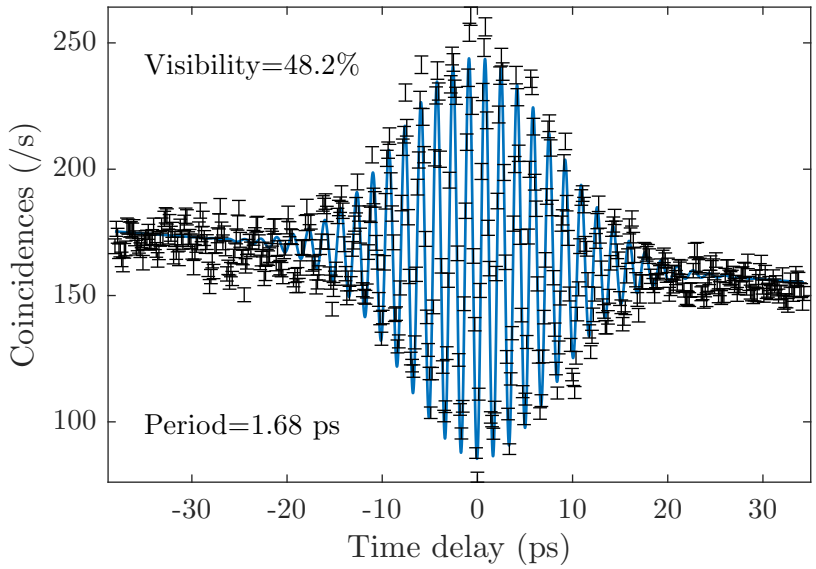

Figure 7.12: HOM experimental interferogram for a sample with facet reflectivity $R \approx 27\%$: raw data points are reported in black while the blue curve is a fit.

Parameter	Theoretical Value	Experimental Value
Visibility V	60%	48%
Modulation Period τ_p	1.3 ps	1.7 ps
Envelope Width $\Delta\tau$	11.5 ps	11.4 ps

Table 7.1: Theoretical and fitted parameters of the HOM interferogram for the device with a facet reflectivity $R \approx 27\%$, reported in Figure 7.12.

The fitting parameters are reported in Table 7.1 and compared to the ones expected from the numerical simulations. The experimental value of the visibility (48%) is lower than the one given by the simulation (60%), but the latter considers only the Fabry-Pérot effect as possible limiting factor. As we have seen in subsection 6.4.2, other factors must be taken into account (i.e. the pump incidence angle and eventual pump spot imperfections) which lower the visibility by about 10%. In conclusion, a reduction of 12% from the expected theoretical visibility is well in agreement with the numerical simulations.

We notice that the measured value of the modulation period $\tau_{p,\mathrm{exp}} = 1.7$ ps differs notably from the expected one $\tau_{p,\mathrm{sim}} = 1.3$ ps. The modulation period is inversely proportional to the frequency difference between the modes $\omega_{-}^{\mathrm{deg}}$ and is thus related to the birefringence, which is difficult to estimate, as we have already commented.

The modulation period can be also derived from the experimental value of the distance $\omega_{-}^{\mathrm{deg}}$ that we have reported above, measured with the fiber spectrograph. Doing so we obtain an expected value of τ_p =1.67 ps, which is much better in agreement with the experimentally measured one, $\tau_{p,\mathrm{exp}} = 1.7$ ps. From this value we can evaluate the modal birefringence of the device $\Delta n_{\mathrm{exp}} \sim 0.009$, slightly smaller than the expected value $\Delta n_{\mathrm{sim}} \sim 0.0125$.

Regarding the experimental value of the envelope width ($\Delta\tau_{\mathrm{exp}} = 11.4$ ps), it is in agreement with the expected one ($\Delta\tau_{\mathrm{sim}} = 11.4$ ps), and both values are also consistent with the value of HOM dip envelope width (10.8 ps), measured in section 6.4. As we have commented in that chapter and in chapter 5, the envelope width is inversely proportional to the phase-matching width and therefore depends on the relative value of the pump beam waist dimension and the device length. Indeed, in our case the waveguide is 1.9 mm long and the waist 1 mm wide, therefore the waveguide acts as a spatial filter on the pump beam spatial profile and the phase-matching is given by the convolution of a sinc function with a Gaussian function (as explained in section 5.2). Conversely, a purely Gaussian phase-matching function, obtainable with a longer waveguide, would have an envelope width $\Delta\tau = \dfrac{\sqrt{2}\, w_z}{\bar{v_g}} = 14.8$ ps, for a 1 mm waist.

7.4.3 Discussion

The results we have presented, in particular the JSI shape and the HOM interferogram, indicate that the emitted quantum state is entangled in the frequency/polarization degree of freedom. Nevertheless the visibility of the HOM interferogram is poor, mainly due to the cavity effect. Indeed our simulations highlight that, if we cannot resolve the modulation at the pump frequency, the reflectivity is detrimental for the visibility. This limits the visibility to 60%. For this reason we have developed a technique to reduce the facet reflectivity by applying an antireflection coating. In the remaining part of this chapter we will present the measurement done on a coated device.

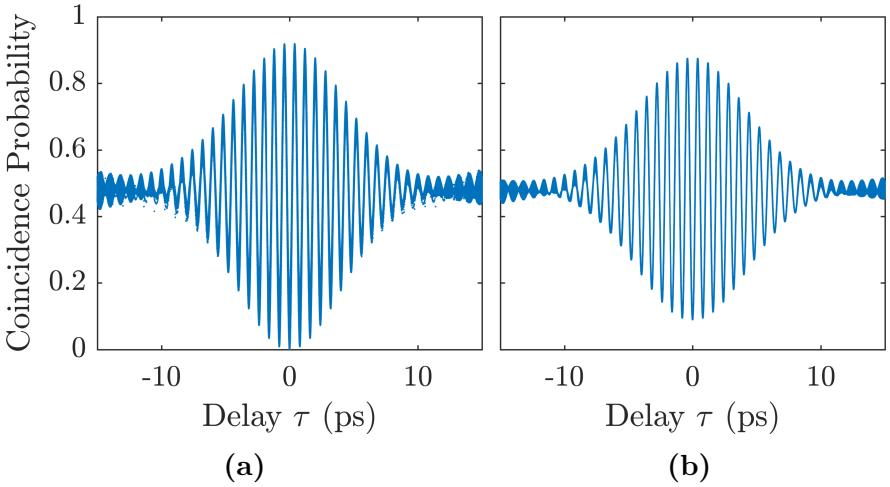

Figure 7.13: Simulated HOM probability of a HPF entangled state, emitted by a counter-propagating source with a facet reflectivity of $R = 10\%$. The left panel (a) reports the raw simulation data while the right panel (b) shows the data time-averaged over the pump frequency ($V = 82\%$).

7.5 Experimental demonstration of HPF entanglement generation by an anti-reflection coated AlGaAs waveguide

In this section we present the result concerning the generation of a HPF entangled state in a counter-propagating source with a low facet reflectivity, obtained by applying an anti-reflection coating. The device has been characterized and it shows a significant reduction of the modal reflectivity, compared to the uncoated device: from $R \approx 27\%$ to $R \approx 10\%$. The sample belongs to the same epitaxial wafer than the uncoated one and has a length of 2.6 mm. The details about the development of the coating technique, its fabrication and characterization steps are reported in the next chapter.

7.5.1 Numerical simulations

By inserting the value ($R = 10\%$) of the obtained experimental reflectivity in the numerical model described in subsection 7.3.2 we simulate the expected HOM interferogram. Figure 7.13 reports the result: the left panel shows the raw simulation data, containing the rapid oscillations at the pump frequency due to the Franson interference effect, while the right panel shows the simulation data averaged over the pump frequency. From the latter we evaluate an expected visibility of the HOM interference around $V = 82$ %.

7.5.2 Experimental results

The experimental measurements are done using the same setup presented in Figure 7.11, except for the detectors. In this case we have used superconducting

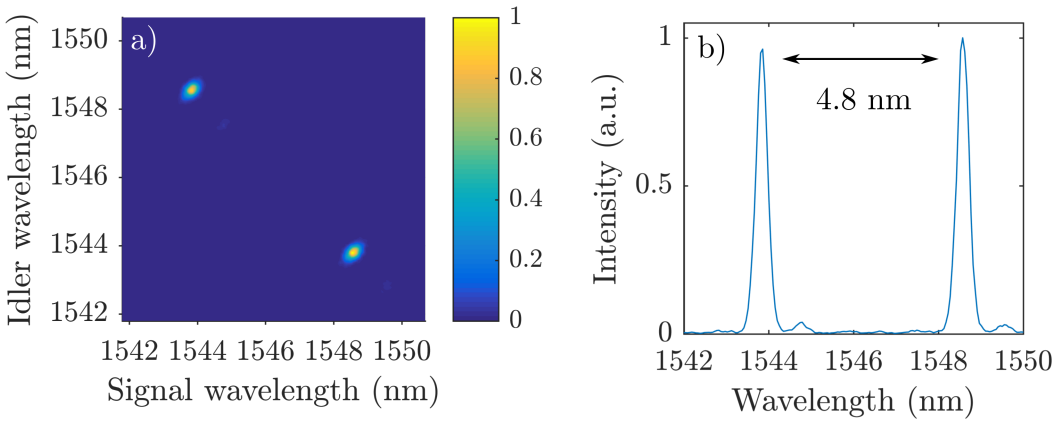

Figure 7.14: JSI (a) and signal marginal spectrum (b) of the HPF entangled state generated by a source with low facet reflectivity (R =10%). The measurement is done with a fiber spectrograph with a total integration time of 5 minutes. The pump wavelength is $\lambda_p = 773.1$ nm and the pump beam has a waist $w_z = 1$ mm and a flat phase profile.

nanowire single-photon detectors (SNSPDs) from Quantum Opus™, which have been purchased in the meantime by the team. These detectors have a better quantum efficiency (around $\eta_d = 80$ %), a lower dark count rate (< 100 counts/s at our working wavelength) and a smaller dead time (50 ns), allowing to speed up the measurement and to reduce the noise.

JSI measurement via the single-photon fiber spectrograph

First of all, we reconstruct the JSI of the state with the pump beam at normal incidence, via the single-photon fiber spectrograph. Figure 7.14a reports the result: the JSI is very similar to the one obtained with the untreated sample (Figure 7.10), only with a better signal to noise ratio due to the SNSPDs.

Figure 7.14b reports the signal marginal spectrum of the experimental JSI: the two peaks have a relative distance of 97 time bins, corresponding to a wavelength difference of 4.8 nm. This value corresponds to the one measured for the uncoated sample, so the two samples have the same value of birefringence ($\Delta n \sim 0.009$).

Experimental HOM interference measurement

Figure 7.15 reports the raw experimental data obtained in the HOM experiment. Each point results from a 3 s integration and the errorbars are calculated assuming a Poissonian statistics. The blue curve is a fit performed using Equation 7.41 and the fitted parameters are reported in Table 7.2. We obtain a visibility of 70%. i.e. a 22% improvement compared to the uncoated sample (see Figure 7.12). As previously, the experimental value is slightly lower than the one obtained from the simulation (82%), which can be explained by slight experimental imperfections of the pumping scheme, as discussed in section 6.4.

The experimental value of the envelope width ($\Delta\tau_{\text{exp}} = 14.1$ ps) is in good agreement with the simulated one ($\Delta\tau_{\text{sim}} = 14.2$ ps). The values differ from the

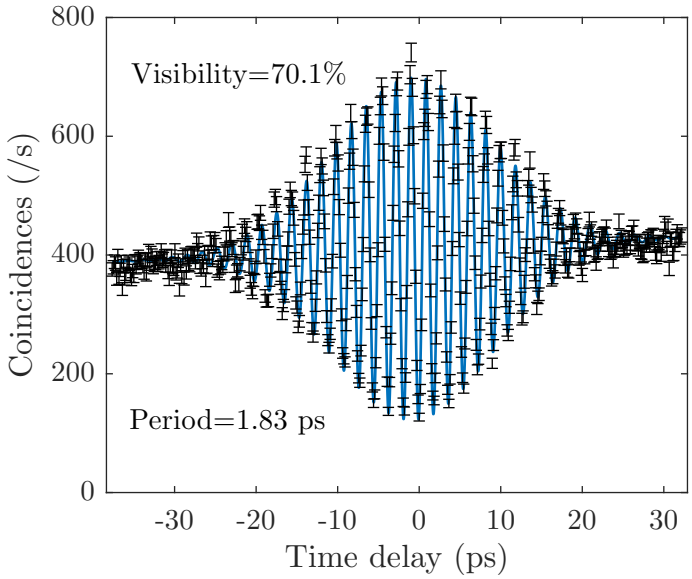

Figure 7.15: Experimentally measured HOM interferogram for a sample with facet reflectivity R=10%: raw data points are reported in black while the blue curve is a fit.

Parameter	Theoretical Value	Experimental Value
Visibility V	82%	70%
Modulation Period τ_p	1.3 ps	1.8 ps
Envelope Width $\Delta\tau$	14.2 ps	14.1 ps

Table 7.2: Theoretical and fitted parameters of the HOM interferogram for a source with a modal facet reflectivity $R = 10\%$.

case of the uncoated waveguide because the two devices have different lengths. Here the waist (w_z =1 mm) is much smaller than the waveguide length (2.6 mm) and therefore the phase-matching function is almost Gaussian, while for the uncoated waveguide the phase-matching function was given by the convolution of a Gaussian and a sinc function. We can also note that in this case the value of $\Delta\tau$ (14.1 ps) is comparable with the expected value for a purely Gaussian phase-matching function (14.8 ps), generated by a 1 mm-waist pump beam.

For the modulation period τ_p, the measured value differs from the expected one as in the previous case, but it is comparable to the one obtained experimentally employing the uncoated waveguide. Moreover, also the experimental value of ω_-^{deg}, obtained from the marginal spectrum, is the same as in the previous case (4.8 nm), as expected since the two devices have been fabricated from the same wafer (**F3W083**) and with the same ridge width.

7.5.3 Entanglement analysis

In order to quantify the entanglement of the generated state we now estimate a restricted density matrix in the hybrid polarization/frequency space.

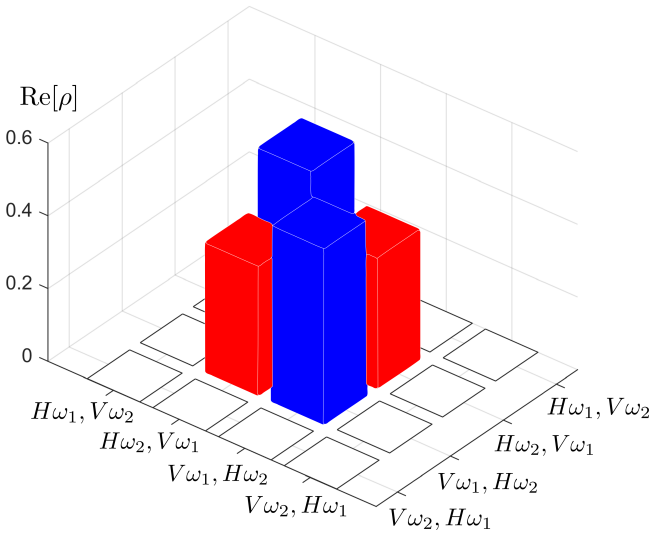

Figure 7.16: Estimated restricted density matrix.

We consider the basis produced by all the possible permutations of the $\{H\}$, $\{V\}$ polarizations and $\{\omega_1\}$, $\{\omega_2\}$ frequencies, with $\omega_1 < \omega_2$. This produces a 16 x 16 density matrix. However, from physical considerations it is possible to restrict it.

Indeed, since the source exploits type II SPDC, generating orthogonally polarized photons, we can discard the HH and VV cases. Moreover, from the energy conservation we know that the source cannot emit photon pairs with the same frequency. Therefore, the elements $\{\omega_1\omega_1\}$ and $\{\omega_2\omega_2\}$ are zero. From the above considerations we obtain the following restricted density matrix:

$$\rho = \begin{pmatrix} 0 & 0 & 0 & 0 \\ 0 & p & \frac{V}{2}e^{i\varphi} & 0 \\ 0 & \frac{V}{2}e^{-i\varphi} & 1-p & 0 \\ 0 & 0 & 0 & 0 \end{pmatrix} \tag{7.42}$$

where we employ the base $\{|H\omega_1\rangle_s |V\omega_2\rangle_i\}$, $\{|H\omega_2\rangle_s |V\omega_1\rangle_i\}$, $\{|V\omega_1\rangle_s |H\omega_2\rangle_i\}$, $\{|V\omega_2\rangle_s |H\omega_1\rangle_i\}$. The additional zero elements in the restricted matrix are determined by the phase-matching condition. Indeed, the photons at frequency ω_1 are always V polarized and the photons at frequency ω_2 are always H polarized. The parameters p and V are real and obey to physical constraints: $0 \leq p \leq 1$ and $0 \leq V/2 \leq \sqrt{p(1-p)}$ [260].

From the JSI measurement we can evaluate the population $p = 0.517$, while the absolute value of the coherences $V/2$ is estimated from the HOM interferogram visibility ($V = 0.71$) [260]. Moreover, since the source is pumped by only one pump beam, the phase φ between the two interactions is zero.

From these values we can evaluate the resulting restricted density matrix, which has been plotted in Figure 7.16.

From this density matrix we can extract some useful physical quantities that characterize the state:

Parameter	Estimated value
Target-state fidelity F	0.855
Purity P	0.753
Concurrence C	0.710
Tangle T	0.504

The target-state fidelity, evaluated as $F = \mathrm{Tr}(\rho\rho_\Phi)$, indicates the fidelity of the generated state to the ideal HPF entangled state $\rho_\Phi = |\Phi\rangle\langle\Phi|$ with:

$$|\Phi\rangle = \frac{1}{\sqrt{2}}\Big(|V,\omega_1\rangle_s\,|H,\omega_2\rangle_i + |H,\omega_2\rangle_s\,|V,\omega_1\rangle_i\Big) \tag{7.43}$$

The estimated value $F = 0.855$ evidences that the generated state is very close to the target one.

The purity, calculated as $P = \mathrm{Tr}(\rho^2)$, evaluates the purity of the state and it is equal to 1 for a pure state.

Finally, the concurrence and the tangle quantify the entanglement level of the state [269]. The first is defined as:

$$C = \max(0, \sqrt{e_1} - \sqrt{e_2} - \sqrt{e_3} - \sqrt{e_4}) \tag{7.44}$$

where $e_1 \geq e_2 \geq e_3 \geq e_4$ are the eigenvalues of $R = \rho\Sigma\rho^t\Sigma$ and Σ is defined as follows:

$$\Sigma = \begin{pmatrix} 0 & 0 & 0 & -1 \\ 0 & 0 & 1 & 0 \\ 0 & 1 & 0 & 0 \\ -1 & 0 & 0 & 0 \end{pmatrix} \tag{7.45}$$

The tangle is simply defined as $T = C^2$. These two quantities are equal to 0 for a separable state and to 1 for a maximally entangled state. Their experimental values ($C = 0.710$ and $T = 0.504$) confirm the entanglement of the hybrid polarization/frequency state and are comparable with those reported in [260] for a two-color entangled state.

7.6 Conclusion

In this chapter we have demonstrated the direct generation, at room temperature and telecom wavelength, of hybrid polarization/frequency entangled states with a chip-based source. First of all we have theoretically detailed the characteristics of the state, showing that it presents simultaneous but not independent entanglement in the frequency and polarization degrees of freedom. Indeed, when only one of the two DOFs is observed the state collapses into a mixed state. We have then presented two possible techniques to recover either frequency or polarization entanglement by erasing the information on the other DOF.

In the second section of the chapter we have shown that the HOM interferometer can be employed to quantify the entanglement in this hybrid DOF. We have

theoretically analyzed the behaviour of this state in a HOM interferometer in two different situations: when the state is generated in a device without Fabry-Pérot cavity effect and in a device with Fabry-Pérot cavity effect. In the first case the state produces a HOM interferogram composed by an oscillation, whose period depends on the frequency difference between the two photons, modulated by a Gaussian envelope. On the other hand, when we considered the presence of the cavity, our theoretical analysis showed that a second modulation at the pump frequency arises (2.3 fs period), due to the Franson interference effect which complexifies the quantum state. This modulation is not accessible with our experimental setup, thus resulting in a reduction of the HOM interferogram visibility.

After the theoretical analysis, we have presented the experimental measurements of JSI and HOM interference. The first was used to ensure that the two frequency modes were well separated and the latter to quantify the hybrid entanglement. Experiments were performed for two samples: the standard source we have analyzed so far with facet reflectivity $R \approx 27\%$ and another one treated with anti-reflection coating ($R \approx 10\%$). In both cases, the results, in good agreement with the numerical simulations, demonstrated that the sources emit genuine HPF entangled states, with well separated frequency modes. In addition, we have reported an increase of the HOM visibility of 22% for the sample with the anti-reflection coating compared to the uncoated one, leading to an increase of the quality of the generated hybrid entangled states.

The next step of this project will be the experimental projection of the HPF entangled state into a polarization Bell state or into a two-color entangled state, as detailed in section 7.1. This will allow to target different applications, increasing the versatility of the source.

An interesting follow-up of this work is the possibility to produce a non-birefringent counter-propagating source, by reducing its ridge width to $\approx$ 1.12 µm (see Figure 7.4). In this case the source would directly emit polarization Bell states. In addition, if the pump beam spatial profile is properly shaped (e.g. with a π phase step, as in chapter 5), biphoton states hyperentangled in the frequency and polarization degrees of freedom could be generated.

Chapter 8

Design and fabrication of sources with low facet reflectivity

In the previous chapter we have demonstrated that our nonlinear source based on counter-propagating geometry can generate polarization/frequency hybrid entanglement, but the quality of the emitted state is spoiled by one main factor: the facet modal reflectivity that creates a Fabry-Pérot cavity.

The modal reflectivity of semiconductor waveguides is a subject that has been studied for many years, since the development of optical amplifiers, for which it is a fundamental parameter [270]. In our case, since we do not couple high-intensity fields inside the waveguide, it was not of fundamental concern. However, the possibility of reducing the modal reflectivity and eliminating the Fabry-Pérot cavity would allow to increase the quality of the polarization/frequency hybrid entanglement and to remove the chessboard-like modulation of the biphoton JSA (subsection 2.2.5).

In the present chapter we illustrate two possible methods to deal with this issue in our counter-propagating sources. First we study the effect of tilting the waveguide facet, in either the horizontal or vertical direction. Then, we focus on the deposition of an anti-reflection coating. For both proposals we perform 3D numerical simulations with Lumerical FDTD.

As we will explain, for practical reasons we have finally decided to implement the anti-reflection coating. In the last part of the chapter, we outline the clean room processes that we followed to fabricate the coating and we report the optical measurements performed on the resulting device.

8.1 Waveguide modal reflectivity

The facet reflectivity of our device results from the refractive index mismatch between the waveguide ($n \approx 3$) and the air. Indeed, the Fresnel equations predict that, when an electromagnetic wave encounters an interface between two optical media, the wave is in part reflected and in part transmitted, depending on the refractive indices and on the wave polarization.

Since our photon pairs are generated in a guided mode, we have to consider the modal reflectivity, which depends on the mode spatial profile. The modal reflectivity is defined as the fraction of incident power that is coupled back into the same or another guided mode of the waveguide, after the reflection from the facet [270]. It can be expressed in the following way:

$$\rho_{kl} = \frac{P_l^r}{P_k^i} \tag{8.1}$$

where P_k^i is the power of the incident mode k, P_l^r is the power reflected in mode l, considering the mode k as the only incident field. The total modal reflectivity of the mode k is then:

$$\rho_k = \sum_l \rho_{kl} \tag{8.2}$$

Following Jaskorzynska et al. [270], ρ_{kl} can be calculated analytically for a waveguide with only one vertical mode (x axis in Figure 8.1) and an arbitrary number of lateral modes (y axis in Figure 8.1). The process could be simplified in the following steps:

- first of all, the incident mode is represented in the spatial frequency space by taking the Fourier Transform of its spatial profile;
- then, each plane wave of the spectrum is reflected using the Fresnel equations, obtaining the spectrum of the reflected mode;
- finally, the overlap between the incident and the reflected mode gives the modal reflectivity.

Even if this is a simple explanation of the actual calculation, it gives very important insights into the modal reflectivity behavior. First of all, we note that the possibility for a mode to be either reflected back into itself, or into other modes, depends on the facet geometry. Indeed, if we consider an untilted facet, the reflected field will have the same spatial profile than the incident one, implying that only the terms ρ_{kk} are different from zero. On the other hand, if we consider a tilted facet the reflection modifies the spatial profile and the field couples in many modes, which can be guided or not.

Among the several different proposals that are present in the literature to reduce the modal reflectivity we consider: the application of an anti-reflection coating [271] or the tilt of the waveguide facets [272]. Both of them act on the reflected mode, reducing its overlap with the incident one, but have different advantages and disadvantages.

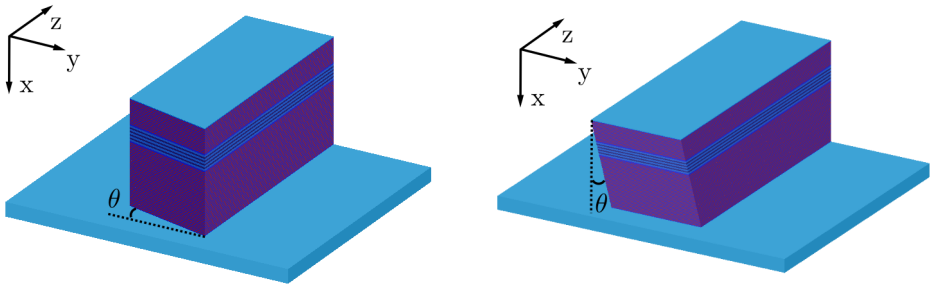

(a) Horizontal tilt **(b)** Vertical tilt

Figure 8.1: 3D sketch of the simulated waveguide: (a) for an horizontal tilt of the facet and (b) for a vertical tilt.

The application of an anti-reflection coating was one of the first proposals; it induces a destructive interference between the incident and the reflected field, if the thickness is properly designed. However, in order to obtain very low reflectivity (near 10^{-3}) single-layer coatings require narrow tolerances for fabrication and in general do not perform well enough for both polarizations [270].

Conversely, tilting the facet allows to reach very low modal reflectivity, in case of a monomode waveguide. Indeed, the whole reflected power can be diverted into non-guided modes radiating out. However, considering multimode waveguides the reflected power may couple back into other guided modes (i.e. $\rho_{kl} \neq 0$ for $k \neq l$) and thus the overall reflectivity is not completely reduced.

From the above considerations it is clear that the good solution to lower the modal reflctivity depends on the waveguide design, in particular on the presence of higher-order guided modes or birefringence. Indeed, the latter may prevent to obtain sufficiently low reflectivity for both polarizations.

In order to obtain a very low modal reflectivity, more than one technique is often used (e.g. antireflecion coating and facet tilt in the same waveguide [270, 273]). In our case, as we are interested in lowering the modal reflectivity only down to a few percents, we study the two techniques separately to identify the more suited one to our case.

8.2 Tilting the facet

In the previous section we have explained the effect of a facet tilt on the modal reflectivity, here we study its implementation on the counter-propagating source, for both horizontal and vertical directions, as illustrated in Figure 8.1. Since the device is multimode in both vertical and lateral directions, we perform 3D simulations using the FDTD module of Lumerical. The software, given an input mode, calculates the fraction of power reflected in each guided mode, which corresponds to the modal reflectivity ρ_{kl}.

8.2.1 Guided modes

Before describing the simulations, we need to focus our attention to the guided modes supported by our source. In the previous chapters, we have studied photon pair emission only in the fundamental mode. However, the source, given its core dimensions (approximately 5 µm x 1 µm), is highly multimode.

Figure 8.2 and Figure 8.3 report the intensity profile of the first guided modes of a 5 µm-wide ridge source for respectively TE and TM polarizations at 1550 nm. In the vertical direction, since the core is less than 1 µm thick, the source has only two guided modes, while in the lateral direction many modes are supported. The figures display only the first three, even if up to 10 modes are supported.

We note that the second-order vertical guided mode is not well confined into the core, but is localized mainly in the Bragg mirrors, with an asymmetry due to the design itself. Indeed, the bottom Bragg mirror, conceived to avoid penetration of the pump in the substrate, is thicker than the top Bragg mirror and this weakens the confinement due to the refractive index difference. On the other hand, the higher-order lateral guided modes are well confined into the core.

Comparing the TE and TM guided modes we note that they have almost the same intensity profiles, except for the fact that the TM polarized fields are influenced by the stack of layers that composes the structure, while the TE polarized fields are not. This induces a modulation of the TM profiles in the x direction: the field is slightly more concentrated inside the high refractive index layers (i.e. the layers with low Al content), as we have already commented in section 1.4.

8.2.2 Numerical simulations

By tilting the facet, the reflected field profile is modified and can couple back into modes different from the incident one. Considering a tilt in the horizontal (vertical) direction, but not in both directions simultaneously, simplifies the problem, because the incident field will couple back only into the lateral (vertical) modes. Thus, in the following, we study first the effect of a horizontal tilt and then of a vertical one. Figure 8.1 displays a 3D sketch of the waveguide for each situation respectively, showing the tilt angle θ used in the numerical simulations.

The simulation results are plotted in Figure 8.4 for both horizontal (Figure 8.4a, Figure 8.4b) and vertical tilt (Figure 8.4c, Figure 8.4d). Since the tilt does not mix the polarizations, it is possible to simulate the modal reflectivity for each polarization separately. We start by analyzing the horizontal tilt. We note that, for both polarizations, the modal reflectivity of the fundamental mode into itself (ρ_{00}) decreases when θ is increased. However, the total reflectivity does not decrease appreciably because the field couples back into higher order modes (in the plot only the first five modes are considered but more are possible). In conclusion, horizontally tilting the facet is not a viable solution to reduce the modal reflectivity, because the light remains coupled inside the device.

We now consider the vertical tilt. The plots, reported in Figure 8.4c and Figure 8.4d, illustrate a slightly different behavior, compared to the horizontal case. Indeed, since the waveguide has only two vertical guided modes, when the tilt increases ρ_{00} decreases and ρ_{01} rises, but for a sufficiently large tilt value both

fall to zero. For instance, a vertical tilt of $\theta = 15°$ results in total reflectivity of approximately 5%, which is low enough for our needs.

In conclusion, by vertically tilting the waveguide facets, the total reflectivity can be lowered to acceptable values. However, a practical caveat has to be considered: this solution introduces also a tilt in the photon propagation direction at the waveguide outputs and thus, in order to efficiently collect the photons, the optical setup has to be modified. The issue can be addressed, but for the sake of simplicity, we decide to focus our attention rather on the second solution: applying an anti-reflection coating.

Figure 8.2: Intensity profile of the lateral and vertical TE-polarized guided modes for a 5 µm-wide ridge waveguide at 1550 nm. Due to its small vertical dimension (the core height is less than 1 µm), the waveguide has only two vertical guided modes. Conversely, it has many lateral guided modes, even if here, for matter of space, only the first three are displayed.

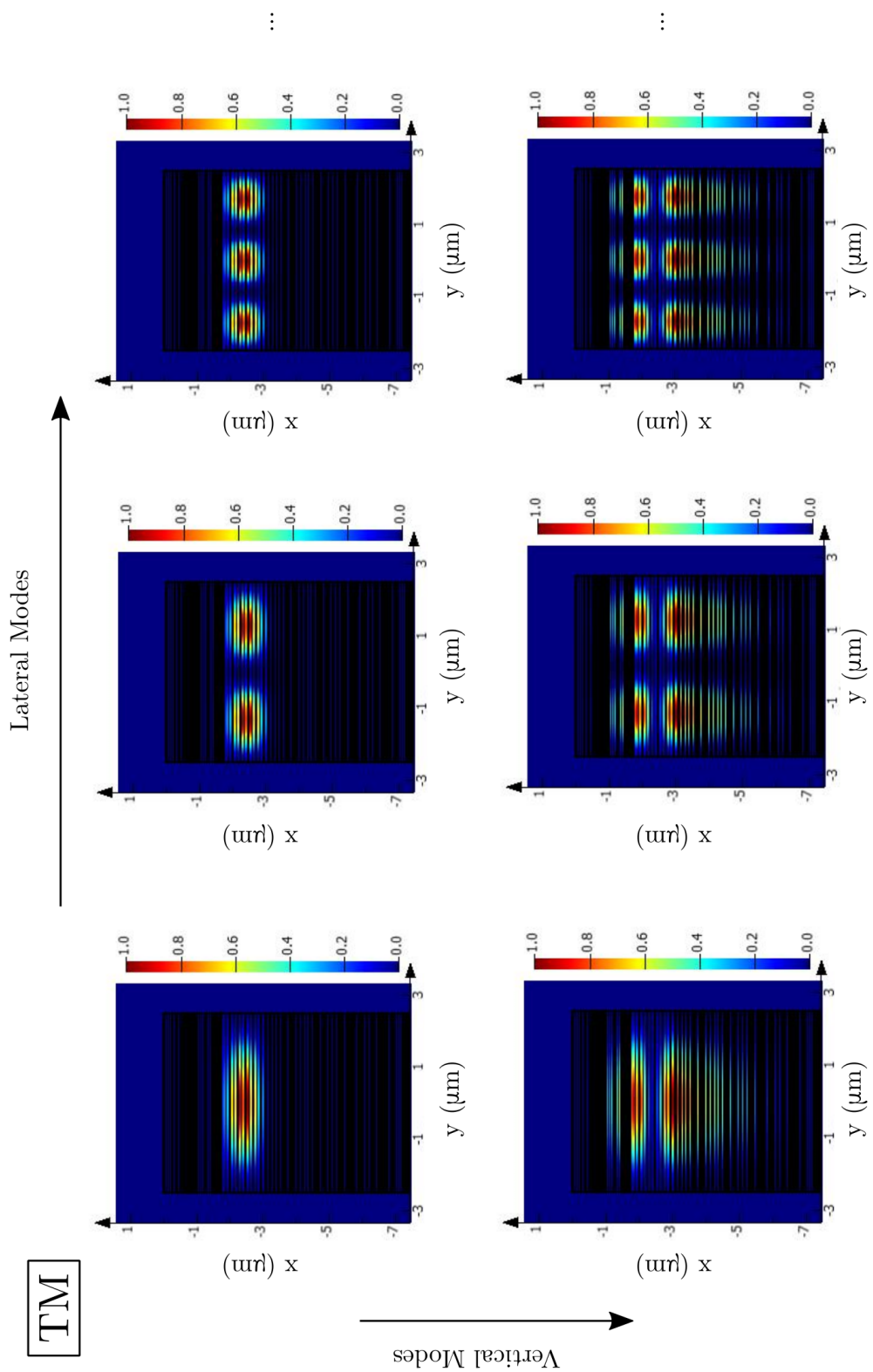

Figure 8.3: Intensity profile of the lateral and vertical TM-polarized guided modes for a 5 µm-wide ridge waveguide at 1550 nm. Due to its small vertical dimension (the core height is less than 1 µm), the waveguide has only two vertical guided modes. Conversely, it has many lateral guided modes, even if here, for matter of space, only the first three are displayed..

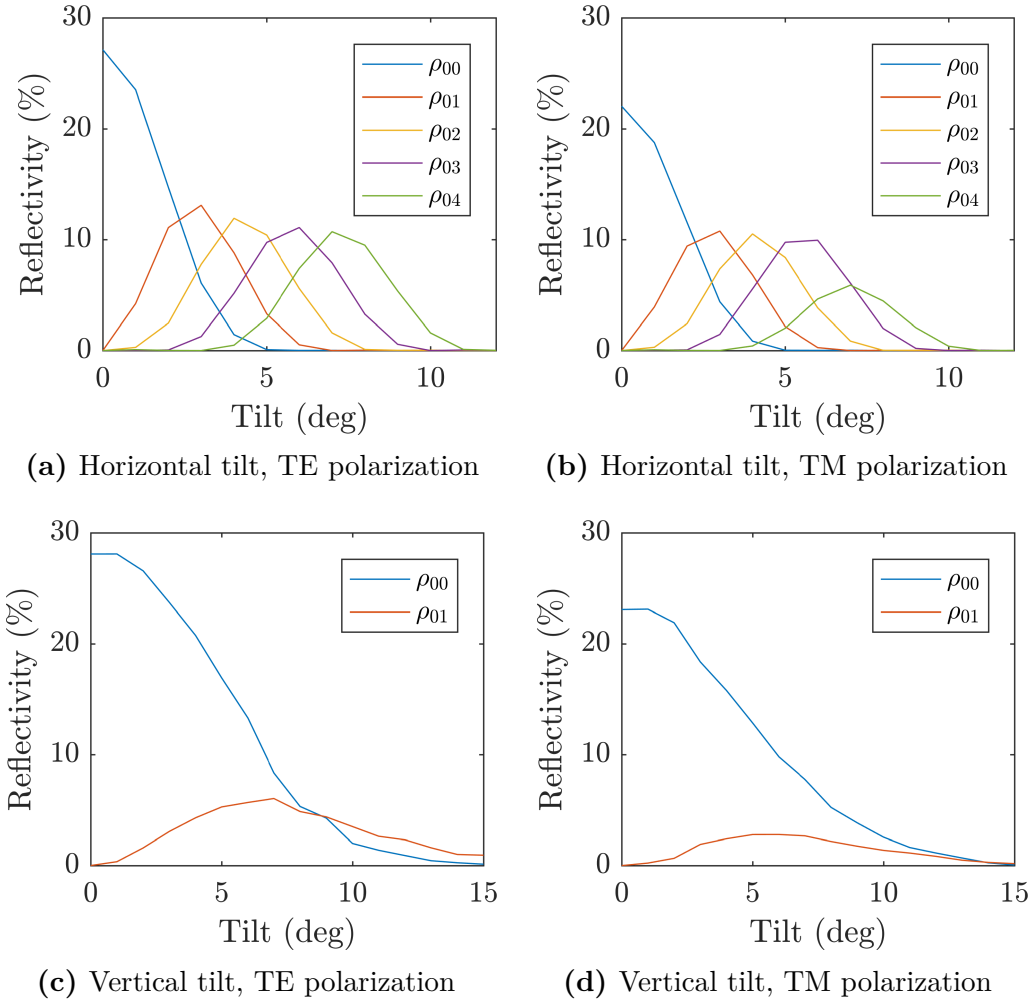

(a) Horizontal tilt, TE polarization

(b) Horizontal tilt, TM polarization

(c) Vertical tilt, TE polarization

(d) Vertical tilt, TM polarization

Figure 8.4: Numerical simulation of the modal reflectivity at a wavelength of 1550 nm, considering the fundamental mode as incident field (ρ_{0l}) and for either horizontal ((a), (b)) or vertical tilt ((c), (d)). In (a) and (b) we consider only the first five lateral guided modes, even if more are possible.

8.3 Anti-reflection coating: design

We have shown that a vertical tilt can decrease the modal reflectivity, but it introduces a tilt in the photon pair beam. The alternative solution that we investigate now is to apply an anti-reflection coating, which would work for all the guided modes, given that they have similar modal refractive indices, without deviating the photon propagation direction.

Thin-film anti-reflection coatings employ single or multilayer depositions to take advantage of the constructive and destructive interference effect among the multiple reflections. Let us start by analyzing the single layer case. Figure 8.5 displays a sketch of the situation. We consider a field guided in the fundamental mode and incident onto the facet: a first reflection is generated at the interface between the waveguide and the coating, and a second one at the interface between the coating and the air. By properly choosing the thickness and the refractive index of the coating, the two reflections can acquire a π relative phase shift and interfere destructively. The reflectivity vanishes completely if the two reflected fields have the same amplitude at the waveguide-coating interface. The resulting conditions for the coating thickness (d) and refractive index (n_c) are [274]:

$$n_c = \sqrt{n_g n_a} \tag{8.3}$$

$$d = \frac{\lambda_0}{4\ n_c} \tag{8.4}$$

where n_g, n_a and λ_0 are respectively the waveguide modal refractive index, the air refractive index and the working wavelength in the air. Therefore, since $n_g \approx 3.1$ and $n_a = 1$ are fixed, we need a material with $n_c = 1.75$. From that we derive a coating thickness of $d \approx 220$ nm, for a working wavelength $\lambda_0 = 1550$ nm.

The choice of the material for the coating is constrained by the refractive index of the available materials and by their adhesion on our samples. A perfect solution would be Aluminium Sesquioxide (Al_2O_3), which has a refractive index $n_{Al_2O_3} = 1.7462$ at 1550 nm and can be efficiently deposited by Atomic Layer Deposition (ALD) [275, 276]. However, ALD is not available in our clean room, we thus decide to employ Silicon Dioxide (SiO_2), a common material that can be deposited by Plasma-Enhanced Chemical Vapor Deposition (PECVD). SiO_2 has a refractive index of $n_{SiO_2} = 1.45$ at 1550 nm, which does not allow to completely eliminate the reflection, but, by properly adjusting the coating thickness, it is possible to obtain acceptably low values of reflectivity.

8.3.1 3D numerical simulations

In order to determine the optimal thickness of a SiO_2 single layer coating to minimize the reflectivity ρ_{00}, we perform 3D numerical simulations with Lumerical FDTD module, considering a 5 µm-wide ridge. Figure 8.6a reports the calculated reflectivity as a function of the coating thickness at a fixed wavelength $\lambda_0 = 1550$ nm; we note that both TE and TM polarizations have a minimum around $d = 270$ nm, corresponding to a reflectivity $R \approx 4\%$.

Fixing the coating thickness to this value, we then evaluate the wavelength dependence of the reflectivity, to check that it remains low for the frequency region

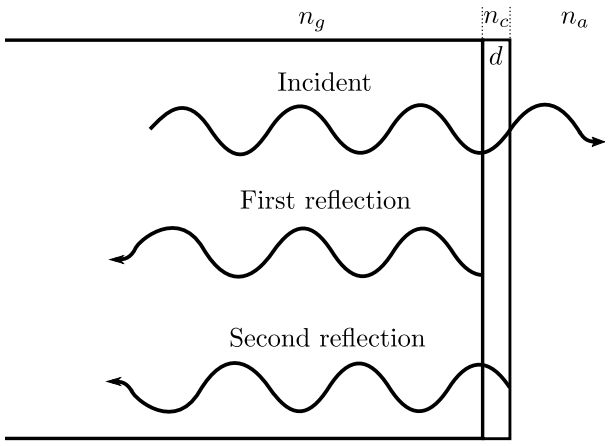

Figure 8.5: Working principle of a single layer anti-reflection coating. The layer produces a π relative phase shift between the first and the second reflection, which thus interfere destructively. Note that both reflected fields do not acquires a π phase shift for the reflection, being reflected from a medium with lower n than that of the medium they are traveling in ($n_g > n_c > n_a$).

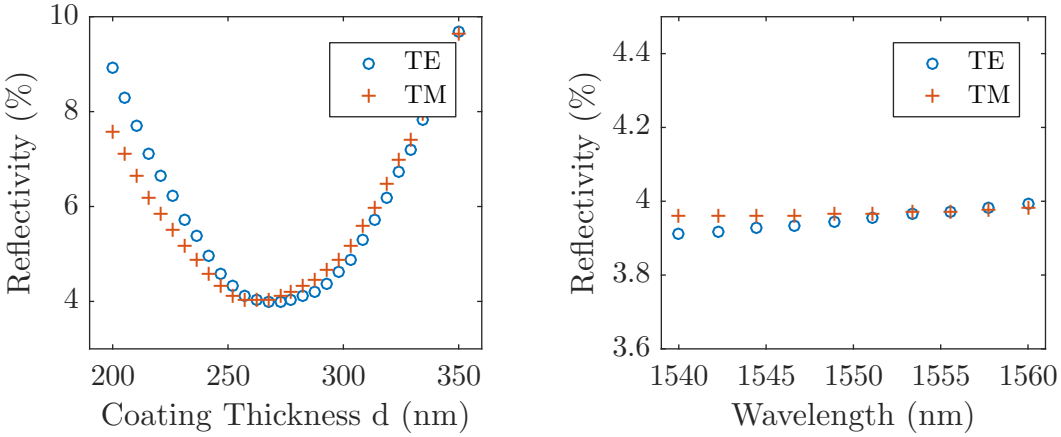

(a) Reflectivity vs thickness

(b) Reflectivity vs wavelength

Figure 8.6: Numerical simulation of the reflectivity ρ_{00} as a function of: (a) the SiO_2 coating thickness, for $\lambda = 1550$ nm, and (b) the wavelength, for a thickness $d = 270$ nm.

of our interest. Figure 8.6b confirms that, in the region between 1540 nm and 1560 nm, the reflectivity for both polarizations is always less than 4%.

The numerical study has been carried out considering the injected field in the fundamental mode and evaluating the intensity of the reflection, but, since the higher-order modes have a refractive index similar to the fundamental mode, the results can be extended to them.

A more complex solution with multi-layer coating could be applied to decrease even more the reflectivity and increase its working bandwidth [277]. However, for our applications the SiO_2 single-layer anti-reflection coating is suitable and therefore in the next part of the chapter we will present its fabrication process and its optical characterization.

8.4 Anti-reflection coating: fabrication

The anti-reflection coating has been fabricated in the MPQ clean room, by depositing a thin film of SiO_2 through a Plasma-Enhanced Chemical Vapor Deposition (PECVD) process. This method allows to deposit thin films from a gas state to a solid state on a substrate. The process has been performed on a sample containing several counter-propagating ridge waveguides (5 µm wide and 2.6 mm long).

As a first step, the machine has been calibrated in order to determine the optimal parameters for the process. In particular, the main parameter to be determined is the time duration of the deposition, which controls the layer thickness. It can be evaluated by depositing various layers on a substrate and by measuring their actual thicknesses. However, this method does not take into account the edge effects: when depositing a thin layer on a surface the deposition near the edges is always of a worse quality. Since the surface of a waveguide facet is very small, the deposition is strongly influenced by such edge effects. And unfortunately, an actual calibration of the process directly using waveguide facets is challenging, because it is not possible to use a profilometer (as a Dektak) on a so small area. Instead, the process has been therefore calibrated on a large flat sample, without considering the edge effect: different depositions of SiO_2 have been done on a large Si substrate and the actual thickness has been related to the process time duration. As we will show in the next section, the experimental measurements of reflectivity validates this approximated calibration technique.

The process has been performed by depositing the thin layer on the sample placed perpendicularly, by using two microscope glasses on each side in order to keep it stable in that position. This configuration enables to deposit the thin film only on the facets and not on the top of the waveguides, where the pump beam impinges. Indeed, due to the high pump intensity the thin film could burn and damage the waveguide. The deposition on the facets on the other side of the waveguide has been done directly after.

Figure 8.7 shows an optical microscope image taken, from above the sample, after the PECVD deposition. It shows two bunches of three waveguides, and close to the waveguide termination (on a region of 300 µm near the facets) it is possible to notice the color change due to the thickness gradient of the thin film deposition (which was directed perpendicularly to the facets). From that, we can conclude

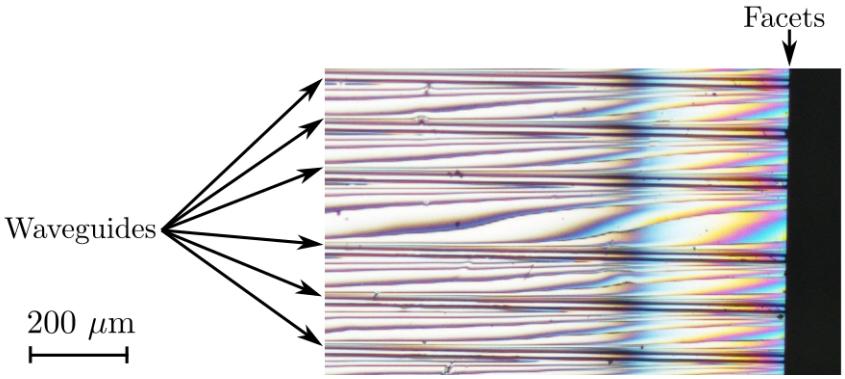

Figure 8.7: Optical microscope image (5x magnification) of the sample after the PECVD deposition of a SiO_2 thin layer. The image is taken from above the sample. From right to left the layer thickness decreases and the colors change. The light and dark modulation is due to the partial etch of the lower Bragg mirror of the sample, leading to an oxidation of the high Al content layers.

that the SiO_2 deposition has "leaked" only in a small portion of the waveguide (which is 2 mm long) and it does not cover the top of it, where the pump beam impinges.

8.5 Optical characterization

In order to determine the effects of the coating on the waveguide, we measure the Fabry-Pérot fringes of the transmitted intensity through the device before and after the process. Figure 8.8 reports the measured Fabry-Pérot oscillations for the TE polarization for both the uncoated and coated samples.

Regarding the sample before the deposition, from the fringe contrast and the facet modal reflectivity ($R_{\mathrm{TE}} = 28.5\%$ and $R_{\mathrm{TM}} = 24.7\%$), calculated with 3D numerical simulations, we can evaluate the propagation losses employing the technique detailed in section 1.4. The obtained values $\alpha_{\mathrm{TE}} = 0.6$ cm^{-1} and $\alpha_{\mathrm{TM}} = 0.6$ cm^{-1} indicate that the waveguide has a good fabrication quality.

After the deposition, we perform the same measurement. Figure 8.8b displays the Fabry-Pérot oscillations of the TE-polarized mode for the coated waveguide. From these data we calculate a contrast K=0.18, which has to be compared with K=0.42 for the uncoated sample. Since the deposition has been performed only on the facets, we can safely assume that the propagation losses are the same than before the process and hence we employ their value ($\alpha = 0.6$ cm^{-1}) to retrieve the modal reflectivity from the fringe contrast. By applying this procedure we find approximately the same value of modal reflectivity for both polarizations: $R \approx 10\%$. This value is higher than the one expected from the numerical simulations ($R_{\mathrm{sim}} \approx 4\%$), probably due to a small difference between the nominal and the actual layer thickness.

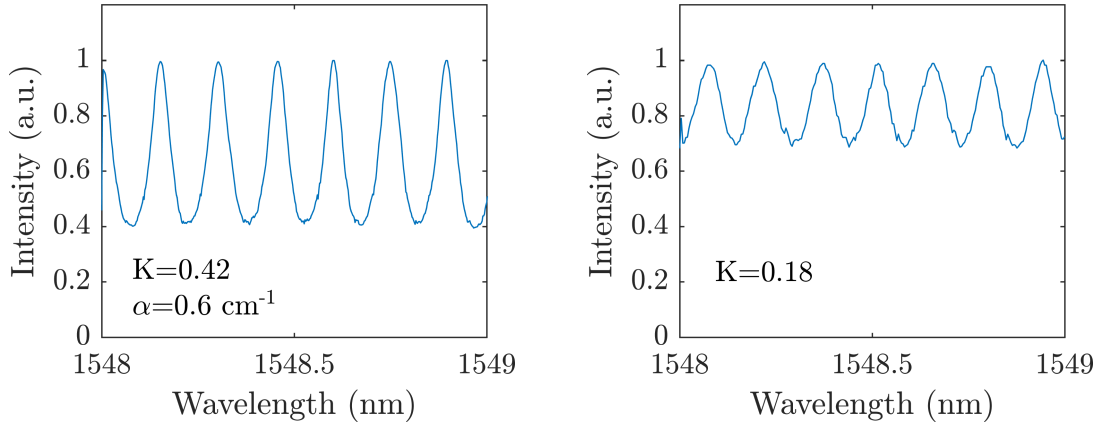

(a) Before deposition **(b)** After deposition

Figure 8.8: Fabry-Pérot oscillation of the transmitted intensity for the TE-polarized infrared fundamental mode of the uncoated sample (a) and for the coated one (b).

8.6 Conclusion

In this chapter we have investigated the possibility of decreasing the facet reflectivity of the counter-propagating source, which can have several applications, e.g. improving the quality of the polarization/frequency hybrid entangled state emitted by the source, as we demonstrated in section chapter 7. Two possible methods have been envisaged: tilting the waveguide facets or depositing an anti-reflection coating.

Tilting the waveguide facet modifies the spatial profile of the reflected mode, which can thus radiate through non-guided modes. However, if the waveguide is not monomode, the reflected field can still be guided inside the device by the higher-order guided modes. In our case, through numerical simulations, we have demonstrated that a horizontal tilt of the facet is not a viable solution, since the waveguide is highly multimode in the lateral direction. On the other hand, only two vartical guided modes exist and therefore a vertical tilt of 15° would allow to decrease the reflectivity to 5% . However this design introduces a tilt in the photon propagation direction at the waveguide outputs and therefore for practical reasons we have discarded it.

By contrast, depositing an anti-reflection coating allows to obtain a low reflectivity, while maintaining the same propagation directions. Performing 3D numerical simulations, we have shown that a 270 nm-thick single-layer of SiO_2 results in an expected modal reflectivity R=4%.

The coating deposition has been performed on both facets of the waveguides by a PECVD technique in the MPQ clean room, followed by the experimental characterization of the coated sample. By measuring the Fabry-Pérot fringes of the intensity transmitted through the waveguide before and after the process, we have evaluated the facet modal reflectivity. The results show a decrease of the modal reflectivity from $R \approx 27\%$ without the coating to approximately $R \approx 10\%$ with the coating, for both polarizations.

To conclude, we have proven that depositing a thin film of SiO_2 as anti-reflection coating is an easy and viable method to decrease the modal reflectivity of our AlGaAs waveguide sources. As we have already described, the coated source has been used in chapter 7 to demonstrate the generation of hybrid polarization/frequency entangled states, obtaining an increase of the experimental HOM visibility from $V = 48\%$ to $V = 70\%$.

This chapter is a proof of principle of the technique and, at the moment, we are optimizing the coating deposition process, in order to reach the expected modal reflectivity of 4%. In addition, more complex techniques could be envisaged to futher decrease the reflectivity, if needed for particular demanding applications. For example, by combing a single-layer coating and a facet tilt it would be possible to obtain reflectivity values as low as 10^{-4} [270].

Part III

Towards the generation of spatial correlations in a waveguide lattice

Chapter 9

Spatial Correlations in a Waveguide Lattice

In the first and second part of this thesis we have exploited the high-dimensional Hilbert space of the frequency degree of freedom of photon pairs and demonstrated the engineering of spectral quantum correlations. We now focus on the spatial degree of freedom, and more precisely, the transverse position of photons in a lattice of waveguides. The choice of the spatial degree of freedom has several motivations: it can be robustly transported in optical fibers and waveguides and it is naturally suited for interfacing channels and modes in a on-chip quantum network.

The device that we have developed consists of a lattice of parallel co-propopagating nonlinear sources (c.f. section 1.5), evanescently coupled (see Figure 9.5). In such device, the generated photons can continuously tunnel from one waveguide to the other during their propagation, undergoing random quantum walks [278] and creating entanglement in the spatial degree of freedom. Quantum walks have proven to be a very promising resource in quantum information, for tasks such as boson sampling [279], Shor factoring algorithm [20] and simulation of complex

condensed matter problems [280].

Our goal is ultimately to employ this platform for quantum simulations tasks; indeed, tailoring the waveguide lattice parameters (statically and/or dynamically) should allow to implement various Hamiltonians of condensed-matter systems and study phenomena such as topological protection in the quantum regime [281] or Anderson localization of multiparticle states [82].

In this chapter, after a brief overview of the state of the art, we detail the device design and the corresponding numerical simulations. Then, we introduce the quantum theory of SPDC in an array of nonlinear waveguides, focusing on the spatial correlations generated by quantum walks and their engineering. Finally, in the last two sections, we present our development and optimization of the device fabrication processes, followed by its first optical characterizations that set the ground for further experimental development.

9.1 Quantum walks in integrated photonics

Quantum random walks are the quantum counterpart of classical random walks. In this case, particles evolve simultaneously towards all their possible quantum states and the coherent nature of the phenomenon leads to interference among the multiple paths. Two distinct models of quantum walks (QWs) exist: discrete-time QWs in which the walkers evolve in randomly chosen discrete steps, and continuous-time QWs in which the walkers dynamics is described by a time-independent lattice Hamiltonian [282]. In both cases, single-particle QWs do not exhibit any different behavior from classical wave propagation; however, when multiple particles are considered (entangled or not) non-classical effects arise.

Several physical systems can be employed to implement QWs, such as spin chains [283], ultra-cold atoms [284], trapped ions [285] and waveguide lattices [18]. Integrated photonic circuits in particular, thanks to the photon long coherence time and the phase stability of integrated interferometers, is a very promising candidate to implement QWs.

Discrete-time QWs have been implemented in photonics employing directional couplers and phase shifters, as illustrated in Figure 9.1. In this contest, two promising platforms have emerged up to now: femtosecond laser written circuits on silicate glass and silicon-based waveguides.

Femtosecond laser written circuits on silicate glass allow to realize very precise arbitrary circuits in a three-dimensional structure, with low propagation losses (0.1 dB cm^{-1}). However, due to the low refractive index contrast of 10^{-3}, the bending radii are limited to the centimeter regime. Moreover, since silicate glass does not present any nonlinearity, the photons have to be produced externally, limiting the device scalability. This platform has been employed to study boson sampling [110], Anderson localization of entangled photon pairs [82], quantum Bloch oscillations [286] and multi-photon interference (boson clouding) [287].

Silicon-based circuits, thanks to a higher refractive index contrast and nonlinearity, allows to achieve a higher integration density and to include SFWM-based photon sources in a monolithic chip [288]. This platform has been employed to study boson sampling [279] and it is also very promising for integrated quantum

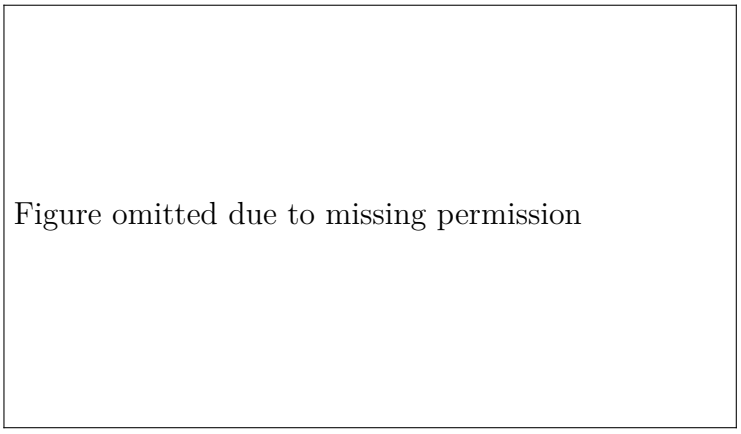

Figure 9.1: Scheme of a network of directional couplers and phase shifters implementing discrete-time QWs. Adapted from [82].

computing; for example a fully programmable two-qubit quantum process has already been realized [51].

Concerning continuous-time QWs, the natural photonic implementation is an integrated lattice of evanescently coupled waveguides. Interestingly, this kind of device has already been employed in the classical regime during the years 1990-2000 to study the phenomenon of discrete diffraction of optical waves. Exploiting the similarities between optical waves in a spatially periodic dielectric structure and electrons in a semiconductor crystal, it was possible to emulate solid-state physics systems, studying effects such as photonic Bloch oscillations, optical discrete solitons and disorder effect [289].

Switching to the quantum regime, the first experiment on continuous-time QWs with evanescently coupled waveguides was carried out by Peruzzo et al. [18] in 2010. Employing an array of silicon oxynitride waveguides, reported in Figure 9.2, and an external source of photon pairs, the authors observed and controlled non-classical spatial photon correlations, by changing the input quantum state.

Then, in 2014, cascaded quantum walks have been experimentally demonstrated for the first time by Solntsev et al. [290] exploiting SPDC in an array of lithium niobate waveguides. In this case, the photons are directly generated inside the device and the generation can take place at any position along the waveguide. This process results in a significantly higher level of spatial entanglement, due to the interference between quantum walks started at all possible longitudinal positions.

Moreover, the possibility of accurately control the gap between adjacent waveguides of the array has allowed to introduce and study topological effects. In 2018, Blanco-Redondo et al. [96], employing an array of silicon nano-wires and taking advantage of their nonlinearity to obtain spontaneous four-wave mixing, demonstrated the topological protection of photon pairs against scattering and imperfections.

These proofs of principle highlight the interest of waveguide arrays as a promising platform to develop not only quantum simulators but also sources of robust quantum states, topologically protected, which can be exploited to increase the scalability of quantum information systems.

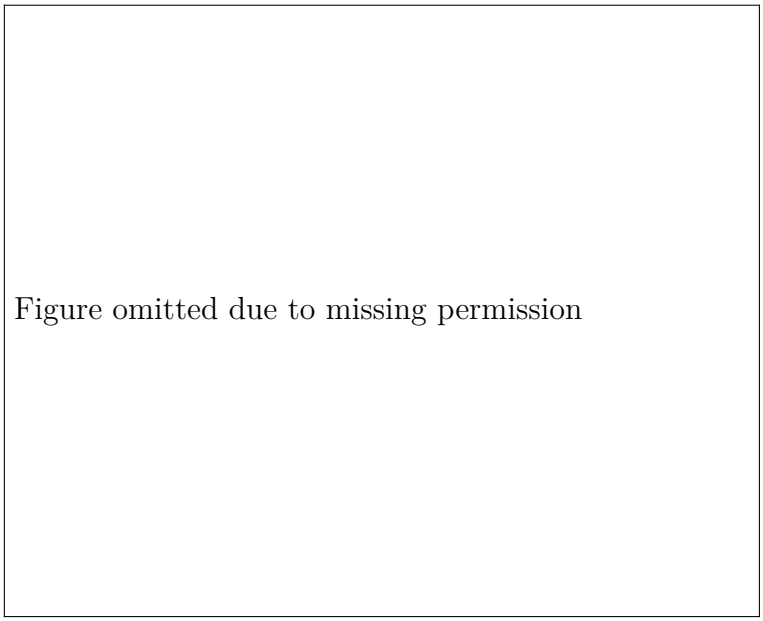

Figure 9.2: A continuously coupled waveguide array for realizing correlated photon quantum walks. (a) Image of the integrated chip. (b) Simulation of the intensity of laser light propagating in the array showing the discrete diffraction of light. (c) Intensity output pattern. Adapted from [18].

In this context the advantages of the AlGaAs material platform could be leveraged to realize arrays of electrically injected nonlinear sources [60] whise parameters are directly controlled in-situ via the electro-optical effect [54]. In addition, the use of AlGaAs will allow reducing the footprint of the devices from the centimeter to the millimeter scale, thanks to its high refractive index contrast.

9.2 Design of the waveguide lattice

In this section we start by introducing the fundamental phenomenon on which the device is based: evanescent coupling. We first consider the case of two waveguides and we briefly introduce the coupled-mode theory. Then, we present our device and we determine its optimal design by means of numerical simulations.

9.2.1 Evanescent coupling

Evanescent coupling is a core effect of integrated photonics that allows to realize a variety of integrated components, such as directional couplers, switches, filters and many others. In order to introduce it, we consider the simple case of two straight monomode waveguides. If they are brought sufficiently close so that the guided modes overlap, light can tunnel from one waveguide to the other. Since the overlap between the two modes typically occurs in the evanescent tails of the field distribution, this effect is called evanescent coupling.

To model this effect we employ an approximated theory, called coupled-mode theory [291], which provides satisfactory results for our experimental conditions.

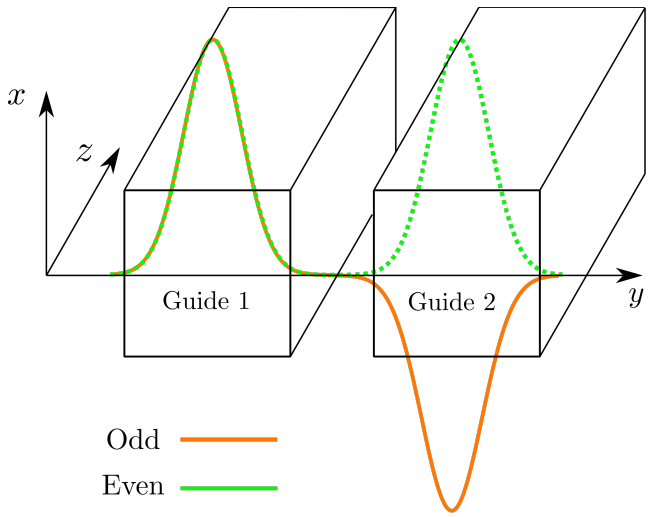

Figure 9.3: Sketch of two weakly coupled waveguides and their even (green) and odd (orange) guided supermodes.

We assume that the two waveguides are weakly coupled so that the presence of the first waveguide does not influence the transverse profile or the propagation constant of the second waveguide mode. The coupling thus induces only a modulation of the amplitude of the guided modes along the propagation direction z. The overall system supports two guided supermodes that are given by the sum (even supermode) and the difference (odd supermode) of the guided mode of each isolated waveguide. Figure 9.3 reports a sketch of the two waveguides and the even (in green) and odd (in orange) supermode transverse profiles.

Calling $a_1(z)$ and $a_2(z)$ the amplitudes of the guided mode of the isolated waveguides, the total field distribution in the device can be written:

$$E_t(x,y,z,t) = a_1(z)E_1(x,y)e^{i(\beta_1 z-\omega t)} + a_2(z)E_2(x,y)e^{i(\beta_2 z-\omega t)} \tag{9.1}$$

where $E_j(x,y)$ is the guided mode transverse profile for waveguide $j=1,2$ and β_j its propagation constant[1]. Under the assumptions detailed above the amplitudes $a_j(z)$ are governed by the following coupled mode first-order differential equations:

$$\begin{cases} \dfrac{\mathrm{d}a_1(z)}{\mathrm{d}z} = -iCe^{i\Delta\beta z}\cdot a_2(z) \\ \dfrac{\mathrm{d}a_2(z)}{\mathrm{d}z} = -iCe^{i\Delta\beta z}\cdot a_1(z) \end{cases} \tag{9.2}$$

where $\Delta\beta = \beta_1 - \beta_2$ is the propagation constant mismatch and C is the coupling coefficient, which is proportional to the overlap between the guided modes of the two isolated waveguides:

$$C \propto \iint \mathrm{d}x\mathrm{d}y E_1^*(x,y)E_2(x,y) \tag{9.3}$$

[1]In this chapter we call the propagation constant β instead of k, to avoid any confusion with the transverse momentum $k^\perp$ that we will introduce later.

Alternatively, the coupling constant C can be calculated from the effective refractive index of the even and odd supermode [291]:

$$C = \frac{\pi}{\lambda}(n_{\text{odd}} - n_{\text{even}}) \tag{9.4}$$

which provides an easier and faster method.

Once the equations are solved and the amplitude retrieved, we can evaluate the power in each waveguide by taking the squared modulus $P_j(z) \propto |a_j(z)|^2$.

Let us consider the particular case in which light is injected only in the first waveguide (i.e. $a_1(0) \neq 0$ and $a_2(0) = 0$). The power in each waveguide as a function of the propagation distance z reads [292]:

$$\begin{cases} P_1(z) = P_1(0)\left[\cos^2(\gamma z) + \left(\dfrac{\Delta\beta}{2\gamma}\right)^2 \sin^2(\gamma z)\right] \\ P_2(z) = P_1(0)\left(\dfrac{C}{\gamma}\right)^2 \sin^2(\gamma z) \end{cases} \tag{9.5}$$

which are oscillating functions of period $2\pi/\gamma$ where:

$$\gamma = \sqrt{\left(\frac{\Delta\beta}{2}\right)^2 + C^2} \tag{9.6}$$

In case of synchronous coupling, defined as $\Delta\beta = 0$ (i.e. the two guided modes have the same propagation constant), Equation 9.5 reduces to:

$$\begin{cases} P_1(z) = P_1(0)\cos^2(Cz) \\ P_2(z) = P_1(0)\sin^2(Cz) \end{cases} \tag{9.7}$$

In this case the optical power completely transfers from one waveguide to the other on a length called coupling distance, $L_c = \pi/2C$.

Figure 9.4 reports the plot of $P_1(z)$ as a function of the propagation distance, for two different values of propagation constant mismatch $\Delta\beta = 0$ (blue) and $\Delta\beta = 4C$ (red). We notice that in the second case the power transfer is not complete and it oscillates at a higher frequency than in the first case.

The coupled-mode theory, presented here in the case of two waveguides, can be generalized to describe the coupling among N equidistant waveguides.

9.2.2 Device design and working principle

Figure 9.5a reports a scheme of the device, which is composed of a lattice of parallel co-propagating nonlinear waveguides, which have been presented in section 1.5. All the waveguides composing the lattice have the same *ridge width* and are separated by a distance that we call *gap*. In the following we will refer to the space between adjacent waveguides as *trenches* and we will call *etching depth* the ridge height, as summarized in Figure 9.5b.

We want to design a device in which the SPDC-generated photons can tunnel into the neighboring waveguides (as sketched in red in Figure 9.5b), while the pump

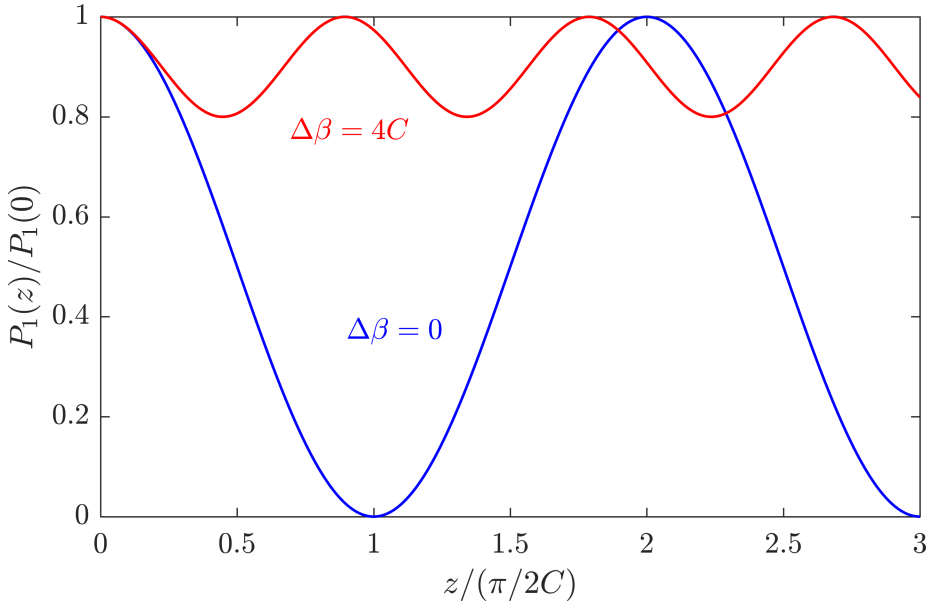

Figure 9.4: Optical power in two weakly-coupled waveguides as a function of the propagation length (in units of $\pi/2C$), as described by Equation 9.5 when waveguide 1 is injected. The blue curve represent the case of synchronous coupling $\Delta\beta = 0$, while for the red curve $\Delta\beta = 4C$.

beam stays confined in only one waveguide without coupling into the others. This can be achieved by evanescently coupling the fundamental Gaussian modes at 1550 nm and preventing the coupling of the Bragg modes at 775 nm (corresponding to the pump beam). In order to interfere, the photons must have the same polarization and thus we will employ a type I SPDC process, in which a TM-polarized pump beam generates TE-polarized photon pairs. In the following calculation we will drop the polarization label, always referring to the fundamental TE mode at 1550 nm and to the TM Bragg mode at 775 nm.

Coupling constant evaluation

In order to determine the device parameters, in particular the gap width and the etching depth, we perform numerical simulations with Lumerical MODE on two coupled waveguides and, since the device consists of identical and periodically distributed waveguides, the results can be generalized.

We start by fixing the gap length to 500 nm, which is a reasonable value achievable with standard clean room processes, and the ridge width to 2 µm. Then we evaluate the modal refractive indices of the odd and even supermodes guided into the device (n_{odd} and n_{even}), while varying the etching depth. Figure 9.6 reports the transverse intensity profile of TE polarized supermodes at 1550 nm.

From the modal refractive indices we then calculate the coupling constant C, employing Equation 9.4. Figure 9.7 reports the calculated coupling length $L_c = \pi/2C$ as a function of the etching depth for both the SPDC Gaussian modes (at 1550 nm) and the pump Bragg mode (at 775 nm). The curves have been obtained by fitting additional data that lay outside the graph range. The vertical blue lines

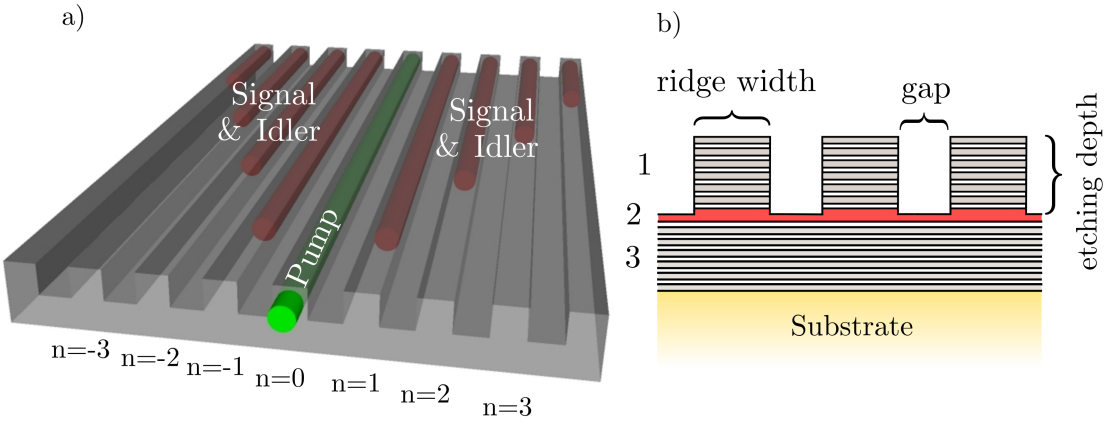

Figure 9.5: (a) Sketch of a lattice of parallel ridge nonlinear waveguides. (b) Epitaxial structure of the device (1: top Bragg mirror, 2: core, 3: bottom Bragg mirror) and definition of the lattice parameters.

indicate the waveguide core position along the epitaxial direction. We note that for both modes the coupling length increases more than linearly with the etching depth and the Bragg modes are less coupled than the infrared ones, as expected since they have a shorter wavelength and a shorter evanescent tail, resulting in a smaller spatial overlap.

From these simulations we choose an etching depth of 2.7 µm, for which the coupling length is about 300 µm for the infrared modes and 2.3 mm for the Bragg modes. These values, in a 2 mm-long device, ensure that the infrared modes are evanescently coupled while the Bragg modes are almost completely uncoupled.

Waveguide addressing

Since the waveguides in the array are too close to each other to allow a precise individual optical addressing, we design two s-bend parts to overcome this issue. Figure 9.8 is a sketch of the complete device that is composed by three injection waveguides (on the left), a central coupling region where the waveguides are brought closer and a collection region (on the right) where the waveguides are separated by 127 µm, which corresponds to the standard pitch of a fibered array that we plan to use to collect light out of the device. The s-bend waveguides are designed with a high curvature radius (approximately 600 µm), in order to minimize losses.

9.3 Spatial entanglement in a nonlinear waveguide array

We now introduce the quantum theory of SPDC in such array of nonlinear waveguides, following the analysis given in [293]. As stated before, we consider an array in which the generated photons can couple from waveguide to waveguide before

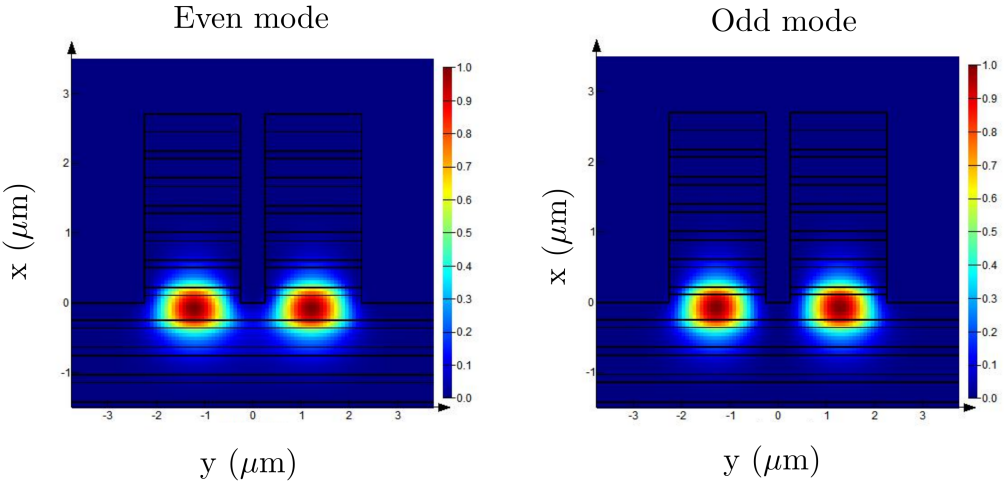

Figure 9.6: Intensity profiles of the even (left) and odd (right) TE guided supermodes at 1550 nm for an etching depth of 2.7 µm. The odd mode has a node in the center, while the even one does not.

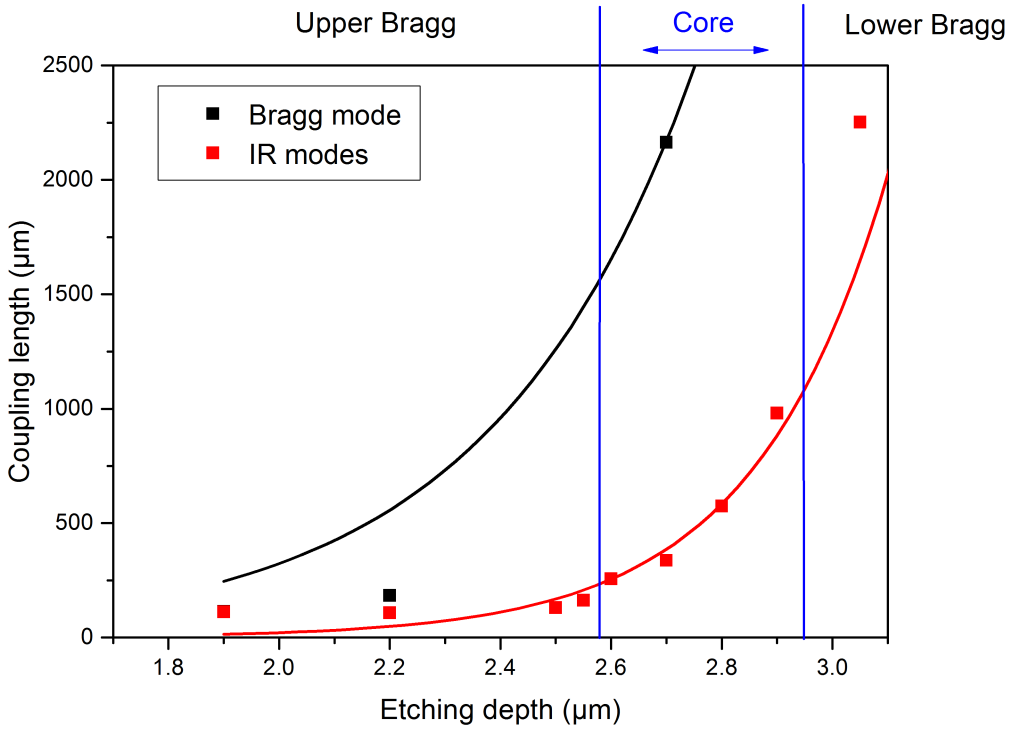

Figure 9.7: Coupling length L_c as a function of the etching depth (for a ridge width of 2 µm and a gap of 500 nm) for the TE Gaussian modes at 1550 nm (red) and the TM Bragg mode at 775 nm (black). The curves are fitted using additional data that lay outside the graph range. In blue we show the position of the waveguide core.

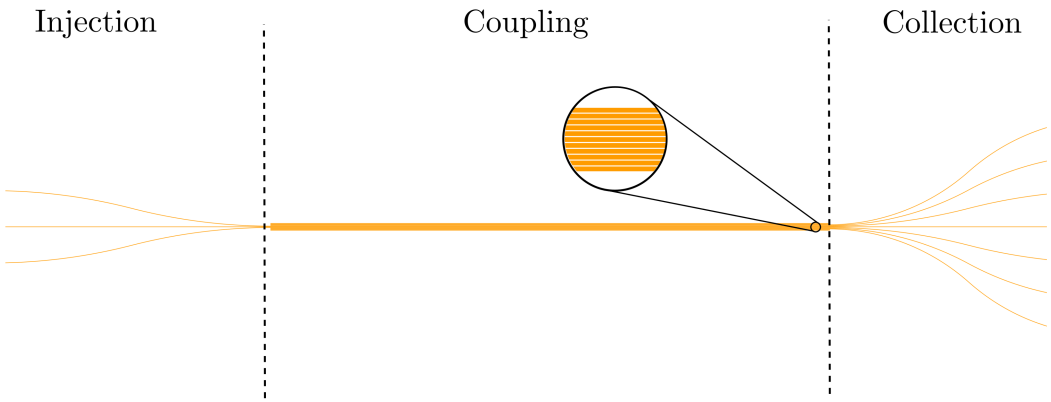

Figure 9.8: Sketch of the complete device. The injection part (left) is made of three s-bend waveguides connected to the central waveguides of the coupling region (center). Conversely, in the collection (right) part all the waveguides are connected.

exiting the device, while the pump beam (injected in one or more waveguides) does not diffract (due to its much smaller coupling constant), as depicted in Figure 9.5a.

The analysis is similar to the one given in chapter 2 for a counter-propagating source, but it includes now also the spatial degree of freedom (i.e. the transverse position in the array). The calculation follows the same steps. We first define the involved fields and the first-order perturbation term of the linear Hamiltonian, and then the biphoton wavefunction is derived by solving the Schrodinger equation.

The nearest neighbor coupling in the array introduces a discretized dispersion relation, modifying the propagation constant in the z direction:

$$\beta(\omega, k^{\perp}) = \beta^{(0)}(\omega) + 2C(\omega)\cos\left(k^{\perp}\right) \tag{9.8}$$

where $\beta^{(0)}(\omega) = \omega n(\omega)/c$ is the propagation constant in a single waveguide at frequency ω, which is governed by the modal refractive index $n(\omega)$. The second term, where $k^{\perp} = k_y d$ is the normalized transverse momentum (d is the center-to-center distance between the waveguides), corresponds to the modification of the dispersion relation induced by the presence of the waveguide array. The coupling parameter $C(\omega)$, previously evaluated, depends primarily on the gap length and secondly on the field frequency.

The signal and idler fields in the nth waveguide can be written as follows:

$$\hat{E}_n^{(+)}(z,t) = \hat{E}_n^{(-)\dagger}(z,t) = B\int_{-\pi}^{\pi} \mathrm{d}k^{\perp} \int_{-\infty}^{\infty} \mathrm{d}\omega\, e^{ik^{\perp}n} e^{i[\beta(\omega,k^{\perp})z-\omega t]} \hat{a}^{\dagger}(\omega, k^{\perp}) \tag{9.9}$$

with B a normalization constant. Since the signal and the idler fields are both TE polarized we have dropped the polarization label in the operator $\hat{a}^{\dagger}$.

On the other hand, the pump field can be considered as a bright undepleted optical beam and thus treated classically. Moreover, as already stated, the pump beam does not couple to neighboring waveguides and thus we can neglect the influence of the array. The pump field in the nth waveguide can be written as

follows:

$$\begin{aligned} E^{(+)}_{p,n}(z,t) =& E^{(-)*}_{p,n}(z,t) = \int_{-\infty}^{\infty} \mathrm{d}\omega_p \; A(n) f_{\mathrm{spectrum}}(\omega_p) e^{i[\beta_p^{(0)}(\omega_p)z - \omega_p t]} \\ =& \int_{-\pi}^{\pi} \mathrm{d}k_p^{\perp} \int_{-\infty}^{\infty} f_{\mathrm{spectrum}}(\omega_p) \tilde{A}(k_p^{\perp}) e^{ik_p^{\perp} n} e^{i[\beta_p^{(0)}(\omega_p)z - \omega_p t]} \end{aligned} \tag{9.10}$$

where $f_{\mathrm{spectrum}}(\omega_p)$ is the spectral shape of the pump beam and $\beta_p^{(0)}$ its propagation constant. In the second line of Equation 9.10 we have expressed the spatial amplitude pattern of the pump $A(n)$ via its Fourier Transform, obtaining its Bloch mode distribution $\tilde{A}(k_p^{\perp}) = \dfrac{1}{2\pi} \sum_n A(n) e^{-ik_p^{\perp} n}$.

We now define the nonlinear Hamiltonian of the SPDC process:

$$\hat{H}_{NL}(t) = \frac{\epsilon_0}{2} \int_0^L \mathrm{d}z \sum_n \chi^{(2)} [E^{(+)}_{p,n}(z,t) \hat{E}^{(-)}_n(z,t) \hat{E}^{(-)}_n(z,t) + \mathrm{h.c.}] \tag{9.11}$$

where L is the length of the array. Since the interaction inside the medium is weak we can employ first-order perturbation theory, as we have done in chapter 2. The biphoton state emerging from the waveguide array is then:

$$|\psi\rangle = \frac{1}{\sqrt{N}} \int_{-\infty}^{\infty} \mathrm{d}\omega_s \int_{-\infty}^{\infty} \mathrm{d}\omega_i \int_{-\pi}^{\pi} \mathrm{d}k_s^{\perp} \int_{-\pi}^{\pi} \mathrm{d}k_i^{\perp} f(\omega_s, \omega_i, k_s^{\perp}, k_i^{\perp}) \hat{a}^{\dagger}(\omega_s, k_s^{\perp}) \hat{a}^{\dagger}(\omega_i, k_i^{\perp}) \, |0\rangle \tag{9.12}$$

where $1/\sqrt{N}$ is a normalization constant. The signal and idler photons are created into a superposition of spectral and spatial modes determined by the joint spatio-spectral amplitude $f(\omega_s, \omega_i, k_s^{\perp}, k_i^{\perp})$, which reads:

$$\begin{aligned} f(\omega_s, \omega_i, k_s^{\perp}, k_i^{\perp}) =& f_{\mathrm{spectrum}}(\omega_s + \omega_i) \tilde{A}(k_s^{\perp} + k_i^{\perp}) \\ & \cdot \underbrace{\mathrm{sinc}\left[\frac{L}{2} \Delta\beta(\omega_s, \omega_i, k_s^{\perp}, k_i^{\perp})\right]}_{\phi(\omega_s, \omega_i, k_s^{\perp}, k_i^{\perp})} \underbrace{e^{-iL\Delta\beta(\omega_s, \omega_i, k_s^{\perp}, k_i^{\perp})/2}}_{\varphi(\omega_s, \omega_i, k_s^{\perp}, k_i^{\perp})} \end{aligned} \tag{9.13}$$

where the phase-mismatch $\Delta\beta$ is defined as:

$$\Delta\beta(\omega_s, \omega_i, k_s^{\perp}, k_i^{\perp}) = \beta_p^{(0)}(\omega_s + \omega_i) - \beta(\omega_s, k_s^{\perp}) - \beta(\omega_i, k_i^{\perp}) \tag{9.14}$$

The first two terms of Equation 9.13, $f_{\mathrm{spectrum}}(\omega_s + \omega_i)$ and $\tilde{A}(k_s^{\perp} + k_i^{\perp})$, are determined respectively by the spectral and spatial characteristics of the pump beam. Then we have identified the phase-matching amplitude $\phi(\omega_s, \omega_i, k_s^{\perp}, k_i^{\perp})$ and phase factor $\varphi(\omega_s, \omega_i, k_s^{\perp}, k_i^{\perp})$, which are given by the waveguide array properties (i.e. the modal dispersion and gap length).

In order to relate $f(\omega_s, \omega_i, k_s^{\perp}, k_i^{\perp})$ to spatially or spectrally resolved correlation measurements, we calculate the correlation function between a photon at $(\omega_s, k_s^{\perp})$ and an other one at $(\omega_i, k_i^{\perp})$:

$$\begin{aligned} \tilde{\Gamma}_{\omega,k}(\omega_s, \omega_i, k_s^{\perp}, k_i^{\perp}) =& \langle \psi | \hat{a}^{\dagger}(\omega_s, k_s^{\perp}) \hat{a}^{\dagger}(\omega_i, k_i^{\perp}) \hat{a}(\omega_i, k_i^{\perp}) \hat{a}(\omega_s, k_s^{\perp}) | \psi \rangle \\ =& \begin{cases} 4/N |f(\omega_s, \omega_i, k_s^{\perp}, k_i^{\perp})|^2 & \text{if } \omega_s = \omega_i \text{ and } k_s^{\perp} = k_i^{\perp} \\ 1/N |f(\omega_s, \omega_i, k_s^{\perp}, k_i^{\perp})|^2 & \text{else} \end{cases} \end{aligned} \tag{9.15}$$

where the factor 4 accounts for the case of indistinguishable photons.

By tracing over the spectral degree of freedom we retrieve the correlation function in the transverse-momentum space:

$$\tilde{\Gamma}_k(k_s^\perp, k_i^\perp) = \int \mathrm{d}\omega_s \int \mathrm{d}\omega_i \, \tilde{\Gamma}_{\omega,k}(\omega_s, \omega_i, k_s^\perp, k_i^\perp) \tag{9.16}$$

In the real space (corresponding waveguide numbers n_s and n_i) the correlation function $\Gamma(n_s, n_i)$ can be calculated as follows:

$$\Gamma_n(n_s, n_i) = \int \mathrm{d}\omega_s \int \mathrm{d}\omega_i \, \Gamma_{\omega,n}(\omega_s, \omega_i, n_s, n_i) \tag{9.17}$$

where $\Gamma_{\omega,n}(\omega_s, \omega_i, n_s, n_i) = |\mathrm{FT}(f(\omega_s, \omega_i, k_s^\perp, k_i^\perp))|^2$ and FT stands for Fourier Transform. $\Gamma_n(n_s, n_i)$ is called Joint Spatial Intensity and gives the probability of detecting the signal and idler photons at the outputs n_s and n_i, respectively.

Phase-matching

In order to obtain a significant down-conversion rate, the phase-matching condition must be nearly perfectly satisfied, i.e. $\Delta\beta(\omega_s, \omega_i, k_s^\perp, k_i^\perp) \approx 0$. This induces spatio-temporal correlations between the frequency (ω_s, ω_i) and the $k^\perp$-components $(k_s^\perp, k_i^\perp)$ of the generated signal and idler photons.

The phase-mismatch $\Delta\beta(\omega_s, \omega_i, k_s^\perp, k_i^\perp)$, Equation 9.14, can be split into two terms:

$$\Delta\beta(\omega_s, \omega_i, k_s^\perp, k_i^\perp) = \Delta\beta_\omega(\omega_s, \omega_i) + \Delta\beta_\mathrm{A}(\omega_s, \omega_i, k_s^\perp, k_i^\perp) \tag{9.18}$$

where the first term $\Delta\beta_\omega(\omega_s, \omega_i)$ describes the spectral phase-matching of an isolated waveguide and reads:

$$\Delta\beta_\omega(\omega_s, \omega_i) = \Delta\beta_p^{(0)}(\omega_s + \omega_i) - \beta^{(0)}(\omega_s) - \beta^{(0)}(\omega_i) \tag{9.19}$$

On the other hand, the second term $\Delta\beta_\mathrm{A}(\omega_s, \omega_i, k_s^\perp, k_i^\perp)$ is the phase-matching induced by the dispersion of the array and reads:

$$\Delta\beta_\mathrm{A}(\omega_s, \omega_i, k_s^\perp, k_i^\perp) = -2C(\omega_s)\cos\Big(k_s^\perp\Big) - 2C(\omega_i)\cos\Big(k_i^\perp\Big) \tag{9.20}$$

which depends on the transverse $k^\perp$-components of the generated photons $(k_s^\perp, k_i^\perp)$ and on the coupling parameter $C(\omega)$, which is frequency dependent.

For our device, consisting of co-propagating nonlinear sources presented in section 1.5 and based on modal phase-matching, the phase-matching condition of an isolated waveguide (Equation 9.19) reads:

$$\Delta\beta_\omega = \frac{1}{c}\Big[\omega_p n_{\mathrm{Bragg,\ TM}}(\omega_p) - \omega_s n_\mathrm{TE}(\omega_s) - \omega_i n_\mathrm{TE}(\omega_i)\Big] \tag{9.21}$$

where we have considered a type I SPDC process, in which a TM pump photon is down-converted into two TE photons; $n_{\mathrm{Bragg,\ TM}}(\omega_p)$ is the effective refractive index of the Bragg guided mode of the pump at 775 nm and $n_\mathrm{TE}(\omega)$ the one of the fundamental guided mode at 1550 nm. For a more detailed discussion about modal phase-matching we refer to section 1.5.

Numerical simulations

In order to gain insight into the generation of spatial correlations, we now consider the simple case of a monochromatic pump beam and perfect spectral phase-matching (i.e. $\Delta\beta_\omega = 0$). Figure 9.9 reports the Joint Spatial Intensity in real space $\Gamma_n(n_s, n_i)$, numerically calculated with a Matlab script, for a 2 mm-long device with a frequency-independent coupling constant $C = 5$ mm^{-1}, corresponding to a coupling length $L_c \approx 310$ µm, as simulated for our device design (ridge width 2 µm, gap 500 nm and etching depth 2.7 µm).

When pumping only the central waveguide (Figure 9.9a), we observe that the photons are more likely to exit through the same waveguide (spatial bunching) or through opposite waveguides (spatial anti-bunching). When pumping the waveguides $n = 0$ and $n = 1$ in phase, anti-bunching is enhanced (Figure 9.9b), while when the same two waveguides are pumped out of phase, bunching is favored (Figure 9.9c). More complex quantum states can be obtained by further tailoring of the pump configuration.

Spatial correlations can be experimentally verified by measuring photon coincidences between output pairs, thus reconstructing the joint spatial intensity. In our case, the source has a typical brightness of 5-10 MHz [59], leading to approximately 100 Hz of measured coincidences using a standard setup with avalanche photodiodes. This requires about 20 min in total to measure a correlation map such as shown in Figure 9.9. Moreover, the quantum nature of the generated quantum state could be directly assessed using Bell-type criteria [290].

In this analysis we have considered the simplest array with equidistant waveguides and fixed coupling constants. However, by controlling these parameters it is possible to simulate condensed-matter systems. Indeed, quantum walks in a waveguide lattice can be described by a tight-binding Hamiltonian which is widely encountered in many condensed-matter phenomena. Each waveguide represents a site and its modal refractive index has the role of the on-site energy. The coupling constant determines the tunneling between sites. The first can be controlled by modifying the waveguide width or by employing the elctro-optic effect, while the latter can be controlled by varying the gap, as we have seen. Thus, the waveguide array offers a wide flexibility to define any form of tight-binding Hamiltonian, and can serve as a platform to simulate fundamental physical effects otherwise difficult to access in condensed- matter systems

In addition, the possibility of varying the lattice parameters, i.e. alternating different values for the gap, would allow to study topological effect: for example implementing the Su-Schriefer-Heeger (SSH) Hamiltonian [294], which is the simplest tight-binding Hamiltonian featuring topological properties [96].

In conclusion, the designed device is a versatile and compact source of spatially high-dimensional entangled photon pairs in the telecom range and operating at room temperature, which could be employed to perform quantum simulations.

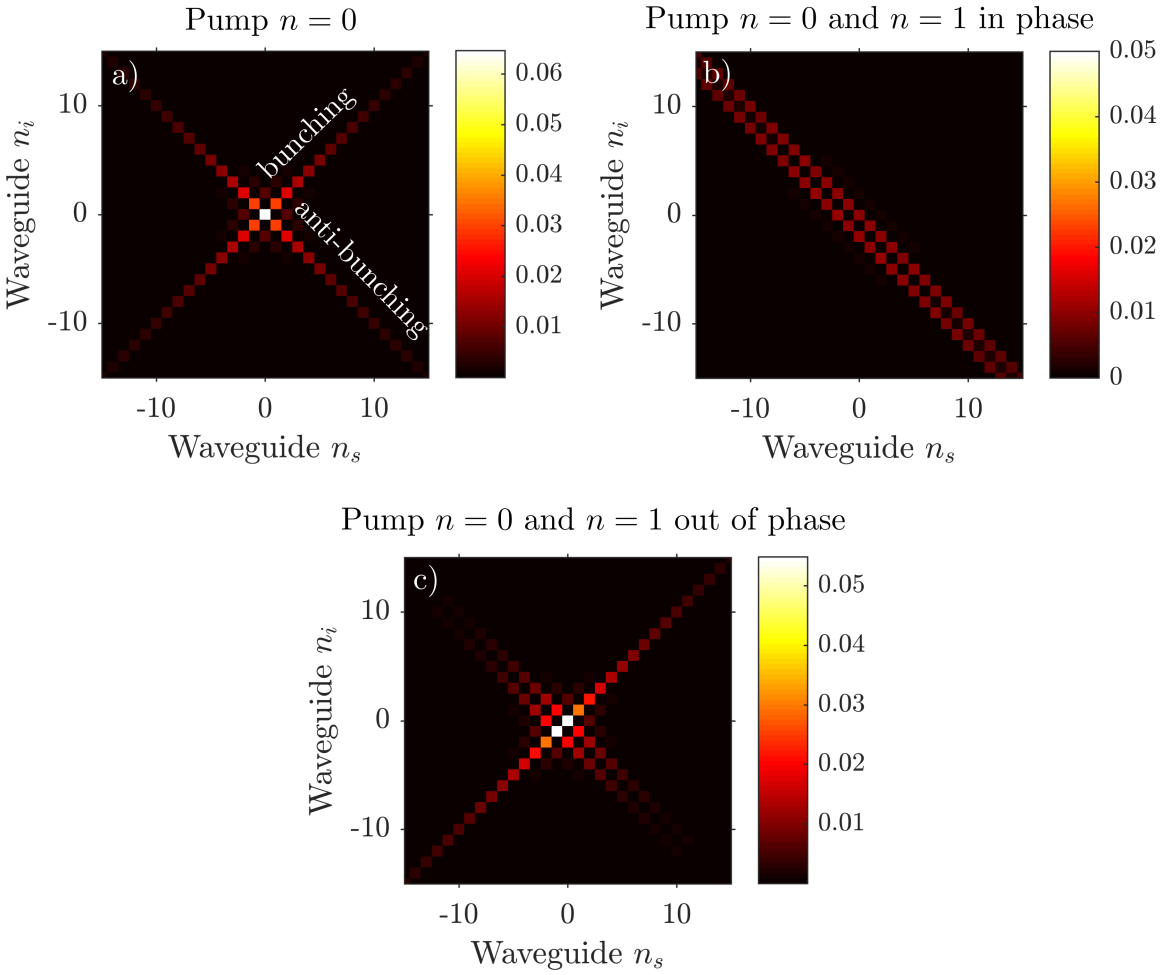

Figure 9.9: Calculated Joint Spatial Intensity in real space $\Gamma_n(n_s, n_i)$ at the output of a $L = 2$ mm lattice with coupling constant $C = 5$ mm^{-1}, when pumping with a CW laser: (a) the central waveguide ($n = 0$), (b) the waveguides $n = 0$ and $n = 1$ in phase and (c) the waveguides $n = 0$ and $n = 1$ out of phase. We assume that the spectral phase-matching condition is perfectly satisfied (i.e. $\Delta\beta_\omega = 0$).

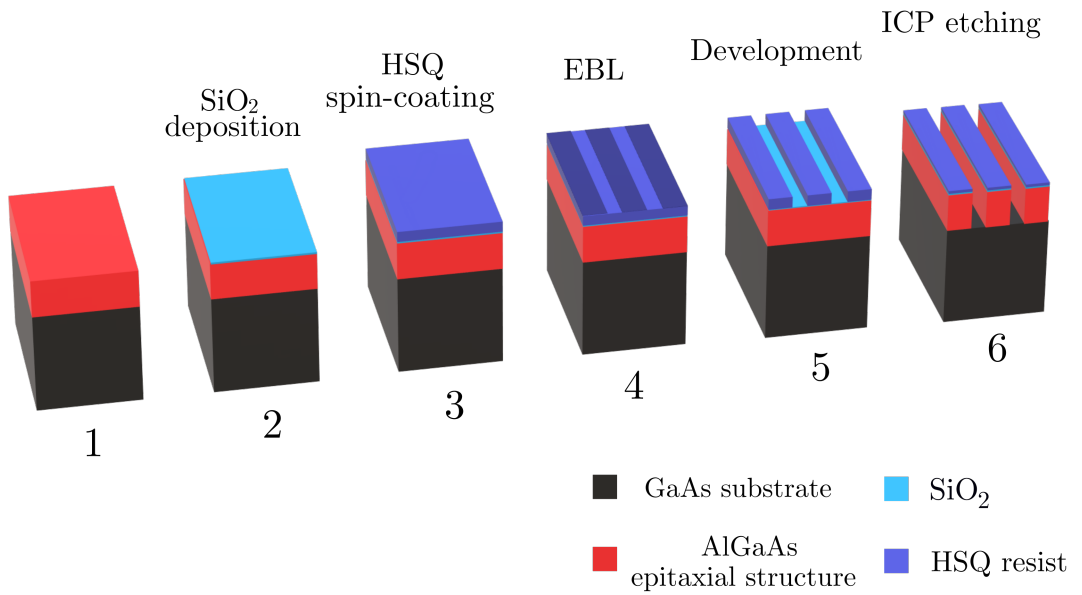

Figure 9.10: Sketch of the clean room fabrication steps for the fabrication of the device.

9.4 Device fabrication

The fabrication of parallel 2 µm-wide ridge waveguides spaced by 500 nm requires a robust clean room process with a good resolution (of the order of 50 nm at least).

The counter-propagating source presented in the previous part of the thesis has been fabricated using photolithography and chemical wet etching, a simple and fast process thanks to the parallel illumination of the whole chip at once. Yet, this technique has several drawbacks when fabricating more complex photonic circuits than simple waveguides. Indeed, the isotropic wet etching produces waveguides with curved sidewalls, which, in our case, would prevent a precise control of the gap and thus of the coupling parameter. Moreover, the wet etching process strongly depends on the employed solvent and on the soaking speed and orientation, resulting in hardly reproducible samples. Finally, the resolution that can be achieved with UV photolitography, in our clean room, is limited to 150 nm.

For all these reasons, for the fabrication of the waveguide array we have optimized a new fabrication process based on electron beam lithography (EBL) and inductively coupled plasma etching (ICP). EBL allows to draw on the resist waveguides with high lateral resolution, thanks to the low electron diffraction-limit. ICP is a technique of directional etching allowing to obtain vertically shaped waveguide sidewalls and to precisely control the etching depth.

In this section we detail the fabrication steps, which are illustrated in Figure 9.10.

9.4.1 Resist deposition

We choose the negative electron-sensitive resist HSQ (hydrogen silsesquioxane) Dow Corning XR-1541 at 6% concentration, for its high resolution (6 nm).

As a first step, in order to optimize the adhesion of the resist on the sample, we deposit a 10 nm-thick film of SiO_2 by Plasma-enhanced Chemical Vapor Deposition (PECVD). Then the resist is deposited by spin-coating using the following recipe:

HSQ resist deposition	
HSQ spin-coating	4000 rpm, t_{ramp}= 3 s, t_{spin}=30 s
baking 1	150°C, t=2 min
baking 2	200°C, t=2 min

obtaining a resist thickness of approximately 160 nm.

9.4.2 Electron beam lithography

Electron beam lithography is a high-resolution and maskless exposure method that allows to draw custom shapes on a surface covered with an electron-sensitive resist. Thanks to the low electron diffraction-limit, the resolution can be less than 10 nm. Yet, the versatility of this technique is counter-balanced by a slow speed, because the electron beam needs to scan the whole sample surface, drawing point by point. For this reason, EBL is not employed for industrial high-volume production and it is mainly adopted for academic research or prototyping.

In this thesis we use the Raith eLine lithographic system of the Ecole Normale Supérieure clean room in Paris belonging to the Paris Centre clean room consortium. This system allows to work both in the normal mode and in the fixed beam moving stage (FBMS) exposure mode, in which the electron beam is fixed and the sample moves. This procedure enables rapid exposure of long structures, such as waveguides, without stitching errors[2] and it is thus particularly suited for the fabrication of our waveguide array.

The main parameter to optimize in EBL lithography is the area dose (the flux of irradiating electrons), which mainly depends on the employed resist. To do so, we perform a dose test employing a mask with 25 arrays of 7 straight waveguides in which the area dose ranges from 100 µC/cm^2 to 1300 µC/cm^2 with steps of 50 µC/cm^2. The EBL is set to 30 µm beam aperture and an acceleration voltage of 20 kV.

After the lithography we develop the resist with the developer AZ400K for 1 min.

[2]During a standard exposure the electron beam is deflected by electromagnetic lenses to write inside an area called writing field (typically 100 µm by 100 µm). To fabricate samples that are larger than the writing field, the stage has to move each time the beam reaches its maximum deflection angle. This procedure is critical and usually results in a misalignment of the order of 10 nm. Such imperfections are not desirable in a waveguide, as they cause optical losses. Conversely, during a FBMS exposure the electron beam is always fixed and the stage moves to write the waveguide, with a high mechanical stability, thus allowing to fabricate long samples without stitching errors.

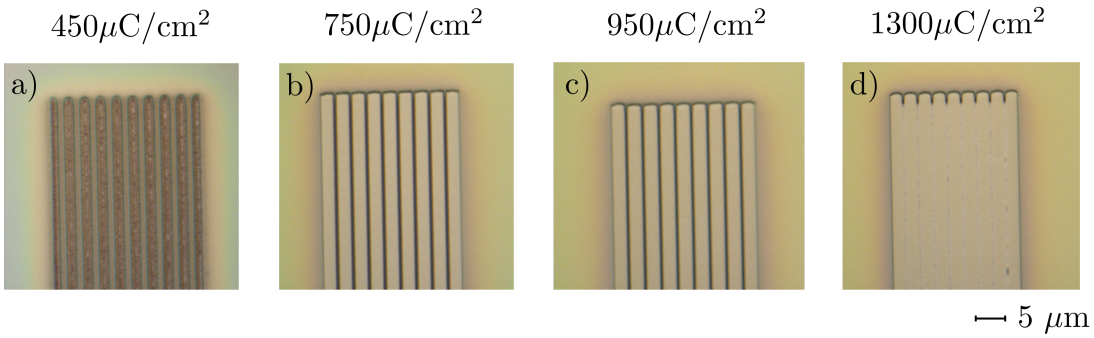

Figure 9.11: Optical microscope images at 150x magnification of the dose test sample after ICP etching: from left to right, increasing values of EBL area dose.

9.4.3 ICP dry etching

After the resist is developed, we start the inductively coupled plasma etching (ICP). ICP is a dry etching technique based on Reactive-Ion Etching (RIE), which uses a chemical reactive plasma to remove material from a piece of wafer. The ions are accelerated by a high voltage and collide with the sample. Two processes occur: the ions react chemically with the materials on the surface, but they also knock off (sputter) materials transferring part of their kinetic energy. Due to the mostly vertical direction of the flux of reactive ions, the technique produces samples with anisotropic etch profiles (i.e. vertical sidewalls), contrary to the typical isotropic profile produced by wet etching. For this work we employ a Sentech SI500 machine and $SiCl_4$ chemistry.

The ICP recipe we employ is based on low RF acceleration voltage and power ($V = 115$ V and $P = 15$ W), low plasma power (20 W) and the etching species $SiCl_4$ (3 sccm)[3] and Ar (3 sccm). This recipe allows to gently etch the sample without completely removing the resist and to obtain a profile with low roughness. On the other hand, the etch rate is low, approximately 10 nm/min.

Figure 9.11 reports images taken with an optical microscope at 150x magnification after the ICP process for four different EBL dose values, ranging from 450 μC/cm² to 1300 μC/cm². We find that for the lower values the resist has not been exposed enough and thus the etching process has completely removed it (Figure 9.11a). Conversely, for the higher dose values the resist has been too exposed and the waveguides have merged (Figure 9.11d). In conclusion, we identify an optimal dose around 800 μC/cm², and in the following fabrication we will always employ this value.

Etching rate and gap

After having determined the optimal dose for EBL, we perform an etching test to evaluate the etching rate in the trenches between adjacent waveguides. Indeed, in this particular situation it is not possible to employ the interferometric system of

[3]Standard cubic centimeters per minute (SCCM) is a unit of flow measurement indicating cubic centimeters per minute (cm³/min) in standard conditions for temperature and pressure of a given fluid.

the machine, because the trenches are too narrow with respect to the laser spot size. We also need to check that the obtained gap width between adjacent waveguides corresponds to the target one.

In order to perform a systematic study, we design a mask with eleven array of straight 2µm-wide waveguides where the gap spans from 200 nm to 700 nm, the target gap being 500 nm. After the ICP etching we cleave the sample in two pieces and observe the waveguide facets with a scanning electron microscope (SEM), as shown in Figure 9.12.

First of all we note that the etched trenches between the waveguides do not have perfectly vertical sidewalls, but are slightly under-etched: the gap is smaller at the top and the bottom of the trenches and bigger in the center, as shown in Figure 9.12a for a nominal gap of 500 nm.

By looking at Figure 9.12b, reporting an array of waveguides with a nominal gap of 700 nm, we observe that this effect is less pronounced when the gap increases. Indeed, in this case the reactive ions employed in the ICP process can etch more easily inside the gap. This behavior is confirmed by the lateral sidewalls of the array, which have almost perpendicular profiles, as can be seen in the same image.

We then compare the nominal gap dimension with the measured one, for each array of waveguides. In general we find that the actual gaps are wider than their nominal dimension and this effect is more pronounced when the gap is increased: for gaps with a small nominal value (< 400 nm) we measure an actual value approximately 5% greater, while for gaps with a larger nominal value (600-700 nm) the difference rises up to approximately 15%. However, this discrepancy can be early corrected by adjusting the EBL mask accordingly.

Finally, we measure the etching rate. By looking at Figure 9.12b we note that the etched depth differs if we consider the central waveguides or the lateral ones. This is a known effect called aspect ratio dependent etching [295] and it is mainly due to a decrease of transport of the reactive species when the trench aspect ratio increases. We evaluate an etching rate of approximately 10 nm/min inside the trenches and of approximately 13 nm/min outside.

9.4.4 Fabrication of the complete device

So far we have performed a dose test and evaluated the etching rate, in order to optimize the fabrication process for arrays of straight waveguides. We now focus on the fabrication of a "complete" device, as depicted in Figure 9.8, which is composed of: an injection region with three waveguides, a coupling region with an array of seven waveguides and a collection region where the waveguides split apart.

In order to overcome the issue of different etching rates inside and outside the array, we add two additional waveguides on each side of the central array, without connecting them to the injection nor to the collection region. In this way, the seven central waveguides, in which we expect the photons to propagate, are etched to the same depth.

Figure 9.13a reports a SEM image of a close-up on the fabricated device, showing the coupling region and the collection waveguides, while Figure 9.13b shows a larger view of the device. For both the coupling region and the s-bend parts we observe a good fabrication quality.

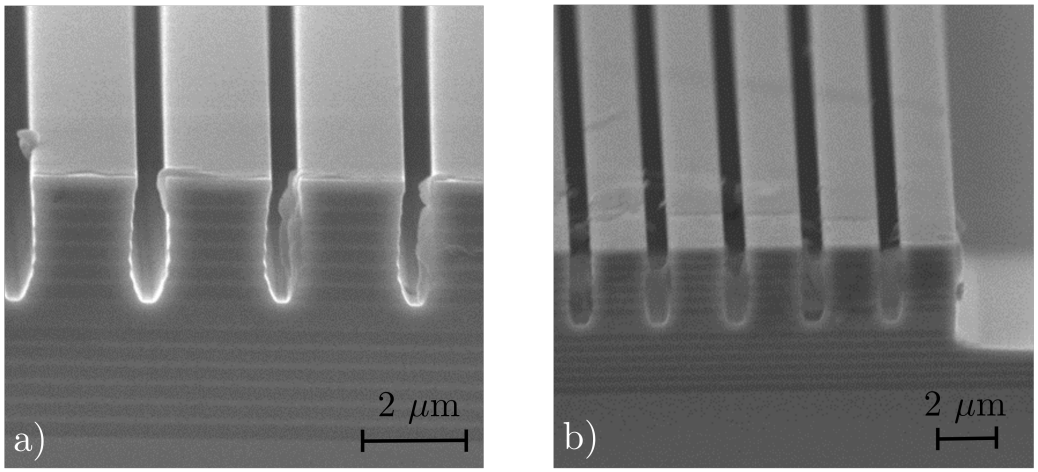

Figure 9.12: SEM images of the waveguide facets for two different nominal gap values: 500 nm (a) and 700 nm (b).

It is worth noting that, without cleaving the sample in two pieces, it is impossible to determine the trench depth in the coupling region. Nevertheless, by measuring the etching depth for a waveguide outside the coupling region (3.5 µm) and knowing the ratio between the inside and outside etching rates, we evaluate that the trenches have been etched to a depth of approximately 2.7 µm, which corresponds to the target depth.

9.5 Optical characterization

We now proceed to the optical characterization of several types of fabricated devices. We start by analyzing a sample containing only arrays of straight waveguides with different gap widths, in order to determine if the devices properly guide light and to evaluate the propagation losses. We then test a sample containing three complete devices with injection and collection s-bent waveguides. The two samples have been fabricated from the same wafer (**EBW002**) but at different dates.

9.5.1 Guided modes

As a first test, we analyze a 0.9 mm-long array of straight waveguides with a nominal gap of 600 nm, employing first a laser beam at 775 nm and then one at 1550 nm.

We use a Ti:Sapphire laser at 775 nm in a quasi-continuous wave regime and inject the beam in the waveguide array employing a microscope objective (x40, NA=0.75), as sketched in Figure 9.14. The output light is collected using another microscope objective (x40, NA=0.65) and focused on a CDD camera with a converging lens (f=300 mm), in order to image at the same time the device facets and the output guided modes.

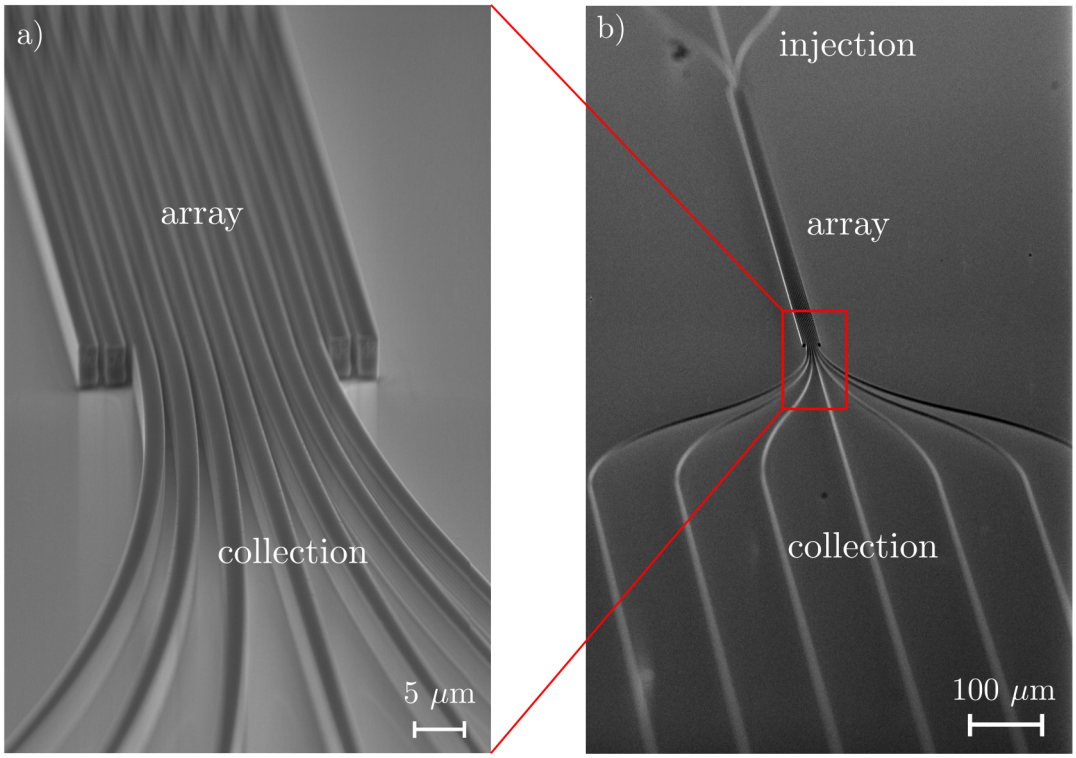

Figure 9.13: SEM images of the waveguide array device. (a) Coupling region and collection waveguides. On the sides of the coupling region it is possible to notice the four waveguides that we have added to obtain a uniform etching depth, which are not connected with the collection region. (b) Top view of the device; starting from the top: injection, coupling and collection regions.

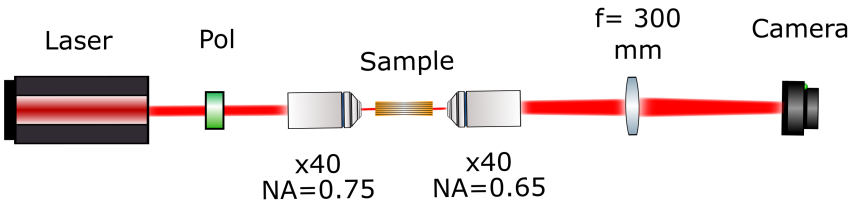

Figure 9.14: Optical setup employed to image the device output facet and the output guided modes at 775 nm. The same setup, without the converging lens, is used to image the infrared guided modes at 1550 nm.

Figure 9.15 reports the images taken with the CDD camera, displaying the output facets (whose envelope is highlighted in white) and the output guided modes. When moving the laser beam from the right to the left we inject a different waveguide of the array and the output mode consequently shifts, as shown from Figure 9.15a to Figure 9.15e. The images show also that the beam is guided in a single waveguide without coupling to the neighboring waveguides. This demonstrates that the waveguides are essentially not evanescently coupled at 775 nm, as required for the correct functioning of the device.

In addition to the modes guided in single waveguides, when injecting light at a lower height in the device we observe a supermode confined in the top part of the lower Bragg mirror, which spans the whole device, as shown in Figure 9.15f. We think that the presence of this mode is due to the device design: the waveguides are very close to each other and the core is not completely etched (see Figure 9.5b), creating a confined supermode in the bottom Bragg mirror.

As a second step, we investigate the infrared guided modes at 1550 nm, by using a setup similar to the one reported in Figure 9.14. We employ a Tunics CW laser, the same two microscope objectives and an infrared camera to image the modes (without converging lens). Figure 9.16 reports the measured output modes. The images have a low quality due to the IR camera low sensitivity and resolution, but it is still possible to distinguish the output light. We observe that light exits from more than one waveguide, on average from three, meaning that the waveguides are evanescently coupled at 1550 nm, as required during the design. Moreover, also for the infrared beam, the device presents a supermode guided in the bottom Bragg mirror, as shown in Figure 9.16d.

9.5.2 Propagation losses

In order to evaluate the quality of the fabrication process, we evaluate the propagation losses at 1550 nm, by employing the technique detailed in section 1.4. We inject the infrared laser beam inside the sample and measure the power of the output light while sweeping the laser wavelength; from the contrast of the Fabry-Pérot fringes we evaluate the propagation losses. This procedure relies on the knowledge of the modal reflectivity of the considered guided modes. In our device, the input beam spreads over multiple waveguides during the propagation but remains guided in their fundamental modes. We can thus reasonably approximate

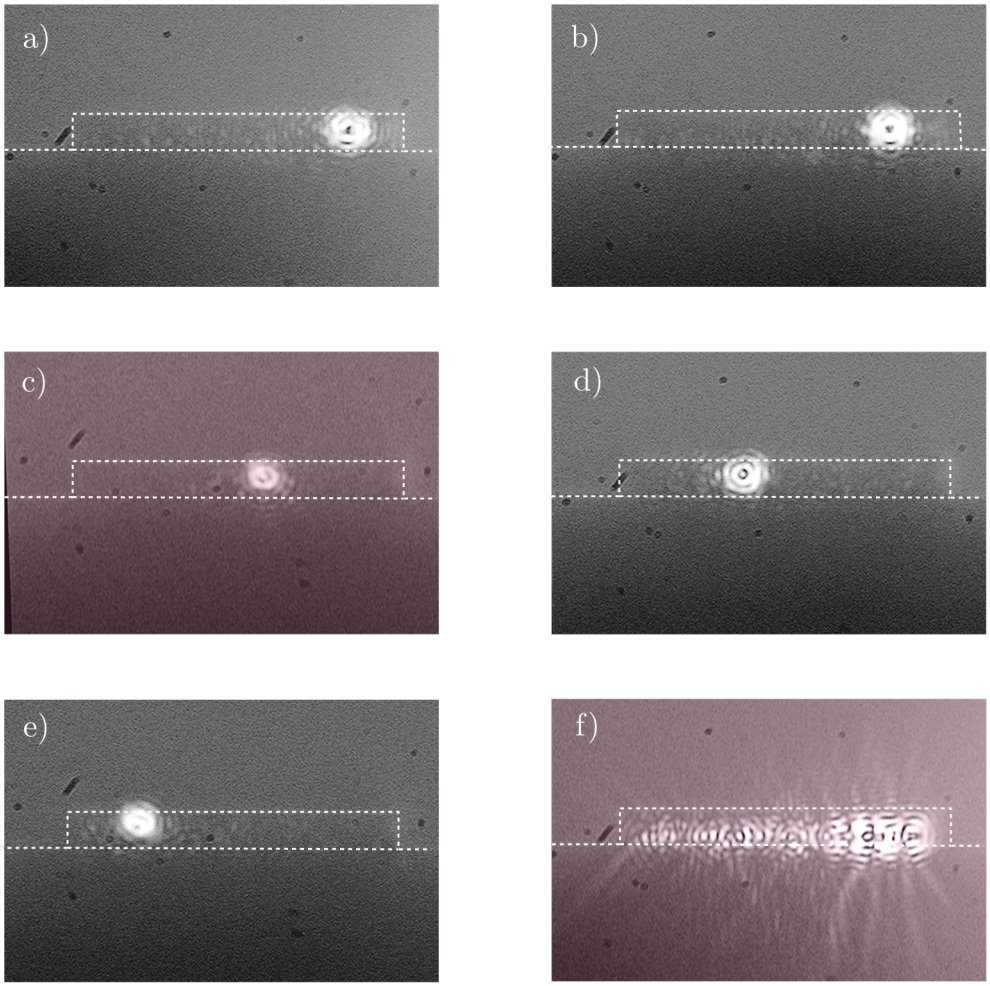

Figure 9.15: Images of the device output facet (highlighted in white) and Bragg guided modes at 775 nm: from (a) to (e) the input beam is moved from right to left and thus coupled into a different waveguide of the array. (f) Supermode guided in the bottom Bragg mirror.

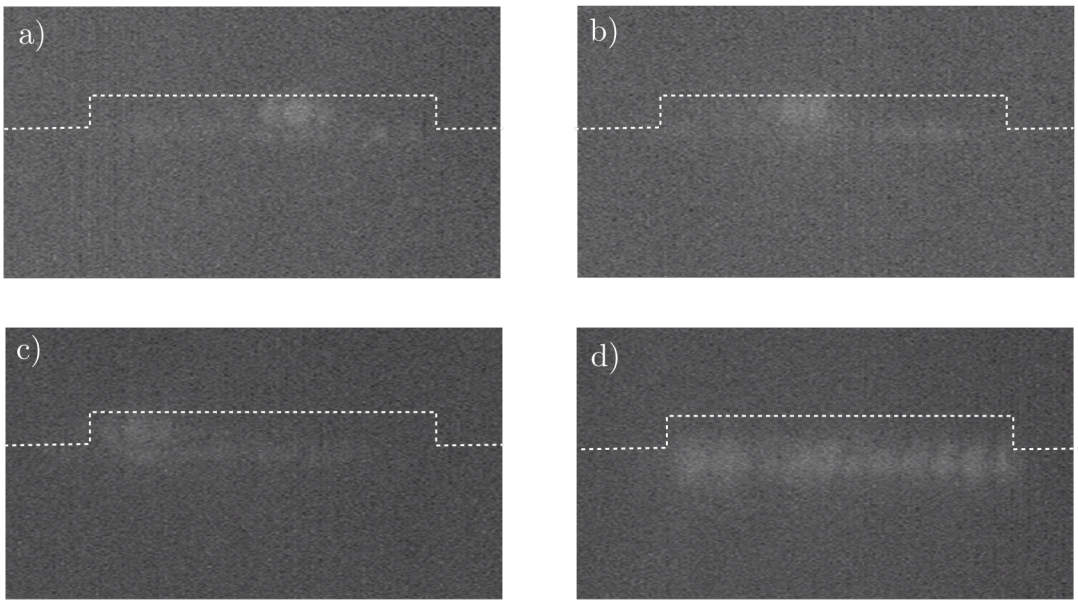

Figure 9.16: Output guided modes at 1550 nm. From (a) to (c) the input beam is moved from right to left. (d) Supermode guided in the bottom Bragg mirror.

the modal reflectivity of the involved modes to that of the fundamental modes in a 2 µm-wide ridge single waveguide, whose values have been numerically calculated in section 1.5 ($R_{\mathrm{TE}} = 28.2\%$ and $R_{\mathrm{TM}} = 27.8\%$).

We perform the loss measurement for several positions of the input beam, thus selecting different waveguides of the array. From the measured fringe contrast we evaluate that the propagation losses are in the range $\alpha = 5 - 9$ cm^{-1}. Figure 9.17 reports a measurement done in one waveguide of the array. Comparing these values to the typical losses that we obtain in single waveguides, processed by wet etching ($\alpha \approx 0.5$ cm^{-1} [159]) that induces very low roughness, we see that these value remain acceptable but there is room for further improvement of the EBL and ICP fabrication process.

9.5.3 Test of the complete device

The complete device has been fabricated from the same wafer than the sample previously analyzed, but since it has been fabricated at different dates, it may have a different fabrication quality and thus different optical losses. The device total length is 8 mm divided as follows: 2 mm for the coupling region and 3+3 mm for the injection and collection parts.

By employing the optical setup reported in Figure 9.14, without the converging lens, we try to couple a laser beam at 775 nm and at 1550 nm inside the device. Yet, it is not possible to identify the guided modes, neither at 755 nm nor at 1550 nm.

In order to have more clues about this apparent absence of guided modes, we couple the 775 nm laser while imaging the top surface of the sample with a CDD

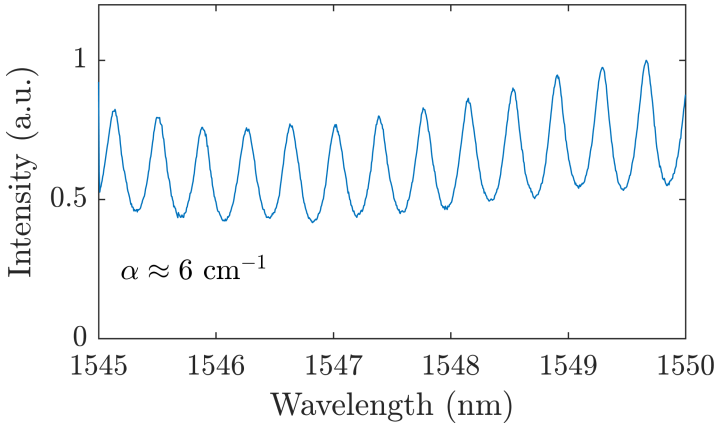

Figure 9.17: Normalized power transmitted through one waveguide of the waveguide array. From the contrast of the Fabry-Pérot oscillations we derive the optical losses.

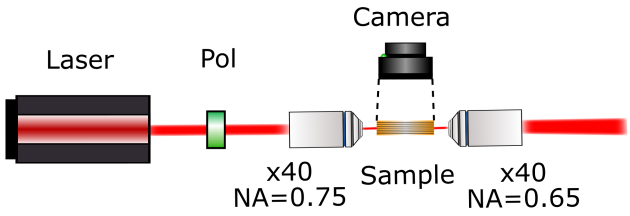

Figure 9.18: Optical setup used to image the top surface of the sample.

camera mounted on a trinocular, as illustrated in Figure 9.18. The resulting image is reported in Figure 9.19. The input beam is injected in the lower input arm (point 1) and propagates through the device while scattering light from the waveguide surface. We notice that the output facets (point 3) are slightly illuminated, meaning that the beam has traveled through the whole device, even if no guided mode is visible after the collection microscope objective (probably the beams are too attenuated).

Moreover at point 2, where the array is connected to the s-bend part, we observe a bright point corresponding to the location of the output facets of the lateral waveguides that we have added to obtain a more uniform etching depth, as explained in subsection 9.4.4. We thus think that the guided mode highly diffracts during the propagation in the coupling region and a part of the injected power reaches the lateral waveguides which are not connected to the collection region (as shown in Figure 9.13a).

As we have said previously, the guided modes at 775 nm are supposed to be uncoupled and this was the case for the array of straight waveguides whose measurements are reported in Figure 9.15. We suppose that in the present sample the coupling at 775 nm is caused by an insufficient etching in the central region and thus by a non-negligible coupling constant of the Bragg mode.

Moreover, the fact that light scatters out of the waveguide top confirms also the hypothesis that the guided modes have high propagation losses, which however

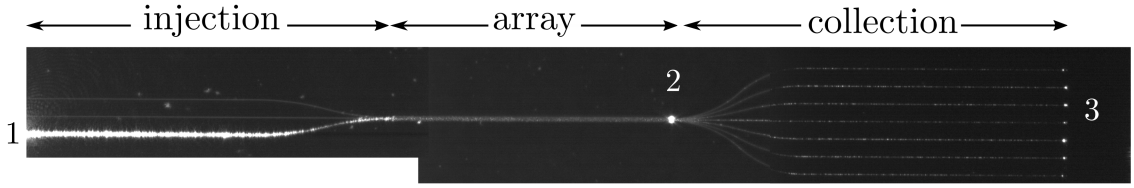

Figure 9.19: Top view of the device while injecting a 755 nm beam in the lower input arm (1). We notice that the output facets (3) are slightly illuminated, meaning that the beam is guided. In (2) we observe a bright spot where the coupling region is connected to the s-bend part. See text for additional details.

are difficult to evaluate without measuring the transmitted power. Alternatively, they can be roughly estimated from the exponential decay of the scattered light measured with the camera [296]. By fitting the exponential decay we obtain a value of propagation losses around $\alpha \approx 25$ cm^{-1} for the pump Bragg mode, which is higher than the one obtained in previous works (approximately 5 cm^{-1} [159]). However, in the latter case the waveguide was fabricated by wet etching, which usually produces smoother sidewalls, and the waveguide ridge was larger (5 µm); therefore, the guided mode was less influenced by eventual fabrication defects.

In conclusion, we presume that the combined factors of high propagation losses and an insufficient etching depth are the causes of the absence of output guided modes of measurable intensity. We are currently working to improve the fabrication processes, in particular the ICP etching step.

9.6 Conclusion and perspectives

In this chapter we have presented a new device designed to produce spatially entangled photon pairs, based on cascaded quantum walks in an array of co-propagating nonlinear waveguides. We have first presented the design of the device and its working principle, focusing on the possibility of engineering the spatial correlations of the generated photon pairs.

Then, we have optimized the clean room process to fabricate the device, determining the best parameters for the electron beam lithography and the inductively coupled plasma etching processes. The fabricated samples, observed with a scanning electron microscope, showed a good fabrication quality, with parameter in accordance with the design.

With an optical characterization, carried out on arrays of straight waveguides, we have determined that the infrared guides at 1550 nm are evanescently coupled while the modes at 775 nm are not, confirming the correct functioning of the device.

However, when we have tested a complete device, containing also two s-bend regions to enable individual waveguide addressing, no output guided modes have been detected. The two probable causes of this issue are the high propagation losses inside the device, which is 8 mm long, and an insufficient etching depth.

In order to fabricate a complete functioning device, we are currently optimizing the clean room processes to improve the quality of the trenches of the coupling region and to reduce the propagation losses.

Conclusions and Perspectives

This PhD thesis is devoted to the study and development of AlGaAs integrated photonic devices to be employed in the field of quantum technologies. The main focus of this work is the generation and the engineering of photon pairs entangled in high-dimensional degrees of freedoms, such as frequency or spatial modes. Indeed, in contrast to polarization, these degrees of freedom span a larger Hilbert space and thus the capability of controlling and shaping them opens novel possibilities for quantum information protocols.

The photon pairs sources studied in this work present several advantages that make them a perfect candidate for the development of integrated photonic chips for quantum information applications. Indeed, they operate at room temperature and emit in the telecom range, which allows the transmission of the generated quantum states over long distance through optical fibers. Moreover, the AlGaAs platform offers the possibility to integrate pump lasers and electro-optic modulators, which are key steps towards the realization of active and monolithic photonic devices.

In the first part of this thesis we have reported the study of the biphoton states emitted by a SPDC source based on a counter-propagating phase-matching scheme, focusing on frequency correlations. To this end, we have first introduced the Joint Spectral Amplitude (JSA), a complex-valued function that describes all the temporal and spectral properties of the photons, and two experimental techniques (a single-photon fiber spectrograph and the Stimulated Emission Tomography) that allow to reconstruct its squared modulus, the Joint Spectral Intensity (JSI).

Then, through numerical simulations and experimental measurements we have demonstrated that both the intensity and phase of the JSA can be shaped by tailoring the pump beam spatial profile, directly at the generation stage and without any post-selection. The pump beam shaping has been achieved by employing a spatial light modulator in a 4f configuration, obtaining either intensity or phase shaping.

In particular, we have shown that tuning the pump beam waist allows to produce correlated, anti-correlated and separable frequency states, while modifying the spatial phase profile allows to switch between symmetric and antisymmetric spectral wavefunctions and to modify the exchange statistics of the photons, which is measured via a Hong-Ou-Mandel interferometer. These results open the possibility to study the effect of exchange statistics (bosonic and fermionic) in various quantum simulation problems, and to implement communication and computation protocols exploiting antisymmetric high-dimensional quantum states.

Moreover, we have also proven that the counter-propagating source, thanks to its structure and design, can emit photon pairs entangled in a hybrid polariza-

tion/frequency degree of freedom. This particular quantum state exhibits simultaneous but not independent entanglement in these two degrees of freedom and when only one is measured the state becomes mixed. The presence of entanglement in this hybrid degree of freedom has been verified through a Hong-Ou-Mandel interferometer, showing also that the cavity effect, produced by the source facets reflectivity, complexifies the quantum state. For this reason we have developed an anti-reflection treatment that has allowed to reduce the facet reflectivity from $R \approx 27\%$ to $R \approx 10\%$ and to increase the quality of the generated hybrid polarization/frequency entangled state.

In the future, more complex high-dimensional frequency entangled states, such as time–frequency compass states, could be generated by a further engineering of the pump beam [240]. An other interesting perspective is the possibility of fabricating non-birefringent waveguide, by reducing the ridge width to ≈ 1.2 µm. This should allow to directly generate polarization Bell states whose frequency can be tuned by tilting the pump beam. In addition, the techniques employed in this thesis to shape the frequency correlations could be used on such a device to generate hyperentangled biphoton states in the frequency and polarization degrees of freedom, this time independently.

Finally, in the last part of the manuscript we have designed and developed a novel device in the aim of emitting spatially entangled photon pairs. The device consists of a lattice of parallel co-propagating SPDC sources evanescently coupled, in which the generated photons, undergoing cascaded quantum walks, are entangled in their spatial position in the lattice. The device fabrication processes have been optimized and a first optical characterization has been carried out. For the moment, the level of optical propagation losses has not allowed to obtain a fully working sample. Thus, we are currently working on the optimization of the fabrication processes.

The proposed and developed device will be eventually a versatile and compact source of spatially entangled photon pairs in the telecom range and operating at room temperature, which could be employed in quantum information protocols. In addition, it could also be used to perform quantum simulation tasks, studying phenomena such as Anderson localization of multipartite particles or topological protection in the quantum regime.

The devices studied in this thesis can be easily integrated in more complex photonic circuits. For instance, the counter-propagating source has already been integrated with a 50:50 beamsplitter [297] and investigation are currently undergoing to integrate the co-propagating source with a polarizing beamsplitter and an electro-optical modulator. These ongoing developments together with the possibility of electrically injecting the co-propagating source, already demonstrated in 2014 [60], will open the way to the realization of quantum tasks completely on-chip with a limited footprint, a key step towards real-world quantum technologies applications.

Software Credit

Numerical and analytic simulations have been performed employing Matlab and Wolfram Mathematica. Numerical simulations of guided modes and light propagation have been done using Lumerical (FDTD and MODE modules).

Plots have been realized in Matlab, while illustrations in Inkscape. I acknowledge Alexander Franzen for *ComponentLibrary*. I have used this free collection of optical components for drawing all the optical setups of this manuscript.

List of Publications and Conferences

Publications

- S. Francesconi, F. Baboux, A. Raymond, N. Fabre, G. Boucher, A. Lemaître, P. Milman, M. I. Amanti, and S. Ducci, "Engineering two-photon wavefunction and exchange statistics in a semiconductor chip", *Optica* 7, 316-322 (2020)

- S. Francesconi, et al., "Two-particle anyonic statistics with a photonic chip", in preparation

- S. Francesconi, et al., "Generation of hybrid polarization-frequency photon states", in preparation

Communications

- **S. Francesconi**, F. Baboux, A. Raymond, N. Fabre, A. Lemaître, P. Milman, M. Amanti and S. Ducci, (poster), "Engineering two-photon wavefunction and exchange statistics in a semiconductor chip", GDR Quantum Engineering, from Fundamental Aspects to Applications (IQFA), (Paris, France) , 13-15 November 2019

- **S. Francesconi**, F. Baboux, A. Raymond, N. Fabre, A. Lemaître, P. Milman, M. Amanti and S. Ducci, (oral), "Engineering two-photon wavefunction and exchange statistics in a semiconductor chip", Single Photon Workshop, (Milan, Italy), 21-25 October 2019

- **S. Francesconi**, F. Baboux, A. Raymond, N. Fabre, A. Lemaître, P. Milman, M. Amanti and S. Ducci, (poster), "Engineering two-photon wavefunction and exchange statistics in a semiconductor chip", SIRTEQ, (Palaiseau, france), 11 October 2019

- **S. Francesconi**, A. Raymond, F. Baboux, G. Boucher, J. Belhassen, A. Lemaître, M. Amanti and S. Ducci, (poster), "Controlling frequency correlations and biphoton statistics in a semiconductor photonic chip", Lindau Nobel Laureate Meeting, (Lindau, Germany) 1-6 July 2019

- **S. Francesconi**, A. Raymond, F. Baboux, G. Boucher, J. Belhassen, A. Lemaître, M. Amanti and S. Ducci, (poster), "Controlling frequency correlations and biphoton statistics in a semiconductor photonic chip", GDR Quantum Engineering, from Fundamental Aspects to Applications (IQFA), (Montpellier, France) 14-16 November 2018

- **S. Francesconi**, F. Baboux, G. Boucher, J. Belhassen, A. Lemaître, M. Amanti and S. Ducci "Quantum frequency engineering in semiconductor photonic chips", International School of Physics "Nano-scale Quantum Optics", (Varenna, Italy) 22-28 July 2018

- **S. Francesconi**, F. Baboux, G. Boucher, J. Belhassen, A. Lemaître, M. Amanti and S. Ducci (poster), "Ingénierie d'états quantiques en fréquence dans une puce photonique semi-conductrice", Congrès Société d'Optique Française, (Toulouse, France) 03-06 July 2018

- J. Belhassen, **S. Francesconi**, Q. Yao, A. Lemaitre, M. Amanti, S. Kolthammer, I. Walmsley, F. Baboux and S. Ducci (poster) ,"On-chip III-V monolithic integration of heralded single photons sources and beam splitters", GDR Quantum Engineering, from Fundamental Aspects to Applications (IQFA), (Nice, France) 29 Novembre – 1 December 2017

Bibliography

[1] J. S. Bell, "On the Einstein Podolsky Rosen paradox", Physics Physique Fizika **1**, 195–200 (1964) (cit. on pp. 1, 146).

[2] M. Giustina, M. A. M. Versteegh, S. Wengerowsky, J. Handsteiner, A. Hochrainer, K. Phelan, F. Steinlechner, J. Kofler, J.-Å. Larsson, C. Abellán, et al., "Significant-loophole-free test of bell's theorem with entangled photons", Phys. Rev. Lett. **115**, 250401 (2015) (cit. on p. 1).

[3] G. J. Dowling J. P.; Milburn, "Quantum technology: the second quantum revolution", Philosophical Transactions Mathematical Physical & Engineering Sciences **361** (2003) 10.1098/rsta.2003.1227 (cit. on p. 1).

[4] S.-K. Liao, W.-Y. Cai Wen-Qiand Liu, L. Zhang, Y. Li, J.-G. Ren, J. Yin, Q. Shen, Y. Cao, Z.-P. Li, F.-Z. Li, et al., "Satellite-to-ground quantum key distribution", Nature (2017) 10.1038/nature23655 (cit. on p. 1).

[5] S.-K. Liao, W.-Q. Cai, J. Handsteiner, B. Liu, J. Yin, L. Zhang, D. Rauch, M. Fink, J.-G. Ren, W.-Y. Liu, et al., "Satellite-relayed intercontinental quantum network", Phys. Rev. Lett. **120**, 030501 (2018) (cit. on p. 1).

[6] A. Acín, I. Bloch, H. Buhrman, T. Calarco, C. Eichler, J. Eisert, D. Esteve, N. Gisin, S. J. Glaser, F. Jelezko, et al., "The quantum technologies roadmap: A European community view", New Journal of Physics **20** (2018) 10.1088/1367-2630/aad1ea (cit. on p. 1).

[7] C. D. Bruzewicz, J. Chiaverini, R. McConnell, and J. M. Sage, "Trapped-ion quantum computing: progress and challenges", Applied Physics Reviews **6**, 021314 (2019) (cit. on p. 1).

[8] M. H. Devoret and R. J. Schoelkopf, "Superconducting circuits for quantum information: an outlook", Science **339**, 1169–1174 (2013) (cit. on p. 1).

[9] F. Arute, K. Arya, R. Babbush, D. Bacon, J. C. Bardin, R. Barends, R. Biswas, S. Boixo, F. G. S. L. Brandao, D. A. Buell, et al., "Quantum supremacy using a programmable superconducting processor", Nature **574** (2019) 10.1038/s41586-019-1666-5 (cit. on pp. 1, 2).

[10] I. Bloch, J. Dalibard, and S. Nascimbène, "Quantum simulations with ultracold quantum gases", Nature Physics **8**, 267–276 (2012) (cit. on p. 2).

[11] B. P. Lanyon, J. D. Whitfield, G. G. Gillett, M. E. Goggin, M. P. Almeida, I. Kassal, J. D. Biamonte, M. Mohseni, B. J. Powell, M. Barbieri, et al., "Towards quantum chemistry on a quantum computer", **2** (2010) 10.1038/nchem.483 (cit. on p. 2).

[12]A. Aspuru-guzik and P. Walther, "Photonic quantum simulators", Nature Physics **8**, 285–291 (2012) (cit. on p. 2).

[13]S. A. Wilkinson and M. J. Hartmann, "Superconducting quantum many-body circuits for quantum simulation and computing", Applied Physics Letters **116**, 230501 (2020) (cit. on p. 2).

[14]C. L. Degen, F. Reinhard, and P. Cappellaro, "Quantum sensing", Rev. Mod. Phys. **89**, 035002 (2017) (cit. on p. 2).

[15]A. Aspect, P. Grangier, and G. Roger, "Experimental tests of realistic local theories via bell's theorem", Phys. Rev. Lett. **47**, 460–463 (1981) (cit. on p. 2).

[16]E. Knill, R. Laflamme, and G. J. Milburn, "A scheme for efficient quantum computation with linear optics", Nature **409**, 46–52 (2001) (cit. on p. 2).

[17]M. A. Nielsen, "Optical quantum computation using cluster states", Phys. Rev. Lett. **93**, 040503 (2004) (cit. on p. 2).

[18]A. Peruzzo, M. Lobino, J. C. Matthews, N. Matsuda, A. Politi, K. Poulios, X. Q. Zhou, Y. Lahini, N. Ismail, K. Wörhoff, et al., "Quantum walks of correlated photons", Science **329**, 1500–1503 (2010) (cit. on pp. 2, 8, 192–194).

[19]A. Peruzzo, J. McClean, P. Shadbolt, M.-H. Yung, X.-Q. Zhou, P. J. Love, A. Aspuru-Guzik, and J. L. O'Brien, "A variational eigenvalue solver on a photonic quantum processor", Nature Communications **5**, 4213 (2014) (cit. on p. 2).

[20]A. Politi, J. C. Matthews, and J. L. O'Brien, "Shor's quantum factoring algorithm on a photonic chip", Science **325**, 1221 (2009) (cit. on pp. 2, 191).

[21]J. C. Adcock, C. Vigliar, R. Santagati, J. W. Silverstone, and M. G. Thompson, "Programmable four-photon graph states on a silicon chip", Nature Communications **10**, 3528 (cit. on p. 2).

[22]J. Wang, D. Bonneau, M. Villa, J. W. Silverstone, R. Santagati, S. Miki, T. Yamashita, M. Fujiwara, M. Sasaki, H. Terai, et al., "Chip-to-chip quantum photonic interconnect by path-polarization interconversion", Optica **3**, 407–413 (2016) (cit. on p. 2).

[23]P. Sibson, C. Erven, M. Godfrey, S. Miki, T. Yamashita, M. Fujiwara, M. Sasaki, H. Terai, M. G. Tanner, C. M. Natarajan, et al., "Chip-based quantum key distribution", Nature Communications **8** (2017) `10.1038/ncomms13984` (cit. on p. 2).

[24]A. Politi, M. J. Cryan, J. G. Rarity, S. Yu, and J. L. O'Brien, "Silica-on-silicon waveguide quantum circuits", Science **320**, 646–649 (2008) (cit. on pp. 2, 4).

[25]C. P. Dietrich, A. Fiore, M. G. Thompson, M. Kamp, and S. Höfling, "Gaas integrated quantum photonics: towards compact and multi-functional quantum photonic integrated circuits", Laser and Photonics Reviews **10**, 870–894 (2016) (cit. on pp. 2, 4).

[26]C. Autebert, G. Boucher, F. Boitier, A. Eckstein, I. Favero, G. Leo, and S. Ducci, "Photon pair sources in algaas: from electrical injection to quantum state engineering", Journal of Modern Optics **62**, 1739–1745 (2015) (cit. on p. 2).

[27]W. H. P. Pernice, C. Schuck, O. Minaeva, M. Li, G. N. Goltsman, A. V. Sergienko, and H. X. Tang, "High-speed and high-efficiency travelling wave single-photon detectors embedded in nanophotonic circuits", Nature Communications **3**, 1325 (2012) (cit. on p. 2).

[28]C. Schuck, X. Guo, L. Fan, X. Ma, M. Poot, and H. X. Tang, "Quantum interference in heterogeneous superconducting-photonic circuits on a silicon chip", Nature Communications **7**, 10352 (2016) (cit. on p. 2).

[29]G. Masada, K. Miyata, A. Politi, T. Hashimoto, J. L. O'Brien, and A. Furusawa, "Continuous-variable entanglement on a chip", Nature Photonics **9**, 316–319 (2015) (cit. on p. 3).

[30]F. Flamini, N. Spagnolo, and F. Sciarrino, "Photonic quantum information processing: a review", Reports on Progress in Physics **82**, 016001 (2018) (cit. on pp. 3, 6).

[31]A. Dousse, J. Suffczyński, A. Beveratos, O. Krebs, A. Lemaître, I. Sagnes, J. Bloch, P. Voisin, and P. Senellart, "Ultrabright source of entangled photon pairs", Nature **466**, 217–220 (2010) (cit. on pp. 3, 147).

[32]M. Müller, S. Bounouar, K. D. Jöns, M. Glässl, and P. Michler, "On-demand generation of indistinguishable polarization-entangled photon pairs", Nature Photonics **8**, 224–228 (2014) (cit. on pp. 3, 147).

[33]D. Huber, M. Reindl, Y. Huo, H. Huang, J. S. Wildmann, O. G. Schmidt, A. Rastelli, and R. Trotta, "Highly indistinguishable and strongly entangled photons from symmetric GaAs quantum dots", Nature Communications **8**, 1–7 (2017) (cit. on pp. 3, 147).

[34]J. Liu, R. Su, Y. Wei, B. Yao, S. F. C. da Silva, Y. Yu, J. Iles-Smith, K. Srinivasan, A. Rastelli, J. Li, et al., "A solid-state source of strongly entangled photon pairs with high brightness and indistinguishability", Nature Nanotechnology **14**, 586–593 (2019) (cit. on p. 3).

[35]D. Huber, M. Reindl, S. F. Covre Da Silva, C. Schimpf, J. Martín-Sánchez, H. Huang, G. Piredda, J. Edlinger, A. Rastelli, and R. Trotta, "Strain-Tunable GaAs Quantum Dot: A Nearly Dephasing-Free Source of Entangled Photon Pairs on Demand", Physical Review Letters **121**, 33902 (2018) (cit. on p. 3).

[36]N. Somaschi, V. Giesz, L. De Santis, J. C. Loredo, M. P. Almeida, G. Hornecker, S. L. Portalupi, T. Grange, C. Antón, J. Demory, et al., "Near-optimal single-photon sources in the solid state", Nature Photonics **10**, 340–345 (2016) (cit. on pp. 3, 5).

[37]H. Wang, Y.-M. He, T.-H. Chung, H. Hu, Y. Yu, S. Chen, X. Ding, M.-C. Chen, J. Qin, X. Yang, et al., "Towards optimal single-photon sources from polarized microcavities", Nature Photonics **13**, 770–775 (2019) (cit. on p. 3).

[38]L. Caspani, C. Xiong, B. J. Eggleton, D. Bajoni, M. Liscidini, M. Galli, R. Morandotti, and D. J. Moss, "Integrated sources of photon quantum states based on nonlinear optics", Light: Science and Applications **6**, e17100–12 (2017) (cit. on p. 4).

[39]A. Orieux, M. A. Versteegh, K. D. Jöns, and S. Ducci, "Semiconductor devices for entangled photon pair generation: A review", Reports on Progress in Physics **80**, 076001 (2017) (cit. on p. 4).

[40]O. Alibart, V. D'Auria, M. D. Micheli, F. Doutre, F. Kaiser, L. Labonté, T. Lunghi, É. Picholle, and S. Tanzilli, "Quantum photonics at telecom wavelengths based on lithium niobate waveguides", Journal of Optics **18**, 104001 (2016) (cit. on p. 4).

[41]V. Ansari, J. M. Donohue, M. Allgaier, L. Sansoni, B. Brecht, J. Roslund, N. Treps, G. Harder, and C. Silberhorn, "Tomography and Purification of the Temporal-Mode Structure of Quantum Light", Physical Review Letters **120**, 213601 (2018) (cit. on pp. 4, 8, 106, 124).

[42]M. L. Fanto, C. C. Tison, G. A. Howland, S. F. Preble, P. M. Alsing, and A. M. Smith, "A bright PPKTP waveguide source of polarization entangled photons", in Quantum information and computation xiii, Vol. 9500, edited by E. Donkor, A. R. Pirich, and M. Hayduk (International Society for Optics and Photonics, 2015), pp. 240–251 (cit. on p. 4).

[43]J. Wang, S. Paesani, Y. Ding, R. Santagati, P. Skrzypczyk, A. Salavrakos, J. Tura, R. Augusiak, L. Mančinska, D. Bacco, et al., "Multidimensional quantum entanglement with large-scale integrated optics", Science **360**, 285–291 (2018) (cit. on pp. 4, 7, 8).

[44]X. Zhang, B. A. Bell, A. Mahendra, C. Xiong, P. H. W. Leong, and B. J. Eggleton, "Integrated silicon nitride time-bin entanglement circuits", Opt. Lett. **43**, 3469–3472 (2018) (cit. on p. 4).

[45]Y. Xuan, Y. Liu, L. T. Varghese, A. J. Metcalf, X. Xue, P.-H. Wang, K. Han, J. A. Jaramillo-Villegas, A. A. Noman, C. Wang, et al., "High-q silicon nitride microresonators exhibiting low-power frequency comb initiation", Optica **3**, 1171–1180 (2016) (cit. on p. 4).

[46]J. B. Spring, P. L. Mennea, B. J. Metcalf, P. C. Humphreys, J. C. Gates, H. L. Rogers, C. Söller, B. J. Smith, W. S. Kolthammer, P. G. R. Smith, et al., "Chip-based array of near-identical, pure, heralded single-photon sources", Optica **4**, 90–96 (2017) (cit. on p. 4).

[47]S. Bogdanov, M. Y. Shalaginov, A. Boltasseva, and V. M. Shalaev, "Material platforms for integrated quantum photonics", Opt. Mater. Express **7**, 111–132 (2017) (cit. on p. 4).

[48]J. Carolan, C. Harrold, C. Sparrow, E. Martín-López, N. J. Russell, J. W. Silverstone, P. J. Shadbolt, N. Matsuda, M. Oguma, M. Itoh, et al., "Universal linear optics", Science **349**, 711–716 (2015) (cit. on p. 4).

[49]J. F. Bauters, M. J. R. Heck, D. D. John, J. S. Barton, C. M. Bruinink, A. Leinse, R. G. Heideman, D. J. Blumenthal, and J. E. Bowers, "Planar waveguides with less than 0.1 db/m propagation loss fabricated with wafer bonding", Opt. Express **19**, 24090–24101 (2011) (cit. on p. 4).

[50]D. Llewellyn, Y. Ding, I. I. Faruque, S. Paesani, D. Bacco, R. Santagati, Y.-J. Qian, Y. Li, Y.-F. Xiao, M. Huber, et al., "Chip-to-chip quantum teleportation and multi-photon entanglement in silicon", Nature Physics **16**, 148–153 (2020) (cit. on p. 4).

[51]X. Qiang, X. Zhou, J. Wang, C. M. Wilkes, T. Loke, S. O'Gara, L. Kling, G. D. Marshall, R. Santagati, T. C. Ralph, et al., "Large-scale silicon quantum photonics implementing arbitrary two-qubit processing", Nature Photonics **12**, 534–539 (2018) (cit. on pp. 4, 193).

[52]J. F. Bauters, M. J. R. Heck, D. John, D. Dai, M.-C. Tien, J. S. Barton, A. Leinse, R. G. Heideman, D. J. Blumenthal, and J. E. Bowers, "Ultra-low-loss high-aspect-ratio si3n4 waveguides", Opt. Express **19**, 3163–3174 (2011) (cit. on p. 4).

[53]C. Taballione, T. A. Wolterink, J. Lugani, A. Eckstein, B. A. Bell, R. Grootjans, I. Visscher, J. J. Renema, D. Geskus, C. G. Roeloffzen, et al., "8×8 Programmable Quantum Photonic Processor Based on Silicon Nitride Waveguides", Optics InfoBase Conference Papers **Part F114-FIO 2018**, 22–24 (2018) (cit. on p. 4).

[54]D. M. Szymanski, B. D. Jones, M. S. Skolnick, A. M. Fox, D. O'Brien, T. F. Krauss, and J. S. Roberts, "Ultrafast all-optical switching in algaas photonic crystal waveguide interferometers", Applied Physics Letters **95**, 141108 (2009) (cit. on pp. 5, 194).

[55]J. Wang, A. Santamato, P. Jiang, D. Bonneau, E. Engin, J. W. Silverstone, M. Lermer, J. Beetz, M. Kamp, S. Höfling, et al., "Gallium arsenide (GaAs) quantum photonic waveguide circuits", Optics Communications **327**, 49–55 (2014) (cit. on p. 5).

[56]S. Deshpande, J. Heo, A. Das, and P. Bhattacharya, "Electrically driven polarized single-photon emission from an ingan quantum dot in a gan nanowire", Nature Communications **4**, 1675 (2013) (cit. on p. 5).

[57]A. Orieux, A. Eckstein, A. Lemaitre, P. Filloux, I. Favero, G. Leo, T. Coudreau, A. Keller, P. Milman, and S. Ducci, "Direct bell states generation on a iii-v semiconductor chip at room temperature", Phys. Rev. Lett. **110**, 160502 (2013) (cit. on pp. 5, 36, 147).

[58]R. T. Horn, P. Kolenderski, D. Kang, P. Abolghasem, C. Scarcella, A. D. Frera, A. Tosi, L. G. Helt, S. V. Zhukovsky, J. E. Sipe, et al., "Inherent polarization entanglement generated from a monolithic semiconductor chip", Scientific Reports **3**, 1–5 (2013) (cit. on pp. 5, 147).

[59]C. Autebert, N. Bruno, A. Martin, A. Lemaitre, C. G. Carbonell, I. Favero, G. Leo, H. Zbinden, and S. Ducci, "Integrated algaas source of highly indistinguishable and energy-time entangled photons", Optica **3**, 143–146 (2016) (cit. on pp. 5, 29, 37, 163, 203).

[60]F. Boitier, A. Orieux, C. Autebert, A. Lemaître, E. Galopin, C. Manquest, C. Sirtori, I. Favero, G. Leo, and S. Ducci, "Electrically injected photon-pair source at room temperature", Physical Review Letters **112**, 1–5 (2014) (cit. on pp. 5, 37, 194, 218).

[61]J. P. Sprengers, A. Gaggero, D. Sahin, S. Jahanmirinejad, G. Frucci, F. Mattioli, R. Leoni, J. Beetz, M. Lermer, M. Kamp, et al., "Waveguide superconducting single-photon detectors for integrated quantum photonic circuits", Applied Physics Letters **99**, 181110 (2011) (cit. on p. 5).

[62]M. Schwartz, E. Schmidt, U. Rengstl, F. Hornung, S. Hepp, S. L. Portalupi, K. Llin, M. Jetter, M. Siegel, and P. Michler, "Fully On-Chip Single-Photon Hanbury-Brown and Twiss Experiment on a Monolithic Semiconductor-Superconductor Platform", Nano Letters **18**, 6892–6897 (2018) (cit. on p. 5).

[63]S. Tanzilli, H. De Riedmatten, H. Tittel, H. Zbinden, P. Baldi, M. De Micheli, D. B. Ostrowsky, and N. Gisin, "Highly efficient photon-pair source using periodically poled lithium niobate waveguide", Electronics Letters **37**, 26–28 (2001) (cit. on pp. 5, 141).

[64]S. Tanzilli, A. Martin, F. Kaiser, M. P. de Micheli, O. Alibart, and D. B. Ostrowsky, "On the genesis and evolution of integrated quantum optics", Laser and Photonics Reviews **6**, 115–143 (2012) (cit. on p. 5).

[65]F. Graffitti, P. Barrow, A. Pickston, A. M. Brańczyk, and A. Fedrizzi, "Direct Generation of Tailored Pulse-Mode Entanglement", Physical Review Letters **124** (2020) 10.1103/PhysRevLett.124.053603 (cit. on pp. 5, 106, 124, 141).

[66]F. Mondain, T. Lunghi, A. Zavatta, E. Gouzien, F. Doutre, M. D. Micheli, S. Tanzilli, and V. D'Auria, "Chip-based squeezing at a telecom wavelength", Photon. Res. **7**, A36–A39 (2019) (cit. on p. 5).

[67]R. Kruse, L. Sansoni, S. Brauner, R. Ricken, C. S. Hamilton, I. Jex, and C. Silberhorn, "Dual-path source engineering in integrated quantum optics", Phys. Rev. A **92**, 053841 (2015) (cit. on pp. 5, 7).

[68]F. Setzpfandt, A. S. Solntsev, J. Titchener, C. W. Wu, C. Xiong, R. Schiek, T. Pertsch, D. N. Neshev, and A. A. Sukhorukov, "Tunable generation of entangled photons in a nonlinear directional coupler", Laser and Photonics Reviews **10**, 131–136 (2016) (cit. on p. 5).

[69]G. Poberaj, H. Hu, W. Sohler, and P. Günter, "Lithium niobate on insulator (lnoi) for micro-photonic devices", Laser & Photonics Reviews **6**, 488–503 (2012) (cit. on p. 5).

[70]C. Wang, M. J. Burek, Z. Lin, H. A. Atikian, V. Venkataraman, I.-C. Huang, P. Stark, and M. Lončar, "Integrated high quality factor lithium niobate microdisk resonators", Opt. Express **22**, 30924–30933 (2014) (cit. on p. 5).

[71]A. Guarino, G. Poberaj, D. Rezzonico, R. Degl'Innocenti, and P. Günter, "Electro–optically tunable microring resonators in lithium niobate", Nature Photonics **1**, 407–410 (2007) (cit. on p. 5).

[72]S. Diziain, R. Geiss, M. Zilk, F. Schrempel, E.-B. Kley, A. Tünnermann, and T. Pertsch, "Second harmonic generation in free-standing lithium niobate photonic crystal l3 cavity", Applied Physics Letters **103**, 051117 (2013) (cit. on p. 5).

[73]R. Brouri, A. Beveratos, J.-P. Poizat, and P. Grangier, "Photon antibunching in the fluorescence of individual color centers in diamond", Opt. Lett. **25**, 1294–1296 (2000) (cit. on p. 5).

[74]P. C. Maurer, G. Kucsko, C. Latta, L. Jiang, N. Y. Yao, S. D. Bennett, F. Pastawski, D. Hunger, N. Chisholm, M. Markham, et al., "Room-temperature quantum bit memory exceeding one second", Science **336**, 1283–1286 (2012) (cit. on p. 5).

[75]L. Rondin, J.-P. Tetienne, T. Hingant, J.-F. Roch, P. Maletinsky, and V. Jacques, "Magnetometry with nitrogen-vacancy defects in diamond", Reports on Progress in Physics **77**, 056503 (2014) (cit. on p. 5).

[76]J. Riedrich-Möller, L. Kipfstuhl, C. Hepp, E. Neu, C. Pauly, F. Mücklich, A. Baur, M. Wandt, S. Wolff, M. Fischer, et al., "One- and two-dimensional photonic crystal microcavities in single crystal diamond", Nature Nanotechnology **7**, 69–74 (2012) (cit. on p. 5).

[77]B. Sotillo, V. Bharadwaj, J. P. Hadden, M. Sakakura, A. Chiappini, T. T. Fernandez, S. Longhi, O. Jedrkiewicz, Y. Shimotsuma, L. Criante, et al., "Diamond photonics platform enabled by femtosecond laser writing", Scientific Reports **6**, 35566 (2016) (cit. on pp. 5, 6).

[78]G. Corrielli, S. Atzeni, S. Piacentini, I. Pitsios, A. Crespi, and R. Osellame, "Symmetric polarization-insensitive directional couplers fabricated by femtosecond laser writing", Opt. Express **26**, 15101–15109 (2018) (cit. on p. 6).

[79]J. Thomas, M. Heinrich, J. Burghoff, S. Nolte, A. Ancona, and A. Tünnermann, "Femtosecond laser-written quasi-phase-matched waveguides in lithium niobate", Applied Physics Letters **91**, 151108 (2007) (cit. on p. 6).

[80]R. Osellame, M. Lobino, N. Chiodo, M. Marangoni, G. Cerullo, R. Ramponi, H. T. Bookey, R. R. Thomson, N. D. Psaila, and A. K. Kar, "Femtosecond laser writing of waveguides in periodically poled lithium niobate preserving the nonlinear coefficient", Applied Physics Letters **90**, 241107 (2007) (cit. on p. 6).

[81]M. A. Ciampini, A. Orieux, S. Paesani, F. Sciarrino, G. Corrielli, A. Crespi, R. Ramponi, R. Osellame, and P. Mataloni, "Path-polarization hyperentangled and cluster states of photons on a chip", Light: Science & Applications **5**, e16064–e16064 (2016) (cit. on p. 6).

[82]A. Crespi, R. Osellame, R. Ramponi, V. Giovannetti, R. Fazio, L. Sansoni, F. De Nicola, F. Sciarrino, and P. Mataloni, "Anderson localization of entangled photons in an integrated quantum walk", Nature Photonics **7**, 322–328 (2013) (cit. on pp. 6, 7, 192, 193).

[83]A. W. Elshaari, W. Pernice, K. Srinivasan, O. Benson, and V. Zwiller, "Hybrid integrated quantum photonic circuits", Nature Photonics **14**, 285–298 (2020) (cit. on p. 6).

[84]S. L. Braunstein and P. van Loock, "Quantum information with continuous variables", Rev. Mod. Phys. **77**, 513–577 (2005) (cit. on p. 6).

[85]A. Aspect, J. Dalibard, and G. Roger, "Experimental test of bell's inequalities using time-varying analyzers", Phys. Rev. Lett. **49**, 1804–1807 (1982) (cit. on pp. 6, 146).

[86]J. C. Matthews, K. Poulios, J. D. Meinecke, A. Politi, A. Peruzzo, N. Ismail, K. Wörhoff, M. G. Thompson, and J. L. O'Brien, "Observing fermionic statistics with photons in arbitrary processes", Scientific Reports **3** (2013) 10.1038/srep01539 (cit. on pp. 6, 123, 142, 143).

[87]P. Walther, K. J. Resch, T. Rudolph, E. Schenck, H. Weinfurter, V. Vedral, M. Aspelmeyer, and A. Zeilinger, "Experimental one-way quantum computing", Nature **434**, 169–176 (2005) (cit. on p. 6).

[88]C. Ma, W. D. Sacher, Z. Tang, J. C. Mikkelsen, Y. Yang, F. Xu, T. Thiessen, H.-K. Lo, and J. K. S. Poon, "Silicon photonic transmitter for polarization-encoded quantum key distribution", Optica **3**, 1274–1278 (2016) (cit. on p. 6).

[89]M. Erhard, R. Fickler, M. Krenn, and A. Zeilinger, "Twisted photons: New quantum perspectives in high dimensions", Light: Science and Applications **7**, 17111–17146 (2018) (cit. on p. 6).

[90]M. Krenn, R. Fickler, M. Fink, J. Handsteiner, M. Malik, T. Scheidl, R. Ursin, and A. Zeilinger, "Communication with spatially modulated light through turbulent air across vienna", New Journal of Physics **16**, 113028 (2014) (cit. on p. 6).

[91]M. Mirhosseini, O. S. Magaña-Loaiza, M. N. O'Sullivan, B. Rodenburg, M. Malik, M. P. Lavery, M. J. Padgett, D. J. Gauthier, and R. W. Boyd, "High-dimensional quantum cryptography with twisted light", New Journal of Physics **17**, 1–12 (2015) (cit. on p. 6).

[92]D. Cozzolino, D. Bacco, B. Da Lio, K. Ingerslev, Y. Ding, K. Dalgaard, P. Kristensen, M. Galili, K. Rottwitt, S. Ramachandran, et al., "Orbital Angular Momentum States Enabling Fiber-based High-dimensional Quantum Communication", Physical Review Applied **11**, 1 (2019) (cit. on p. 6).

[93]A. C. Dada, J. Leach, G. S. Buller, M. J. Padgett, and E. Andersson, "Experimental high-dimensional two-photon entanglement and violations of generalized Bell inequalities", Nature Physics **7**, 677–680 (2011) (cit. on pp. 7, 8).

[94]J. W. Silverstone, D. Bonneau, K. Ohira, N. Suzuki, H. Yoshida, N. Iizuka, M. Ezaki, C. M. Natarajan, M. G. Tanner, R. H. Hadfield, et al., "On-chip quantum interference between silicon photon-pair sources", Nature Photonics **8**, 104–108 (2014) (cit. on pp. 7, 148).

[95]C. Sparrow, E. Martín-López, N. Maraviglia, A. Neville, C. Harrold, J. Carolan, Y. N. Joglekar, T. Hashimoto, N. Matsuda, J. L. O'Brien, et al., "Simulating the vibrational quantum dynamics of molecules using photonics", Nature **557**, 660–667 (2018) (cit. on p. 7).

[96]A. Blanco-Redondo, B. Bell, D. Oren, B. J. Eggleton, and M. Segev, "Topological protection of biphoton states", Science **362**, 568–571 (2018) (cit. on pp. 7, 193, 203).

[97]J. L. Tambasco, G. Corrielli, R. J. Chapman, A. Crespi, O. Zilberberg, R. Osellame, and A. Peruzzo, "Quantum interference of topological states of light", Science Advances **4**, eaat3187 (2018) (cit. on p. 7).

[98]I. Marcikic, H. de Riedmatten, W. Tittel, H. Zbinden, and N. Gisin, "Long-distance teleportation of qubits at telecommunication wavelengths", Nature **421**, 509–513 (2003) (cit. on p. 7).

[99]O. Landry, J. A. W. van Houwelingen, A. Beveratos, H. Zbinden, and N. Gisin, "Quantum teleportation over the swisscom telecommunication network", J. Opt. Soc. Am. B **24**, 398–403 (2007) (cit. on p. 7).

[100]A. Boaron, G. Boso, D. Rusca, C. Vulliez, C. Autebert, M. Caloz, M. Perrenoud, G. Gras, F. Bussières, M.-J. Li, et al., "Secure quantum key distribution over 421 km of optical fiber", Phys. Rev. Lett. **121**, 190502 (2018) (cit. on p. 7).

[101]N. T. Islam, C. C. W. Lim, C. Cahall, B. Qi, J. Kim, and D. J. Gauthier, "Scalable high-rate, high-dimensional time-bin encoding quantum key distribution", Quantum Science and Technology **4**, 035008 (2019) (cit. on p. 7).

[102]C. Xiong, X. Zhang, A. Mahendra, J. He, D.-Y. Choi, C. J. Chae, D. Marpaung, A. Leinse, R. G. Heideman, M. Hoekman, et al., "Compact and reconfigurable silicon nitride time-bin entanglement circuit", Optica **2**, 724 (2015) (cit. on p. 7).

[103]L. Olislager, E. Woodhead, K. Phan Huy, J. M. Merolla, P. Emplit, and S. Massar, "Creating and manipulating entangled optical qubits in the frequency domain", Physical Review A - Atomic, Molecular, and Optical Physics **89**, 1–8 (2014) (cit. on p. 7).

[104]M. Kues, C. Reimer, P. Roztocki, L. R. Cortés, S. Sciara, B. Wetzel, Y. Zhang, A. Cino, S. T. Chu, B. E. Little, et al., "On-chip generation of high-dimensional entangled quantum states and their coherent control", Nature **546**, 622–626 (2017) (cit. on pp. 7, 8, 104).

[105]J. Cussey, F. Patois, N. Pelloquin, and J.-M. Merolla, "High frequency spectral domain qkd architecture with dispersion management for wdm network", in Optical fiber communication conference/national fiber optic engineers conference (2008), OWJ3 (cit. on p. 7).

[106]N. J. Cerf, M. Bourennane, A. Karlsson, and N. Gisin, "Security of quantum key distribution using d-level systems", Phys. Rev. Lett. **88**, 127902 (2002) (cit. on p. 7).

[107]G. M. Nikolopoulos, K. S. Ranade, and G. Alber, "Error tolerance of two-basis quantum-key-distribution protocols using qudits and two-way classical communication", Physical Review A - Atomic, Molecular, and Optical Physics **73**, 1–9 (2006) (cit. on pp. 7, 147).

[108]B. P. Lanyon, M. Barbieri, M. P. Almeida, T. Jennewein, T. C. Ralph, K. J. Resch, G. J. Pryde, J. L. O'Brien, A. Gilchrist, and A. G. White, "Simplifying quantum logic using higher-dimensional Hilbert spaces", Nature Physics **5**, 134–140 (2009) (cit. on p. 7).

[109]D. Collins, S. Popescu, D. Collins, S. Popescu, N. Gisin, N. Linden, and S. Massar, "Bell Inequalities for Arbitrarily High-Dimensional Systems", Physical Review Letters **88**, 4 (2002) (cit. on p. 7).

[110]A. Crespi, R. Osellame, R. Ramponi, D. J. Brod, E. F. Galvão, N. Spagnolo, C. Vitelli, E. Maiorino, P. Mataloni, and F. Sciarrino, "Integrated multimode interferometers with arbitrary designs for photonic boson sampling", Nature Photonics **7**, 545–549 (2013) (cit. on pp. 7, 8, 123, 142, 143, 192).

[111]A. F. Abouraddy, T. Yarnall, B. E. Saleh, and M. C. Teich, "Violation of Bell's inequality with continuous spatial variables", Physical Review A - Atomic, Molecular, and Optical Physics **75** (2007) 10.1103/PhysRevA.75.052114 (cit. on p. 8).

[112]D. S. Tasca, R. M. Gomes, F. Toscano, P. H. Souto Ribeiro, and S. P. Walborn, "Continuous-variable quantum computation with spatial degrees of freedom of photons", Physical Review A - Atomic, Molecular, and Optical Physics **83**, 52325 (2011) (cit. on p. 8).

[113]N. Fabre, A. Keller, and P. Milman, "Wigner distribution on a double-cylinder phase space for studying quantum error-correction protocols", Phys. Rev. A **102**, 022411 (2020) (cit. on p. 8).

[114]S. Lloyd and S. L. Braunstein, "Quantum computation over continuous variables", Physical Review Letters **82**, 1784–1787 (1999) (cit. on p. 8).

[115]V. Giovannetti, S. Lloyd, and L. Maccone, "Positioning and clock synchronization through entanglement", Physical Review A - Atomic, Molecular, and Optical Physics **65**, 9 (2002) (cit. on pp. 8, 104, 114).

[116]Y. Zhang, M. Agnew, T. Roger, F. S. Roux, T. Konrad, D. Faccio, J. Leach, and A. Forbes, "Simultaneous entanglement swapping of multiple orbital angular momentum states of light", Nature Communications **8** (2017) 10.1038/s41467-017-00706-1 (cit. on p. 8).

[117]T. Lutz, P. Kolenderski, and T. Jennewein, "Demonstration of spectral correlation control in a source of polarization-entangled photon pairs at telecom wavelength", Optics Letters **39**, 1481 (2014) (cit. on pp. 8, 104, 114).

[118]G. Brida, M. Genovese, and I. R. Berchera, "Experimental realization of sub-shot-noise quantum imaging", Nature Photonics **4**, 227–230 (2010) (cit. on p. 8).

[119]T. Ono, R. Okamoto, and S. Takeuchi, "An entanglement-enhanced microscope", Nature Communications **4**, 1–7 (2013) (cit. on p. 8).

[120]S. P. Walborn, A. N. de Oliveira, S. Pádua, and C. H. Monken, "Multimode hong-ou-mandel interference", Phys. Rev. Lett. **90**, 143601 (2003) (cit. on pp. 8, 123, 132).

[121]A. S. Solntsev and A. A. Sukhorukov, "Path-entangled photon sources on nonlinear chips", Reviews in Physics **2**, 19–31 (2017) (cit. on p. 8).

[122]Z. Xie, T. Zhong, S. Shrestha, X. A. Xu, J. Liang, Y. X. Gong, J. C. Bienfang, A. Restelli, J. H. Shapiro, F. N. Wong, et al., "Harnessing high-dimensional hyperentanglement through a biphoton frequency comb", Nature Photonics **9**, 536–542 (2015) (cit. on pp. 8, 147).

[123]T. Zhong, H. Zhou, R. D. Horansky, C. Lee, V. B. Verma, A. E. Lita, A. Restelli, J. C. Bienfang, R. P. Mirin, T. Gerrits, et al., "Photon-efficient quantum key distribution using time-energy entanglement with high-dimensional encoding", New Journal of Physics **17** (2015) 10.1088/1367-2630/17/2/022002 (cit. on p. 8).

[124]C. Schaeff, R. Polster, R. Lapkiewicz, R. Fickler, S. Ramelow, and A. Zeilinger, "Scalable fiber integrated source for higher-dimensional path-entangled photonic qunits", Opt. Express **20**, 16145–16153 (2012) (cit. on p. 8).

[125]P. Imany, J. A. Jaramillo-Villegas, O. D. Odele, K. Han, D. E. Leaird, J. M. Lukens, P. Lougovski, M. Qi, and A. M. Weiner, "50-GHz-spaced comb of high-dimensional frequency-bin entangled photons from an on-chip silicon nitride microresonator", Optics Express **26**, 1825 (2018) (cit. on p. 8).

[126]G. Maltese, M. I. Amanti, F. Appas, G. Sinnl, A. Lemaître, P. Milman, F. Baboux, and S. Ducci, "Generation and symmetry control of quantum frequency combs", npj Quantum Information **6** (2020) 10.1038/s41534-019-0237-9 (cit. on pp. 8, 37).

[127]R. W. Boyd, *Nonlinear optics*, 3rd (Academic Press, Inc., USA, 2008) (cit. on pp. 13, 17, 18, 24).

[128]T. H. Maiman, "Stimulated optical radiation in ruby", Nature **187**, 493–494 (1960) (cit. on p. 14).

[129]P. A. Franken, A. E. Hill, C. W. Peters, and G. Weinreich, "Generation of optical harmonics", Phys. Rev. Lett. **7**, 118–119 (1961) (cit. on p. 14).

[130]J. Ota, W. Narita, I. Ohta, T. Matsushita, and T. Kondo, "Fabrication of periodically-inverted algaas waveguides for quasi-phase-matched wavelength conversion at 1.55 um", Japanese Journal of Applied Physics **48**, 04C110 (2009) (cit. on p. 20).

[131]A. Yariv and P. Yeh, *Photonics: optical electronics in modern communications (the oxford series in electrical and computer engineering)* (Oxford University Press, Inc., USA, 2006) (cit. on p. 21).

[132]J. Chilwell and I. Hodgkinson, "Thin-films field-transfer matrix theory of planar multilayer waveguides and reflection from prism-loaded waveguides", **1**, 742 (1984) (cit. on pp. 22, 95).

[133]A. Orieux, "Sources semiconductrices d'états à deux photons à tempéraure ambiante", PhD Thesis (Université Paris Diderot, 2012) (cit. on pp. 23, 37).

[134]X. Caillet, "Une microcavité semicondutrice source de photons jumeaux contrapropageants à tempéraure ambiante", PhD Thesis (Université Paris Diderot, 2009) (cit. on pp. 23, 30, 42, 44, 54, 134).

[135]M. A. Afromowitz, "Refractive index of $Ga_{1-x}Al_xAs$", Solid State Communications **15**, 59–63 (1974) (cit. on pp. 24, 25).

[136]S. Gehrsitz, F. K. Reinhart, C. Gourgon, N. Herres, A. Vonlanthen, and H. Sigg, "The refractive index of $Al_xGa_{1-x}As$ below the band gap: Accurate determination and empirical modeling", Journal of Applied Physics **87**, 7825–7837 (2000) (cit. on pp. 26, 31).

[137]M. Ohashi, T. Kondo, and R. Ito, "Determination of quadratic nonlinear optical coefficient of $Al_xGa_{1-x}As$ system by the method of reflected second harmonics", J. Appl. Phys. **74**, 596–601 (1993) (cit. on p. 26).

[138]I. Shoji, T. Kondo, A. Kitamoto, M. Shirane, and R. Ito, "Absolute scale of second-order nonlinear-optical coefficients", **14**, 2268 (1997) (cit. on p. 26).

[139]J. E. Midwinter and J. Warner, "The effects of phase matching method and of uniaxial crystal symmetry on the polar distribution of second-order non-linear optical polarization", British Journal of Applied Physics **16**, 1135–1142 (1965) (cit. on p. 27).

[140]J. M. Dallesasse, N. Holonyak, A. R. Sugg, T. A. Richard, and N. El-Zein, "Hydrolyzation oxidation of algaas-alas-gaas quantum well heterostructures and superlattices", Applied Physics Letters **57**, 2844–2846 (1990) (cit. on p. 27).

[141]A. Fiore, S. Janz, L. Delobel, P. van der Meer, P. Bravetti, V. Berger, E. Rosencher, and J. Nagle, "Second-harmonic generation at λ=1.6 µm in algaas/al2o3 waveguides using birefringence phase matching", Applied Physics Letters **72**, 2942–2944 (1998) (cit. on p. 27).

[142]J. A. Armstrong, N. Bloembergen, J. Ducuing, and P. S. Pershan, "Interactions between light waves in a nonlinear dielectric", Phys. Rev. **127**, 1918–1939 (1962) (cit. on p. 27).

[143]H. G. de Chatellus, A. V. Sergienko, B. E. A. Saleh, M. C. Teich, and G. D. Giuseppe, "Non-collinear and non-degenerate polarization-entangled photon generation via concurrent type-i parametric downconversion in ppln", Opt. Express **14**, 10060–10072 (2006) (cit. on p. 27).

[144]A. C. Busacca, E. D'Asaro, A. Pasquazi, S. Stivala, and G. Assanto, "Ultraviolet generation in periodically poled lithium tantalate waveguides", Applied Physics Letters **93**, 121117 (2008) (cit. on p. 27).

[145]M. Fiorentino, S. M. Spillane, R. G. Beausoleil, T. D. Roberts, P. Battle, and M. W. Munro, "Spontaneous parametric down-conversion in periodically poled ktp waveguides and bulk crystals", Opt. Express **15**, 7479–7488 (2007) (cit. on p. 27).

[146]S. J. B. Yoo, R. Bhat, C. Caneau, and M. A. Koza, "Quasi-phase-matched second-harmonic generation in algaas waveguides with periodic domain inversion achieved by wafer-bonding", Applied Physics Letters **66**, 3410–3412 (1995) (cit. on p. 27).

[147]M. Ravaro, Y. Seurin, S. Ducci, G. Leo, V. Berger, A. De Rossi, and G. Assanto, "Nonlinear AlGaAs waveguide for the generation of counterpropagating twin photons in the telecom range", Journal of Applied Physics **98** (2005) 10.1063/1.2058197 (cit. on pp. 27, 148).

[148]A. De Rossi and V. Berger, "Counterpropagating Twin Photons by Parametric Fluorescence", Physical Review Letters **88**, 4 (2002) (cit. on pp. 29, 34).

[149]Y. J. Ding, S. J. Lee, and J. B. Khurgin, "Transversely pumped counterpropagating optical parametric oscillation and amplification", Physical Review Letters **75**, 429–432 (1995) (cit. on p. 29).

[150]L. Lanco, S. Ducci, J. P. Likforman, X. Marcadet, J. A. Van Houwelingen, H. Zbinden, G. Leo, and V. Berger, "Semiconductor waveguide source of counter-propagating twin photons", Physical Review Letters **97**, 25–28 (2006) (cit. on p. 29).

[151]Z. Liao, S. J. Wagner, M. Z. Alam, V. Tolstikhin, and J. S. Aitchison, "Vertically integrated spot-size converter in algaas-gaas", Opt. Lett. **42**, 4167–4170 (2017) (cit. on p. 29).

[152]L. Lanco, "Sources semiconductrices de photons jumeaux", PhD Thesis (Université Paris Diderot, 2006) (cit. on pp. 30, 54).

[153]G. Boucher, "Biphoton frequency-correlations engineering and measurement with a semiconductor microcavity", PhD Thesis (Université Paris Diderot, 2016) (cit. on pp. 31, 47, 55, 60, 97, 99).

[154]P. Yeh and A. Yariv, "Bragg reflection waveguides", Optics Communications **19**, 427–430 (1976) (cit. on p. 37).

[155]A. S. Helmy, "Phase matching using bragg reflection waveguides for monolithic nonlinear optics applications", Opt. Express **14**, 1243–1252 (2006) (cit. on p. 37).

[156]B. R. West and A. S. Helmy, "Properties of the quarter-wave bragg reflection waveguide: theory", J. Opt. Soc. Am. B **23**, 1207–1220 (2006) (cit. on p. 37).

[157]P. Abolghasem, J. Han, B. J. Bijlani, and A. S. Helmy, "Type-0 second order nonlinear interaction in monolithic waveguides of isotropic semiconductors", Optics Express **18**, 12681 (2010) (cit. on p. 40).

[158]G. Maltese, "Generation and manipulation of high-dimensional photonics states with algaas chips", PhD Thesis (Université Paris Diderot, 2019) (cit. on pp. 41, 48, 131).

[159]C. Autebert, "Algaas photonic devices: from quantum state generation to quantum communications", PhD Thesis (Université Paris Diderot, 2016) (cit. on pp. 42, 213, 215).

[160]K. H. Park, M. W. Kim, Y. T. Byun, D. Woo, S. H. Kim, S. S. Choi, Y. Chung, W. R. Cho, S. H. Park, and U. Kim, "Nondestructive propagation loss and facet reflectance measurements of GaAs/AlGaAs strip-loaded waveguides", Journal of Applied Physics **78**, 6318–6320 (1995) (cit. on p. 44).

[161]A. De Rossi, V. Ortiz, M. Calligaro, L. Lanco, S. Ducci, V. Berger, and I. Sagnes, "Measuring propagation loss in a multimode semiconductor waveguide", Journal of Applied Physics **97** (2005) 10.1063/1.1873059 (cit. on p. 44).

[162]R. Ghosh, C. K. Hong, Z. Y. Ou, and L. Mandel, "Interference of two photons in parametric down conversion", Physical Review A **34**, 3962–3968 (1986) (cit. on p. 47).

[163]Z. Yang, M. Liscidini, and J. E. Sipe, "Spontaneous parametric down-conversion in waveguides: A backward Heisenberg picture approach", Physical Review A - Atomic, Molecular, and Optical Physics **77**, 1–13 (2008) (cit. on p. 47).

[164]Z. D. Walton, A. V. Sergienko, B. E. Saleh, and M. C. Teich, "Generation of polarization-entangled photon pairs with arbitrary joint spectrum", Physical Review A - Atomic, Molecular, and Optical Physics **70**, 1–5 (2004) (cit. on pp. 47, 56).

[165]R. Loudon, *The quantum theory of light* (Oxford Science Publications, 2000) (cit. on pp. 49, 50, 59).

[166]C. K. Law, I. A. Walmsley, and J. H. Eberly, "Continuous frequency entanglement: Effective finite hilbert space and entropy control", Physical Review Letters **84**, 5304–5307 (2000) (cit. on p. 57).

[167]S. Parker, S. Bose, and M. B. Plenio, "Entanglement quantification and purification in continuous-variable systems", Physical Review A - Atomic, Molecular, and Optical Physics **61**, 8 (2000) (cit. on p. 57).

[168]J. P. W. Maclean, J. M. Donohue, and K. J. Resch, "Direct Characterization of Ultrafast Energy-Time Entangled Photon Pairs", Physical Review Letters **120**, 53601 (2018) (cit. on pp. 59, 90, 101).

[169]Y. Jeronimo-Moreno, S. Rodriguez-Benavides, and A. B. U'Ren, *Theory of cavity-enhanced spontaneous parametric downconversion*, tech. rep. 5 (2010), pp. 1221–1233 (cit. on p. 60).

[170]Z.-Y. J. Ou, *Multi-photon quantum interference*, 1st ed. (Springer US, 2007) (cit. on pp. 60, 157, 160).

[171]J. Paye, "Chronocyclic representation of ultrashort light pulses", Springer Series in Chemical Physics **28**, 133–135 (1993) (cit. on p. 63).

[172]W. Grice, "Interference and indistinguishability in ultrafast spontaneous parametric downconversion", PhD Thesis (University of Rochester, 1997) (cit. on p. 63).

[173]B. Brecht and C. Silberhorn, "Characterizing entanglement in pulsed parametric down-conversion using chronocyclic Wigner functions", Physical Review A - Atomic, Molecular, and Optical Physics **87**, 1–6 (2013) (cit. on p. 63).

[174]U. L. Andersen, J. S. Neergaard-Nielsen, P. Van Loock, and A. Furusawa, "Hybrid discrete- and continuous-variable quantum information", Nature Physics **11**, 713–719 (2015) (cit. on p. 66).

[175]R. M. Gomes, A. Salles, F. Toscano, P. H. Souto Ribeiro, and S. P. Walborn, "Quantum entanglement beyond Gaussian criteria", Proceedings of the National Academy of Sciences of the United States of America **106**, 21517–21520 (2009) (cit. on pp. 66, 116).

[176]Y. X. Ren, R. D. Lu, and L. Gong, "Tailoring light with a digital micromirror device", Annalen der Physik **527**, 447–470 (2015) (cit. on p. 69).

[177]T. W. Clark, R. F. Offer, S. Franke-Arnold, A. S. Arnold, and N. Radwell, "Comparison of beam generation techniques using a phase only spatial light modulator", Optics Express **24**, 6249 (2016) (cit. on pp. 69, 83).

[178]D. Stuart and A. Kuhn, "Single-atom trapping and transport in DMD-controlled optical tweezers", New Journal of Physics **20** (2018) 10.1088/1367-2630/aaa634 (cit. on p. 69).

[179]Z. Xu, C. Yang, P. Zhang, X. Zhang, Z. Cao, Q. Mu, Q. Sun, and L. Xuan, "Visible light high-resolution imaging system for large aperture telescope by liquid crystal adaptive optics with phase diversity technique", Scientific Reports **7** (2017) 10.1038/s41598-017-09595-2 (cit. on p. 69).

[180]Y. Zhi, B. Wang, and X. Yao, "Super-Resolution Scanning Laser Microscopy Based on Virtually Structured Detection", Critical reviews in biomedical engineering **43**, 297–322 (2015) (cit. on p. 69).

[181]J. H. Choi, J.-E. Pi, C.-Y. Hwang, J.-H. Yang, Y.-H. Kim, G. H. Kim, H.-O. Kim, K. Choi, J. Kim, and C.-S. Hwang, "Evolution of spatial light modulator for high-definition digital holography", ETRI Journal **41**, 23–31 (2019) (cit. on p. 69).

[182]S. A. Goorden, J. Bertolotti, and A. P. Mosk, "Superpixel-based spatial amplitude and phase modulation using a digital micromirror device", Optics Express **22**, 17999 (2014) (cit. on p. 69).

[183]Y. Ohtake, T. Ando, N. Fukuchi, N. Matsumoto, H. Ito, and T. Hara, "Universal generation of higher-order multiringed Laguerre-Gaussian beams by using a spatial light modulator", Optics Letters **32**, 1411 (2007) (cit. on p. 70).

[184]A. M. Weiner, "Femtosecond pulse shaping using spatial light modulators", Review of Scientific Instruments **71**, 1929–1960 (2000) (cit. on p. 70).

[185]A. Farré, M. Shayegan, C. López-Quesada, G. A. Blab, M. Montes-Usategui, N. R. Forde, and E. Martín-Badosa, "Positional stability of holographic optical traps", Opt. Express **19**, 21370–21384 (2011) (cit. on p. 70).

[186]B. Platt and R. Shack, "History and principles of shack-hartmann wavefront sensing", Journal of refractive surgery (Thorofare, N.J. : 1995) **17**, S573–7 (2001) (cit. on p. 76).

[187]J. C. Chanteloup, "Multiple-wave lateral shearing interferometry for wave-front sensing", Applied Optics **44**, 1559–1571 (2005) (cit. on p. 76).

[188]E. Bolduc, N. Bent, E. Santamato, E. Karimi, and R. W. Boyd, "Exact solution to simultaneous intensity and phase encryption with a single phase-only hologram", Optics Letters **38**, 3546 (2013) (cit. on pp. 78, 83, 88).

[189]L. G. Neto, D. Roberge, and Y. Sheng, "Full-range, continuous, complex modulation by the use of two coupled-mode liquid-crystal televisions", Applied Optics **35**, 4567 (1996) (cit. on p. 83).

[190]L. Zhu and J. Wang, "Arbitrary manipulation of spatial amplitude and phase using phase-only spatial light modulators", Scientific Reports **4**, 1–7 (2014) (cit. on p. 83).

[191]J. P. Kirk and A. L. Jones, "Phase-only complex-valued spatial filter", J. Opt. Soc. Am. **61**, 1023–1028 (1971) (cit. on p. 83).

[192]J. A. Davis, D. M. Cottrell, J. Campos, M. J. Yzuel, and I. Moreno, "Encoding amplitude information onto phase-only filters", Applied Optics **38**, 5004 (1999) (cit. on pp. 83, 84).

[193]V. Arrizón, U. Ruiz, R. Carrada, and L. A. González, "Pixelated phase computer holograms for the accurate encoding of scalar complex fields", Journal of the Optical Society of America A **24**, 3500 (2007) (cit. on p. 83).

[194]P. J. Mosley, J. S. Lundeen, B. J. Smith, and I. A. Walmsley, "Conditional preparation of single photons using parametric downconversion: A recipe for purity", New Journal of Physics **10** (2008) 10.1088/1367-2630/10/9/093011 (cit. on pp. 89, 104, 114).

[195]Y.-H. Kim and W. P. Grice, "Measurement of the spectral properties of the two-photon state generated via type ii spontaneous parametric downconversion", Opt. Lett. **30**, 908–910 (2005) (cit. on p. 89).

[196]W. Wasilewski, P. Wasylczyk, P. Kolenderski, K. Banaszek, and C. Radzewicz, "Joint spectrum of photon pairs measured by coincidence Fourier spectroscopy", Optics Letters **31**, 1130 (2006) (cit. on p. 89).

[197]M. Avenhaus, A. Eckstein, P. J. Mosley, and C. Silberhorn, "Fiber-assisted single-photon spectrograph", Opt. Lett. **34**, 2873–2875 (2009) (cit. on p. 89).

[198]M. Liscidini and J. E. Sipe, "Stimulated emission tomography", Physical Review Letters **111**, 1–5 (2013) (cit. on pp. 90, 96).

[199]A. Eckstein, G. Boucher, A. Lemaître, P. Filloux, I. Favero, G. Leo, J. E. Sipe, M. Liscidini, and S. Ducci, "High-resolution spectral characterization of two photon states via classical measurements", Laser and Photonics Reviews **8**, 76–80 (2014) (cit. on pp. 90, 97).

[200]S. Mittal, V. V. Orre, A. Restelli, R. Salem, E. A. Goldschmidt, and M. Hafezi, *Temporal and spectral manipulations of correlated photons using a time lens*, tech. rep. 4 (2017) (cit. on p. 90).

[201]Y. H. Kim and W. P. Grice, "Measurement of the spectral properties of the two-photon state generated via type-II spontaneous parametric down-conversion", Optics InfoBase Conference Papers **30**, 908–910 (2005) (cit. on p. 91).

[202]G. Brida, V. Caricato, M. V. Chekhova, M. Genovese, M. Gramegna, and T. S. Iskhakov, "Testing ultrafast two-photon spectral amplitudes via optical fibres", Optics Express **18**, 12915 (2010) (cit. on p. 91).

[203]A. O. C. Davis, P. M. Saulnier, M. Karpiński, and B. J. Smith, "Pulsed single-photon spectrometer by frequency-to-time mapping using chirped fiber Bragg gratings", Optics Express **25**, 12804 (2017) (cit. on p. 93).

[204]K. Zielnicki, K. Garay-Palmett, D. Cruz-Delgado, H. Cruz-Ramirez, M. F. O'Boyle, B. Fang, V. O. Lorenz, A. B. U'Ren, and P. G. Kwiat, "Joint spectral characterization of photon-pair sources", Journal of Modern Optics **65**, 1141–1160 (2018) (cit. on p. 96).

[205]C. K. Hong, Z. Y. Ou, and L. Mandel, "Measurement of Subpicosecond Time Intervals between Two Photons by Interference", **59**, 2044–2046 (1987) (cit. on pp. 101, 120, 124).

[206]T. Douce, A. Eckstein, S. P. Walborn, A. Z. Khoury, S. Ducci, A. Keller, T. Coudreau, and P. Milman, "Direct measurement of the biphoton Wigner function through two-photon interference", Scientific Reports **3**, 1–6 (2013) (cit. on pp. 101, 116, 132, 133, 142).

[207]I. Jizan, B. Bell, L. G. Helt, A. C. Bedoya, C. Xiong, and B. J. Eggleton, "Phase-sensitive tomography of the joint spectral amplitude of photon pair sources", Optics Letters **41**, 4803 (2016) (cit. on p. 101).

[208]J.-P. W. Maclean, S. Schwarz, and K. J. Resch, "Reconstructing ultrafast energy-time-entangled two-photon pulses", PHYSICAL REVIEW A **100**, 33834 (2019) (cit. on p. 101).

[209]R. W. Gerchberg and W. O. Saxton, "A Practical Algorithm for the Determination of Phase from Image and Diffraction Plane Pictures By", Optik **35**, 237–246 (1972) (cit. on p. 101).

[210]A. M. Brańczyk, T. C. Ralph, W. Helwig, and C. Silberhorn, "Optimized generation of heralded fock states using parametric down-conversion", New Journal of Physics **12**, 063001 (2010) (cit. on p. 104).

[211]A. Pe'er, B. Dayan, A. A. Friesem, and Y. Silberberg, "Temporal shaping of entangled photons", Physical Review Letters **94** (2005) `10.1103/PhysRevLett.94.073601` (cit. on p. 104).

[212]C. Bernhard, B. Bessire, T. Feurer, and A. Stefanov, "Shaping frequency-entangled qudits", Physical Review A - Atomic, Molecular, and Optical Physics **88**, 32322 (2013) (cit. on p. 104).

[213]J. M. Donohue, M. Mastrovich, and K. J. Resch, "Spectrally Engineering Photonic Entanglement with a Time Lens", Physical Review Letters **117**, 1–5 (2016) (cit. on p. 104).

[214]W. P. Grice, A. B. U'Ren, and I. A. Walmsley, "Eliminating frequency and space-time correlations in multiphoton states", Physical Review A - Atomic, Molecular, and Optical Physics **64**, 7 (2001) (cit. on p. 105).

[215]A. U'Ren, C. Silberhorn, R. Erdmann, K. Banaszek, W. Grice, I. Walmsley, and M. Raymer, "Generation of pure-state single-photon wavepackets by conditional preparation based on spontaneous parametric downconversion", Laser Physics **15** (2006) (cit. on p. 105).

[216]V. Ansari, J. M. Donohue, B. Brecht, and C. Silberhorn, "Tailoring nonlinear processes for quantum optics with pulsed temporal-mode encodings", Optica **5**, 534 (2018) (cit. on p. 105).

[217]F. Graffitti, D. Kundys, D. T. Reid, A. M. Brańczyk, and A. Fedrizzi, "Pure down-conversion photons through sub-coherence-length domain engineering", Quantum Science and Technology **2**, 35001 (2017) (cit. on p. 106).

[218]F. Graffitti, P. Barrow, M. Proietti, D. Kundys, and A. Fedrizzi, "Independent high-purity photons created in domain-engineered crystals", Optica **5**, 514 (2018) (cit. on p. 106).

[219]A. Dosseva, Ł. Cincio, and A. M. Brańczyk, "Shaping the joint spectrum of down-converted photons through optimized custom poling", Physical Review A **93**, 1–7 (2016) (cit. on p. 106).

[220]C. Chen, C. Bo, M. Y. Niu, F. Xu, Z. Zhang, J. H. Shapiro, and F. N. Wong, "Generation and characterization of factorable biphotons with 99% spectral purity", Optics InfoBase Conference Papers (2017) 10.1364/CLEO_QELS.2017.FW4E.1 (cit. on p. 106).

[221]A. Valencia, A. Ceré, X. Shi, G. Molina-Terriza, and J. P. Torres, "Shaping the waveform of entangled photons", Physical Review Letters **99**, 1–4 (2007) (cit. on p. 106).

[222]R. Kumar, J. R. Ong, M. Savanier, and S. Mookherjea, "Controlling the spectrum of photons generated on a silicon nanophotonic chip", Nature Communications **5**, 1–7 (2014) (cit. on pp. 106, 107).

[223]N. Tischler, A. Büse, L. G. Helt, M. L. Juan, N. Piro, J. Ghosh, M. J. Steel, and G. Molina-Terriza, "Measurement and Shaping of Biphoton Spectral Wave Functions", Physical Review Letters **115**, 1–5 (2015) (cit. on p. 106).

[224]R.-B. Jin, R. Shiina, and R. Shimizu, "Quantum manipulation of biphoton spectral distributions in a 2D frequency space toward arbitrary shaping of a biphoton wave packet", Optics Express **26**, 21153 (2018) (cit. on pp. 106, 124, 147).

[225]X. Caillet, V. Berger, G. Leo, and S. Ducci, "A semiconductor source of counterpropagating twin photons: A versatile device allowing the control of the two-photon state", Journal of Modern Optics **56**, 232–239 (2009) (cit. on p. 107).

[226]A. Crespi, L. Sansoni, G. Della Valle, A. Ciamei, R. Ramponi, F. Sciarrino, P. Mataloni, S. Longhi, and R. Osellame, "Particle statistics affects quantum decay and Fano interference", Physical Review Letters **114** (2015) 10.1103/PhysRevLett.114.090201 (cit. on pp. 123, 142, 143).

[227]I. Jex, G. Alber, S. Barnett, and A. Delgado, "Antisymmetric multi-partite quantum states and their applications", Fortschritte der Physik **51**, 172–178 (2003) (cit. on pp. 123, 143).

[228]S. K. Goyal, P. E. Boukama-Dzoussi, S. Ghosh, F. S. Roux, and T. Konrad, "Qudit-Teleportation for photons with linear optics", Scientific Reports **4** (2014) 10.1038/srep04543 (cit. on pp. 123, 143).

[229]Y. Zhang, F. S. Roux, T. Konrad, M. Agnew, J. Leach, and A. Forbes, "Engineering two-photon high-dimensional states through quantum interference", Science Advances **2** (2016) 10.1126/sciadv.1501165 (cit. on pp. 123, 126).

[230]J. Howell, "Beam Splitter Input-Output Relations", Tutorials in quantum information and quantum optics (Lectures Course - University of Rochester), 1–11 (cit. on p. 124).

[231]T. B. Pittman, D. V. Strekalov, A. Migdall, M. H. Rubin, A. V. Sergienko, and Y. H. Shih, "Can two-photon interference be considered the interference of two photons?", Physical Review Letters **77**, 1917–1920 (1996) (cit. on p. 126).

[232]I. Aharonovich, D. Englund, and M. Toth, "Solid-state single-photon emitters", Nature Photonics **10**, 631–641 (2016) (cit. on p. 126).

[233]J.-W. Pan, Z.-B. Chen, C.-Y. Lu, H. Weinfurter, A. Zeilinger, and M. Żukowski, "Multiphoton entanglement and interferometry", Rev. Mod. Phys. **84**, 777–838 (2012) (cit. on p. 126).

[234]D. Branning, A. L. Migdall, and A. V. Sergienko, "Simultaneous measurement of group and phase delay between two photons", **62**, 063808–063801 (2000) (cit. on p. 126).

[235]Y. Chen, M. Fink, F. Steinlechner, J. P. Torres, and R. Ursin, "Hong-Ou-Mandel interferometry on a biphoton beat note", npj Quantum Information **5** (2019) 10.1038/s41534-019-0161-z (cit. on pp. 126, 147).

[236]A. M. Brańczyk, "Hong-Ou-Mandel Interference", arXiv 1711.00080, 1–17 (2017) (cit. on p. 127).

[237]K. Wang, "Quantum theory of two-photon wavepacket interference in a beamsplitter", Journal of Physics B: Atomic, Molecular and Optical Physics **39** (2006) 10.1088/0953-4075/39/18/R01 (cit. on pp. 128, 129, 142).

[238]A. Fedrizzi, T. Herbst, M. Aspelmeyer, M. Barbieri, T. Jennewein, and A. Zeilinger, "Anti-symmetrization reveals hidden entanglement", New Journal of Physics **11** (2009) 10.1088/1367-2630/11/10/103052 (cit. on pp. 129, 142).

[239]L. Sansoni, F. Sciarrino, G. Vallone, P. Mataloni, A. Crespi, R. Ramponi, and R. Osellame, "Polarization entangled state measurement on a chip", Physical Review Letters **105** (2010) 10.1103/PhysRevLett.105.200503 (cit. on p. 132).

[240]G. Boucher, T. Douce, D. Bresteau, S. P. Walborn, A. Keller, T. Coudreau, S. Ducci, and P. Milman, "Toolbox for continuous-variable entanglement production and measurement using spontaneous parametric down-conversion", Physical Review A - Atomic, Molecular, and Optical Physics **92**, 1–5 (2015) (cit. on pp. 134, 143, 218).

[241]X. Caillet, A. Orieux, A. Lemaître, P. Filloux, I. Favero, G. Leo, and S. Ducci, "Two-photon interference with a semiconductor integrated source at room temperature", **18**, 9967 (2010) (cit. on p. 134).

[242]N. Fabre, G. Maltese, F. Appas, S. Felicetti, A. Ketterer, A. Keller, T. Coudreau, F. Baboux, M. I. Amanti, S. Ducci, et al., "Generation of a time-frequency grid state with integrated biphoton frequency combs", Phys. Rev. A **102**, 012607 (2020) (cit. on pp. 142, 147).

[243]L. Sansoni, F. Sciarrino, G. Vallone, P. Mataloni, A. Crespi, R. Ramponi, and R. Osellame, "Two-particle bosonic-fermionic quantum walk via integrated photonics", Physical Review Letters **108**, 1–5 (2012) (cit. on p. 143).

[244]S. Francesconi, F. Baboux, A. Raymond, N. Fabre, G. Boucher, A. Lemaitre, P. Milman, M. I. Amanti, and S. Ducci, "Engineering two-photon wavefunction and exchange statistics in a semiconductor chip", Optica **7** (2020) 10.1364/optica.379477 (cit. on p. 143).

[245]J. F. Clauser, M. A. Horne, A. Shimony, and R. A. Holt, "Proposed experiment to test local hidden-variable theories", Phys. Rev. Lett. **23**, 880–884 (1969) (cit. on p. 146).

[246]P. W. Shor, "Polynomial-time algorithms for prime factorization and discrete logarithms on a quantum computer", SIAM J. Comput. **26**, 1484–1509 (1997) (cit. on p. 146).

[247]D. Bouwmeester, J.-W. Pan, K. Mattle, M. Eibl, H. Weinfurter, and A. Zeilinger, "Experimental quantum teleportation", Nature **390**, 575–579 (1997) (cit. on p. 146).

[248]A. K. Ekert, "Quantum cryptography based on bell's theorem", Phys. Rev. Lett. **67**, 661–663 (1991) (cit. on p. 146).

[249]P. G. Kwiat, K. Mattle, H. Weinfurter, A. Zeilinger, A. V. Sergienko, and Y. Shih, "New high-intensity source of polarization-entangled photon pairs", Phys. Rev. Lett. **75**, 4337–4341 (1995) (cit. on p. 146).

[250]P. G. Kwiat, E. Waks, A. G. White, I. Appelbaum, and P. H. Eberhard, "Ultrabright source of polarization-entangled photons", Phys. Rev. A **60**, R773–R776 (1999) (cit. on p. 146).

[251]B.-S. Shi and A. Tomita, "Generation of a pulsed polarization entangled photon pair using a sagnac interferometer", Phys. Rev. A **69**, 013803 (2004) (cit. on p. 146).

[252]N. Matsuda, H. Le Jeannic, H. Fukuda, T. Tsuchizawa, W. J. Munro, K. Shimizu, K. Yamada, Y. Tokura, and H. Takesue, "A monolithically integrated polarization entangled photon pair source on a silicon chip", Scientific Reports **2**, 817 (2012) (cit. on p. 147).

[253]P. Sarrafi, E. Y. Zhu, B. M. Holmes, D. C. Hutchings, S. Aitchison, and L. Qian, "High-visibility two-photon interference of frequency–time entangled photons generated in a quasi-phase-matched algaas waveguide", Opt. Lett. **39**, 5188–5191 (2014) (cit. on p. 147).

[254]M. de Burgh and S. D. Bartlett, "Quantum methods for clock synchronization: beating the standard quantum limit without entanglement", Phys. Rev. A **72**, 042301 (2005) (cit. on p. 147).

[255]J. Nunn, L. J. Wright, C. Söller, L. Zhang, I. A. Walmsley, and B. J. Smith, "Large-alphabet time-frequency entangled quantum key distribution by means of time-to-frequency conversion", Optics Express **21**, 15959 (2013) (cit. on p. 147).

[256]Z. Y. Ou and L. Mandel, "Observation of spatial quantum beating with separated photodetectors", Physical Review Letters **61**, 54–57 (1988) (cit. on p. 147).

[257]J. G. Rarity and P. R. Tapster, "Two-color photons and nonlocality in fourth-order interference", **41** (1990) (cit. on p. 147).

[258]F. Kaneda, H. Suzuki, R. Shimizu, and K. Edamatsu, "Direct generation of frequency-bin entangled photons via two-period quasi-phase-matched parametric downconversion", Optics Express **27**, 1416 (2019) (cit. on p. 147).

[259]X. Li, L. Yang, X. Ma, L. Cui, Z. Y. Ou, and D. Yu, "All-fiber source of frequency-entangled photon pairs", Physical Review A - Atomic, Molecular, and Optical Physics **79** (2009) 10.1103/PhysRevA.79.033817 (cit. on p. 147).

[260]S. Ramelow, L. Ratschbacher, A. Fedrizzi, N. K. Langford, and A. Zeilinger, "Discrete tunable color entanglement", Physical Review Letters **103**, 2–5 (2009) (cit. on pp. 147, 172, 173).

[261]"Counterpropagating entangled photons from a waveguide with periodic nonlinearity", Physical Review A - Atomic, Molecular, and Optical Physics **66**, 8 (2002) (cit. on p. 148).

[262]N. K. Langford, "Encoding, manipulating and measuring quantum information in optics", PhD Thesis (University of Queensland, 2007) (cit. on p. 151).

[263]P. G. Kwiat, "Hyper-entangled states", Journal of Modern Optics **44-11**, 2173–2184 (1997) (cit. on p. 151).

[264]Y.-H. Kim, S. P. Kulik, M. V. Chekhova, W. P. Grice, and Y. Shih, "Experimental entanglement concentration and universal bell-state synthesizer", Phys. Rev. A **67**, 010301 (2003) (cit. on p. 152).

[265]J. D. Franson, "Bell inequality for position and time", Physical Review Letters **62**, 2205–2208 (1989) (cit. on p. 163).

[266]M. Halder, S. Tanzilli, H. De Riedmatten, A. Beveratos, H. Zbinden, and N. Gisin, "Photon-bunching measurement after two 25-km-long optical fibers", Physical Review A - Atomic, Molecular, and Optical Physics **71** (2005) `10.1103/PhysRevA.71.042335` (cit. on p. 163).

[267]Z. Y. Ou, X. Y. Zou, L. J. Wang, and L. Mandel, "Observation of nonlocal interference in separated photon channels", Physical Review Letters **65**, 321–324 (1990) (cit. on p. 163).

[268]P. G. Kwiat, W. A. Vareka, C. K. Hong, H. Nathel, and R. Y. Chiao, "Correlated two-photon interference in a dual-beam Michelson interferometer", Physical Review A **41**, 2910–2913 (1990) (cit. on p. 163).

[269]W. K. Wootters, "Entanglement of formation of an arbitrary state of two qubits", Phys. Rev. Lett. **80**, 2245–2248 (1998) (cit. on p. 173).

[270]B. Jaskorzynska, L. Thylén, and J. Nilsson, "Modal reflectivity of uptapered, tilted-facet, and antireflection-coated diode-laser amplifiers", **8**, 484 (1991) (cit. on pp. 175–177, 188).

[271]T. Saitoh, T. Mukai, and O. Mikami, "Theoretical analysis and fabrication of antireflection coatings on laser-diode facets", Journal of Lightwave Technology **3**, 288–293 (1985) (cit. on p. 176).

[272]D. Marcuse, "Reflection loss of laser mode from tilted end mirror", Journal of Lightwave Technology **7**, 336–339 (1989) (cit. on p. 176).

[273]Z. Wang, B. Mikkelsen, K. E. Stubkjaer, and D. S. Olesen, "Single-layer coating for angled facet amplifier", Electronics Letters **25**, 1139–1141 (1989) (cit. on p. 177).

[274]D. A. Steck, *Classical and modern optics* (available online at http://steck.us/teaching (revision 1.7.6, 20 February 2020), 2006) (cit. on p. 183).

[275]P. Kumar, M. K. Wiedmann, C. H. Winter, and I. Avrutsky, "Optical properties of Al2O3 thin films grown by atomic layer deposition", Applied Optics **48**, 5407–5412 (2009) (cit. on p. 183).

[276]L. A. Dobrzański, M. Szindler, A. Drygała, and M. M. Szindler, "Silicon solar cells with Al2O3 antireflection coating", Central European Journal of Physics **12**, 666–670 (2014) (cit. on p. 183).

[277]J. D. Rancourt, *Optical thin films: user handbook*, 1st ed. (SPIE Optical Engineering Press, 1996) (cit. on p. 185).

[278]J. Kempe, "Quantum random walks: An introductory overview", Contemporary Physics **44**, 307–327 (2003) (cit. on p. 191).

[279]J. B. Spring, B. J. Metcalf, P. C. Humphreys, W. S. Kolthammer, X. M. Jin, M. Barbieri, A. Datta, N. Thomas-Peter, N. K. Langford, D. Kundys, et al., "Boson sampling on a photonic chip", Science **339**, 798–801 (2013) (cit. on pp. 191, 192).

[280]S. Panahiyan and S. Fritzsche, "Simulation of the multiphase configuration and phase transitions with quantum walks utilizing a step-dependent coin", Phys. Rev. A **100**, 062115 (2019) (cit. on p. 192).

[281]A. Blanco-Redondo, I. Andonegui, M. J. Collins, G. Harari, Y. Lumer, M. C. Rechtsman, B. J. Eggleton, and M. Segev, "Topological Optical Waveguiding in Silicon and the Transition between Topological and Trivial Defect States", Physical Review Letters **116**, 1–5 (2016) (cit. on p. 192).

[282]M. Gräfe, R. Heilmann, M. Lebugle, D. Guzman-Silva, A. Perez-Leija, and A. Szameit, "Integrated photonic quantum walks", Journal of Optics (United Kingdom) **18** (2016) 10.1088/2040-8978/18/10/103002 (cit. on p. 192).

[283]C. A. Ryan, M. Laforest, J. C. Boileau, and R. Laflamme, "Experimental implementation of a discrete-time quantum random walk on an nmr quantum-information processor", Phys. Rev. A **72**, 062317 (2005) (cit. on p. 192).

[284]P. M. Preiss, R. Ma, M. E. Tai, A. Lukin, M. Rispoli, P. Zupancic, Y. Lahini, R. Islam, and M. Greiner, "Strongly correlated quantum walks in optical lattices", Science **347**, 1229–1233 (2015) (cit. on p. 192).

[285]F. Zähringer, G. Kirchmair, R. Gerritsma, E. Solano, R. Blatt, and C. F. Roos, "Realization of a quantum walk with one and two trapped ions", Phys. Rev. Lett. **104**, 100503 (2010) (cit. on p. 192).

[286]M. Lebugle, M. Gräfe, R. Heilmann, A. Perez-Leija, S. Nolte, and A. Szameit, "Experimental observation of N00N state Bloch oscillations", Nature Communications **6**, 1–7 (2015) (cit. on p. 192).

[287]T. Giordani, F. Flamini, M. Pompili, N. Viggianiello, N. Spagnolo, A. Crespi, R. Osellame, N. Wiebe, M. Walschaers, A. Buchleitner, et al., "Experimental statistical signature of many-body quantum interference", Nature Photonics **12**, 173–178 (2018) (cit. on p. 192).

[288]S. Paesani, Y. Ding, R. Santagati, L. Chakhmakhchyan, C. Vigliar, K. Rottwitt, L. K. Oxenløwe, J. Wang, M. G. Thompson, and A. Laing, "Generation and sampling of quantum states of light in a silicon chip", Nature Physics **15**, 925–929 (2019) (cit. on p. 192).

[289]D. N. Christodoulides, F. Lederer, and Y. Silberberg, "Discretizing light behaviour in linear and nonlinear waveguide lattices", Nature **424**, 817–823 (2003) (cit. on p. 193).

[290]A. S. Solntsev, F. Setzpfandt, A. S. Clark, C. W. Wu, M. J. Collins, C. Xiong, A. Schreiber, F. Katzschmann, F. Eilenberger, R. Schiek, et al., "Generation of nonclassical biphoton states through cascaded quantum walks on a nonlinear chip", Physical Review X **4**, 1–13 (2014) (cit. on pp. 193, 203).

[291]W.-p. Huang, "Coupled-mode theory for optical waveguides : an overview", **11**, 963–983 (1994) (cit. on pp. 194, 196).

[292]B. E. A. Saleh and M. C. Teich, *Fundamentals of photonics; 2nd ed.* Wiley series in pure and applied optics (Wiley, New York, NY, 2007) (cit. on p. 196).

[293]R. Kruse, F. Katzschmann, A. Christ, A. Schreiber, S. Wilhelm, K. Laiho, A. Gábris, C. S. Hamilton, I. Jex, and C. Silberhorn, "Spatio-spectral characteristics of parametric down-conversion in waveguide arrays", New Journal of Physics **15** (2013) 10.1088/1367-2630/15/8/083046 (cit. on p. 198).

[294]W. P. Su, J. R. Schrieffer, and A. J. Heeger, "Solitons in polyacetylene", Phys. Rev. Lett. **42**, 1698–1701 (1979) (cit. on p. 203).

[295]J. Yeom, Y. Wu, and M. A. Shannon, "Critical aspect ratio dependence in deep reactive ion etching of silicon", **2**, 1631–1634 vol.2 (2003) (cit. on p. 208).

[296]Y. Okamura, S. Yoshinaka, and S. Yamamoto, "Measuring mode propagation losses of integrated optical waveguides: a simple method", Appl. Opt. **22**, 3892–3894 (1983) (cit. on p. 215).

[297]J. Belhassen, F. Baboux, Q. Yao, M. Amanti, I. Favero, A. Lemaître, W. S. Kolthammer, I. A. Walmsley, and S. Ducci, "On-chip III-V monolithic integration of heralded single photon sources and beamsplitters", Applied Physics Letters **112**, 071105 (2018) (cit. on p. 218).

Génération sur puce d'états photoniques intriqués à haute dimension

Introduction

La photonique joue actuellement un rôle clé dans le développement des technologies pour l'information quantique. En effet les photons, grâce à leur vitesse de propagation et leur robustesse à la décohérence, transportent efficacement l'information sur de longues distances. Jusqu'à présent les protocoles d'information quantique ont principalement utilisé les degrés de liberté associés à des variables discrètes des photons (par exemple la polarisation), mais pour exploiter au mieux tous les avantages de la mécanique quantique on assiste à un intérêt croissant pour les degrés de liberté associés à des variables continues. La définition d'un alphabet dans des espaces de Hilbert de dimension infinie permettrait par exemple d'accroître la sécurité et la densité de codage dans la transmission d'information. Dans cette perspective, il est donc essentiel de développer des outils pour générer et contrôler les états quantiques dans ces degrés de liberté.

Grâce à leur maturité technologique et leur propriétés optoélectroniques, les matériaux III-V constituent une plateforme idéale pour développer des sources de lumière quantique sur puce. Grâce à sa forte nonlinéarité du deuxième ordre, la plateforme GaAs/AlGaAs permet la génération de paires de photons aux longueurs d'onde télécom, par conversion paramétrique spontanée (SPDC en anglais) à température ambiante.

Dans ce contexte, cette thèse de doctorat est consacrée au développement de nouvelles sources semi-conductrices de paires de photons. En exploitant la grande flexibilité offerte par la conversion paramétrique spontanée dans les guides d'ondes AlGaAs, nous démontrons la génération et l'ingénierie d'états de lumière non classiques à haute dimension, en particulier dans les degrés de liberté de fréquence et de modes spatiaux.

Dans cette thèse deux types de sources sont développées et analysées. D'abord, nous démontrons qu'en utilisant l'accord de phase contra-propageant et une géométrie de pompage transverse il est possible d'obtenir un haut niveau de contrôle sur l'état quantique en fréquence émis. Ensuite, nous commençons le développement d'un nouveau dispositif formé par un réseau de guides d'ondes nonlinéaires parallèles capable d'émettre des paires de photons intriquées dans le degré de liberté spatial en exploitant des marches quantiques en cascade.

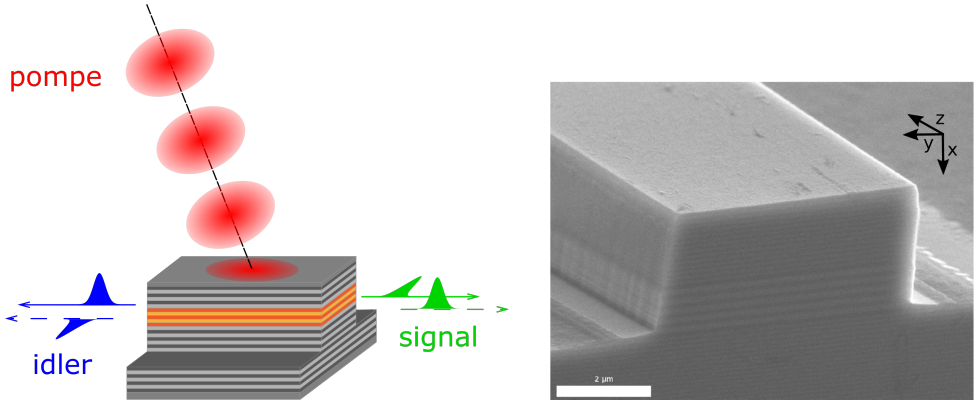

(a) (b)

Figure 9.1: Schéma de la source de photons jumeaux basée sur l'accord de phase contra-propageant (a) et image au microscope électronique à balayage (MEB) de sa facette (b).

.

Ingénierie d'états en fréquence

Dans cette partie de la thèse, nous utilisons un guide d'onde avec microcavité verticale intégrée, émettant des photons jumeaux se propageant dans des directions opposées, comme montré sur la Figure 9.1. Ce dispositif est basé sur une configuration de pompage transverse, dans laquelle un champ de pompe (à 775 nm) est incident avec un angle θ sur le dessus du guide d'onde et génère par SPDC deux champs guidés, appelés signal (à droite) et idler (à gauche), avec des polarisations orthogonales.

Notre travail démontre expérimentalement l'ingénierie des corrélations en fréquence des paires de photons générées. À cette fin, nous avons d'abord introduit l'amplitude spectrale jointe (JSA en anglais), une fonction à valeur complexe qui décrit toutes les propriétés temporelles et spectrales des photons, et deux techniques expérimentales (la tomographie par émission stimulée et un spectographe à fibre pour photons uniques) qui permettent de reconstruire le module carré de la JSA, appelé intensité spectrale jointe (JSI en anglais).

Les propriétés spectrales des états générés par la source sont directement héritées des propriétés de la pompe via les relations de conservation de l'énergie et du vecteur d'onde. Ainsi, en modifiant la taille et la phase spatiale du faisceau de pompe on peut soit générer soit effacer des corrélations spectrales selon l'application visée.

La Figure 9.2 montre l'intensité spectrale jointe (JSI) mesurée par tomographie par émission stimulée. Nous avons changé la taille du faisceau de pompe pour générer des états corrélés, non corrélés et anti-corrélés (de gauche à droite).

D'autre part, le profil de phase spatial du faisceau de pompe détermine la phase de la JSA et permet donc une ingénierie plus poussée de l'état quantique. Dans la Figure 9.3, en utilisant un modulateur spatial de lumière, nous avons ajouté un déphasage au centre du faisceau de pompe ; on observe alors une séparation de la densité spectrale jointe en deux lobes distincts lorsque le déphasage introduit est

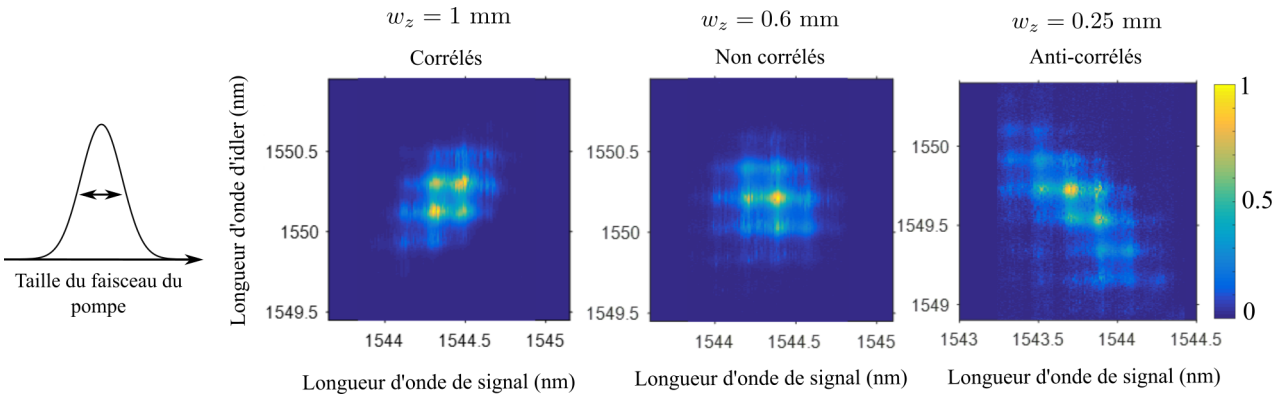

Figure 9.2: Corrélations en fréquence mesurées expérimentalement en changeant la taille du faisceau de pompe.

de π (Figure 9.3d), par rapport à un déphasage nul (Figure 9.3a).

Ensuite, en utilisant un interféromètre de Hong-Ou-Mandel (HOM) nous avons analysé la parité de la fonction d'onde de ces deux états quantiques (sans et avec déphasage). Les simulations numériques de la probabilité de coïncidences (troisième colonne de la figure) et les mesures expérimentales (quatrième colonne) montrent un net changement allant d'un comportement coalescent (creux de coïncidences), typique de la statistique bosonique, à un comportement anti-coalescent (pic de coïncidences), typique de la statistique fermionique.

Ces résultats pourraient ainsi être exploités pour étudier l'effet des statistiques d'échange dans divers problèmes de simulation quantique, et pour mettre en œuvre des protocoles de communication et de calcul exploitant des états quantiques antisymétriques à haute dimension.

De plus, nous avons également prouvé que cette source, grâce à sa structure et à son design, peut émettre des paires de photons intriqués dans un degré de liberté hybride polarisation/fréquence. Cet état quantique présente une intrication simultanée mais non indépendante dans ces deux degrés de liberté. La présence d'intrication dans ce degré de liberté hybride a été vérifiée par un interféromètre de Hong-Ou-Mandel, montrant également que l'effet de cavité, produit par la réflectivité des facettes de la source, complexifie l'état quantique produit. Pour cette raison, nous avons développé un traitement anti-reflet qui a permis de réduire la réflectivité des facettes de R=27% à R=10% et ainsi d'augmenter la qualité de l'intrication hybride. La Figure 9.4 montre les interferogrammes HOM expérimentaux : à gauche sans le traitement anti-reflet (visibilité V=48.2%) et à droite avec le traitement anti-reflet (visibilité V=70.1%).

Ingénierie d'états intriqués spatialement

Dans la deuxième partie du manuscrit, nous avons détaillé le développement d'un nouveau dispositif capable d'émettre des paires de photons intriqués spatialement. Le dispositif consiste en un réseau de sources SPDC parallèles et couplées par couplage évanescent. Un schéma du dispositif est montré dans la Figure 9.5a. Les photons générés, effectuant des marches quantiques en cascade, sont intriqués dans

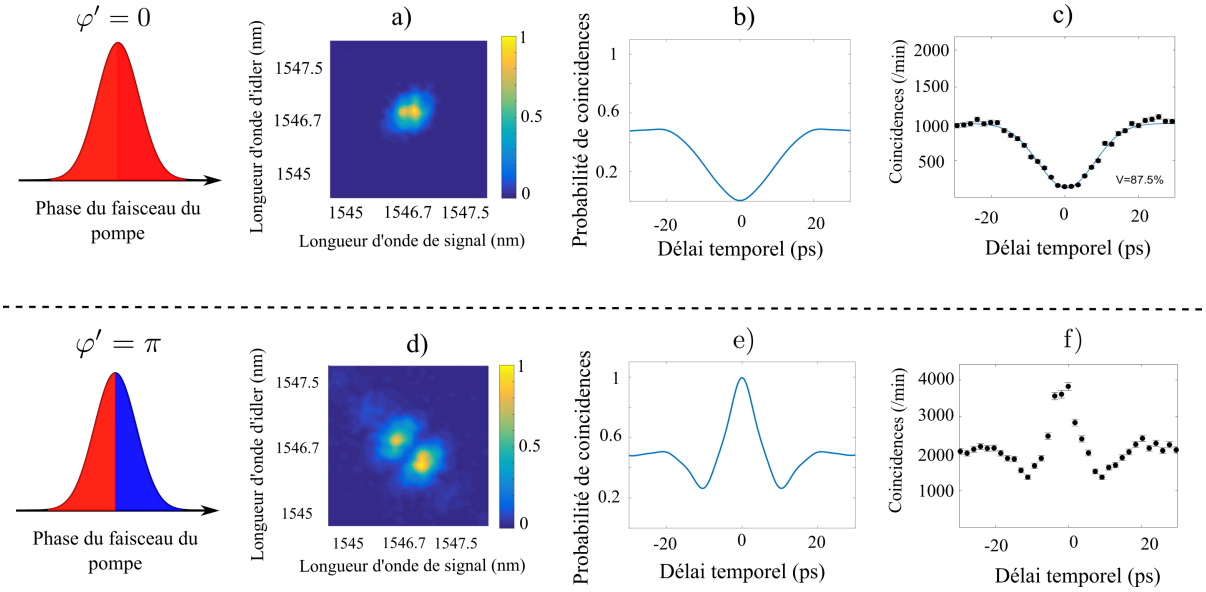

Figure 9.3: Intensité spectrale jointe (JSI) mesurée avec un spectrographe fibré à photons uniques pour un faisceau de pompe à phase plate ($\varphi' = 0$) (a), et interférogrammes HOM correspondants calculé (b) et mesuré (c). Intensité spectrale jointe (d) et interférogrammes HOM (e-f) pour un faisceau de pompe avec un déphasage ($\varphi' = \pi$).

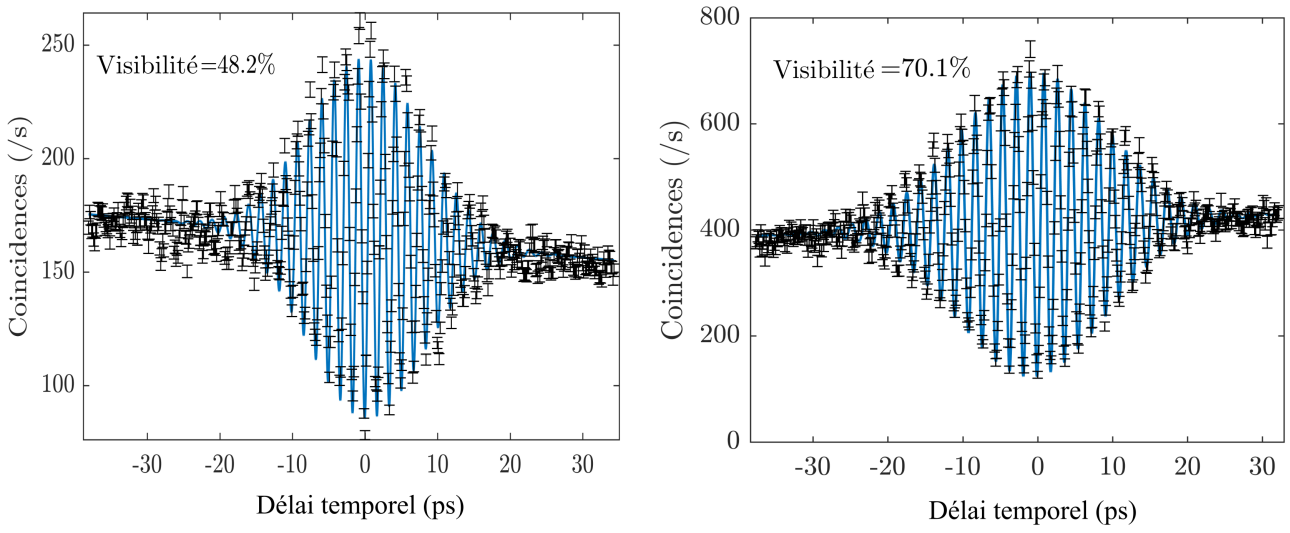

Figure 9.4: Interférogrammes HOM générés par un état intriqué dans le dégrée de liberté hybride polarisation/fréquence dans le cas d'un dispositif sans (gauche) et avec (droite) traitement antireflets.

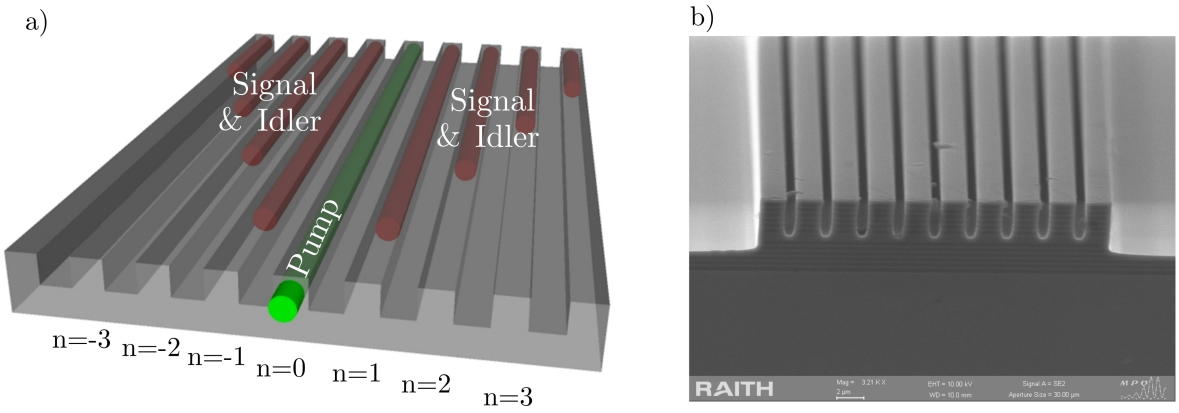

Figure 9.5: (a) Schéma d'un réseau de guides d'ondes non linéaires. Le faisceau de pompe (en vert) génère des paires de photons qui subissent des marches quantiques (rouge), qui entraîne une intrication spatiale sur l'ensemble du réseau. (b) Image MEB d'un réseau de guides d'ondes AlGaAs.

leur position spatiale dans le réseau.

Les procédés de fabrication de ce dispositif ont été optimisés et la caractérisation optique d'une première génération du dispositif a été réalisée. La Figure 9.5b montre une image MEB d'un réseau de guides. Ceci nous a permis d'identifier des pistes pour l'optimisation des processus de fabrication du dispositif.

Ces réseaux de guides doivent permettre à terme d'effectuer des tâches de simulation quantique, pour étudier des phénomènes comme la localisation d'Anderson d'état multipartites ou la protection topologique dans le régime quantique.

Conclusions

Les résultats présentés dans ce travail de thèse démontrent l'ingénierie d'états photoniques à haute dimension générés dans des puces photoniques semi-conductrices. Ces dispositifs fonctionnent à température ambiante et aux longueurs d'onde télécom et peuvent donc être intégrés dans des circuits photoniques plus complexes, capable d'effectuer des tâches quantiques avec une empreinte limitée , une étape clé pour le déplacement hors-laboratoire des technologies quantiques du monde réel.

Université de Paris

LISTE DES ÉLÉMENTS SOUS DROITS

Liste de **tous les éléments retirés** de la version complète de la thèse
faute d'en détenir les droits

Document à intégrer dans la version partielle de la thèse

Illustrations, figures, images...

Légende de l'image	N° de l'image	Page(s) dans la thèse
Three group-velocity matching conditions…	Figure 5.1	105
Numerical simulations of the JSI produced by…	Figure 5.2	107
Scheme of a network of directional couplers…	Figure 9.1	193
A continuously coupled waveguide array for…	Figure 9.2	194